NNT : 0000AIXM0000

THÈSE DE DOCTORAT

Soutenue à Aix-Marseille Université
le 30 septembre 2024 par

Victor VIALLON

Analysis of the Reactivity Loss of the Phenix Core Cycles for the Experimental Validation of APOLLO3®

Discipline
Physique et sciences de la matière

Spécialité
Energie, Rayonnement et Plasma

École doctorale
ED 352 – Physique et sciences de la matière

Laboratoire/Partenaires de recherche
CEA/DES/IRESNE/DER/SPRC/LEPh
(Laboratoire d'Etudes Physiques)

Composition du jury
Adrien BIDAUD – Rapporteur / Président du jury
Professeur, Grenoble INP

Oscar CABELLOS - Rapporteur
Professeur, Universidad Politécnica de Madrid

Mariya BROVCHENKO - Examinatrice
Ingénieur Docteur, IRSN

Cyrille DE-SAINT-JEAN - Examinateur
Directeur de recherche, CEA/DAM-DIF

Christophe SCHNEIDESCH - Examinateur
Ingénieur Docteur, Tractebel

Laurent BUIRON - Directeur de thèse
Directeur de recherche, CEA Cadarache

Elias-Yammir GARCIA-CERVANTES - Membre invité
Ingénieur Docteur, CEA Cadarache

Affidavit

Je soussigné, Victor Viallon, déclare par la présente que le travail présenté dans ce manuscrit est mon propre travail, réalisé sous la direction scientifique de Laurent Buiron, dans le respect des principes d'honnêteté, d'intégrité et de responsabilité inhérents à la mission de recherche. Les travaux de recherche et la rédaction de ce manuscrit ont été réalisés dans le respect à la fois de la charte nationale de déontologie des métiers de la recherche et de la charte d'Aix-Marseille Université relative à la lutte contre le plagiat.
Ce travail n'a pas été précédemment soumis en France ou à l'étranger dans une version identique ou similaire à un organisme examinateur.

Fait à Aix-en-Provence, le 27 juin 2024



Cette œuvre est mise à disposition selon les termes de la Licence Creative Commons Attribution - Pas d'Utilisation Commerciale - Pas de Modification 4.0 International.

Liste de publications et/ou brevets et participation aux conférences

1) Liste des publications et/ou brevet réalisées dans le cadre du projet de thèse :

    1. V. Viallon, E. Y. Garcia Cervantes, and L. Buiron, “Numerical validation of the APOLLO3®-FR deterministic calculation route based on a simplified Phenix configuration”, in *Annals of Nuclear Energy*, Volume 208, 2024, 110782, ISSN 0306-4549, https://doi.org/10.1016/j.anucene.2024.110782.

2) Participation aux conférences et écoles d’été au cours de la période de thèse :

    1. V. Viallon, E.Y. Garcia-Cervantes and L. Buiron, ”Interpretation of weight absorber rod experiment BALZAC-1H with APOLLO-3® and TRIPOLI-4®”, Gyeongju-Korea, Proceedings of the 2023 International Congress on Advances in Nuclear Power Plants (ICAPP 2023), 2023,– Poster presentation

    2. V. Viallon, E. Y. Garcia Cervantes, and L. Buiron, “Impact of the multiphysics coupling on the reactivity swing and fuel depletion of an SFR Phenix like subassembly”, San Francisco-USA, Proceedings of the international conference on physics of reactors (PHYSOR 2024), 2024 – Oral presentation delivered by peer.

    3. V. Viallon, E. Y. Garcia Cervantes, and L. Buiron, “Impact of irradiation history on Boltzmann/Bateman coupled sensitivities: Application to SFR subassembly”, Lucca-Italy, Proceedings of the Best Estimate Plus Uncertainty International Conference (BEPU 2024), 2024 – Oral presentation delivered by peer.

Résumé

Le développement de futurs réacteurs repose sur des méthodologies de conception se basant sur un recours massif aux outils de calcul scientifique (OCS). Pour assurer leur capacité de prédiction, les codes doivent être validés expérimentalement sur tous les phénomènes possibles et toutes les technologies de réacteurs cibles. Parmi ces différents phénomènes, la perte de réactivité des réacteurs à neutrons rapides refroidis au sodium a un intérêt du point de vue de la sûreté et d'un point de vue technico-économique. Cependant, les données expérimentales pour ce phénomène sont peu nombreuses et l'objectif de la thèse a été de déterminer si les cycles d'irradiation du réacteur Phénix pouvaient fournir des éléments de validation pour l'OCS APOLLO3®.

Pour aborder cette problématique, un cycle permettant de mener dans de bonnes conditions les différentes analyses a pu être déterminé. La valeur expérimentale de la perte de réactivité a pu être réinterprétée avec des méthodes de référence et en assurer la fiabilité. Ensuite, la fidélité de la modélisation de la perte de réactivité avec APOLLO3®-RNR a été augmentée jusqu'à la prise en compte de phénomènes multiphysiques. A l'aide des sensibilités couplées Boltzmann/Bateman récemment implémentées dans APOLLO3®, il a été possible de calculer l'incertitude due aux données nucléaires et le biais de la modélisation. Cela a permis de caractériser l'OCS APOLLO3® vis-à-vis de la perte de réactivité et d'identifier que l'incertitude due aux données nucléaires était supérieure à l'incertitude expérimentale et bien supérieure au biais de calculs. Cela a permis de confirmer que les cycles de puissances du réacteur Phénix pouvaient être utiliser pour la validation des OCS modernes mais aussi d'identifier leur potentiel pour la production de bibliothèques ajustées en soutient au déploiement des futurs réacteurs.

Mots clés : Perte de réactivité, Phénix, VVQI, APOLLO3®, MENDEL, RNR-Na, Assimilation

Abstract

The development of future reactors relies heavily on design methodologies that utilize Scientific Computational Tools (SCTs). To ensure their predictive capability, these codes must be experimentally validated across all possible phenomena and target reactor technologies. Among these phenomena, the reactivity loss in sodium-cooled fast reactors is of interest from both safety and techno-economic perspectives. However, experimental data for this phenomenon are scarce. This thesis aims to determine if the irradiation cycles of the Phenix reactor can provide validation elements for the APOLLO3® tool.

To address this issue, a suitable cycle for conducting various analyses under favorable conditions was identified. The experimental value of reactivity loss was reinterpreted using reference methods to ensure its reliability. Subsequently, the accuracy of modeling reactivity loss with APOLLO3®-FR was enhanced by incorporating multiphysics phenomena. Utilizing the recently implemented coupled Boltzmann/Bateman sensitivities in APOLLO3®, the uncertainty due to nuclear data and modeling bias was calculated. This allowed for characterizing the APOLLO3® tool concerning reactivity loss and identifying that the uncertainty due to nuclear data was higher than the experimental uncertainty and significantly greater than the calculation bias.

This has made it possible to confirm that the power cycles of the Phenix reactor can be used for the validation of modern OCS, and also to identify their potential for producing tailored libraries to support the deployment of future reactors.

Keywords: Reactivity loss, Phenix, VVUQ, APOLLO3®, MENDEL, Sodium Fast Reactors, Assimilation

Résumé étendu

1. Introduction

Dans le contexte actuel de crises environnementales et énergétiques, l'énergie nucléaire, précédemment mise de côté par certaines politiques énergétiques mondiales après l'accident de Fukushima Daiichi en 2011, connaît un regain d'intérêt global. À mesure que les défis et les contraintes énergétiques évoluent, de nouvelles exigences en termes de sûreté, de durabilité et d'économie apparaissent et nécessitent des concepts innovants. Le développement et le dimensionnement de ces nouveaux réacteurs se basent sur l'utilisation intensive des outils de calcul scientifique (OCS). Ceux-ci se doivent donc d'être validés, avec des biais maitrisés, tout en étant capables de quantifier l'incertitude due aux données d'entrée pour tous les phénomènes et technologies possibles. Cette démarche d'évaluation des OCS se nomme Vérification, Validation et Quantification des Incertitudes (VVQI). Pour cela, il est nécessaire de se baser sur des expériences représentatives des domaines d'utilisation visés par l'OCS pour que sa prédictibilité soit assurée.

Une des technologies considérées parmi les multiples technologies visées est le Réacteur à Neutrons Rapides refroidis au sodium (RNR-Na). Pour ce type de réacteur, la connaissance de l'évolution des grandeurs neutroniques pendant l'irradiation est primordiale pour la sûreté (l'effet de vidange qui se dégrade avec l'augmentation du taux de combustion) mais aussi pour des considérations économiques - par exemple le temps de cycle, la quantité de matière fissile nécessaire en début de cycle, etc. Le nombre d'expériences fournissant des données sur le comportement général d'un cœur de RNR-Na en irradiation est relativement limité. Néanmoins, la France dispose d'un retour d'expérience important concernant cette technologie avec notamment le réacteur Phénix qui a fonctionné pendant plus de 40 ans à travers plus de 50 cycles d'irradiation.

La validation expérimentale de l'évolution de l'inventaire isotopique dans le réacteur est complexe, car il n'est actuellement pas possible de la mesurer directement. Cependant, son effet sur la réactivité du cœur, notamment la perte de réactivité, peut potentiellement fournir des informations pour la validation expérimentale des codes concernant l'usure du combustible. Le principal défi pour valider expérimentalement la perte de réactivité réside dans l'acquisition de données expérimentales. De plus, cela nécessite d'avoir la capacité de modéliser ce phénomène tout en gérant les contraintes de décomposition des biais et de quantification des incertitudes inhérentes aux exigences de VVQI moderne.

Par conséquent, l'objectif de cette thèse a été d'étudier les cycles du réacteur Phénix, afin de déterminer s'ils peuvent fournir des informations utiles pour la validation expérimentale de la perte de réactivité due à l'évolution du combustible des OCS

modernes. Le tout, en se basant sur les capacités de l'OCS de nouvelle génération APOLLO3®.

2. Évolution du combustible

L'évolution du combustible est un phénomène neutronique couplant le flux neutronique, gouverné par l'équation du transport des neutrons (équation de Boltzmann) aux compositions isotopiques gouvernées par l'équation de Bateman. Dans un réacteur de puissance, la production d'énergie, les flux neutroniques et les températures entraînent des modifications des matériaux/structures avec des dilatations thermiques, du fluage sous irradiation, des restructurations des pastilles combustibles, etc. Ces phénomènes apportent une complexité additionnelle au problème initial et nécessitent de coupler les équations de la neutronique aux équations de la mécanique des milieux continus et de la thermo-hydraulique. Dans ce manuscrit ces équations sont désignées par « équations Multi-Physiques » (MP).

Dans la pratique, le problème est simplifié en remplaçant ces équations par des valeurs moyennes globales. Par exemple une température moyenne uniforme au lieu de la distribution réelle des températures. Or, dans un contexte de validation numérique avancée, ces hypothèses ne peuvent plus être considérées, ou alors le biais qu'implique ces hypothèses doit être estimé. Ainsi, avec les capacités de modélisations de l'OCS APOLLO3® (notamment le schéma de calcul spécifique aux RNR-Na, APOLLO3®-RNR) pour l'équation de Boltzmann et de MENDEL pour l'équation de Bateman, il est possible d'envisager une modélisation couplée globale avec le code combustible GERMINAL V2 (cf. Figure A).

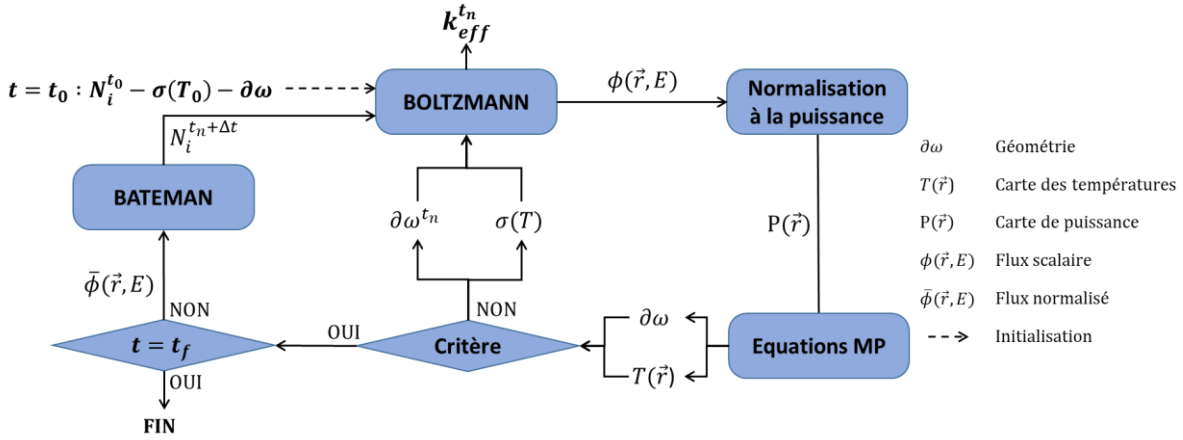

Figure A. Schéma général d'un calcul d'évolution du combustible

Néanmoins, aborder directement cet exercice pour une configuration existante d'un cœur de Phénix pourrait masquer des compensations entre les différentes hypothèses du schéma. Pour initier le travail de décomposition de ces biais, une validation numérique a été effectuée sur un modèle simplifié du cœur Phénix (Phenix-Like). Réaliser cela dans un

premier temps permet de déterminer le biais du schéma de calcul APOLLO3®-RNR pour l'équation du transport seul. Les résultats, sur l'efficacité des barres de commande et la distribution des taux de réaction présentent de bons accords avec les calculs stochastiques de référence TRIPOLI-4®. Cela indique que ce schéma peut être considéré pour des calculs d'évolution dans des configurations cœur plus complexes. Par ailleurs, le couplage avec GERMINALV2 a été mis en œuvre et appliqué à l'évolution d'un assemblage Phénix en milieu infini. Cela a permis de montrer la pertinence de ce couplage pour le phénomène de perte de réactivité et qu'il devrait être étendu à un calcul d'évolution à l'échelle du cœur.

3. Perte de réactivité expérimentale

En amont du calcul à l'échelle cœur avec APOLLO3®, il a fallu étudier les cycles de Phénix et en sélectionner un qui permettait d'avoir des conditions de calcul optimales (puissance quasi-constante) et des conditions expérimentales permettant son analyse. Dans le cas du réacteur Phénix, la perte de réactivité était compensée par l'extraction des barres de commande. Pour réaliser l'analyse expérimentale de la perte de réactivité d'un cycle de Phénix, il suffit donc de trouver un cycle ayant à ses débuts, une expérience de pesée de barre. La pesée permet d'obtenir la courbe de réactivité extraite par les barres de commande et donc d'obtenir la perte de réactivité du cycle en connaissant la position des barres à chaque instant (cf. la Figure B).

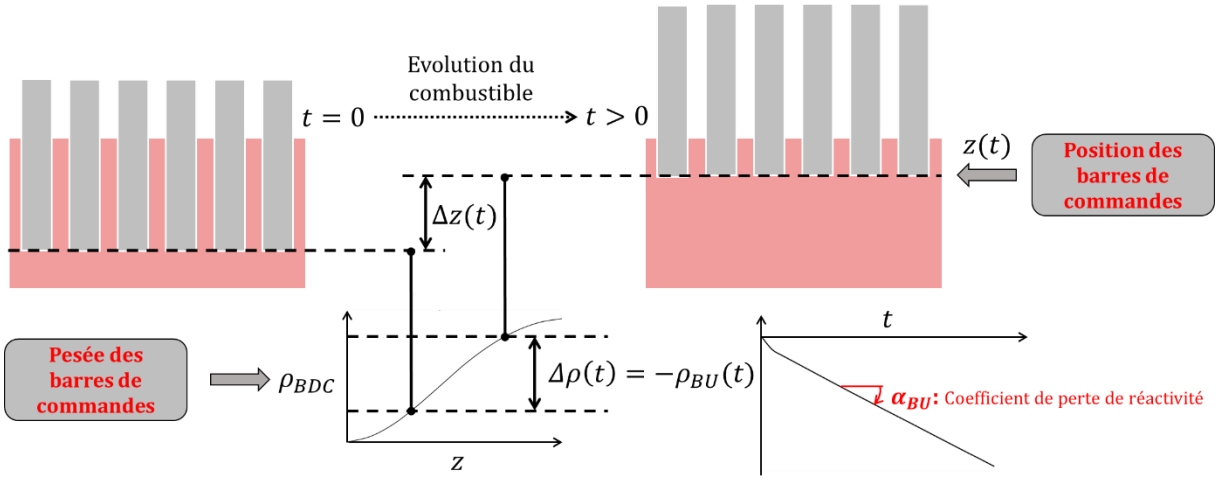

Figure B. Description simplifiée de la détermination de la valeur de la perte de réactivité expérimentale pour le réacteur Phénix

Avec ces différents critères le cycle N° 42-115 a pu être choisi. Cependant, les anciennes analyses comportaient un certain nombre de limitations qu'il a fallu lever pour obtenir une valeur expérimentale fiable et associée à une incertitude. Pour cela, un certain nombre de coefficients ont été recalculés avec des méthodes de référence Monte-Carlo. Le coefficient de perte de réactivité expérimentale a pu être amélioré et évalué à **-4.644 ¢/JEPP** (Jours Équivalents Pleine Puissance) au lieu de **-5.622 ¢/JEPP** avec les données initiales (cf. la Figure C).

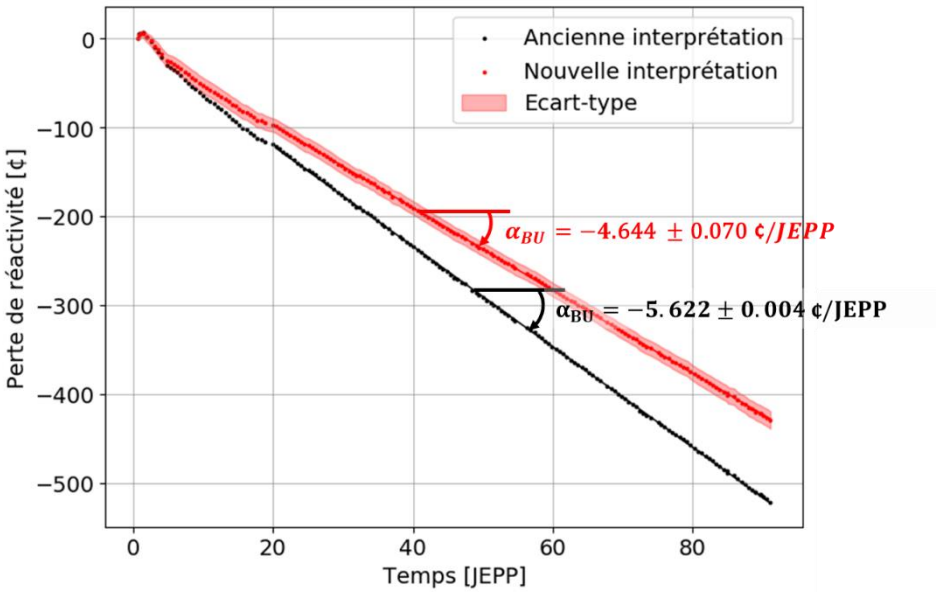

Figure C. Réinterprétation de la perte de réactivité du cycle 42-115 de Phénix avec des outils modernes comparativement à l'ancienne interprétation (sans considérer l'incertitude due à la puissance)

Pour établir la confiance de cette nouvelle valeur, une propagation des incertitudes des paramètres d'entrée a été effectuée en utilisant une méthode Monte-Carlo. Cette approche a permis de quantifier l'incertitude du coefficient de perte de réactivité à une valeur conservatrice de 3.35% et d'identifier les principaux contributeurs, notamment la puissance (3% pour la puissance et 1.5% pour le reste des contributeurs).

Il a été montré qu'un effort de calcul plus important en augmentant le critère de convergence pour les calculs TRIPOLI-4® et des calculs de structure pour la loi de dilatation thermique pourrait permettre de réduire les composantes secondaires. Cependant pour la puissance expérimentale utilisée pour normaliser le coefficient de perte de réactivité, la principale limitation réside dans la disponibilité de l'information. Les diverses sources d'informations trouvées dans les archives permettent d'estimer une incertitude conservatrice, mais difficilement de determinier une incertitude de facon rigureuse et realiste. Ainsi, la reconstruction des données expérimentales provenant des anciens réacteurs de puissance à l'aide de méthodes modernes est possible et apporte une amélioration significative par rapport aux interprétations précédentes. Néanmoins, la disponibilité limitée de l'incertitude de certains composants restreint la réduction significative de l'incertitude expérimentale réalisable avec les OCS modernes.

4. Perte de réactivité calculée avec APOLLO3®

Avec la détermination de la valeur expérimentale de la perte de réactivité du cycle 42 de Phénix, il a été possible de valider expérimentalement le schéma APOLLO3®-FR en évolution. Pour effectuer la validation, certaines hypothèses couramment utilisées dans

les calculs d'évolution du combustible ont été partiellement supprimées afin de réaliser la simulation la plus réaliste possible jusqu'au couplage multiphysique avec GERMINAL V2. Cela a permis de quantifier l'impact des diverses hypothèses couramment utilisées sur le coefficient de perte de réactivité et d'identifier les choix de modélisation importants à prendre en compte lors du calcul de ce coefficient. Ainsi, il a été montré qu'il était important de considérer les paramètres de modélisation suivants :

- Évolution du ^{10}B des barres de commande
- Évolution de la carte de températures
- Migration des gaz de fission
- Extraction des barres de commande durant le cycle

Relever ces différentes hypothèses en les considérant dans la simulation a permis d'obtenir la valeur Best-Estimate du schéma de calcul APOLLO3®-FR en évolution pour le cycle de Phénix N°42, de **-4.650 ¢/JEPP** (C/E=1.0013), ce qui est en très bon accord avec la valeur expérimentale.

Pour les exigences actuelles de validation expérimentale, l'écart avec l'expérience doit cependant être considéré en prenant en compte à la fois les incertitudes expérimentales et les incertitudes de calcul, composées de l'incertitude due aux données nucléaires et des biais numériques restants. Usuellement, la quantification des biais restants pour une modélisation donnée se fait par la comparaison avec une méthode de référence. Or pour un problème complexe comme la perte de réactivité d'un réacteur de puissance comme Phénix, un tel calcul n'est pas disponible. Néanmoins, il est possible d'estimer ces biais par une méthode détournée et il a été montré que la connaissance des sensibilités du coefficient de perte de réactivité aux données nucléaires pouvait permettre une telle estimation, en plus d'être nécessaires pour la quantification des incertitudes dues aux données nucléaires.

5. Sensibilités couplées Boltzmann/Bateman

En neutronique, les sensibilités dues aux données nucléaires peuvent être déterminé en un seul calcul grâce à des formulations adjointes des différentes théories des perturbations. Or, pour les problématiques de couplage Boltzmann/Bateman, un formalisme spécifique est nécessaire, la théorie des perturbations en évolution, ou, sensibilités couplées Boltzmann/Bateman. Ces sensibilités se calculent en réalisant une évolution adjointe de la fin de l'irradiation vers son début. Elles sont construites via plusieurs termes (un terme direct, un terme de Bateman, deux termes de Flux et un terme de puissance) qui modélisent l'impact des différentes équations impliquées dans le couplage Boltzmann/Bateman et leurs différentes interconnexions et s'expriment avec l'équation suivante :

$$S_p^R = \frac{p}{R}\left\{\frac{\partial R}{\partial p} + \sum_{i=1}^{I}\langle\int_{t_i}^{t_{i+1}} dt\boldsymbol{N}^*\frac{\partial \mathcal{A}_i}{\partial p}\boldsymbol{N}\rangle + \sum_{i=1}^{I}\langle\Gamma_i^*\frac{\partial \mathcal{H}_i}{\partial p}\phi_i\rangle + \sum_{i=1}^{I}\langle\Gamma_i\frac{\partial \mathcal{H}_i^*}{\partial p}\,\phi_i^*\rangle - \sum_{i=1}^{I}P_i^*\langle\frac{\partial \kappa\sigma_{fc}}{\partial p}\boldsymbol{N_i}\phi_i\rangle\right\}$$

Ce formalisme, de par sa complexité de mise en place, n'avait encore jamais été utilisé pour un réacteur de puissance (ou avec des hypothèses majeures comme par exemple une modélisation RZ du cœur). Cependant, ce formalisme a été implémenté dans le code APOLLO3®, ce qui a permis de calculer les sensibilités liées la perte de réactivité du cycle 42 du réacteur Phénix.

Ces sensibilités, dans un premier temps, apportent une aide précieuse pour la compréhension des phénomènes étudiés et leur quantification. Par exemple, dans la Figure E, il est présenté le profil 33-groupes des sensibilités couplées de la capture de l'^{238}U pour les différents termes Boltzmann/Bateman. Ceux-ci montrent que le terme de Bateman est prépondérant notamment parce que c'est grâce à la capture de l'^{238}U que le ^{239}Pu est produit (qui lui, a un impact majeur sur l'évolution du coefficient de multiplication). De plus, la différence majeure avec le terme direct seul (terme qui aurait été obtenu sans le formalisme couplé Boltzmann/Bateman) montre l'importance de ce formalisme pour les phénomènes d'évolution du combustible.

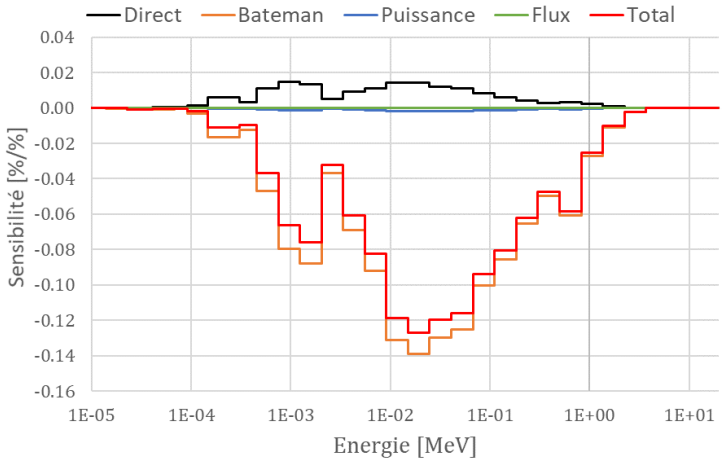

Figure E. Illustration des différents termes des sensibilités couplées de la capture de l'^{238}U pour la perte de réactivité (le signe négatif implique qu'une pertubation positive sur la capture de l'^{238}U diminue la perte de réactivité)

Avec ces sensibilités et la compréhension des phénomènes physiques qu'elles apportent, il a été possible d'estimer le biais numérique du schéma APOLLO3®/MENDEL à environ 1% sur le coefficient de perte de réactivité. Néanmoins, l'implémentation actuelle de ce formalisme dans APOLLO3® implique que l'historique d'irradiation antérieur au cycle 42 ne peut pas être pris en compte à cause de l'impossibilité de projeter les compositions adjointes entre deux cycles (deux configurations différentes). Or, pour l'incertitude due aux données nucléaires, il est nécessaire de réaliser l'évolution adjointe jusqu'au début de l'irradiation de tous les assemblages qui sont présents au cycle 42 (donc en remontant sur plusieurs cycles en non uniquement le 42). Ainsi, ignorer cet historique d'irradiation introduit un biais dans les sensibilités.

Le biais d'une telle considération a été étudié sur le cas simplifié d'un assemblage Phénix en milieu infini (comme pour l'étude du couplage multiphysique dans la première partie). Dans ce cas maîtrisé, il a été possible de réaliser des évolutions adjointes complètes (FB) et partielles en ignorant le début d'irradiation (LC) pour les comparer. Il a été montré que les sensibilités partielles surestiment les sensibilités pour les captures et fissions des noyaux lourds (d'environ 20% pour les taux de combustions impliqués dans le cycle 42) et sous-estiment celles des rendements de fission (10% pour les taux de combustions impliqués dans le cycle 42) comme l'illustre la Figure F.

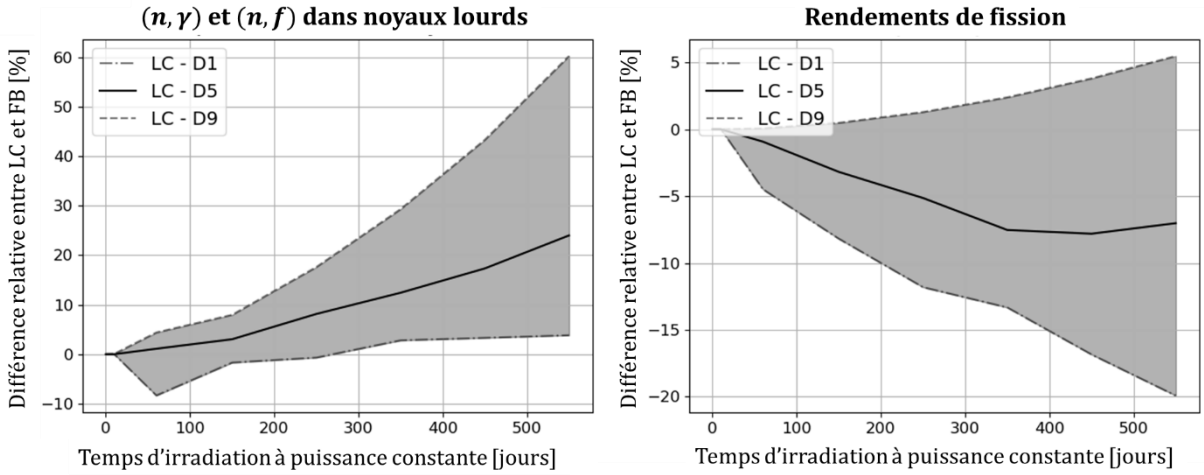

Figure F. Différence entre les sensibilités LC et FB pour les 150 premiers contributeurs à l'incertitude. D1 signifie premier décile, D5, la médiane et D9, le neuvième décile.

Étant donné les similarités entre les sensibilités des cas assemblage et cœur, cette tendance a pu être extrapolée au cycle 42. Par conséquent, cela a permis de calculer l'incertitude des données nucléaires JEFF 3.1.1 pour la perte de réactivité.

Pour quantifier une telle incertitude, la matrice de covariance COMAC V1 a été utilisée. Étant donné que les sensibilités associées aux rendements de fission, aux rapports de branchement, aux constantes de désintégration et aux énergies de fission étaient difficilement accessibles auparavant, leurs covariances n'étaient pas directement disponibles. Ainsi, la matrice COMAC V1 a été mise à jour avec les données manquantes, ce qui a permis de quantifier l'incertitude totale due aux données nucléaires à 7,33 % sur le coefficient de perte de réactivité du cycle 42 de Phénix (cf. le Tableau 1). Comme la contribution principale est faite par la capture et la fission des noyaux lourds, il a pu être considéré que cette incertitude calculée avec les sensibilités LC était conservatrice.

Tableau 1. Décomposition des différents contributeurs à l'incertitude due aux données nucléaires de JEFF 3.1.1 pour la perte de réactivité du cycle 42-115 de Phénix

Données nucléaires	Incertitude [%]
COMAC V1	**7.333**

Ancienne COMAC V1	7.250
Produits de Fission manquants	0.191
Noyaux lourds manquants	0.067
Rendements de fission	1.019
Constante de désintégration	0.016
Énergie de fission	0.343

Finalement, l'analyse expérimentale couplée avec une approche Best-Estimate pour la détermination de la valeur calculée et le formalisme des sensibilités couplées Boltzmann/Bateman a rendu possible de caractériser la perte de réactivité du cycle 42 et le schéma APOLLO3®/MENDEL :

- $\frac{C}{E} - 1 = +0.13\ \%$
- $\frac{\Delta E}{E} = 3.35\ \%$
- $\frac{\Delta C_{DN}^{JEFF3.1.1}}{C} = 7.33\% \left| \frac{\Delta C_{biais}}{C} = 1\ \% \right| \frac{\Delta C_{puissance}}{C} = 2.76\ \%$

Cela a donc permis de déterminer que l'écart calcul/expérience et le biais numérique associé étaient significativement plus faibles que l'incertitude expérimentale et l'incertitude due aux données nucléaires JEFF 3.1.1.

6. Perspectives d'assimilation de données

Dans ces conditions, l'expérience peut permettre de contraindre les données nucléaires via l'assimilation de données pour obtenir des valeurs a posteriori qui coïncident avec l'expérience. Pour étudier l'apport que pourrait avoir la perte de réactivité pour les données nucléaires, un exercice d'assimilation de données (en multigroupe et avec des méthodes simples dans le cadre de ce manuscrit) a été proposé avec l'outil CONRAD. Étant donné un écart à l'expérience faible, les sections efficaces ne sont que très peu touchées et ne montrent pas d'inconsistances particulières. De plus, l'assimilation a permis une réduction significative de l'incertitude due aux données nucléaires, en partie par la réduction de la variance des différentes réactions, mais surtout et principalement par la production de nouvelles corrélations comme l'illustre la Figure G.

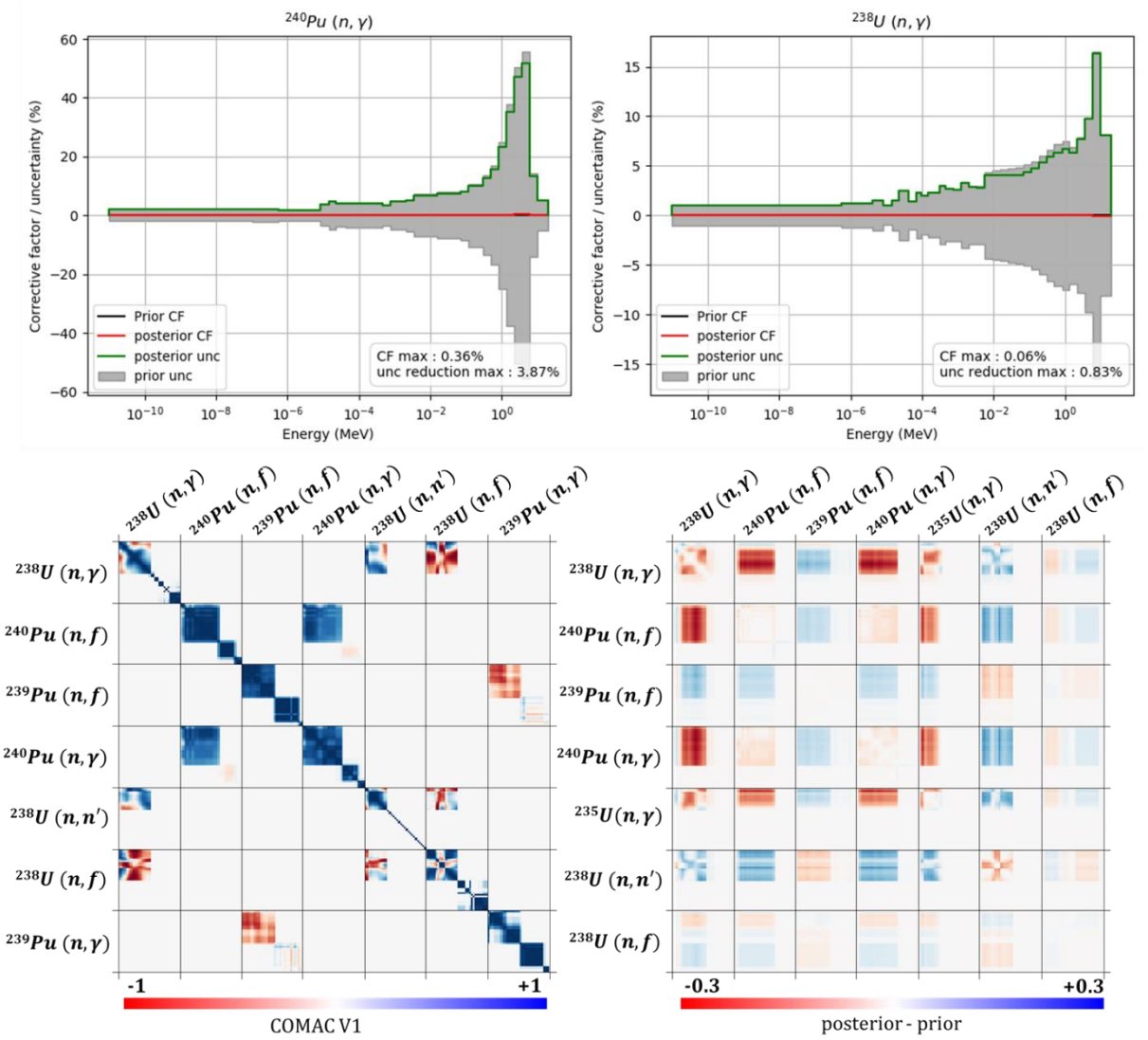

Figure G. Résultats de l'assimilation de données pour la perte de réactivité du cycle 42 de Phénix. En haut, les facteurs correctifs (CF) et incertitudes a posteriori des deux réactions les plus impactées. En bas, la matrice de corrélation a priori et les nouvelles corrélations produites

Le sens physique de ces corrélations et leurs utilisations restent des débats ouverts dans le domaine de l'assimilation des données nucléaires et devront être abordés dans des travaux dédiés, hors du champ de cette thèse. En attendant, les limitations dues aux données d'entrées ont été étudiées (sur les sensibilités partielles à la place des sensibilités totales, le biais du schéma APOLLO3®/MENDEL et l'impact des corrélations initiales) et ne montrent pas d'inconsistances particulières qui remettraient en cause les conclusions principales.

L'intérêt principal de l'assimilation de données, pour le soutien au développement des réacteurs futurs, est dans son potentiel à produire des bibliothèques de données nucléaires ajustées pour des cas d'utilisations/technologies spécifiques. Avec ces

bibliothèques, les incertitudes sont plus faibles et maîtrisées qu'avec les bibliothèques générales et permettent une optimisation plus poussée des marges de conception (mais uniquement dans un domaine d'application restreint). Dans les bibliothèques ajustées qui ont pu être réalisées dans le passé comme avec ERALIB pour Superphénix (qui avait démontrer les gains et l'intérêt d'une telle approche), les données en irradiations n'étaient pas disponibles, car les formalismes nécessaires n'étaient pas disponibles. Pour étudier l'intérêt que peut avoir la perte de réactivité dans ce cadre, l'exercice a donc été étendu et appliqué sur d'autres expériences. En réalisant cela, il a pu être obtenu une réduction significative de l'incertitude due aux données nucléaires pour des expériences sur d'autres réacteurs, comme une expérience de poids de barres de Superphénix ou la perte de réactivité du réacteur JOYO.

7. Conclusion

L'exercice de VVQI et d'assimilation présenté pour la perte de réactivité de Phénix a permis d'étendre la confiance dans le schéma APOLLO3®/MENDEL et d'entrevoir la possibilité d'élargir son domaine de validation avec ce type d'expérience. Cela a démontré que les codes de dernière génération permettent de supprimer les anciennes hypothèses, tout en considérant des méthodes avancées et des capacités de couplage. Les défis expérimentaux précédents concernant les réacteurs de puissances peuvent être relevés avec une confiance accrue grâce à ces outils de dernière génération ce qui permet une meilleure maîtrise de la valeur expérimentale et a fortiori de la validation expérimentale des codes et éventuellement des bibliothèques ajustées obtenue via l'assimilation.

Cependant pour consolider ces résultats et atteindre ces objectifs de validation expérimentale et d'assimilation de données, certaines limitations doivent encore être résolues :

- Être en capacité de calculer les sensibilités avec une évolution adjointe totale plutôt que partielle en pouvant projeter les compositions adjointes entre deux configurations différentes
- Réduire le biais numérique pour éviter la transmission de celui-ci aux données nucléaires en considérant des schémas plus avancés, en visant de plus, à obtenir des solutions de références Monte-Carlo sur lequel se baser pour l'évolution du combustible
- Étendre le domaine de VVQI à la multiphysique en quantifiant les incertitudes dues aux données d'entrées des autres physiques (mécanique combustible, thermo-hydraulique) et en proposant un couplage plus avancé avec les OCS de dernières générations pour tous les domaines impliqués (notamment un code de thermo-hydraulique dédié)
- Étudier l'impact que peut avoir le couplage multiphysique sur les sensibilités couplées Boltzmann/Bateman et déterminer si ce formalisme doit être généralisé en introduisant de nouveaux termes

- Réaliser l'assimilation de données avec les méthodes les plus avancées disponibles (marginalisation par exemple) et un ensemble d'expérience plus grand couvrant le plus de phénomènes possibles pour être capable d'évaluer et de tester la contribution de la perte de réactivité en tant qu'expérience intégrale. Un tel travail pourrait être envisagé, en particulier avec les expériences disponibles dans des bases de données partagées comme DICE et IDAT, ainsi que des outils d'analyse comme NDaST.

De plus, le plein potentiel des sensibilités couplées Boltzmann/Bateman désormais disponibles peut être exploré. Un certain nombre d'expériences d'irradiation, telles que PROFIL, peuvent être utilisées avec le formalisme approprié pour quantifier l'incertitude due aux données nucléaires. De plus, l'étude sur la perte de réactivité, principalement menée pour un cycle spécifique du réacteur Phénix, peut être appliquée à d'autres cycles, mais aussi à d'autres réacteurs et technologies. En outre, en permettant la connexion de la fin du cycle à son début et en réduisant l'évolution du combustible à un vecteur de sensibilité représentatif, ce formalisme offre des perspectives pour la méta-modélisation de l'irradiation dans des domaines avec un grand nombre de paramètres à étudier et où le temps de calcul neutronique est une contrainte significative (par exemple la conception, les scénarios, etc.).

Finalement, avec ces nouveaux outils, les couplages multiphysiques sont de plus en plus accessibles. Les contraintes expérimentales pour la VVQI des codes soutenant le développement des nouvelles technologies nucléaires évoluent alors avec eux, et les programmes expérimentaux doivent s'adapter. Par conséquent, il est nécessaire de mettre en place un programme expérimental pour soutenir la R&D, en utilisant un réacteur flexible permettant d'étudier tous types de phénomènes et d'analyser simultanément toutes les composantes multiphysiques, afin de correspondre au niveau de détails des modélisations actuelles et futures. Ainsi, les dernières limitations dues aux incertitudes des données d'entrées (données nucléaires ou autres) pourront être surpassées grâce à l'assimilation, permettant leur transposition aux réacteurs en développement dans le cadre d'une approche unifiée VVQI-AT (VVQI – Assimilation/Transposition). Dans ce contexte, des travaux avancés de conception et d'instrumentation seront nécessaires pour déterminer le niveau de flexibilité requis et les incertitudes expérimentales cibles afin de répondre à ces nouveaux besoins.

Mots clés : Perte de réactivité, Phénix, VVQI, APOLLO3®, MENDEL, RNR-Na, Assimilation

Remerciements

Je tiens tout d'abord à remercier très chaleureusement mon directeur de thèse Laurent Buiron qui m'a encadré depuis le début de mon stage jusqu'à la fin de ma thèse. Merci de m'avoir permis de donner le meilleur de moi-même en me fournissant les outils informatiques et le soutien techique et scientifique qui m'a permis de le faire et de rester les pieds sur Terre durant les grands moments de panique lors de la rédaction…

Je remercie aussi immensément Elias Garcia, qui m'a encadré pendant cette thèse, pour sa disponibilité et son soutien sur les aspects techniques, physiques et les inombrables doutes. Merci pour avoir subi mon anglais et mon style d'écriture … dense… jusqu'au bout (pour le meilleur je l'espère) et surtout, un grand merci pour avoir su me transmettre, avec Laurent, ce qu'est la beauté d'une thèse dans son ensemble et me permettre de pouvoir être fier de ce travail.

Je remercie les membres du jury Adrien Bidaud, Oscar Cabellos, Mariya Brovchenko, Cyrille De-Saint-Jean et Christophe Schneidesch pour avoir accepté de faire partie de mon jury. Merci pour vos différents retours et les discussions lors de la soutenance qui ont permis d'améliorer le manuscrit.

Ensuite je tiens à remercier Véronique Bellanger-Villard, Jean-Christophe Bosq et Edwige Richebois pour m'avoir permis de réaliser cette thèse au sein du SPRC/LEPh mais aussi de pouvoir continuer en tant qu'ingénieur chercheur dans le même laboratoire.

Je remercie tous mes collègues du LEPh et LE2C qui m'ont aidé à un moment ou à un autre dans mes travaux de thèse, que ce soit sur des problématiques techniques, de codes ou de physique. Merci à Johann M. et Ettore G. pour leurs aides avec INCA. Merci à Jean T. et Giorgio V. pour leurs aides sur des points de neutronique. Merci à Frederic M., Geraud P., Pierre S. et Dorian D.C. pour leurs aides dans les archives et les souvenirs du réacteur Phénix. Merci, à David B., Abdelhazize C., Grégoire K., Pierre T., Oliver S. et Gilles N. pour leurs aides et leurs retours sur l'exercice d'assimilation.

Et bien évidemment je remercie tous les doctorants et amis qui ont permis de m'offrir le meilleur des cadres possibles, que ce soit au CEA ou en dehors : Mathias, François, Simon, Maxime, Emilie, Pauline, Dusan, Baptiste, Guillaume, Sophie, Damien, Clementine, Dorian, Pierre-Louis, Maël, Nicolas, Kevin, Barbara et encore bien d'autres.

Contents

Affidavit 3
Liste de publications et/ou brevets et participation aux conférences 4
Résumé 5
Abstract 6
Résumé étendu 7
Remerciements 18
Contents 19
List of Figures 23
List of Table 27
List of Abbreviations 29
Chapter 1. Introduction 31
Chapter 2. Fuel depletion 35
2.1. Fuel Depletion calculation 36
2.1.1. Physical description 36
2.1.2. Solving the Bateman equation 42
2.1.3. Solving the stationary Boltzmann equation 43
2.1.4. APOLLO3®/MENDEL deterministic scheme 52
2.1.5. Contribution of the new approach 53
2.2. Phenix reactor 56
2.2.1. Reactor presentation 56
2.2.2. Phenix Geometry modeling 60
2.2.1. Specific features of the Phenix reactor and fuel depletion 63
2.3. APOLLO3®-FR numerical validation with a Phenix-Like model 64
2.3.1. Control rod worth 65
2.3.2. Reaction rates 66
2.4. A Multiphysics approach to fuel depletion calculations: application to a fuel sub-assembly. 67
2.5. Conclusion 71
Chapter 3. Experimental reactivity loss 73
3.1. Introduction 74
3.2. Interpretation process of the reactivity loss 75
3.2.1. Control rod worth experiment 75
3.2.2. Changes in rod bank driveline during the cycle 77
3.2.3. Former interpretation limitations 79
3.2.4. Reinterpretation process 80
3.3. Reinterpretation for cycle 42-115 83

3.3.1. Recalibration of the experimental reactivity measurement 83
3.3.2. Shadow-effect coefficient 84
3.3.3. Determination of the rod bank S-curve and its derivative 86
3.3.4. Experimental reactivity loss curve 89
3.3.5. Uncertainty propagation 92
3.4. Conclusion 95
Chapter 4. APOLLO3®/MENDEL calculation 97
4.1. Introduction 98
4.2. Calculated 42th Phenix cycle reactivity loss 98
4.2.1. Temporal mesh 99
4.2.2. In-core experiment modeling 100
4.2.3. Control rod extraction 101
4.2.4. Control rod depletion 102
4.2.5. Multiphysics coupling 104
4.2.6. Best-Estimate result 107
4.2.7. Experimental validation of the APOLLO3®/MENDEL scheme 109
4.3. APOLLO3®/MENDEL Bias decomposition and uncertainty quantification 110
4.3.1. MENDEL numerical bias 110
4.3.2. Bias induced by geometrical assumptions 110
4.3.3. Bias induced by PROJERIX initialization 112
4.3.4. Neutronics scheme deterministic bias 112
4.3.5. Uncertainty due to power normalization 113
4.3.6. Uncertainties coming from nuclear data 113
4.3.7. Uncertainty due to delayed neutron fraction 114
4.3.8. Biases and uncertainties induced by Multiphysics coupling 114
4.4. Conclusion 115
Chapter 5. Boltzmann/Bateman coupled sensitivities 117
5.1. Introduction 118
5.2. Reactivity loss sensitivity theory 118
5.2.1. Standard Perturbation Theory 118
5.2.2. Depletion Perturbation Theory 120
5.2.3. Computational scheme for coupled sensitivities 123
5.2.4. Limitations for power reactor experimental application 127
5.3. Partial adjoint depletion implications: application to a fuel sub-assembly 128
5.3.1. Fully backtrack sensitivities 129
5.3.2. Partial consideration of the irradiation history 131
5.3.3. Nuclear data uncertainty 133
5.4. Application to the 42th Phenix cycle 137
5.4.1. Reactivity loss sensitivities as a tool for analysis 137
5.4.2. Reactivity loss uncertainty due to nuclear data and its limitations in operation condition 140

5.4.3. APOLLO3®/MENDEL decomposition bias with coupled sensitivities 142
5.5. Conclusion 144
Chapter 6. Integral data assimilation perspectives 146
6.1. Introduction 147
6.2. Data assimilation principles 148
6.3. Synthesis of data assimilation input data for Phenix reactivity loss 149
6.4. Data assimilation based on the Phenix reactivity loss 151
6.4.1. C/E influence on IDA 155
6.4.2. Influence of considering biased sensitivities 156
6.4.3. Prior covariances impact on IDA 158
6.5. Application of posterior nuclear data to other experiments 161
6.6. Conclusion 166
Chapter 7. General Conclusion 168
Reference 173
APPENDIXES 181
A. Point Kinetics 181
B. Deterministic solving methods for fuel transport equation 183
Multigroup formalism 184
Self-shielding method with TDT/CPM 186
Flux calculation with TDT/MOC 187
Cross-section homogenization and condensation 189
Leakage Model at the lattice scale 190
Flux calculation with MINARET 191
C. APOLLO3®-FR deterministic characteristics 192
D. TRIPOLI-4® modeling 193
E. Data exchange between GERMINAL and APOLLO3® 194
F. Uncertainty propagation with sensitivities and the first linear approximation 196
G. Isotopes and reactions initially contain in COMAC V1 197
H. Relation between cycles for adjoint depletion 199
I. Overall sensitivity to nuclear data for the reactivity loss coefficient 200
J. Burnup-based cell correction for “Last-Cycle” sensitivities 202

List of Figures

Figure 1. Fuel depletion calculation general scheme with the quasi-static approach 41
Figure 2. Illustrative reactivity loss curve of a classical SFR 42
Figure 3. ^{239}Pu production process by fertile capture of ^{238}U 42
Figure 4. Illustrative homogenization of a fictitious SFR pin cell and cross-section energy condensation of a fictitious isotope 45
Figure 5. Different geometry description in the cluster paradigm for lattice calculation: fundamental mode (left) for fissile fuels and cluster mode (right) for fertile and non-fissile subassemblies (here a control rod) 46
Figure 6. Homogenization process for a classical SFR fertile blanket cluster (left) and a control rod cluster (right) 47
Figure 7. Lattice calculation and MPO production in the APOLLO3®-FR deterministic scheme for temperature and burnup multiparametrization 48
Figure 8. Multiparametrization (temperatures + BU) structure inside the MPO 49
Figure 9. Description of the adaptive radial mesh around control rod (left) radial mesh of the rest of the fissile/fertile subassemblies (upper right) and inside radial reflectors (lower right) 50
Figure 10. Multiphysics coupling between the APOLLO3®-FR deterministic scheme and the GERMINAL V2 tool 52
Figure 11. APOLLO3®/MENDEL/GERMINAL V2 calculation route for fuel depletion calculation 53
Figure 12. Phenix reactor block [44] 57
Figure 13. Standard Phenix fissile subassembly [45] 58
Figure 14. Standard Phenix fertile subassembly [45] 58
Figure 15. Standard Phenix control rod subassembly 59
Figure 16. Illustration of a Phenix loading plan [45] 60
Figure 17. Axial description of the main subassembly type inside Phenix cycles 62
Figure 18. Geometrical modeling of different subassembly axial zone section of the Phenix model 63
Figure 19. APOLLO3® modeling of the Phenix-like configuration with a 1/6 symmetry 65
Figure 20. Rod Bank (RB) S curve and its efficiency for TRIPOLI-4® (with 2σ error bars) and APOLLO3® on the Phenix-like model 66
Figure 21. APOLLO3®-FR/ TRIPOLI-4® discrepancy distribution of the main reaction rates on the Phenix-like RZ traverse (statistical uncertainty <0.1%) 67
Figure 22. Schematic axial description of subassembly in an infinite lattice case (fresh C1 subassembly) 68

Figure 23. FG leakage (left) and fuel temperature (right) evolution through irradiation at the hottest point of the subassembly for 600 days of irradiation at 5MW (73.5 GWd/t_{C1}). 69
Figure 24. Impact of the multiphysics coupling on the flux in the fissile fuel for the 4 MW power scenario (left) and the 5 MW power scenario (right) at 38 000 MWd/tFF 71
Figure 25. Simplified diagram of the experimental determination of the reactivity loss due to fuel depletion in Phenix 74
Figure 26. Control rod weighting 76
Figure 27. 42-114 experimental control rod S-curve evaluated by weight balancing 77
Figure 28. Reactivity loss of the cycle 42-115 with corrected rod bank driveline values in black and non-corrected values in blue. 79
Figure 29. Global reinterpretation process of the experimental reactivity loss coefficient for cycle 42-115 of the Phenix reactor 81
Figure 30. Illustration of the rod bank shift during rod balancing 84
Figure 31. Shadow-effect coefficient computed by TRIPOLI-4® and APOLLO3®-FR (divided by the former constant value of the shadow-effect) 86
Figure 32. Experimental S-curves of each control rod of the rod balancing at the beginning of cycle 42 86
Figure 33. Impact of the interpolation model on the differential rod bank worth (TRIPOLI-4® calculation) 87
Figure 34. Experimental rod bank S curve with its differential worth compared to the TRIPOLI-4® and APOLLO3® calculations 88
Figure 35. Experimental differential control rod worth curve compared to the TRIPOLI-4® calculation 89
Figure 36. Two main components of the transmission function evolution through axial axis 90
Figure 37. Reinterpretation of the reactivity loss of the cycle 42-115 91
Figure 38. Reinterpretation of the reactivity loss of cycle 42-115 with the propagated uncertainties. (μ Being the mean, σ the standard deviation, Skew the skewness and Kurt the excess of kurtosis) 93
Figure 39. Evolution of the excess of kurtosis of the sampled output reactivity loss 93
Figure 40. APOLLO3® modeling of the 42nd Phenix cycle 98
Figure 41. Discrepancy map (in percent) of the ^{239}Pu consumption at mid-height of the core for between 1 time-step against 20-day time-step depletion calculation (left) and between 20-day against 5-day time-step (right) 99
Figure 42. Discrepancy map (in percent) at mid-height of ^{239}Pu consumption between of considering in-core experiment modeling 100
Figure 43. Discrepancy map (in percent) at three axial positons of ^{239}Pu consumption of considering control rod extraction during cycle compared to a calculation with control rod at EoC axial position 102
Figure 44. ^{10}B depletion chain 103
Figure 45. Discrepancy map (in percent) of ^{239}Pu consumption with and without consideration of the ^{10}B depletion chain (for the control rods and in-core absorbing

experiments). Axial position: upper part of the fissile zone, axial position concerned with facing control rod during the cycle....104
Figure 46. Local power discrepancy map (in percent) with different levels of consideration of multiphysics coupling with GERMINALV2 during fuel depletion (in BoC and EoC state)....105
Figure 47. Discrepancy map (in percent) at several levels of ^{239}Pu consumption with consideration of multiphysics coupling with GERMINALV2 during fuel depletion 106
Figure 48. Discrepancy map (in percent) at mid height of ^{239}Pu consumption with consideration of different coupling methodologies....107
Figure 49. Reactivity contribution to the reactivity loss between BoC and EoC for each isotope (contribution > 1¢). Contribution in blue are negative and in red for positive contribution.....109
Figure 50. General scheme for direct and adjoint depletion calculation for DPT sensitivity calculation with APOLLO-3®....126
Figure 51. Illustration of backward depletion for power reactor for an initialization at time tEOCC (end of cycle of the cycle C). Black arrows represent the irradiation history of the subassembly present in the cycle C. Red arrows represent the irradiation history of other subassemblies that have common in-core irradiation time with subassemblies in black 127
Figure 52. 33g profile of the different term composing the FB sensitivities for the reactivity loss between 300 days and 400 days of irradiation at 5 MW for ^{238}U (n,γ) (left) and ^{239}Pu (n,f) (right)....131
Figure 53. Discrepancy between LC/FB sensitivities of the first 150 contributors depending on their reaction types and sensitivity terms. D1 meaning the 1st decile.....133
Figure 54. JEFF 3.1.1. uncertainty of the main contributors to the reactivity loss uncertainty....134
Figure 55. Radial flux redistribution at mid-height between the end and the beginning of the Phenix cycle 42 138
Figure 56. Flux spectrum changes between the end and the beginning of the Phenix cycle 42 for different media....138
Figure 57. Prior correlation matrix (left) and the differences between posterior and prior correlations (right) for the most impacted isotope-reaction pairs when performing IDA with the Phenix reactivity loss and COMAC V1....152
Figure 58. Posterior uncertainty distribution between the different isotope-reaction pairs when performing IDA with the Phenix reactivity loss and COMAC V1 (and by considering the power as uncertain)....153
Figure 59. Comparison on data assimilation main results when the power is considered as uncertain or not....154
Figure 60. Posterior value and uncertainties of the main isotope-reaction pairs impacted by the IDA with Phenix reactivity loss for C/E=1.0096....156
Figure 61. Comparison of posterior corrective factors (top) and uncertainty (bottom) for ^{238}U (n,γ) (left), ^{240}Pu (n,γ) (centre) and ^{240}Pu (n,f) (right) between two different sets of

sensitivities. Respectively the nominal case with LC sensitivities (red) and the one with perturbed sensitivities CLC (blue) 157
Figure 62. Posterior correlations difference between DA performed with LC sensitivities and CLC sensitivities 158
Figure 63. ENDF/B-VII.1 33G-covariance matrix for the seven main isotope-reaction pairs considered 159
Figure 64. Posterior corrective factors (top) and uncertainties (bottom) when performing DA with the Phenix reactivity loss starting with COMAC V1 (red) and COMAC V1 without cross-correlations (blue) for $^{238}U\ (n,\gamma)$ (left) and $^{240}Pu\ (n,\gamma)$ (right) 160
Figure 65. Posterior/Prior correlations difference when performing DA with the Phenix reactivity loss starting with COMAC V1 (left) and COMAC V1 without cross-correlations (right). Black squares represent the locations of the initial cross-correlations 161
Figure 66. Schematic description of the various spatial dimensions of the Phenix core 183
Figure 67. Microscopic total cross-section of the Plutonium 239 [JEFF 3.1.1] 184
Figure 68. MOC characteristic tracking 188
Figure 69. Connection between two cycles if the core configuration changes during an adjoint depletion calculation 199
Figure 70. Remaining discrepancy with FB through irradiation time after LC sensitivity cell correction for the 150 main reactivity loss contributors 203

List of Table

Table I. Calculation scheme difference between the ECCO/ERANOS fuel depletion scheme and the APOLLO3®/MENDEL scheme 54
Table II. Different subassembly axial zones of each of the subassemblies in the core of cycle 42-115 of the Phenix reactor 60
Table III. Discrepancy between APOLLO3® and TRIPOLI-4® on integrated reaction rates (statistical uncertainty <0.1%) for each of the media of the Phenix-like configuration traverse (control rod being at a representative height of a Phenix cycle) 67
Table IV. Reactivity decomposition for the reactivity loss coefficient with different multiphysics approaches for different power scenarios (between 25 and 45 GWd/tFF) 69
Table V. Average temperature evolution depending on the power scenario 70
Table VI. Input data considered for the uncertainty propagation of the reactivity loss coefficient 82
Table VII. Impact of the different input parameter on the reactivity loss coefficient 91
Table VIII. Uncertainty propagation (1σ) of different sets of input data for the reactivity loss coefficient of the Phenix cycle 42-115 94
Table IX. Reactivity loss of cycle 42-115 depending on the fidelity of the modeling 108
Table X. Discrepancy between APOLLO3® and TRIPOLI-4® on global reaction rates for each media of the BOC configuration of Phenix cycle 42 (control rod in the EOC position) 112
Table XI. Modeling parameter guidelines for fuel depletion calculation 115
Table XII. Contributors to the most important coupled Boltzmann/Bateman sensitivities (FB) for the reactivity loss between 300 days (37 GWd/t_{C1}) and 400 days (49 GWd/t_{C1}) 130
Table XIII. Comparison of the reactivity loss sensitivities computed with FB and LC for the irradiation between 300 days (37 GWd/t_{C1}) and 400 days (49 GWd/t_{C1}) at 5 MW 131
Table XIV. Uncertainty on reactivity loss due to nuclear data for diverse irradiation time with FB sensitivities and the COMAC V1 covariance Matrix 134
Table XV. Reactivity loss nuclear data uncertainty for different irradiation time with LC sensitivities and the COMAC V1 covariance Matrix 135
Table XVI. Uncertainty on reactivity loss due to nuclear data between 300 days and 400 days of irradiation at 5 MW with the updated COMAC V1 (for the main contributors representing 99% of the total uncertainty) 136
Table XVII. 42nd Phenix cycle reactivity loss one group sensitivities integrated over the different media and BPF terms 139
Table XVIII. BoC multiplication factor sensitivities to the isotopic composition integrated over the different media (computed with SPT) 139
Table XIX. Sensitivity and nuclear data uncertainty with COMAC V1 for the 42nd Phenix cycle reactivity loss (contribution separated in BPF terms) 141

Table XX. Uncertainty breakdown of the 42nd cycle Phenix reactivity loss depending on the type of nuclear data....142
Table XXI. Reactivity loss sensitivity per fissile/fertile medium of the main isotope-reaction pairs for cycle 42....143
Table XXII. Corrective factors and uncertainty reductions obtained with data assimilation of the Phenix reactivity loss....151
Table XXIII. Integral experiment available for this work....164
Table XXIV. Posterior χind of the experiment database....165
Table XXV. Posterior uncertainty of the experiment database....165
Table XXVI. APOLLO3®-FR lattice calculation solver and parmaeters....192
Table XXVII. APOLLO3®-FR core calculation solver and parameters....192
Table XXVIII. Isotopes and reactions initially contain in COMAC V1....197
Table XXIX. Global sensitivities when considering delayed neutron fraction for the calculated value....200

List of Abbreviations

Abbreviation	Meaning
AMR	Advanced Modular Reactor
ASA	Radial reflector
BEPU	Best-Estimate Plus Uncertainty
BOC	Beginning Of Cycle
BU	Burn-Up
C1	Inner Core
C2	Outer Core
CENDL	Chinese Evaluated Nuclear Data Library
CLC	Corrected Last-Cycle (DPT sensitivities)
CPM	Collision Probability Method
CPU	Central Processing Unit
CRW	Control Rod Worth
DA	Data Assimilation
DCC	DIMEP à Canal Central
DCRW	Differential Control Rod Worth
DICE	Database for ICSBEP
DIMEP	Dispositifs d'Irradiation et de Mesure En Pile (Irradiation and Measurement Device)
DPT	Depletion Perturbation Theory
EFPD	Equivalent Full Power Days
EGPT	Equivalent Generalized Perturbation Theory
ENDF	Evaluated Nuclear Data File
EOC	End Of Cycle
ERANOS	European Reactor ANalysis Optimized calculation System
FB	Fully Backtracked (DPT sensitivities)
FCAI	Fertile Couverture Axiale Inférieure, Lower Axial Blanket
FCAS	Fertile Couverture Axiale Supérieure, Upper Axial Blanket
FCR	Fertile Couverture Radiale, Radial Blanket
FG	Fission Gas
FP	Fission Product
GLS	Generalized Least Square
GPT	Generalized Perturbation Theory
HN	Heavy nuclei
ICSBEP	International Criticality Safety Benchmark Evaluation Project
IDA	Integral Data Assimilation
IDAT	IRPhE Database and Analysis Tool
IFP	Iterated Fission Probability
IRPhE	International Handbook of Evaluated Reactor Physics Benchmark Experiments

JEFF	Joint Evaluated Fission and Fusion file
JENDL	Japanese Evaluated Nuclear Data Library
LC	Last-Cycle (DPT sensitivities)
LFP	Lumped Fission Product
LFR	Lead-cooled Fast Reactor
LWR	Light Water Reactor
MASURCA	Maquette SURgénératrice Cadarache (Cadarache breeder mock-up)
MOC	Method Of Characteristics
MOX	Mixed Oxide
MPO	MultiParameter Output
MSR	Molten Salt Reactor
NDaST	NEA's Nuclear Data Sensitivity Tool
PNSC	Protection Neutronique Supérieur Combusitble, upper fuel neutron shield
PNSF	Protection Neutronique Supérieur Fertile, upper fertile neutron shield
PX	Phenix
RAM	Random-Access Memory
RB	Rod Bank
RL	Reactivity Loss
RP	Rotating Plug
SCT	Scientific Computational Tool
SE	Shadow-Effect
SFR	Sodium-cooled Fast Reactor
SMR	Small Modular Reactor
SPN	Lower axial reflector
SPT	Standard Perturbation Theory
SPX	Superphenix
SSVI	Lower axial part of the control rod
SSVS	Upper axial part of the control rod
TDT	Two/Three Dimension Transport
VVUQ	Verification, Validation and Uncertainty Quantification
ZTRS	Plenum

Chapter 1. Introduction

Amid today's environmental and energy crises, nuclear power, previously put aside by some global energy policies after the 2011 Fukushima Daiichi accident, is experiencing a revival [1]. As energy challenges and constraints evolve, there is a growing interest in new reactor types that need to meet new requirements in terms of safety level, sustainability and economics. These demands now include production of electricity in synergy with renewable energy sources or generation of industrial heat, all whilst addressing long-term goals such as the closing of the fuel cycle and reduction of nuclear waste. Consequently, interest is once again growing in target reactor designs like those highlighted by the Generation IV international forum [2]— molten salt reactors (MSR), sodium-cooled fast reactors (SFR), and lead-cooled fast reactors (LFR). Additionally, new reactor types such as Small Modular Reactors (SMRs) and Advanced Modular Reactors (AMRs) are being developed to meet a wider range of applications (heat generation, adaptation to smart grids,…). This renewed interest in nuclear power, with so many new concepts emerging and flourishing is not unique to the current period. Similar exploration has been observed in various phases experienced by the nuclear industry from its beginning to the present day.

During those periods, the development of various reactor technologies was heavily based on extensive experimental work using zero-power reactors and demonstrators of various scales and power levels. This approach allowed for the calibration and qualification of the computational tools and methods of the era, facilitating studies for industrial-scale reactors.

This methodology is well illustrated by the SFR development of "The French trilogy" as mentioned in [3]. Based on low estimation of the available fissile material at the end of the 1950s and 60s, concerns were raised worldwide regarding the availability and sustainability of fissile raw materials. This led France (among others) to commit to the development of a fast breeder reactor program. In order to achieve the high-power prototype Superphenix, intermediate-power experimental reactors and demonstrators had to be constructed. Rapsodie was built for the purpose of acquiring experience in sodium management and to validate choices regarding materials, design, and fuel for the intermediate-power reactor Phenix. The Phenix reactor subsequently confirmed important technological choices for the SFR technology, demonstrated the reliability of certain components, and provided significant experimental feedback in terms of power operations. All of this was achieved with extensive support from the MASURCA zero-

power reactor, by means of mock-up characterization for validation of the neutronics computational tools of that time.

All of this development was achieved using a conservative safety approach, which, coupled with the need to build numerous intermediate-scale facilities, led to robust but limited designs. However, given the current safety standards and the high construction costs for new facilities, the process of development of new reactors with a variety of innovative designs can no longer depend solely on this method.

The calculation capacities of today has significantly increased, compared with those of the 1970s to 90s period. This enables design approaches to rely much more on the predictive capacity of scientific computational tools (SCTs) for optimization of margins and experimental needs by better characterizing both of them. This new development paradigm is based on the Best-Estimate Plus Uncertainty (BEPU) method rather than a conservative approach. It primarily involves computing each of the relevant quantities of interest related to safety or operational purposes, using the best available models and methodologies, whilst also incorporating associated uncertainties due to input data.

Adopting this type of approach entails ensuring that these tools can accurately model various phenomena occurring in a reactor for both nominal and perturbed states. This therefore requires intensive work to be performed, in order to master the accuracy level of these SCTs for all aspects of a reactor's lifecycle across different technologies based on experimental data. This process, known as Verification, Validation, and Uncertainty Quantification (VVUQ), involves comparing a computed value with a reliable experimental one [4], [5]. As the computed value depends on hypotheses and imperfectly known input data, the impact of each hypothesis considered should be estimated (bias breakdown), and the consequence of partial knowledge of the input data should be quantified (uncertainty quantification).

This process should be applied to SCTs for diverse technologies to explore the range of applications. The future target technologies include the SFR concept, which is the second most widespread technology after LWRs and has the most extensive experimental feedback in nuclear history, when LWRs are excluded. It can therefore provide significant feedback for specific and general fast reactor phenomena and is a clear advantage for VVUQ of modern tools.

Among the SFR experimental feedback, mock-ups from zero power reactors represent the vast majority of the available set of experiments. These often deal with fresh fuel at cold temperatures. Regarding requirements for a nominal state power reactor, validation can only be based on a very few set of experiments. The only open-access experiments are those using SEFOR, which can provide valuable information on the beginning of cycle core state. For cases dealing with irradiated fuel, experimental data are even fewer as this

requires a power reactor that has gone through several irradiation cycles with fuel depletion to actually extract relevant data for the VVUQ process.

For this purpose, some dedicated irradiation experiments were performed within the Phenix reactor [6] but they only involved limited number of pins [7]. These experiments provide prime information related to individual isotopes and the nuclear reaction, but were too restrictive to provide data on global behavior of the core itself with irradiation. Nevertheless, validation of SCTs for global neutronics coefficients, which depend on the overall reactor fuel depletion, is crucial for safety. This is especially true for this type of reactor, where the sodium void coefficient tends to become more penalizing with irradiation [8]. Managing fuel depletion and the isotopic composition through the cycle at core scale is therefore a key feature, as is its validation.

Experimental validation of the isotopic inventory variation in the reactor is challenging, as it is currently not possible to measure it directly. However, its impact on core reactivity, in terms of reactivity loss, can provide validation insights into the phenomenon of fuel depletion. In addition, fuel depletion is closely tied to reactor economics since cycle length, material balance, and waste buildup are directly dependent on it. Therefore, focusing on reactivity loss is inherently valuable, as this influences other key factors that need to be optimized in reactor design.

The main challenge in experimental validation of such a coefficient lies in the acquisition of experimental data, which could be provided by Phenix, for example. Moreover, it mainly requires the ability to model this phenomenon whilst managing the bias breakdown constraints and uncertainty quantification inherent in VVUQ requirements, along with the ablity to attest the reliability and uncertainty of the experimental value. The purpose of this PhD, then, is to determine how the experimental reactivity loss of a power reactor can be used to provide significant information for the experimental validation of modern tools, especially for the APOLLO3®/MENDEL scheme used in CEA for fuel depletion purposes.

To address this question, it is first necessary to understand the phenomenon of fuel depletion and the complexity of its modeling. The reactor's power operation during fuel depletion, which is primarily a neutronics-based issue, involves a multiphysics aspect with thermal-hydraulics and fuel behavior, significantly complicating the analysis. The second chapter will therefore present the various phenomena and tools considered for conducting such an analysis, with numerical validation and the prior establishment of the methodology on simplified cases representative of the main experimental validation case.

Next, to determine the experimental value of the Phenix reactivity loss, it is essential to analyze the interpretation method of the reactivity loss for the Phenix cycles. The interpretation method primarily requires the presence of a control rod worth experiment at the beginning of the cycle, which restricted the analysis to cycle 42. A detailed analysis

of the interpretation process reveals several limitations that will be discussed in the third chapter, as well as the various methods used to address these limitations and quantify the experimental uncertainty.

Once the experimental reactivity loss is determined, the best-estimate value must be evaluated using the APOLLO3®/MENDEL scheme to estimate the discrepancy with the experiment. In the fourth chapter, this issue is addressed by incrementally eliminating as many commonly used assumptions as possible, down to the multiphysics component, using the scheme developed in the first chapter, allowing the calculation-experiment discrepancy for the reactivity loss of the cycle 42 to be obtained. In line with modern VVUQ requirements, the factors contributing to the calculation-experiment discrepancy must be identified and quantified. For the remaining modeling biases, a bias breakdown partially mitigates the absence of a reference calculation. However, for a complete characterization of the biases and input data uncertainties, reactivity loss sensitivities according to a specific formalism are necessary.

Thus, in the fifth chapter, this formalism, derived from the depletion perturbation theory, is described and applied to the reactivity loss of the Phenix cycle 42. Nevertheless, its concrete application to a power reactor that already have an irradiation background, introduces a number of biases that will be addressed and quantified. With the complete characterization of both the calculated and experimental values, it will be possible to close the VVUQ process and evaluate experimentally the APOLLO3®/MENDEL calculation scheme.

Finally, with this new experimental feedback, it will be possible to explore, in the last chapter, perspectives for nuclear data assimilation and how this experiment can contribute to experimental databases for the production of engineering libraries to support the development of future reactors.

Chapter 2. Fuel depletion

Chapter 2. Fuel depletion 35
2.1. Fuel Depletion calculation 36
2.1.1. Physical description 36
2.1.2. Solving the Bateman equation 42
2.1.3. Solving the stationary Boltzmann equation 43
2.1.4. APOLLO3®/MENDEL deterministic scheme 52
2.1.5. Contribution of the new approach 53
2.2. Phenix reactor 56
2.2.1. Reactor presentation 56
2.2.2. Phenix Geometry modeling 60
2.2.1. Specific features of the Phenix reactor and fuel depletion 63
2.3. APOLLO3®-FR numerical validation with a Phenix-Like model 64
2.3.1. Control rod worth 65
2.3.2. Reaction rates 66
2.4. A Multiphysics approach to fuel depletion calculations: application to a fuel sub-assembly. 67
2.5. Conclusion 71

Summary - This chapter presents the physics of fuel depletion and the different equations that may be used to solve such a phenomenon. The current tools used at CEA allow such an analysis to be performed with the APOLLO3®/MENDEL deterministic scheme, which needs to be validated with irradiation experiments. There are few such experiments for Sodium fast reactors, but specific tests for the reactivity loss of the Phenix cycle can potentially contribute significant information for the experimental validation of the APOLLO3®/MENDEL scheme. Power reactors like Phenix are complex systems to represent, combining a number of phenomena that can accumulate different biases. The complexity of the modeling has therefore been incrementally increased. First, a numerical validation of the neutronics scheme on a simplified Phenix configuration has been carried out. This allowed the impacts of the hypotheses to be separated and identified. Then, a multiphysics coupling between APOLLO3®, MENDEL FR and GERMINAL V2 was carried out, which can be used to establish methodology and confirm interest in terms of the possibility of extending it to a core calculation.

Objectives

- Presentation of the theoretical background involved in a fuel depletion problem, the specificities of such a phenomenon in an SFR such as Phenix and the SCTs considered for solving it: APOLLO3-FR, MENDEL and GERMINAL V2.
- Numerical validation of the neutronics scheme on a simplified model.
- Evaluation of multiphysics coupling on a test case.

Highlights

- APOLLO3-FR scheme is able to correctly represent the local and integral parameters such as control rod worth and reaction rates on a simplified Phenix configuration
- As expected, the multiphysics coupling has a significant impact on a simplified configuration so it must be extended to the core scale
- The optimal scheme was identified with APOLLO3®-FR

2.1. Fuel Depletion calculation

2.1.1. Physical description

Neutron physics is the study of neutron behavior in different materials. Neutrons are uncharged particles, so they are only able to interact with matter through nuclear reactions. The probability that a neutron with energy E will undergo reaction x with isotope N_i in an interval of size dr is given by the following quantity $N_i(\vec{r}\,)\sigma_x^i(E)dr$ [9]. The coefficient $\sigma_x^i(E)$ is called the microscopic cross section and it is energy dependent and specific to each isotope. The values of these reactions are determined semi-empirically, using nuclear data evaluations:

- ENDF (Evaluated Nuclear Data File) in North America
- JEFF (Joint Evaluated Fission and Fusion file) in Europe
- JENDL (Japanese Evaluated Nuclear Data Library) in Japan
- CENDL (Chinese Evaluated Nuclear Data Library) in China

Microscopic cross-sections are stored in these nuclear data libraries, which are then used as input data for neutronics calculations. The product of the microscopic cross-section (in cm^2) of an isotope and its concentration (in at/cm^3) is referred to as the macroscopic cross-section, denoted by Σ (in cm^{-1}).
The main reactions that occur in a nuclear reactor are scattering[1], capture, and fission. Fission produces a certain number of neutrons (typically 2 or 3, which is denoted by the letter ν), making the medium a neutron multiplier. The reactor is said to be:

- **Subcritical** when the number of neutrons produced by fission[2] is less than the number of neutrons lost by fission, capture and leakage;
- **Critical** when the latter two quantities are equal;
- **Supercritical** when the neutron production is greater than their absorption.

The quantity defining the reactor's state is called the effective multiplication factor, denoted as k_{eff}. It represents the ratio of neutron productions to disappearances (absorptions + leakage) in the system.

Due to the very slight variations in the multiplication factor around its critical value in reactor physics, another coefficient derived from the multiplication factor is employed: reactivity. Reactivity is defined as the relative deviation of the multiplication factor from criticality, expressed in a more suitable unit, the pcm (per cent mille), and is denoted as $\rho = \frac{k_{eff}-1}{k_{eff}} \cdot 10^5\ [pcm]$ or in delayed neutron fraction units: $\rho = \frac{k_{eff}-1}{k_{eff}\cdot\beta_{eff}}$ [$].

[1] Scattering can manifest as either elastic or inelastic. The distinction between the two lies in the fact that, in inelastic scattering, there is no conservation of the kinetic energy of the neutron and isotope system. The missing portion of kinetic energy is transferred to the target nuclei, which remains in an excited state.
[2] or rare reactions such as (n,2n) capture

The determination of the multiplication factor (and reactivity) therefore requires knowledge of nuclear data, isotopic concentrations (which are considered as known) and the neutron distribution (which is a priori unknown). The neutron distribution, also called neutron density, is the number of neutrons for a given time t, position $\vec{r}$, energy E and direction $\vec{\Omega}$, and it is denoted $n(\vec{r}, E, \vec{\Omega}, t)$. For the neutron population, the number of parameters is seven ($\vec{r}, E, \vec{\Omega}\, t$) and is called the phase space. Usually, the neutron flux is the quantity used, rather than neutron density: $\psi(\vec{r}, E, \vec{\Omega}, t) = vn(\vec{r}, E, \vec{\Omega}, t)$ with v the velocity of the neutron at the energy E.

To address this question mathematically, the pioneers of neutron physics treated the neutron population as a free gas [10]. By considering the neutron population in this manner, they were able to invoke the particle transport equation from kinetic gas theory: the Boltzmann equation. The formulation of the Boltzmann equation takes account of the interaction of the population of a particular particle type with itself (non-linear term). In a reactor, the number of neutrons (10^8) is much smaller than the number of atoms (10^{24}). This means that neutron-neutron interactions are rare and can be ignored. This simplifies the Boltzmann equation into a linear form. Additionally, the free-neutron decay can be neglected as its half-life is around 15 minutes [11] which is much longer than the average neutron lifetime in a reactor. This equation, under the given two assumptions, can be derived by performing a neutron balance in an infinitesimal volume of phase space (further elaborated in [12]), resulting in its final integro-differential form:

$$\left(\frac{1}{v}\frac{\partial}{\partial t} + \nabla\cdot\vec{\Omega} + \Sigma_t(\vec{r}, E, t)\right)\psi(\vec{r}, E, \vec{\Omega}, t)$$

$$= \int_0^\infty dE' \sum_i \chi^i_{p,E'}(E)\bar{\nu}^i(E')\left(1-\beta^i(E')\right)\Sigma^i_{\mathrm{t}}(\vec{r}, E', t)\,\phi\,(\vec{r}, E', t)$$

$$+ \int_0^\infty dE' \sum_{i\in precursor} \chi^i_{d,E'}(E) B^i_{\beta^-,n}\,\lambda_i N_i(\vec{r}, t)$$

$$+ \int_0^\infty dE' \sum_i \int_0^{4\pi} d\vec{\Omega}'\,\Sigma^i_s(\vec{r}, E'\to E, \vec{\Omega}'\to\vec{\Omega}, t)\psi(\vec{r}, E, \vec{\Omega}, t) \qquad (2\text{-}1)$$

With:

- $\psi(\vec{r}, E, \vec{\Omega}, t)$: The neutron flux (also called angular neutron flux)
- $\phi(\vec{r}, E, t)$: The scalar neutron flux (integration of the angular neutron flux over $\vec{\Omega}$)
- $\chi^i_{p,E'}(E)$: Prompt (p for prompt or d for delayed) fission neutron spectrum of the isotope N_i for a fission with an incident neutron at the E' energy
- $\bar{\nu}^i(E)$: average number of neutrons produced by fission for the isotope N_i
- $\beta^i(E)$: delayed neutron fraction of the isotope N_i

- $B^{i}_{\beta^-,n}$: Branching ratio of the isotope N_i to decay into (β^-, n) and to produce a delayed neutron
- λ_i : Decay constant of the isotope N_i

The neutron transport equation has a steady-state solution only if the disappearance terms perfectly balance the source terms, in other words, when the reactor is in a critical state (k_{eff} = 1). Otherwise, the phase flux evolves, and the transport equation alone is not sufficient to solve the problem.

Indeed, this equation can be used in determination of the neutron flux in the phase space by considering fixed input data such as cross-sections and isotopic compositions. However, isotopic compositions also change over time due to radioactive decay phenomena and, more importantly, due to nuclear reactions induced by the neutron flux. The equations governing the evolution of isotopic compositions under neutron flux are the generalized Bateman equations [13], [14]. These equations involve performing an isotopic balance (production minus disappearance terms) for all isotopes within a medium. Thus, the result is:

$$\frac{dN_k(\vec{r},t)}{dt} = \sum_{m\neq k} \lambda_m B_{k\leftarrow m} N_m(\vec{r},t) + \sum_{m\neq k} N_m(\vec{r},t) \int_0^\infty dE\, \sigma_{x,m}(E) P_{x,k\leftarrow m}(E) \phi(\vec{r},E,t)$$
$$-\lambda_k N_k(\vec{r},t) - N_k(\vec{r},t) \sum_{x\neq s} \int_0^\infty \sigma_{x,k}(E)\phi(\vec{r},E,t) \qquad (2\text{-}2)$$

With:

- $B_{k\leftarrow m}$: The branching ratio of the isotope N_m to decay preferentially towards the isotope N_k
- λ_m: Decay constant of the isotope N_m
- $P_{x,k\leftarrow m}(E)$: Probability of obtaining the N_m isotope from the isotope N_k with the reaction x at the energy E. When the reaction is the fission reaction, this probability is called **independent fission yield ($\gamma^i_{k\leftarrow m}$)**

With the Boltzmann and Bateman equations, it is observed that isotopic compositions and neutron flux are related. Isotopic compositions influence macroscopic cross-sections and the source of delayed neutrons. Initially, this may seem like a strong coupling between these two equations. However, the time constants associated with the variation of the prompt neutron source, the quantity of precursors (the source of delayed neutrons), and isotopic compositions have a significant order of magnitude difference:

- $\Delta t < 10^{-3}$s : time-constant associated with prompt neutron kinetics
- $10^{-2} < \Delta t < 10^{3}$s : time-constant associated with precursor isotopes evolution (delayed neutron source)
- $\Delta t > 10^{3} s$: time-constant associated with isotopic evolution of non-precursor isotopes

This difference in order of magnitude can be used to observe the evolution of a given population by considering the others in equilibrium state.

The analysis of neutron kinetics is important in transient studies for core design and safety report. Their associated models will not be addressed here.

On the other hand, the delayed neutron source evolution is important for normal operation transient and experimental reactivity measurement. A specific modeling approach, such as point kinetics, can be used (see Appendix A).

Finally, to study the isotopic composition evolution, the timescale allows for consideration of precursor isotopes in equilibrium state and so do the delayed and prompt neutron population. Consequently, the reactor can be considered in a state of constant equilibrium, and explicit variations in time can be treated as negligible $\left(\frac{1}{v}\frac{\partial \psi}{\partial t} = 0\right)$. This is the quasi-static hypothesis.

Thus, the Boltzmann equation is used in its stationary form to compute the neutron flux for a given isotopic composition. The Bateman equation is then used for a constant neutron flux in a Δt time interval.

The stationary form for the Boltzmann equation is formulated using the λ mode, which makes it possible to obtain an eigenvalue problem that ensures that the largest eigenvalue is real and positive and that the associated eigenvector (the flux) is defined as positive in the whole domain [15]. This gives the stationary Boltzmann equation (in its condensed operator form):

$$\left[\frac{1}{\lambda}\boldsymbol{\mathcal{F}}(\mathcal{N}) + \boldsymbol{\mathcal{B}}(\mathcal{N})\right]\psi\left(\vec{r}, E, \vec{\Omega}\right) = 0 \qquad (2\text{-}3)$$

With:

- λ: the equation eigenvalue, where the largest value is equal to the multiplication factor k_{eff}.
- $\boldsymbol{\mathcal{F}}$: The fission operator
- $\boldsymbol{\mathcal{B}}$: The scattering, leakage and absorption operator

This formulation can be used to obtain the reactivity of a fixed reactor configuration without necessarily being critical, which makes it possible to study a reactivity variation due to changes in equation parameters. Nevertheless, the equation has an infinite number of solutions for the flux (any linear combination of eigenvectors is a solution to the equation). As the neutron flux produces capture and fission, which produces energy, the flux is related to the global power with the following equation, which closes the system, and gives, for a given power, a unique solution for the neutron flux.

$$P = \int_{\partial\omega} \sum_{k} N_k(\vec{r}) \cdot \left(\lambda_i \kappa_\lambda^k + \int \left(\sigma_f^k(E)\, \kappa_f^k + \sigma_c^k(E)\, \kappa_c^k \right) \bar{\phi}(\vec{r}, E) dE \right) d\vec{r} \qquad (2\text{-}4)$$

With:

- κ_f^k: The fission reaction energy release of the isotope N_k
- κ_c^k: The capture reaction energy release of the isotope N_k
- κ_λ^k: The decay (α, β and γ) energy release of the isotope N_k
- $\bar{\phi}$: The neutron flux normalized to the power P
- $\partial\omega$: The geometry

In power reactor conditions, the power is high enough to induce a temperature rise of the fuel, cladding, coolant, and surrounding structures. The Boltzmann equation does not explicitly depend on temperature. However, several parameters in the equation are temperature-dependent through various physical phenomena.

Microscopic cross-sections depend on temperature due to the Doppler Effect. Cross-sections are given based on the incident neutron energy, assuming the target nucleus is stationary (temperature at 0 K). The actual motion of target nuclei resulting from thermal energy alters the apparent neutron energy and consequently modifies the cross-section.

By increasing temperatures, thermal expansion of the components occurs. In the case of fluids, while the geometry remains unchanged, the fluid isotopic density decreases, reducing the macroscopic cross-section and reaction rates. Structures and fuel elements are also impacted by thermal expansion, altering the core component geometry. Moreover, high reaction rates and temperatures lead to various physicochemical and mechanical phenomena. These phenomena (which are not detailed here) reshape the pellet, the cladding, and the gap between both and influence thermal exchanges with the coolant. The heat exchange between the coolant and the fuel is therefore modified and leads to temperature variations, which alter the reactivity, primarily through the Doppler Effect.

Boltzmann equation input data (cross-sections and geometry) depends on temperatures, driven by the power. Hence, the Boltzmann equation and therefore the fuel depletion is a coupled problem with additional equations from thermal-hydraulics, thermomechanics and fuel performance,[3] which will hereinafter be referred to as multiphysics equations (MP equations). To incorporate the influence of other physics on the neutron flux an iterative loop (based on a given convergence criterion, for instance, temperature discrepancy between two steps) can be considered with the Boltzmann equation. Once the multi-physics criteria is met, the resulting reaction rates are transferred to solve the Bateman equation.

[3] The fuel performance in this context refers to the thermomechanical response of the fuel when subjected to irradiation, along with its physicochemical characteristics.

With the quasi-static assumption and the use of the transport equation in its stationary form, the delayed neutron precursors are constantly in equilibrium and determined directly by the reaction rates. The Bateman equation is therefore used to evolve isotopic compositions of Heavy Nuclei (HN), Fission Products (FP) and activation products, shown below in matrix form:

$$\frac{\partial \mathcal{N}(t)}{\partial t} = \boldsymbol{\mathcal{A}}(\bar{\phi})\mathcal{N}(t) \tag{2-5}$$

$\boldsymbol{\mathcal{A}}$ represents the evolution matrix that relates isotopes together according to the reactions and decays in which they are involved. The fuel depletion can be computed by solving a stationary Boltzmann equation, the MP equations and the Bateman equation under a constant flux hypothesis, as depicted in the scheme presented in Figure 1. The Δt of each time-step has to be short enough to "capture" the flux evolving spectra effect.

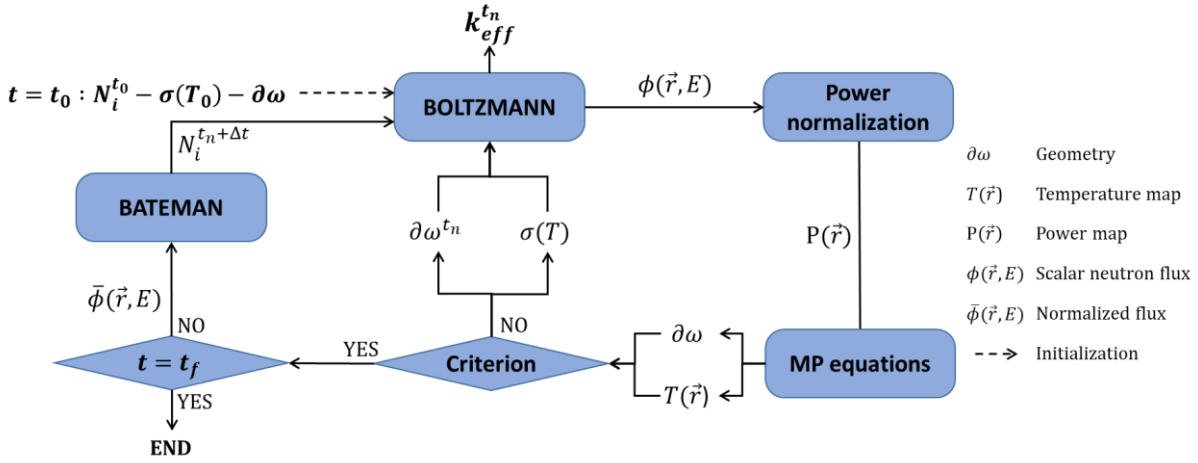

Figure 1. Fuel depletion calculation general scheme with the quasi-static approach

By following this calculation route, the time-dependent reactivity curve $\rho(t)$ due to fuel depletion can be determined. The classical behavior of this curve in SFRs is presented in Figure 2 and it may be divided into two different parts in time.

The first one, during the initial 10-20 days, is called the Neptunium effect and it represents the delay before the saturated ^{239}Pu production is attained. This is caused by the fertile capture of the ^{238}U that breeds into ^{239}Np with its decay constant of 2.35 days to produce ^{239}Pu (see Figure 3). Although the ^{239}Pu fission rate tends to remain constant, the ^{239}Pu production is lagged with ^{239}Np decay; it implies a greater net loss of ^{239}Pu (and so greater reactivity loss).

Beyond the first 20 days of irradiation, once the ^{239}Pu production saturates, the reactivity decreases linearly and the slope of this curve is called **reactivity loss coefficient** (α_{BU}).

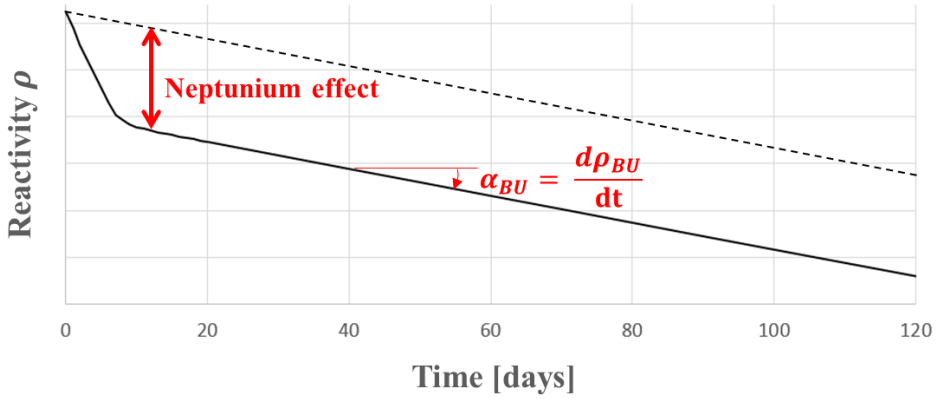

Figure 2. Illustrative reactivity loss curve of a classical SFR

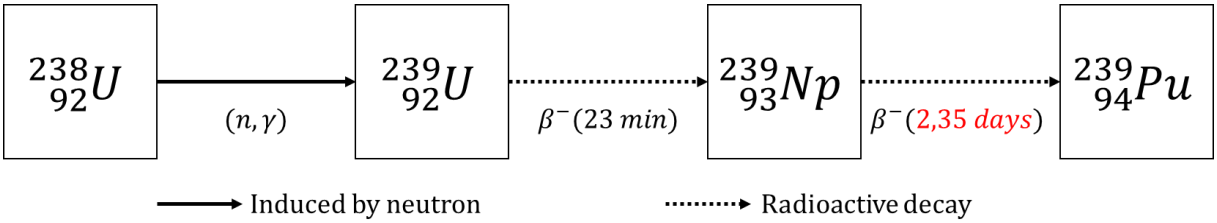

Figure 3. ^{239}Pu production process by fertile capture of ^{238}U

2.1.2. Solving the Bateman equation

The quasi-static assumption allows fuel depletion to be treated as a succession of stable neutron states, thus making it possible to solve the generalized Bateman equations under a constant neutron flux hypothesis. Hence, the generalized Bateman equations transform into first-order differential equations with constant coefficients, and consequently, they admit a solution in the form of a matrix exponential:

$$\mathcal{N}(t) = \mathcal{N}(0)exp(\mathcal{A}t) = \mathcal{N}(0)\sum_{k=0}^{\infty}\frac{t^k}{k!}\mathcal{A}^k \qquad (2\text{-}6)$$

This matrix exponential method is the approach employed by the ERANOS[4] [16] system code for the evolution of isotopic compositions in former SFR fuel depletion analysis in CEA. To solve it numerically, the infinite sum was truncated to order n, where n depends on the chosen time step and the elements of matrix $\mathcal{A}$.

Another way to compute the fuel depletion, without using the analytical solution, is to solve the differential equation with a numerical scheme. The MENDEL [17] solver available through APOLLO3® uses a fourth-order Runge-Kutta numerical scheme to solve the Batman equation.

[4] ERANOS (European fast Reactor neutronics ANalysis Optimized System) is a platform consisting of several deterministic solvers for the study of SFR. This platform has undergone extensive experimental validation and has been used to track certain Phenix and Superphénix cycles.

To solve the Bateman equation, the evolution matrix should be constructed with the decay constants, branching ratios, fission yields, and reaction rates of every isotope present in the core. The list of isotopes and the reactions that link them together is called a depletion chain. In a reactor, one can find over a thousand different isotopes due to fuel depletion, primarily fission products. Some coefficients, such as decay heat at the end of an irradiation, need this type of full depletion chain [18]. However, most of these isotopes have a negligible impact on reactivity or a half-life significantly shorter than a calculation time-step, so a partial depletion chain may be considered. The role of the partial depletion chain is then to find a good balance between calculation time, accuracy, and uncertainty of the different independent/cumulated[5] Fission Yields. The depletion chain used for fuel depletion study in this PhD is the chain developed specifically for reactivity loss purpose in [8]. This chain contains 32 heavy nuclei and 141 fission products.

2.1.3. Solving the stationary Boltzmann equation

There are two possible ways to provide a solution to the neutron transport problem. The first and most intuitive one is the stochastic method, also commonly named the Monte-Carlo method [19]. The Monte Carlo approach is based on neutron sampling from their emission to their absorption or leakage from the reactor (the neutron's life is also called a history). The individual treatment of each neutron makes it possible to respect the physics at the microscopic scale by representing the interactions taking place without any (or with only a few) assumptions, regardless of the order of magnitude (energetic, spatial and angular) of the phenomenon.

For each neutron life, each state change in phase space has a certain probability of occurrence. The goal of the Monte Carlo method is, therefore, successively:

1. **To calculate the probability of state changes**: The first step is to calculate the probabilities of each possible state change for a neutron. These probabilities are based on the physical laws that govern neutron-matter interactions.
2. **To carry out a random draw**: The next step is to carry out a random draw to determine the next state of the neutron. The probability of each state is equal to the probability of state change that was calculated in the previous step.
3. **To modify the state of the neutron**: The third step is to modify the state of the neutron to the state that was determined by the random draw.
4. **To record information about the neutron's life**: The final step is to record information about the neutron's life, such as its energy, position, and direction.

By repeating these steps for a large number of neutrons and also applying the central limit theorem, the Monte Carlo method may be used to obtain accurate information about the macroscopic behavior of a system.

[5] A cumulative yield of an isotope is the sum of its independent fission yield and the independent fission yields of its radioactive parents (potentially weighted by radioactive branching if multiple decay paths exist for certain isotopes), which are disregarded through chain reduction.

Within the framework of this PhD, the Monte Carlo code developed by CEA, TRIPOLI-4® [20], is used. The quasi-exact representation of physical phenomena by Monte Carlo codes makes them reference codes in neutronics. However, the slow convergence rate implies that a very large number of neutron histories must be simulated, leading to lengthy computations (and potentially heavy memory usage, as in the case of fuel depletion) which would require high computational power. In a context of more restricted computing power, a deterministic approach to the transport equation is preferred for fuel depletion and multiphysics calculations.

The goal of deterministic methods for solving the equations of neutron physics is to subdivide the global equation defined in the entire phase space into a multitude of smaller bounded problems in the phase space (the boundaries defining a mesh) where the equation is locally easier to solve[6]. The different methods to solve the transport equation are exact methods if the dimensions of the discretization (in time, space, energy, and direction in the case of Boltzmann and Bateman system) are less than the dimensions of the different phenomena that take place in a reactor. However, respecting such constraint for a reactor requires computational power (in CPU time and RAM) too high for usual computing power.

Then, to solve the problem by deterministic means, the phase space has to reduced, which leads to modification of the problem as shown by the following points and Figure 4 :

- Geometrical homogenization of different media.
- Energy condensation: continuous cross-sections to **multigroup formalism** (one Boltzmann equation to several coupled mono-kinetic equations. It mainly implies the use of **multigroup cross-sections** as input data. For more detail, see Appendix B).
- Angular quadrature formula and anisotropy truncate for scattering treatment (see Appendix B)

[6] In reality, the equation is the same everywhere, but subdividing it into infinitesimal entities allow to use a linearity hypothesis (or other known functions) at the scale of the mesh that converges to the exact solution when the mesh dimension decreases.

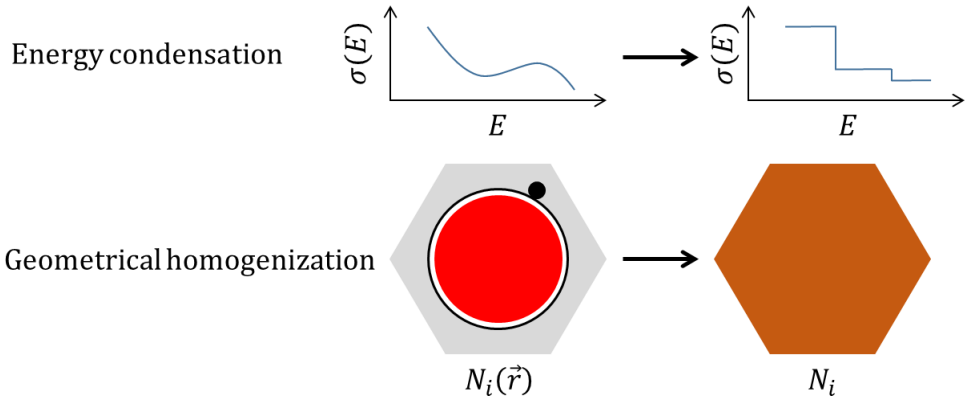

Figure 4. Illustrative homogenization of a fictitious SFR pin cell and cross-section energy condensation of a fictitious isotope

Such change needs representative input data (i.e. condensed cross-sections and homogenized isotopic compositions) able to correctly predict the main physical quantities as integrated reaction rates[7]. For that, cross-sections for the new macro-domain (D) and energy groups (G) should be averaged with the neutron flux:

$$\Sigma_{i,D}^{G} = \frac{\int_D d\vec{r} \int_G dE\ \sigma_i(E) N_i(\vec{r}) \phi(\vec{r},E)}{\int_D d\vec{r} \int_G dE\ \phi(\vec{r},E)} \quad (2\text{-}7)$$

However, the neutron flux is the unknown quantity of the Boltzmann equation. To overcome this problem, a classical approach is to use a two-step calculation scheme.

- The first step is the **lattice calculation** (2D subassembly scale). This step tends to produce the most representative flux for homogenizing and condensing effective cross-sections for the second step. For that, fine spatial, energetic, and angular discretization is considered to capture local phenomena. This calculation is performed for a representative configuration of each subassembly types with simplified neighboring.

- The second step is the **core calculation** (3D core). The spatial, energy, and angular mesh at this scale is coarser than at the lattice calculation. However, the boundary conditions and the neighboring of each region at this scale correspond to the actual core conditions. This scale takes account of fine heterogeneities through the homogenized and condensed cross-sections from the previous step. The core calculation can be used to study the reactor's behavior through diverse coefficients.

[7] The choice of the quantity of interest to be conserved may depend on the study being carried out, and the conservation of a certain number of quantities does not necessarily ensure the conservation of others. The question of homogenisation and the different theories are not discussed here, but it is explored in greater detail in [21]

APOLLO3®-FR is the 2-step calculation scheme used for sodium fast reactor analysis in this work and it is shown in detail below.

2.1.3.1. APOLLO3®-FR Lattice calculation

To produce the representative flux and homogenized/condensed cross-sections, the following workflow is performed for each different subassembly type.

Geometry

For the different input geometry considered at the lattice calculation step, the cluster paradigm is used. For fissile fuel, it consists of considering the flux generated by them in an infinite lattice (fundamental mode, see left subfigure of Figure 5). For fertile and non-fissile zones, the representative neutron flux is provided by a fissile subassembly positioned around it (cluster mode, see right subfigure of Figure 5). In both cases, the reflective boundary condition is considered for modeling of the infinite lattice.

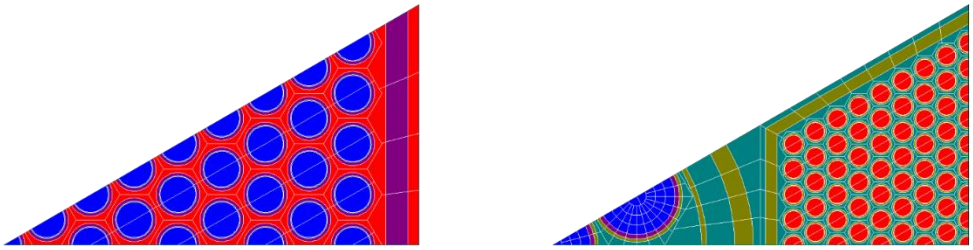

Figure 5. Different geometry description in the cluster paradigm for lattice calculation: fundamental mode (left) for fissile fuels and cluster mode (right) for fertile and non-fissile subassemblies (here a control rod)

Nuclear data

Nuclear data used in this work are taken from the JEFF 3.1.1 nuclear data library [22]. In the lattice calculation 1760 energy groups [23] are used to solve the Boltzmann equation. To get multigroup cross-sections for a given temperature from the JEFF 3.1.1 continuous cross-sections, the GALILEE system is used [24].

Self-shielding

The 1760-multigroup cross-sections have been condensed without the representative flux of the current geometry. In order to produce cross-sections that consider the dependence of spatial and energy terms, a correction step called self-shielding is performed. In order to do this, the subgroup formalism [25] and the Tone simplification [26], [27] is used with the Collision Probability Method available with the TDT solver (TDT/CPM). Appendix B provides more detail concerning this process. The resulting cross-sections are called self-shielded cross-sections.

Flux calculation

Once the self-shielded cross-sections are available, it is possible to compute the neutron flux for the given geometry. For such calculation, the Method Of Characteristics with the TDT solver is used [28] (TDT/MOC). In the cluster paradigm, configurations are

significantly supercritical (or subcritical). To simulate a critical state, a B1-homogenous leakage model is added to the flux calculation. Once the critical state flux is computed, cross-sections can be homogenized to one or several targeted macro-regions and condensed into a coarser energy mesh (h/c process). The resulting effective cross-sections are then stored in a database called MultiParameter Output (MPO) for APOLLO3®.

Classical homogenization macro-regions in cluster mode are the subassemblies sections as shown by the left subfigure of Figure 6 . For subassemblies with a strong absorbing part (such as control rods), different macro-regions may be considered to maintain fine modeling at the core level (right subfigure of Figure 6). In this process, the 1760 energy group cross-sections are collapsed into a 33-energy group inherited by historical ECCO/ERANOS SFR studies.

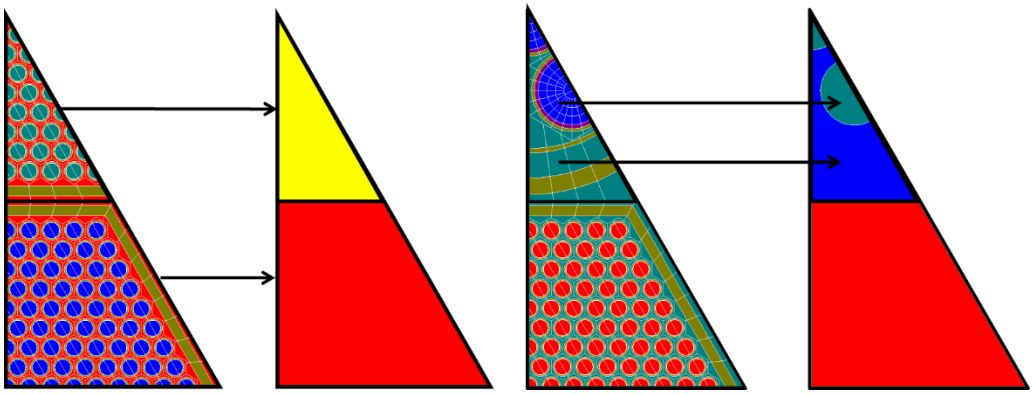

Figure 6. Homogenization process for a classical SFR fertile blanket cluster (left) and a control rod cluster (right)

Temperature and depletion parametrization

The lattice calculation aims to generate cross-sections of a representative core condition. In a fuel depletion and multiphysics analysis, local temperatures and isotopic compositions are unable to be determined precisely beforehand to the core calculation. To avoid having two calculation scales exchanging information in real-time, a tabulation of varying parameters is implemented, and the lattice calculation is performed for a range of temperature/irradiation history and stored in the MPO. The parameter used to represent the irradiation history is the BurnUp (BU – the total energy released by a given medium in MWd/HNtonnes). At the core calculation scale, cross-sections can be interpolated based on local temperature characteristics (such as the fuel temperature for the Doppler Effect), burnup, or any other significant parameter (such as sodium density for thermal expansion effect/void coefficient).

To build this multi-parameter library, fuel depletion is considered separately from the other parameters. For the multi-parametrization in temperature, cross-sections are

produced for a set of perturbed state in relation to a reference state[8]. The fuel depletion is performed only on the reference state, corresponding to the average nominal core conditions, with an APOLLO3®/MENDEL coupling following the scheme presented in Figure 7. At each time-step of the reference depletion calculation, cross-sections are also produced for the set of perturbed temperatures (see Figure 8).

Implementing multi-parameter tabulation in this manner assumes that the parameter discrepancy from the reference state does not influence the evolution of isotopic compositions, or at least that it introduces a negligible bias in the homogenized and energy collapsed cross-sections.

Moreover, the isotopic composition obtained in the lattice configuration will not be the same as the one obtained at the core scale. However, the distribution of heavy nuclei is supposed to be representative enough for cross-section homogenization.

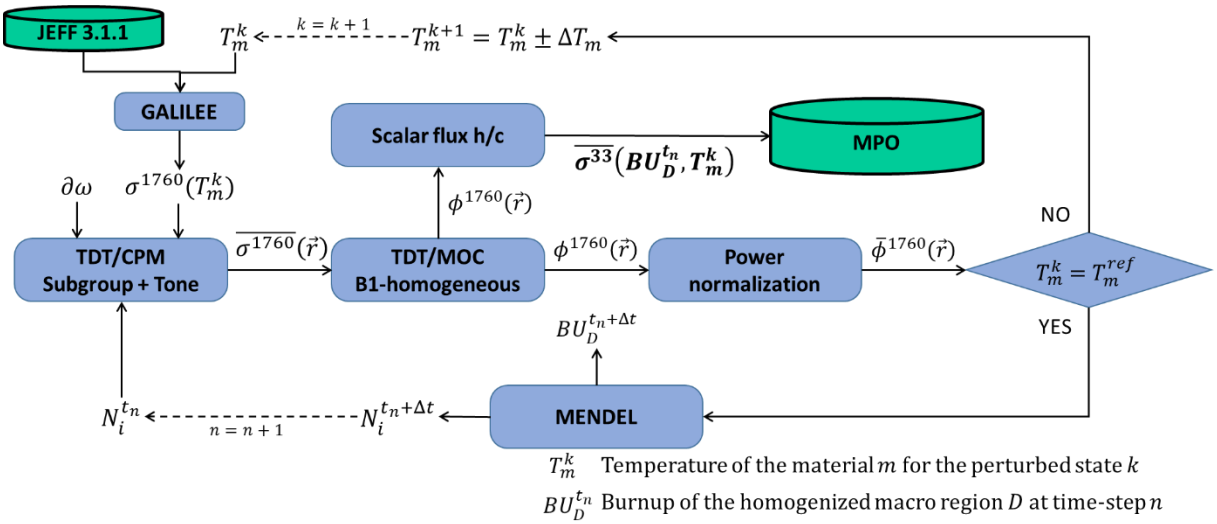

Figure 7. Lattice calculation and MPO production in the APOLLO3®-FR deterministic scheme for temperature and burnup multiparametrization

[8] The perturbations for a given reference state are the set of combinations of all the perturbed states defined by the user. Thus, if the user requests 3 temperatures for the fuel, 3 temperatures for the coolant and 3 temperatures for the steel structures, this gives 27 combinations and therefore 27 calculations to be performed: 26 perturbed calculations and 1 reference calculation. The notion of reference here is not related to a good accuracy.

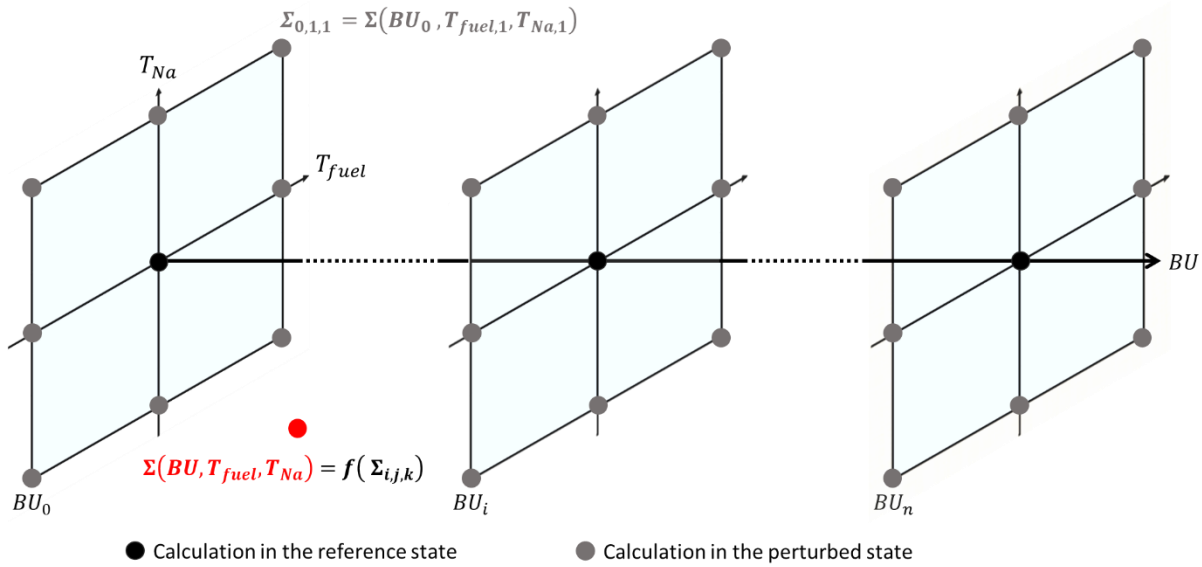

Figure 8. Multiparametrization (temperatures + BU) structure inside the MPO

2.1.3.2. APOLLO3®-FR Core calculation

The neutron flux at the core scale is computed with the discrete ordinate method (S_n) and a finite element method with the MINARET [29] solver in APOLLO3® (explained in detail in Appendix B). The S_n method is based on an angular discretization and a quadrature formula to transform a continuous angular integral into a sum of discretized angles. In this work, a sixth order is used (S_6) with a quadrature formula specific for a hexagonal lattice which implies 72 directions.

The finite element method requires a spatial mesh, which is, for the MINARET solver, radially unstructured and based on triangles. Axially, the triangle mesh is extruded to form prismatic 3D mesh (axially structured). The core geometry is formed with homogenized subassemblies and the triangle mesh allows for having an adaptive size of elements that may be finer in some specific area of interest and makes it possible to model an explicit strong absorbent lattice.

For the reflector area, the mesh size considered is larger (4 cm) than in the fissile and fertile media (2 cm). To properly mesh the absorber lattice pin, a finer mesh of around 0.5 cm is used inside the control rod subassembly. Moreover, control rods induce a strong flux dip around them, so that an intermediate mesh size of 1 cm is considered in order to follow the flux variation in that area (see Figure 9 to illustrate the different mesh size with the subassembly dimensions).

The neutron flux inside the different mesh is considered as linear radially and quadratic axially which makes it possible to have a larger axial mesh size (10 cm).

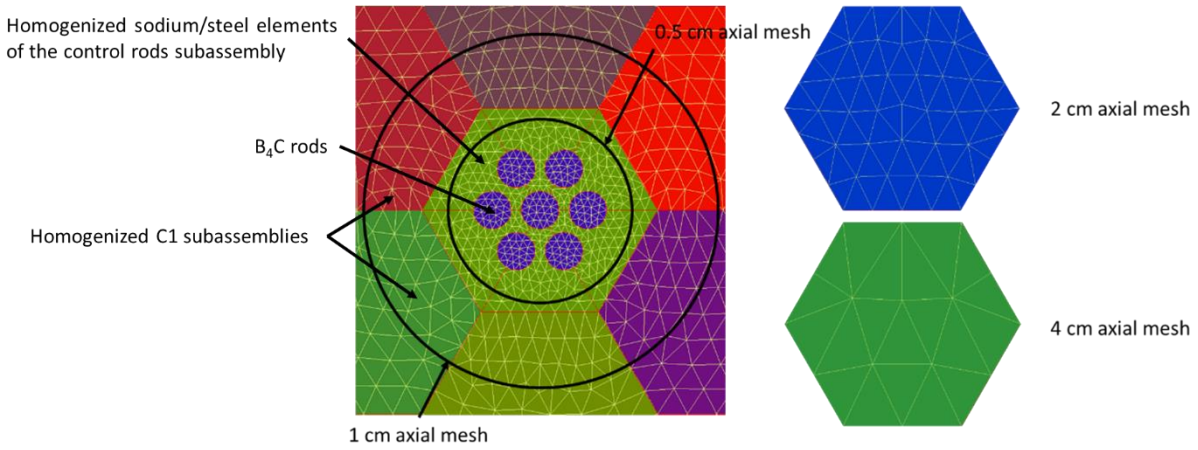

Figure 9. Description of the adaptive radial mesh around control rod (left) radial mesh of the rest of the fissile/fertile subassemblies (upper right) and inside radial reflectors (lower right)

To determine the neutron flux, the MINARET solver relies on the effective cross-section of the different medium. Therefore, MPOs are interpolated to obtain the cross-sections based on the local temperature and the local burnup.

2.1.3.1. Consideration of temperature map and thermal expansion

In the former depletion calculation scheme for conventional SFRs, the temperature map was considered uniform with an averaged value of the actual temperature map. The same assumption was used for the thermal expansion by choosing thermally expanded average dimensions of the full power condition. In that case, no coupling is performed and the normalized neutron flux is sent directly to MENDEL to compute the next time-step isotopic composition.

To take the temperature map and thermal expansion into consideration, it is necessary to solve the different thermal-hydraulics, thermomechanics and fuel behavior equations, which depend on the power map computed by the MINARET solver. Such a calculation must model the different scale of phenomena coming from other physics in a single calculation, for instance:

- Pellet cladding mechanical interaction (fuel performance);
- Fuel restructuration (fuel performance);
- Heat transfer at the sodium-cladding interface (thermal-hydraulics);
- Structural thermal expansion (thermomechanics).

A 3D model with state of the art methodologies for each individual physics, such as finite element method for fuel performance and thermomechanics and a CFD method for thermal-hydraulics, is able to accurately produce such a temperature map and the

geometry after thermal expansion. However, such a calculation requires high performance computing and is not attainable with the usual computing power. Therefore, some modeling hypotheses are commonly used, such as sub-channel computation [30] or system computation [31] for thermal-hydraulics and 1D½ axisymmetric modeling for the fuel behavior [32].

However, simulating a phenomenon with codes dedicated to each physics coupled together is mostly required for transient and accident studies, where each physics plays a significant role in the phenomenon (as studied in [33] for SFR control rod withdrawal or in [34] for determining Superphenix power feedback).

In normal operation, if the irradiation is at stable power, structural thermal expansion over time is negligibly affected as it depends on input/output sodium temperatures, directly related to the power. Moreover, the flow regime within each assembly should not change significantly over time to justify pin-by-pin thermal-hydraulic modeling. Only the fuel behavior significantly changes during irradiation. The constant pellet restructuring and the swelling of cladding under irradiation will continuously change the local temperature over time. Subsequently, depending on the cycle progress and the local fuel temperature, a certain amount of Fission Gas (FG – fission products that are in a gaseous state) is released from pellets and migrates into plenums, tending to change the local FG isotopic composition.

To study the fuel performance aspect, the GERMINAL V2 fuel performance code, dedicated to SFR MOX fuel, is used [35],[32] in which 1 representative average pin is considered per subassembly and modeled with a 1D½ axisymmetric modeling. This modeling consists of dividing the pin (fuel pellet, gap and cladding) into slices and solving the different equations using a 1D radial mesh. The boundary condition of the first slice will be the assembly inlet temperature and the output temperature of each slice will be the input for the next one. The sodium temperature rise in each slice is computed with the local heat flux (all the power generated by a slice is entirely extracted by the coolant).

In conventional SFRs, each subassembly is contained in a hexagonal tube without sodium exchange between subassemblies. Therefore, the simplified thermal-hydraulics model implemented in GERMINAL V2 is considered sufficiently representative of the average pin behavior in normal operation. Finally, the GERMINAL V2 code has been through the Verification and Validation (V&V) process with a wide experimental set, including the test from Phenix. This makes it possible to use it reliably in the present work.

With the power map computed with MINARET, GERMINAL can compute the fuel, sodium and cladding temperatures of each slice of the average pin of each subassembly (identified as SA_k in Figure 10). Then, cross-sections can be updated by interpolation between the chosen temperatures at the lattice level and stored in the MPO. At the lattice level, the

sodium density has been linked with the sodium temperature with a thermal expansion law so the sodium density is also updated with its temperature.

Concerning the fission gas migration, the leakage rate can be obtained from GERMINAL and the isotopic composition of fission gas updated (Krypton and Xenon isotopes). GERMINAL input data and output data treatment for APOLLO3® are detailed in Appendix E.

Finally, the geometry description corresponds to full power dimensions and this is considered as constant during irradiation (the underlying assumption is that the minor dimension changes during irradiation have a negligible impact on the reactivity).

This iterative calculation loop is performed between MINARET and GERMINAL until the temperature convergence is reached as the Figure 10 illustrates it. The temperature criterion (ε_T) is a temperature discrepancy between two multiphysics steps lower than 1°C for fissile fuel (3°C for fertile fuel and 1°C for structures).

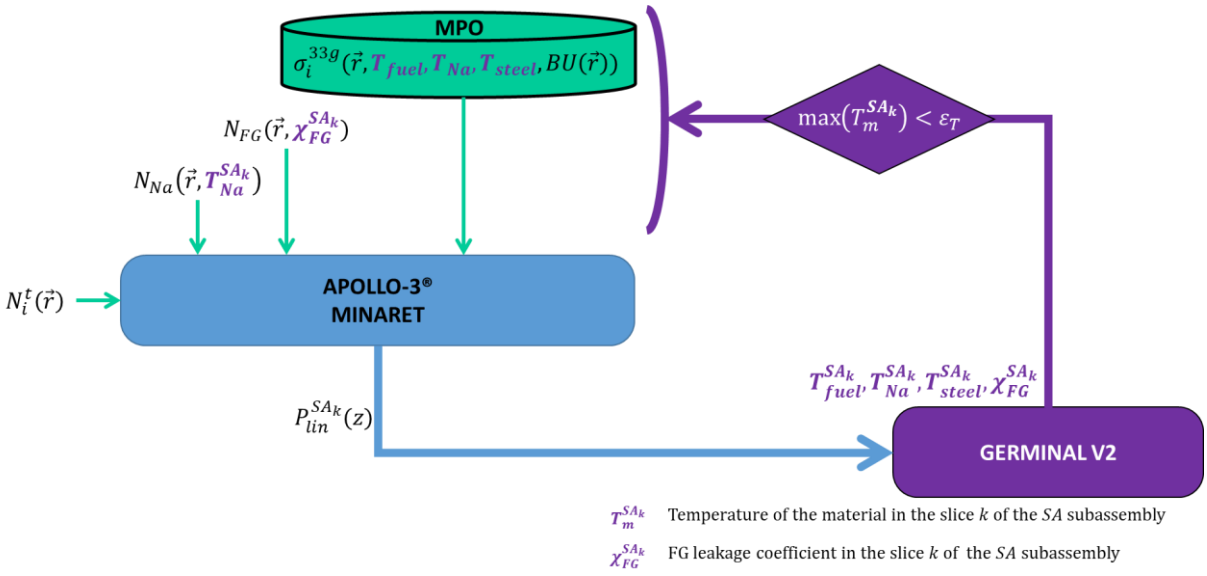

Figure 10. Multiphysics coupling between the APOLLO3®-FR deterministic scheme and the GERMINAL V2 tool

2.1.4. APOLLO3®/MENDEL deterministic scheme

The global scheme to solve a fuel depletion problem deterministically with the APOLLO3®-FR scheme and the MENDEL solver is presented in
Figure 11. With the APOLLO3® architecture, the multiphysics coupling can be considered during irradiation with an additional iterative loop and cross-section multiparametrization. One average pin is considered per subassembly so that in a core simulation more than hundred pins are considered in order to obtain the correct temperature map at each time-step.

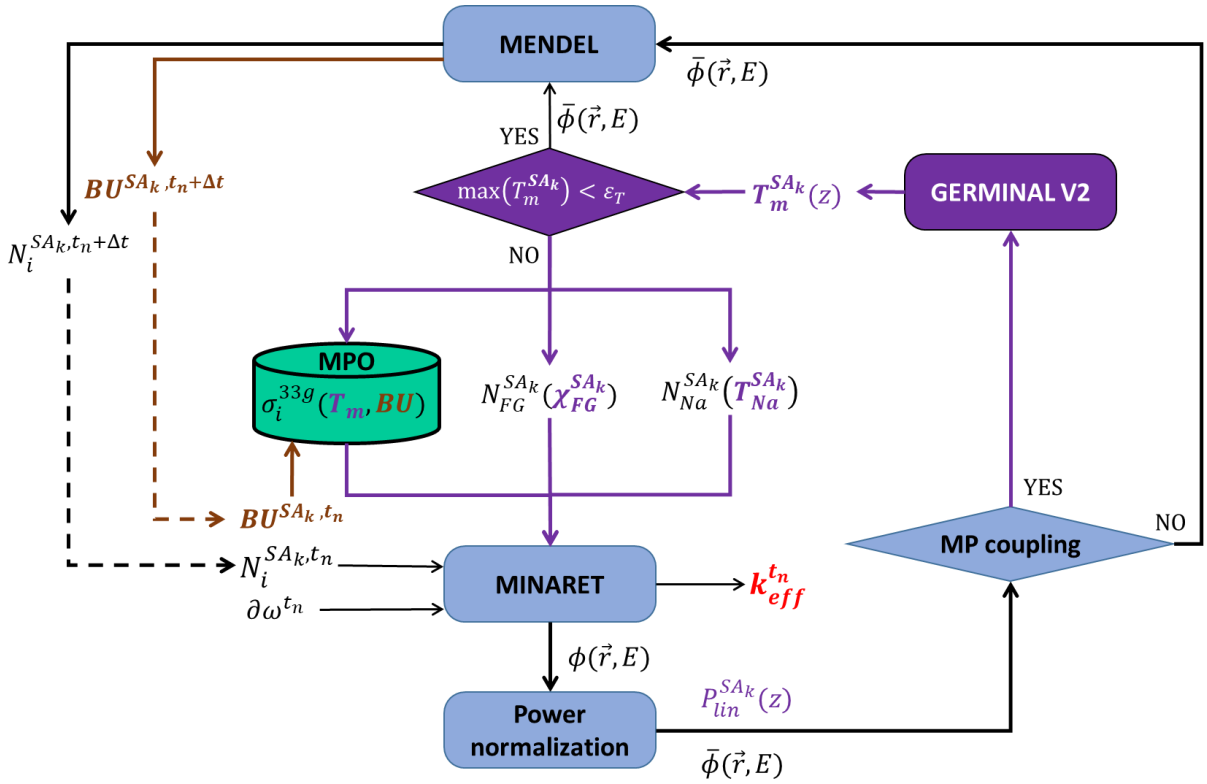

Figure 11. APOLLO3®/MENDEL/GERMINAL V2 calculation route for fuel depletion calculation

With this global scheme and a given time-step, (depending on how the neutron flux spectrum could change during irradiation), the reactivity loss coefficient can be obtained by the curve slope of the multiplication factor computed at each time-step ($k_{eff}^{t_n}$ in Figure 11). As shown in this section, the fuel depletion scheme with APOLLO3® allows for advanced modeling capabilities by removing systematically considered assumptions in former SCTs.

2.1.5. Contribution of the new approach

Modern computational tools allow for more accurate modeling by increasing the number of phenomena taken into account in simulations. Besides, it is possible to assess the sensitivity of the various contributors to a specific phenomenon, which was previously difficult to achieve due to the architecture and modeling assumptions in former tools. Table I summarizes the difference and improvements brought with the actual neutronics scheme compared to the last validated tool used in CEA for SFR core analysis (ECCO/ERANOS code package [16]).

Table I. Calculation scheme difference between the ECCO/ERANOS fuel depletion scheme and the APOLLO3®/MENDEL scheme

	ECCO/ERANOS (2012)	APOLLO3®/MENDEL (2021)
Lattice calculation		
Energy groups	1968	1760
Self-shielding	Subgroups multicell CPM	Subgroups + Tone exact CPM
Flux calculation	Exact CPM	MOC
Leakage model	No (P1 consistent in the last version)	B1-homogeneous
Fissile SA geometry	Fundamental mode	Fundamental mode
Non-fissile SA geometry	**Fundamental mode (imposed fissile source)**	**Cluster model**
BU tabulation	**No**	**Yes**
T tabulation	**1 Cold + 1 averaged Hot**	**Yes, unlimited (+Sodium density)**
h/c process	Scalar flux weighting	Scalar flux weighting
Core calculation		
Energy groups	33	33
Flux calculation	SP3 + nodal method	S6 + Galerkin finite element
Control rod geometry	**Homogeneous with corrected cross sections** [34]	**Heterogeneous**
Explicit definition of subregions	**No**	**Yes**
Depletion calculation		
HN	32	32
FP	15 LFP (Lumped Fission Product)	141 FP
FG leakage	**inside LFP fission yield**	**Yes with MP coupling**
Temperature map	**Averaged temperature**	**Yes with MP coupling**
Control rod movement	Yes	Yes
Control rod depletion	**No**	**Yes**

A major improvement of the APOLLO3® code is the ability to handle radial unstructured mesh at the core scale with MINARET that allows a given area of interest to be represented explicitly, for a more accurate reproduction of the spatial self-shielding due to a strong absorber as is the case for the in-core experimental device and control rods. The explicit

modeling of the absorbing lattice mainly improves the ^{10}B capture reaction rate accuracy and the control rod worth without reactivity equivalence correction as was the case in the ERANOS package (shown in [36]).

Moreover, the multiparametrization in temperature and burnup has mainly been optimized (at both calculation scales) to be used in APOLLO3® to ease the simulation of multiphysics and fuel depletion calculations [37].

The experimental validation of the APOLLO3®/MENDEL coupling needs to rely on irradiation experiments. The first limitation is that the number of fast-spectrum facilities able to provide such experimental feedback are quite limited and most of them are not openly available. To isolate fuel depletion specifically some irradiation devices could be studied as for PROFIL [38], TRAPU and DOUBLON [6], [39] experiments but it restricts the study of fuel depletion to a limited set of pins with particular characteristics. Moreover, it does not allow evaluation of large scale fuel depletion and its influence on the main neutronics coefficient, as for instance the sodium void coefficient in SFR [8]. One way to validate large-scale fuel depletion experimentally is to study its consequence, the reactivity loss. In addition, this coefficient on its own is of prime importance for design as it is related to cycle time and to the control rod worth (to pilot the reactivity and compensate the reactivity loss due to fuel depletion).

In order to study this global coefficient, computed as the slope of the reactivity loss curve (see Figure 2), the core power should be as stable and long as possible to avoid neptunium non-linearity effect. Secondly, in order to simplify its validation, consistent operating conditions over irradiation time should be maintained to avoid structural changes due to thermal expansion. In this regard, the Phenix reactor operated for 40 years by CEA can provide a large amount of relevant experimental feedback. Hence, this work will focus on the reactivity loss of the Phenix reactor with the APOLLO3®/MENDEL scheme in order to establish if such a coefficient, specific to the power reactor with the modeling challenges that this implies, can contribute significant information for fuel depletion validation.

More advanced schemes for SFR in APOLLO3® are available, other than the one considered for the scheme presented:

- momentum homogenization with a B-heterogeneous leakage model for fissile material [40]
- “traverse” modeling at the lattice level to better take into account the flux softening from the fissile zone to the radial reflector
- 2D-1D modeling [41]
- 3D MOC [28]

However, those advanced schemes or models were developed for innovative designs in which conventional schemes have limited capabilities when dealing with complex designs. For breeder SFR design like the Phenix reactor, advanced schemes provide a

limited gain as shown for the Superphenix core in [34], so that the presented scheme is considered acceptable as will be shown in the 3th section of this chapter.

2.2. Phenix reactor

2.2.1. Reactor presentation

The Phenix reactor was a French SFR that achieved criticality in 1973 at the CEA Marcoule site and operated until 2009. This intermediate power reactor was designed to investigate various phenomena that the experimental Rapsodie reactor, due to its lower power, could not demonstrate. Its purpose was to contribute to the demonstration of SFR technology and pave the way for the Superphénix design. The 40 years of operation of the reactor have provided significant experimental feedback for this technology, as documented in [42]. The features outlined in this section are derived from the same source.

This reactor is referred to as an integrated pool-type reactor, meaning that the core, heat exchangers, and pumps are in the same large vessel (main vessel in Figure 12) suspended and supported by the upper concrete slab. The sodium pumps ensured a flow rate of 2800 kg/s of sodium at 400°C into the core. The generated power raised the temperature of sodium by a ΔT of 160°C when the core was at its full power of 563 MWth. The hot sodium then expelled excess heat in the sodium-sodium heat exchanger. Mixing of hot and cold sodium was prevented by a conical baffle (primary vessel in Figure 12). The secondary sodium, heated by the primary sodium in the exchanger, then went into a sodium-water exchanger capable of producing steam to drive the turbine and generate 250 MWe (at full power).

Regarding the core design, power generation was ensured by two different fissile zones:

- The inner fuel (C1) composed with a 18.2% $^{239}Pu_{eq}$[9] MOX fuel
- The outer fuel (C2) composed with a 23.3% $^{239}Pu_{eq}$ MOX fuel. The outer zone of the fissile part has a higher enrichment to account for a homogeneous power map inside the core.

[9] The $^{239}Pu_{eq}$ quantity represents, for a given configuration with a multiplication factor k, the reactivity equivalent $^{238}U/^{239}Pu$ composition to the actual isotopic vector composed of other actinides [43]. It can be expressed as follows:

$$N_{^{239}Pu_{eq}} = \sum_i \frac{\sigma_i^+ - \sigma_{238U}^+}{\sigma_{239Pu}^+ - \sigma_{238U}^+} N_\mathrm{i}$$

$$\sigma_i^+ = \frac{\nu\sigma_{f,i}}{k} - \sigma_{a,i}$$

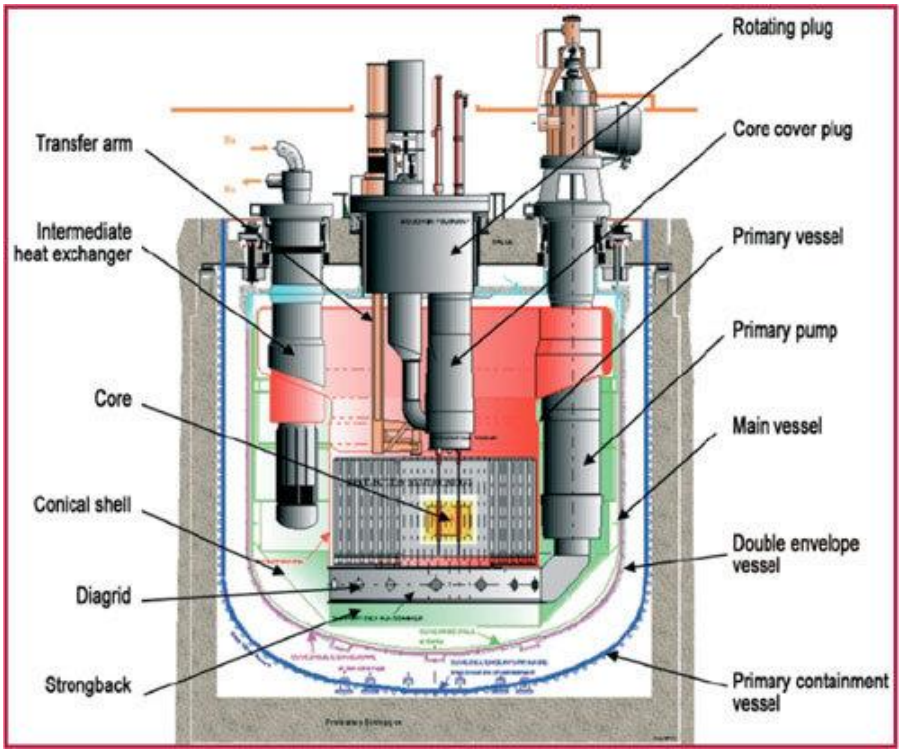

Figure 12. Phenix reactor block [44]

The fuel rods consisted of cylindrical pellets stacked in a hexagonal lattice of 217 stainless steel pins. The entire set of pins was then arranged inside a hexagonal tube made of stainless steel (see Figure 13). In order to prevent contact among pins, each pin was encircled with a helically wound spacer wire.

Fertile fuel with depleted uranium oxide was arranged axially and radially on the periphery of the fissile zone. This depleted uranium can produce fissile material (plutonium) through the capture of the leaked neutrons from fissile zones. Axial blankets were part of the fissile subassembly. The lower axial blanket (FCAI) was made with depleted uranium pellets of the same dimension as the fissile pellets and inside the same pins. On the contrary, the upper axial blanket (FCAS) was separated from the fissile pin lattice by a plenum (ZTRS) in a different hexagonal lattice with different dimensions as shown in the Figure 13.

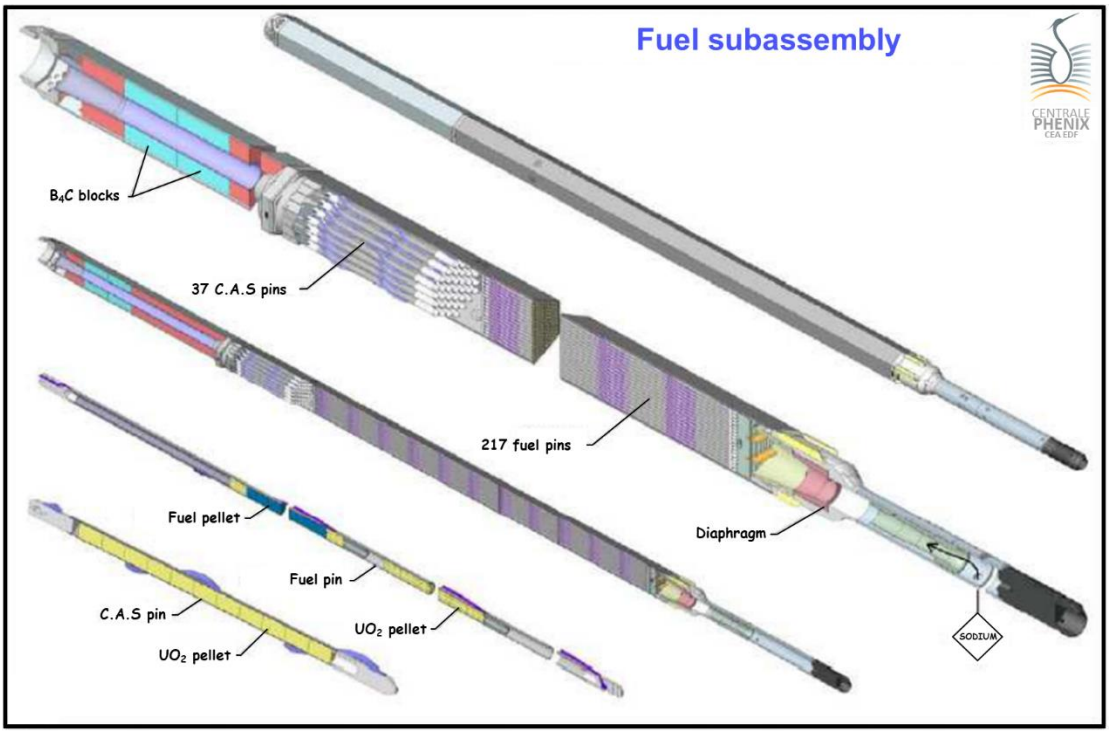

Figure 13. Standard Phenix fissile subassembly [45]

Concerning the radial blanket (FCR), the subassembly was composed of 61 fertile pins in a hexagonal lattice (see Figure 14).

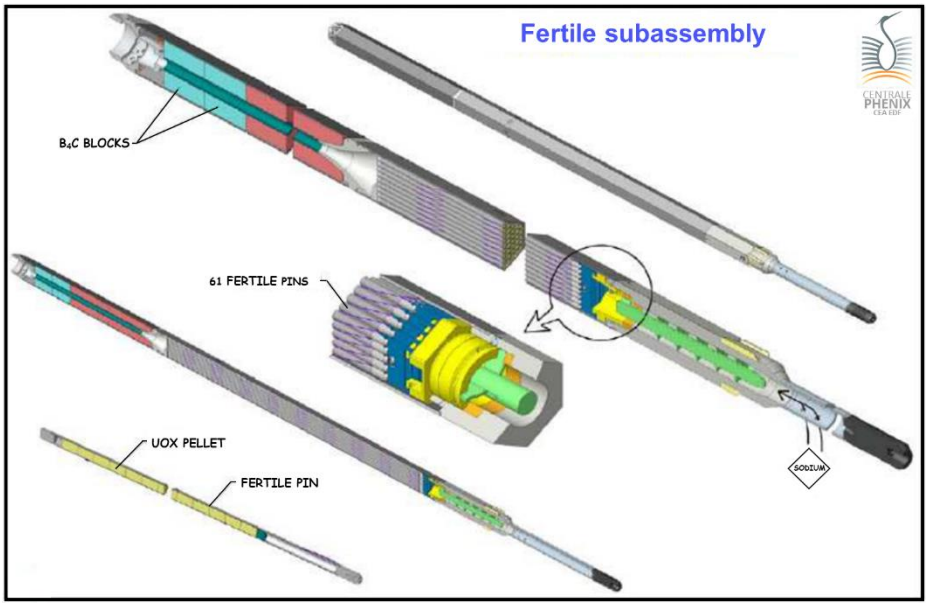

Figure 14. Standard Phenix fertile subassembly [45]

The core was surrounded by steel neutron protection to lower the heat-exchanger sodium activation and decrease neutron leakage. Axially, the reflector was part of the

subassembly as was the axial blanket. Radially, steel reflectors were positioned at the periphery, cooled by forced or natural convection depending on the distance from the core.

In contrast to thermal reactors, it is not possible to dilute a neutron poison in the coolant in order to control the neutron chain reaction. This reactor control was therefore ensured only by the control rods (6 in the Phenix reactor). A control rod consists of a cylindrical sheath inside which is the absorber composed of a hexagonal lattice of 7 rods where B_4C pellets with a 48% ^{10}B enrichment are stacked (see Figure 15).

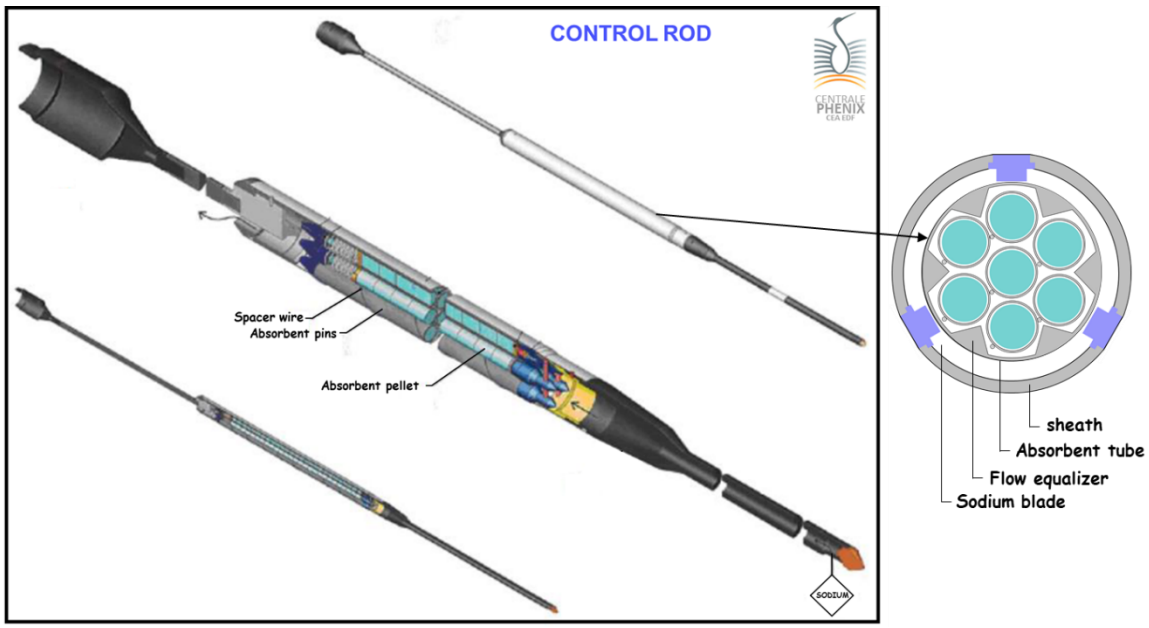

Figure 15. Standard Phenix control rod subassembly

Fissile, fertile, absorbing, reflecting subassemblies or other non-standard subassemblies were arranged in a hexagonal lattice (see Figure 16). A hexagonal lattice allows a more compact core compared to a Cartesian lattice.

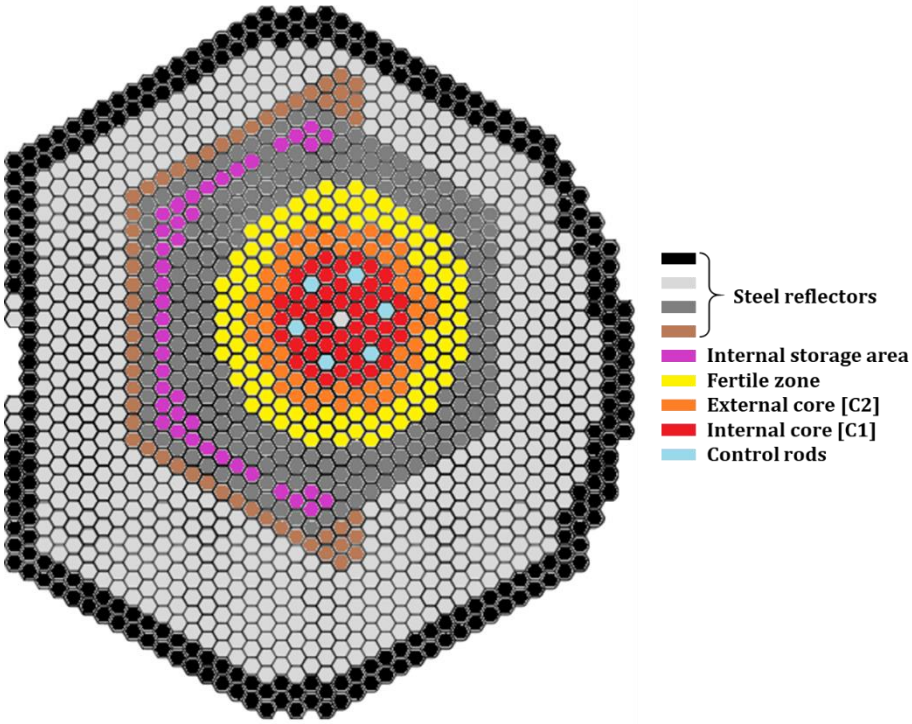

Figure 16. Illustration of a Phenix loading plan [45]

2.2.2. Phenix Geometry modeling

The purpose of the Phenix modeling is to be as accurate as possible to the actual reactor. This model corresponds to a hexagonal lattice with the 12 first rings of the core presented in Figure 16. Each node of the lattice is filled with the subassembly following the loading plan (i.e. depending on the cycle simulated). The geometry and the material description follow the technical specification of the Phenix reactor. Each subassembly type is presented in Figure 17 and each of the subparts of the subassemblies are listed in the Table II.

Table II. Different subassembly axial zones of each of the subassemblies in the core of cycle 42-115 of the Phenix reactor

Subassembly axial zone		Subassembly type	Lattice geometrical representation
C1	Fissile fuel of the inner core *(Coeur 1)*	C1	technological
C2	Fissile fuel of the outer core *(Coeur 2)*	C2	technological
FCAI	Lower axial blanket *(Fertile Couverture Axiale Inférieure)*	C1/C2/DCC	technological

FCAS	Upper axial blanket *(Fertile Couverture Axiale Supérieure)*	C2/C2	technological
FCR	Radial blanket *(Fertile Couverture Radiale)*	FCR	technological
PNSC	Upper axial reflector of the fissile subassembly (Protection Neutronique Supérieur Combusitble)	C1/C2	technological
PNSF	Upper axial reflector of the fertile subassembly (Protection Neutronique Supérieur Fertile)	FCR	technological
ROD	Absorbing part of the control rod	ROD	technological
ASA	Radial reflector	ASA	technological
SPN	Lower axial reflector	*C1/C2/FCR/DCC*	*homogeneous*
ZTRS	Plenum	*C1/C2*	*homogeneous*
SSVS$_X$	Upper axial part of the control rod	*ROD*	*homogeneous*
SSVI$_X$	Lower axial part of the control rod	*ROD*	*homogeneous*
C1 (DCC)	Fissile fuel without the central pins to host an experimental device	DCC	technological

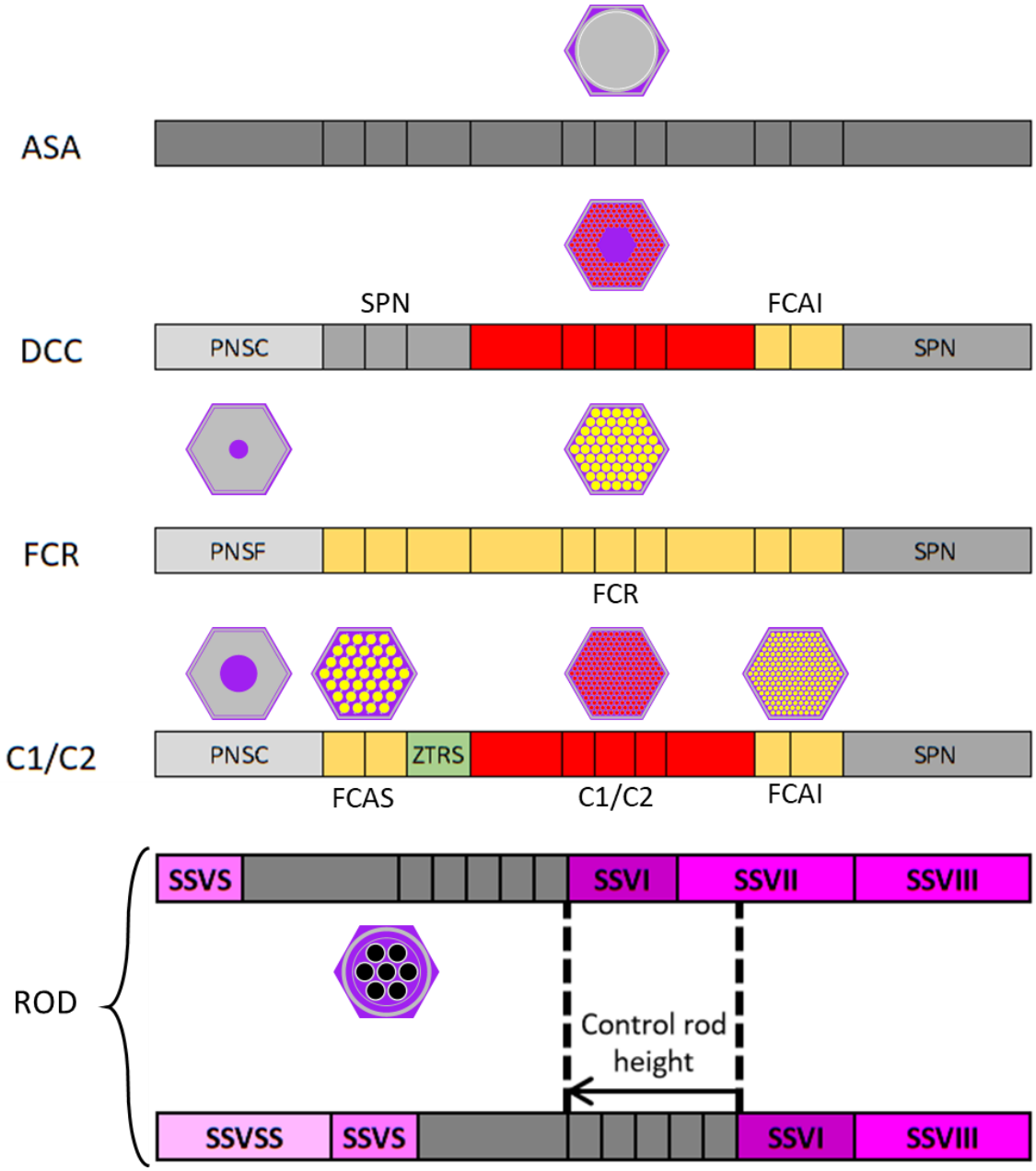

Figure 17. Axial description of the main subassembly type inside Phenix cycles

Experimental irradiation devices were located inside the Phenix core. These devices were inserted inside the DCC-type subassemblies presented in the previous Figure. To model their influence in the core, dedicated cross-sections are produced for each device with a cluster lattice calculation (the DCC subassembly with the device inside, surrounded by a C1 fissile subassembly).

For non-standard subassemblies with complex geometry as DCC with an experimental device inside (capsule) and for control rod with strong spatial self-shielding, partial homogenization is implemented (see Figure 18). Regarding absorber subassemblies, B_4C pellets are independently homogenized in a different macro-domain, surrounded by sodium/steel. The same process is performed for the capsule where only the capsule is

homogenized (green domain of the b subfigure in Figure 18) with the rest of the DCC being taken as the C1 fuel.

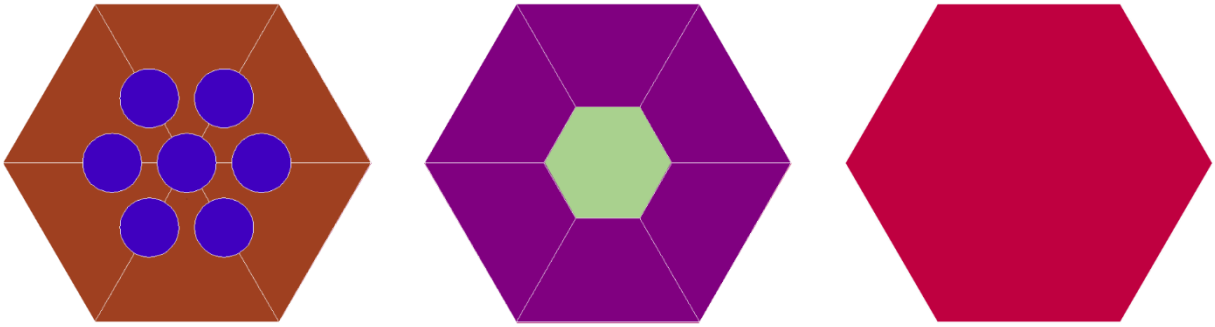

Figure 18. Geometrical modeling of different subassembly axial zone section of the Phenix model

2.2.1. Specific features of the Phenix reactor and fuel depletion

The modeling of a given cycle for a power reactor like Phenix involves a number of specific features that should be highlighted, as well as the various assumptions associated with them.

2.2.1.1. Isotopic composition initialization

The Phenix reactor operated through more than 50 cycles over 40 operational years. The loading plan management during those cycles was to replace 1/6 with fresh fissile fuel. It implies that at the Beginning of Cycle (BoC), 5/6 of the subassemblies were already irradiated with an unknown experimental isotopic composition (except during the core start-up). When simulating Phenix reactor cycles, the isotopic composition initialization is a source of bias to investigate.

To manage the loading plan for every cycle, a computational tool was used to estimate the isotopic composition. The most recent validated one used for this purpose was based on the ECCO/ERANOS codes with the characteristics presented in Table I. This version of the ECCO/ERANOS scheme, called PROJERIX, has performed the Phenix fuel depletion from cycle 34 to the last cycle and the isotopic composition at each beginning of cycle was stored in a database.

Even if those compositions are computed instead of experimental measured, the BoC compositions have been validated in relation to the predicted BoC reactivity [46]. This validation engenders some confidence regarding the heavy nuclei composition. Hence, it is the database used to initialize the isotopic composition for the fuel depletion calculation on a Phenix cycle.

However, for the PROJERIX database production, the depletion chain was composed with Lumped Fission Products (LFP) instead of individual fission product. In contrast, the depletion chain considered in this work is based on real fission products. To estimate a fission product distribution based on the burnup, the fission product distribution is taken from the MPO for a given heavy nuclei quantity. The bias of such a model should be limited to differential coefficients as reactivity loss, due to the negligible effect of fission products on the neutron spectrum of a fast reactor.

2.2.1.2. In-cycle control rod extraction

During the cycle, the reactivity loss due to fuel depletion is compensated at any time by the control rod extraction. This extraction induces a flux redistribution that perturbs local reaction rates and then the fuel depletion and temperature map. Usually, a fuel depletion calculation is performed with geometry that remains unchanged over time, which can induce local over/under-estimation of the reaction rate in the influence zone of the control rod. This hypothesis for fuel depletion calculations will be revisited so that the influence of considering the control rod extraction at each time-step (geometry changes) can be estimated.

The Phenix reactor is a complex object to model, which implies a complex methodology with the APOLLO3®-FR deterministic scheme coupled with MENDEL and GERMINAL. Before modeling the Phenix cycle experimental reactivity loss, the methodology must be evaluated by incrementally increasing the complexity.

First, the APOLLO3®-FR deterministic scheme on a simplified Phenix-model at cold temperature (without any multiphysics or fuel depletion) will be validated numerically in order to extract the intrinsic bias of such a scheme.

Then, a fuel depletion of a Phenix subassembly in an infinite lattice will be performed with the APOLLO3®/MENDEL scheme coupled with the GERMINAL tool to establish the methodology for the core-scale multiphysics fuel depletion calculation.

2.3. APOLLO3®-FR numerical validation with a Phenix-Like model

To validate the neutronics scheme used in this document, a Phenix-like “numerical” model is proposed. For this model, only fresh fuel has been used without in-core experimental devices, at cold uniform temperature in the following configuration (see also Figure 19):

- Internal core subassembly C1 for the central subassembly to the 4th ring
- External core subassembly C2 for the 5th and 6th ring
- Radial fertile subassembly FCR for the 7th ring and 8th ring
- Steel reflector from the 9th ring to the last 12th ring

- 6 control rods in the 3rd ring

The axial description of these subassemblies has been described in section 2.2.2 in the Figure 17.

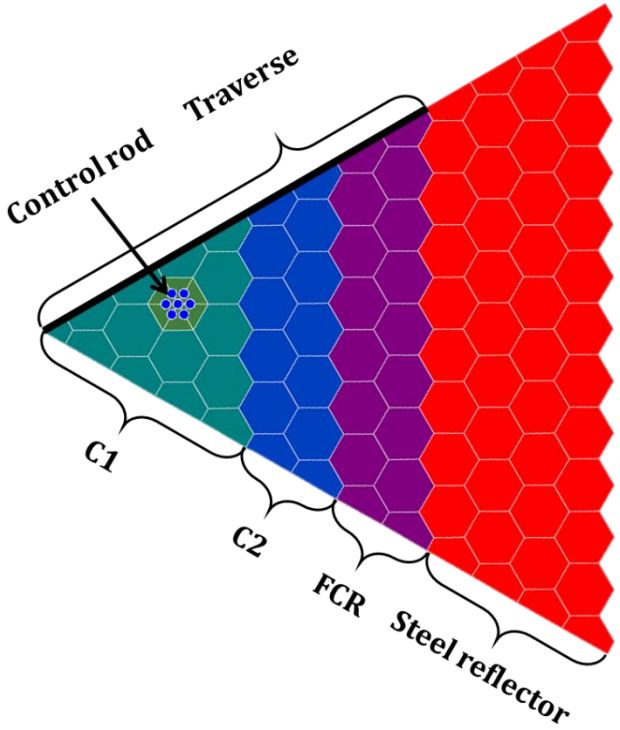

Figure 19. APOLLO3® modeling of the Phenix-like configuration with a 1/6 symmetry

The numerical validation of the APOLLO3®-FR deterministic scheme has been achieved by comparison with the Monte-Carlo TRIPOLI-4® computational tool for the main heavy nuclei reaction rates (^{238}U, ^{239}Pu, ^{240}Pu and ^{241}Pu on the traverse in Figure 19) and the control rod worth (see Appendix D for the modeling details). Extended analysis on this validation exercise is available in [REF 1], in which the various modeling parameters were studied in order to select the optimum solver parameters (spatial, angular mesh size, etc.). In this section, only the main results for the optimal set of parameters (see Appendix C) are provided.

2.3.1. Control rod worth

The control rod worth is the reactivity variation due to the control rod movement. In conventional SFRs and especially in Phenix, control rods were used to regulate the reactivity. Hence, it is a key safety feature to manage for SCTs. In Phenix, control rods are used together to control the reactivity. In such configuration, they form the Rod Bank (RB). This rod bank is characterized through axial axis by its S curve, which is the reactivity that can be inserted in the core by rod bank extraction: $\rho_{RB}^{SCT}(z) = \rho^{SCT}(z) - \rho^{SCT}(0)$. The Differential Control Rod Worth (DCRW) is the derivative of the S curve through axial axis.

To compute such curves, the multiplication factor is computed with TRIPOLI-4® and APOLLO3®-FR for each 10 cm control rod driveline starting with the fully inserted case (0 cm relative to the bottom of the fissile column). Results of the different simulations show that the APOLLO3®-FR neutronics deterministic scheme is able to simulate the differential control rod worth within the 2σ statistical uncertainty range of the TRIPOLI-4® simulations (see Figure 20).

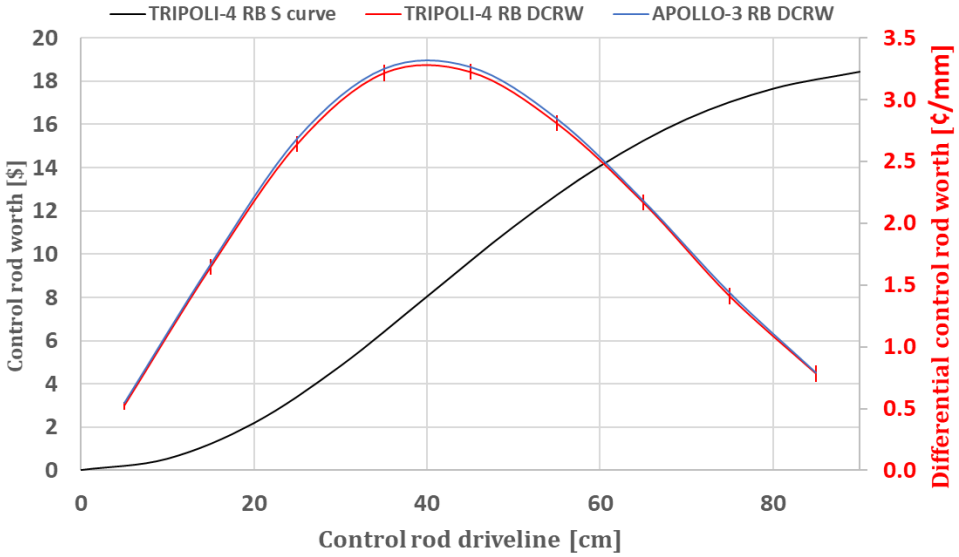

Figure 20. Rod Bank (RB) S curve and its efficiency for TRIPOLI-4® (with 2σ error bars) and APOLLO3® on the Phenix-like model

The APOLLO3®-FR scheme is able to accurately model such parameters and especially in the higher part of the core where the control rods are used to compensate for reactivity loss during cycle. However, control rod worth is an integral parameter that can hide local compensations. Therefore, validation on local parameters, such as reaction rates, has to be achieved.

2.3.2. Reaction rates

The reaction rates analysis, besides extending the numerical validation exercise, is important since these are the input data for the fuel depletion calculation (for MENDEL solver) and for multiphysics analysis with the local heat rate (for the GERMINAL tool).

The main results are presented in Table III. The two most impacting reaction rates for fissile media (^{238}U Capture and ^{239}Pu Fission) on the multiplication factor are accurately represented compared to a reference Monte Carlo model (< 0.62%) and engender confidence in the neutronics scheme for Phenix cycle depletion analysis.

Table III. Discrepancy between APOLLO3® and TRIPOLI-4® on integrated reaction rates (statistical uncertainty <0.1%) for each of the media of the Phenix-like configuration traverse (control rod being at a representative height of a Phenix cycle)

AP3/T4 – 1 [%]	^{238}U		^{239}Pu		^{240}Pu		^{241}Pu	
	(n,γ)	(n,f)	(n,γ)	(n,f)	(n,γ)	(n,f)	(n,γ)	(n,f)
C1	**0.11**	1.22	-0.78	**0.62**	-0.43	1.30	-0.42	0.51
C2	**0.53**	-2.67	-0.12	**0.04**	-0.25	-1.00	-0.31	0.23
FCAI	-1.51	-0.91						
FCAS	-0.14	4.88						
FCR	0.43	-0.69						

The spatial distribution of these discrepancies are presented in Figure 21 for the ^{239}Pu fission and the ^{238}U absorption. The distribution shows that the reaction rates are globally uniformly distributed around zero and that the global integrated results are not due to significant compensations. It has to be noted that the control rod has a significant and specific impact on the reaction rates of the surroundings subassemblies due to the strong induced flux dip. However, during cycle irradiation control rods are located in the upper part of the core and do affect a limited area of the core. Hence, this bias can be considered as acceptable for general analysis.

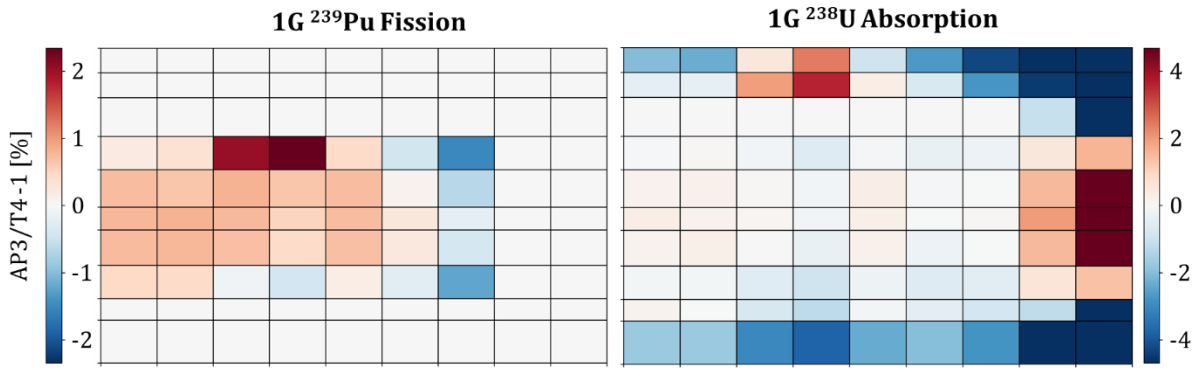

Figure 21. APOLLO3®-FR/ TRIPOLI-4® discrepancy distribution of the main reaction rates on the Phenix-like RZ traverse (statistical uncertainty <0.1%)

2.4. A Multiphysics approach to fuel depletion calculations: application to a fuel sub-assembly.

Fuel depletion modeling for the power reactor aims to reproduce the physics phenomena, namely, the temperature map and the fission gas that migrates outside the pellet in order to correctly compute local reaction rates for the depletion solver. To evaluate the impact

of computing and update through irradiation the temperature map and FG migration rate, a test case with a Phenix C1 subassembly in an infinite radial lattice has been considered (see Figure 22) to investigate the benefits of such coupling for a 3D core fuel depletion calculation.



Figure 22. Schematic axial description of subassembly in an infinite lattice case (fresh C1 subassembly)

The power distribution varies per subassembly depending upon its position in the core. For the C1 subassembly, the integrated power is between 4 MW and 6 MW with an average value of 5 MW. Hence, the multiphysics coupling impact on this test case is studied for three different scenarios at constant power (4 MW – 5 MW – 6 MW) for 600 irradiation days to be able to investigate different range depletion conditions.

The APOLLO3®/MENDEL scheme presented previously in this chapter is used for such calculation. To model the multiphysics phenomena, the fuel performance code GERMINAL V2 is used (with a global scheme presented in
Figure 11, detailed upon data exchange between APOLLO3® and GERMINAL in Appendix E). One average pin, from the lower part of the lower axial blanket to the upper part of the upper axial blanket[10], is modeled. The 1D½ axisymmetric modeling is considered with a 19 axial slices (4 of the same size in the lower FCAI, 10 of the same size in the C1, 1 of zero power for the ZTRS and 4 of the same size in the upper FCAI) aligned with the neutronics axial mesh with MINARET. For each slice, the pin is divided radially into 35+1 meshes (25 for the fuel, 10 for the cladding and 1 for the gap when there is one) to compute the main thermo-mechanical quantities needed for APOLLO3® (fission gas migration coefficient and fuel, sodium and cladding temperatures).

In this coupling, two quantities are considered: the temperature and the FG composition. To break down the impact of both parameters, three calculations per scenario are used:

- The reference one with a uniform and constant temperature distribution (1474K[11] in the fissile fuel, 730K for the lower axial blanket, 900K for the upper one and 724K for structures and coolant) and no FG migration (NoC – No Coupled case)
- The coupled case with a temperature map updated during irradiation without FG migration (T)
- The fully coupled case with the temperature map actualization and the consideration of the FG leakage from the fuel (T+FG)

[10] The FCAI medium is considered also in the upper part (and not the FCAS as in the exact Phenix subassembly modeling) in order to keep the same pin lattice for the entire subassembly.
[11] This temperature is supposed to represent the equivalent homogeneous temperature of the fissile medium. In other words, the uniform temperature that conserve the global reactions rates of the actual temperature map.

First, the different parameters (temperature and FG composition) are significantly affected during irradiation. The majority of the fission gas produced leaves the pellet to the plenum (only 12% remains at 600 days) at the hottest point of the subassembly. Moreover, the fissile fuel temperature varies in a wide range during irradiation (480K between the minimum temperature and the maximum temperature for the hottest point) with a different variation mode depending on the irradiation (see Figure 23).

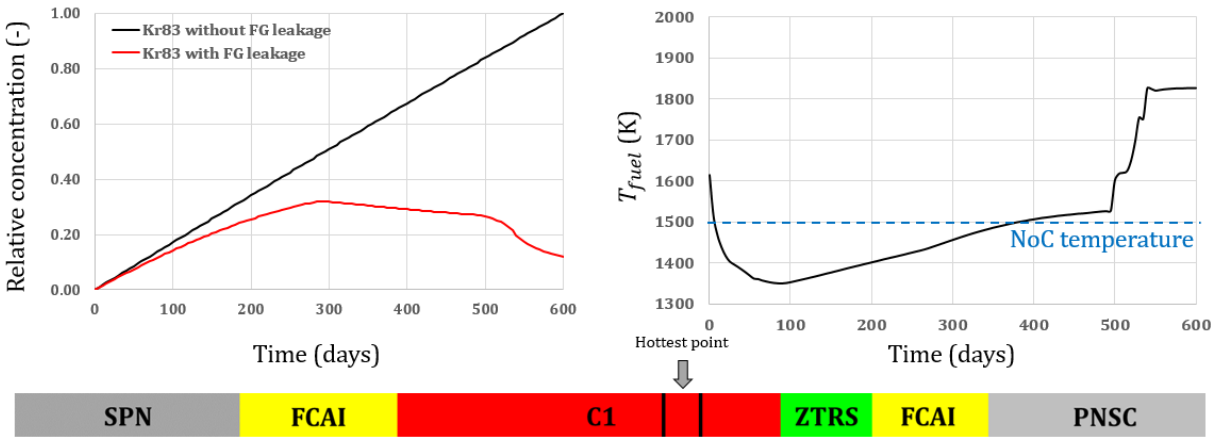

Figure 23. FG leakage (left) and fuel temperature (right) evolution through irradiation at the hottest point of the subassembly for 600 days of irradiation at 5MW (73.5 GWd/tC1[12]).

The impact of such a discrepancy between these cases is further analyzed for the reactivity loss coefficient (the impact on the isotopic composition and power distribution has been presented in PHYSOR 2024 [47]). The reactivity loss coefficient has been computed between 25 000 MWd/t_{C1} and 45 000 MWd/t_{C1} in order to be able to compare the different scenarios.

First, it can be seen in Table IV that the full coupling has a rather limited impact on the reactivity loss coefficient (between -0.30% and 0.62% for the different scenarios). However, this outcome is the result of compensations between the temperature and the fission gas release since they have a counter effect on each other.

Table IV. Reactivity decomposition for the reactivity loss coefficient with different multiphysics approaches for different power scenarios (between 25 and 45 GWd/t_{FF})

Power	NoC	T	T+FG	T	FG	T+FG
	α_{BU} (¢/MWd/t_{C1})			Impact [%]		
4 MW	-0.03716	-0.03720	-0.03705	0.11	-0.41	**-0.30**
5 MW	-0.03695	-0.03748	-0.03718	1.42	-0.79	**0.62**

[12] The burnup up unit considered (GWd/t_{FF}) represented the fission energy generated by the Fissile Fuel (FF) normalized to the initial heavy nuclei quantity of fissile fuel only. Heavy nuclei in fertile blankets are not considered, in order to maintain an understandable order of magnitude for burnup.

6 MW	-0.03662	-0.03703	-0.03666	1.13	-1.02	**0.10**

The coupling with the temperature has a positive impact (i.e. more reactivity is lost) because the fuel temperature during irradiation tends to increase as Table V illustrates, with changes in the average temperature[13]. As the Doppler Effect is negative, an additional reactivity loss at each time-step is added to the reactivity loss due to fuel depletion.

Table V. Average temperature evolution depending on the power scenario

Power	Average Temperature at 25 GWd/t_{C1} (K)	Average temperature difference between 25 and 45 GWd/t_{C1} (K)
4	1236	+20
5	1402	+27
6	1541	+25

Part of the impact of considering a coupled temperature could also be explained by the flux differences induced by the initial average temperature discrepancy with the NoC case (1236K for the coupled case in the 4 MW power scenario compared to the 1474K in the NoC case). This implies a difference on neutron spectrum that propagates to the reactivity loss (different cross-sections induce different isotopic compositions at the next step, etc.). Figure 24 shows that this discrepancy is noticeable in the ^{16}O resonance at 435 keV and between 2-3 keV but stays below ±0.1% for the highest fluxes for the 5 MW case, which tends to suggest that this term is secondary in the temperature impact. Nevertheless, in the 4 MW power scenario, the discrepancy significantly increases below 2 keV. In that case, the effect of the initial flux is not negligible and tends to compensate the contribution of the average temperature evolution.

The coupling with the fission gas release model has a negative impact on the reactivity loss coefficient as purely capturing elements (Xenon and Krypton) are removed from the fissile area. It induces a reactivity gain compared to the NoC case where all isotopes stay in the fuel. As the FG migration rate increases with temperature, the impact of such parameter increases with power. Fission product cross-sections are significantly lower than the heavy nuclei ones in the high-energy range so the impact on the neutron spectrum is low as Figure 24 shows. Hence, not considering the FG coupling will have low effect on neutron flux and heavy nuclei composition during irradiation.

[13] The average homogeneous temperature is computed only for the fissile fuel and weighted with the total reaction rate as follows :

$$T_{avg} = \frac{\sum_m T_{fuel}^m \sum_g \Sigma_t^{g,m} \phi^{g,m}}{\sum_m \sum_g \Sigma_t^{g,m} \phi^{g,m}}$$

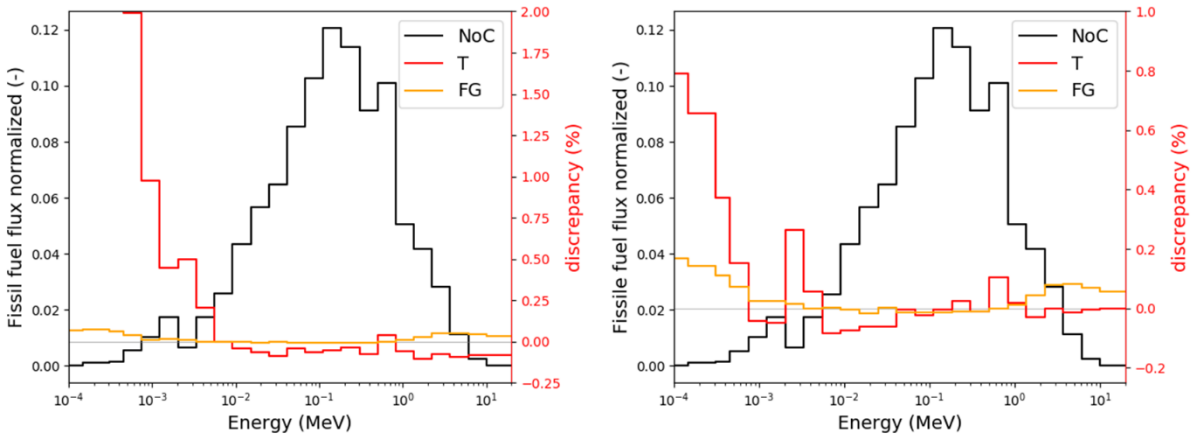

Figure 24. Impact of the multiphysics coupling on the flux in the fissile fuel for the 4 MW power scenario (left) and the 5 MW power scenario (right) at 38 000 MWd/t_{FF}

As it has been highlighted, the temperature parameter and fission gas migration has a significant impact on the reactivity loss and this impact is sensitive to the power. In a simple subassembly case in an infinite lattice, both contributions mostly canceled each other out. However, in a realistic reactor in nominal conditions, each assembly has its own power, which can also vary during irradiation with a flux redistribution that differs eventually from this simple case. It is then important to consider such coupling at core scale for reactivity loss analysis. Here, the methodology has been implemented and will be able to demonstrate such calculation on the Phenix reactor to estimate the impact of the temperature and FG migration.

2.5. Conclusion

Fuel depletion of a power reactor is a complex phenomenon that couples the Boltzmann and the Bateman equations. In addition, the temperature map induced by the power map and pellet restructuring induced by the high fluxes and temperatures will influence the Boltzmann equation. This is a complex coupled problem with equations from thermal-hydraulics, thermomechanics and fuel behavior.

To simulate Phenix reactor cycles, the APOLLO3®-FR neutronics deterministic scheme for the Boltzmann equation, the MENDEL solver for the Bateman equation and the GERMINAL V2 fuel performance code for the non-neutronics physics are coupled.

The Phenix reactor is a complex case study to model, so to establish the methodology, a numerical validation of the APOLLO3-FR® neutronics scheme has been used, by comparing the reaction rates and the control rod worth of a simplified Phenix-like model with the reference neutronics tools TRIPOL-4®. It shows a good agreement between both tools for control rod worth and local reaction rates for the media most sensitive to

reactivity loss in the core. This allows such a neutronics scheme to be considered for more complex modeling as fuel depletion for the Phenix cycles.

Additionally, a multiphysics fuel depletion study on a test case has been performed to evaluate the interest of such coupling for fuel depletion and shows a significant impact on the reactivity loss coefficient, which offers justification for consideration of this for an actual Phenix cycle.

However, in order to validate the APOLLO3®/MENDEL scheme for the reactivity loss on a Phenix cycle, it is necessary to ensure the availability and reliability of the experimental value on which the scheme is to be compared.

Chapter 3. Experimental reactivity loss

Chapter 3. Experimental reactivity loss 73
3.1. Introduction 74
3.2. Interpretation process of the reactivity loss 75
3.2.1. Control rod worth experiment 75
3.2.2. Changes in rod bank driveline during the cycle 77
3.2.3. Former interpretation limitations 79
3.2.4. Reinterpretation process 80
3.3. Reinterpretation for cycle 42-115 83
3.3.1. Recalibration of the experimental reactivity measurement 83
3.3.2. Shadow-effect coefficient 84
3.3.3. Determination of the rod bank S-curve and its derivative 86
3.3.4. Experimental reactivity loss curve 89
3.3.5. Uncertainty propagation 92
3.4. Conclusion 95

Summary – The experimental validation of the APOLLO3®/MENDEL scheme regarding reactivity loss must be based on reliable experimental values with realistic experimental uncertainties. After investigation available cycles of the Phenix reactor, it was possible to extract one in particular: cycle 42. In this chapter, it is shown that the former analyses had limitations that needed to be overcome. The process of interpreting the experimental value was therefore revisited using a number of coefficients recalculated with reference methods. Additionally, an uncertainty propagation of the input data was performed using a Monte Carlo method. This exhaustive and conservative analysis established the reactivity loss of Phenix cycle 42 at **-4.644 ± 0.156 ¢/EFPD** and paved the way for experimental validation of the APOLLO3®/MENDEL scheme.

Objectives

- Identification of a Phenix cycle that combines the various conditions required to carry out an experimental analysis
- Determination of the experimental value of the reactivity loss of a cycle with an associated uncertainty

Highlights

- Limitations of the previous analysis have been overcome for Phenix cycle 42
- Exhaustive and conservative analysis made it possible to identify the most sensitive steps in this process for a new reinterpretation, and to determine the reactivity loss of Phenix cycle 42: -4.644 $\pm$ 0.156 ¢/EFPD

3.1. Introduction

Comparison with experiment is a key stage in the validation of scientific computational tools, as it forms a link between the world of simulation and calculation and that of "reality". The experimental value must therefore be determined as precisely as possible, without any bias, to ensure that the comparison with the results of the calculation is relevant.

During an irradiation cycle, the amount of fissile material changes, which implies that the reactor gradually loses its ability to multiply neutrons, the reactivity loss. However, in operation, the reactor remains critical throughout the cycle. A sustainable criticality level can be maintained by means control rods withdrawal, which compensates for the reactivity loss in most of the conventional SFRs including Phenix. Since the reactor is constantly critical, a direct measurement of reactivity does not provide information on the reactivity loss. However, determining the changes in reactivity compensated by the control rods to maintain criticality would allow to obtain the reactivity loss curve. The process of determining the experimental value for the reactivity loss must then require knowledge of the changes in the control rod driveline during the cycle ($z(t)$) as well as the axial variation of the integral control rod worth. Combining these two information gives the direct opposite of the reactivity loss curve $\rho_{BU}(t)$ as illustrated by Figure 25.

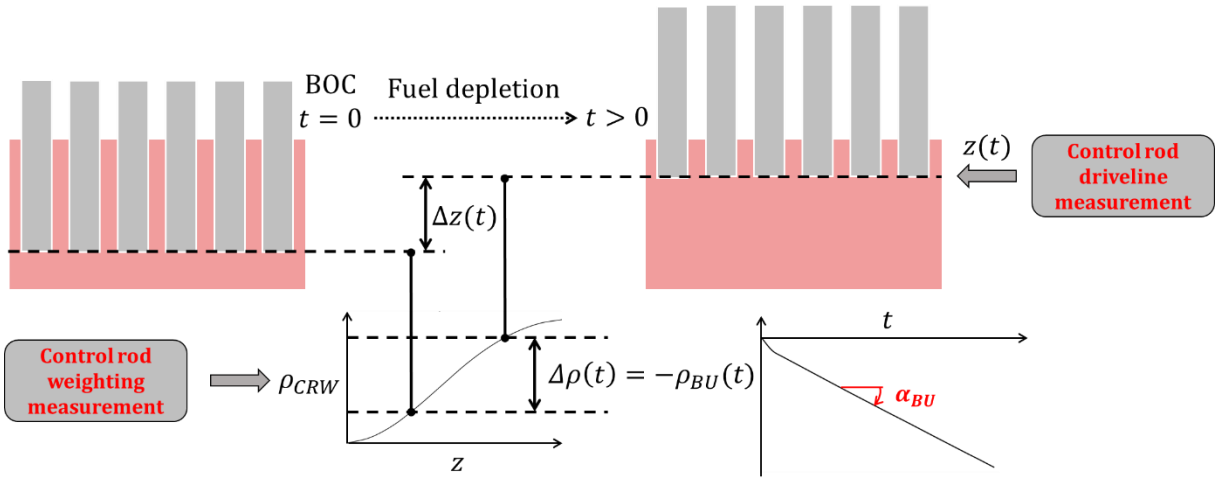

Figure 25. Simplified diagram of the experimental determination of the reactivity loss due to fuel depletion in Phenix

For the Phenix reactor, all six-control rods are used at the same time to compensate reactivity loss. Nevertheless, for some cycles, the control rods may be offset, making the analysis significantly more complex. In addition, the integral control rod worth changes at each cycle due to reloading pattern. It is then necessary to find a cycle with a control rod worth measurement at the beginning of the cycle. Also, the chosen cycle must be long enough to ease the discrimination between the reactivity loss coefficient and transient phenomena such as the neptunium effect and structural expansion (as presented in the

previous chapter). These different criteria restrict the number of cycles that can be analyzed, but these different criteria are met for the Phenix cycle 42-115 that took place in 1987.

The next section will provide a more detailed description of the method used to establish the reactivity loss coefficient. A number of limitations not suited to modern analysis requirements will be identified, which therefore require a reinterpretation of the experiment.

3.2. Interpretation process of the reactivity loss

The experimental reactivity loss curve relies on determining two curves (illustrated in Figure 25):

- Axial variation of the integral rod bank worth: $\rho_{RB}^{exp}(z)$
- Rod bank driveline evolution during the cycle: $z_{RB}(t)$

The main purpose of the experimental interpretation process is then to determine these curves experimentally. These two curves can be used as the basis for obtaining the reactivity loss curve, with the following formula:

$$\rho_{BU}(t) = \int_{u=0}^{u=t} -\frac{d\rho_{RB}^{exp}}{dz}\left(z_{RB}(u)\right) du = \rho_{RB}^{exp}(z_{RB}^{BOC}) - \rho_{RB}^{exp}(z_{RB}(t)) \qquad (3\text{-}1)$$

3.2.1. Control rod worth experiment

The main challenge in interpreting the reactivity loss lies in determining the integral rod bank worth in the rod bank extraction range of the cycle. For such a purpose, measurements were performed at the beginning of the cycle. However, a direct measurement of the rod bank is not possible as the axial range involved would imply measurements for states that are too overcritical. In the Phenix reactor, the reference method for integral control rod worth measurement in the entire axial range is the rod balancing method.

The rod balancing method consists of incrementally inserting one control rod and extracting the opposed one, starting from a critical state at zero power as illustrated in Figure 26.

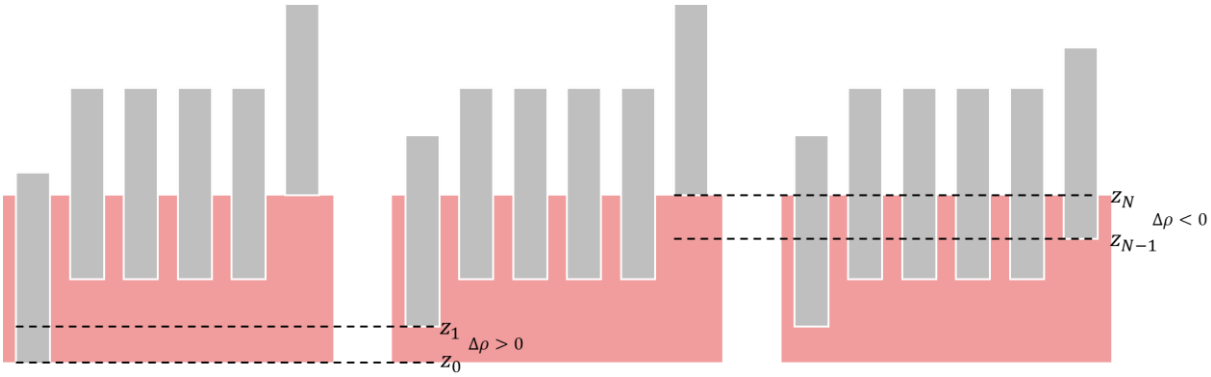

Figure 26. Control rod weighting

Each extraction and insertion induced a positive and a negative reactivity respectively. This reactivity change produces a neutron population change detected by a fission chamber located under the vessel. To convert a changing count rate in a fission chamber to a reactivity insertion, point kinetic hypothesis [15] was used. The main hypothesis of using point kinetics is assuming a constant flux shape, which is not strictly the case when control rods are moved. Nevertheless, control rod movements in rod balancing induce a small reactivity perturbation (-32 ¢ $< \rho <$ 20 ¢). Additionally, the flux perturbation is confined to a limited zone around the moving control rod, far from the fission chamber, so that these measurements are not affected by the flux perturbation induced by the rod balancing. Hence, the flux shape, from the point of view of the fission chamber, can be considered as constant.

To use the point kinetic equation inversion from a count rate to estimate the reactor's reactivity, the kinetic data of the precursor families (β_i, λ_i) are needed. For analyses carried out at the time of the measurements, the kinetic data was said to be determined under a consensus [48]. From each individual reactivity measurement $\Delta\rho_i^{exp}(z_k, z_{k-1})$ (expressed in ¢ so divided by the delayed neutron fraction β_{eff}), it was possible to reconstruct the changes in integral control rod worth:

$$\rho_i^{exp}(z_k) = \sum_{i=1}^{i=k} \Delta\rho_i^{exp}(z_i, z_{i-1}) \qquad (3\text{-}2)$$

To obtain a continuous function, experimental points were interpolated by a 5-degree polynomial fitting as shown in Figure 27 (hereinafter referred to as the S-curve).

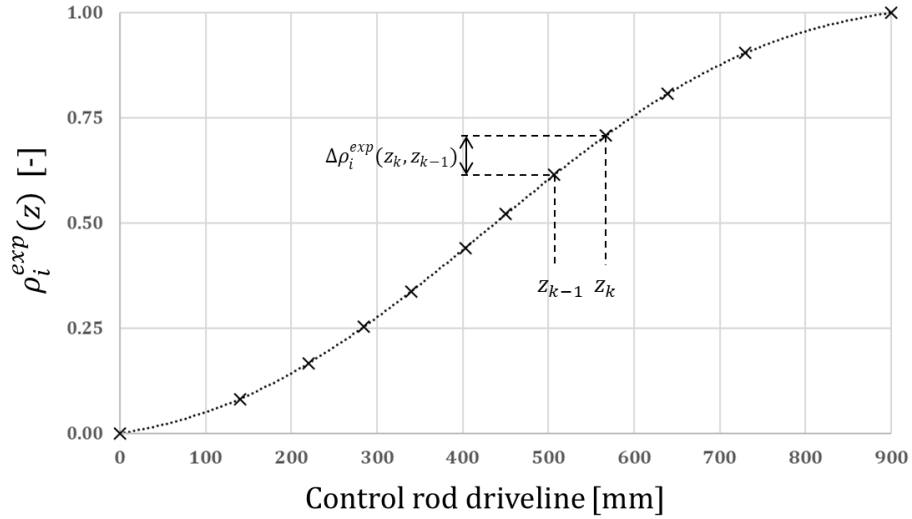

Figure 27. 42-114 experimental control rod S-curve evaluated by weight balancing

The rod balancing method allowed the S-curve to be obtained for each control rod, but the required curve for reactivity loss calculation is the rod bank one. However, during insertion/extraction of the control rods in the rod balancing method, flux conditions are significantly different from the flux condition with rod bank insertion/extraction.

With the rod bank, the neutron flux is relatively homogeneous whereas it is depleted in the area where the control rod is inserted and vice versa for the extracted one. Therefore, it implies that the rod bank S-curve is not equal to the sum of each of the individual S-curves. This is called the Shadow-effect. This effect is well known and is common to all reactor technologies where several control rods are present in a core [49], [50], [51].

The shadow-effect cannot be measured directly for the entire axial range in the Phenix reactor (for the same reason as for the rod bank measurement). It is therefore necessarily a calculated coefficient. Historically, the shadow-effect coefficient was considered axially constant and the rod bank S-curve is determined as follow:

$$\rho_{RB}^{exp}(z) = \rho_{RB}^{exp}(z_{max}) - \sum_{i=1}^{6}\left(\rho_i^{exp}(z_{max}) - \rho_i^{exp}(z)\right)\left(1 + SE \cdot \frac{\rho_i^{exp}(z_{max}) - \rho_i^{exp}(z)}{\rho_i^{exp}(z_{\max})}\right) \quad (3\text{-}3)$$

$$\rho_{RB}^{exp}(z_{max}) = (1 + SE) \cdot \sum_{i=1}^{6}\rho_i^{exp}(z_{max}) \quad (3\text{-}4)$$

With SE the shadow-effect coefficient.

3.2.2. Changes in rod bank driveline during the cycle

Changes in the rod bank driveline during the cycle can be found in the cycle reports for cycle 42. This report regularly recorded the axial position of the six control rods displayed in the control room. The difficulty with these rod bank drivelines, when the reactor is not

at cold temperature, is that they do not represent the actual position of the control rods. The increase in temperature of the structures produces thermal expansion, which induces an artificial insertion or extraction of the control rods. To account for this axial displacement, a phenomenological formula was used:

$$z^c = z^m + A \cdot \Delta T_c + B \cdot (T_{RP} - C) + D = f_{expansion}(z^m) \quad (3\text{-}5)$$

With:

- z^c : Corrected control rod driveline
- z^m : Control rod driveline recorded in the cycle report
- ΔT_c : Temperature difference between the inlet and outlet sodium[14] (recorded in the cycle report)
- T_{RP} : Average temperature of the rotating plug, where the control rods are fixed (recorded in the cycle report)
- $A, B, C \text{ and } D$: Phenomenological law parameters
- $f_{expansion}$: Name of the Phenomenological law in this manuscript

With the rod bank S-curve and the changes in the rod bank driveline, it was possible to compute the experimental reactivity loss curve with the formula (3-1). By performing this interpretation with former values and assumptions, the reactivity curve presented in Figure 28 is obtained (black curve). The reactivity loss coefficient is then computed with a least square fit of the curve between 20 days of irradiation and the end of the cycle where the curve is linear after different transient phenomena. The reactivity loss coefficient estimated with former analysis, therefore, was $\mathbf{-5.622 \pm 0.004\ ¢/EFPD.}$

With the correction at hot temperature, the rod bank is shifted downwards in a more efficient zone of the S-curve. If thermal expansion is not considered, the blue curve in Figure 28 is obtained with a reactivity loss coefficient of $\mathbf{-5.048 \pm 0.009\ ¢/EFPD}$. Thermal expansion then has a significant impact on the estimation of the reactivity loss coefficient (11%), which raises the question of the reliability of the law and its various parameters. The origin of these values is poorly known and no uncertainty values are associated with them.

More generally, most of the coefficients and laws used were intended for operational use, with sufficient margins to ensure reactor safety. However, for the purpose of the analysis, the various assumptions used must be highlighted and overcome to avoid possible biases and compensations.

[14] Each subassembly has thermocouples that measure the output temperature. The value considered was the average temperature rise of fissile subassemblies.

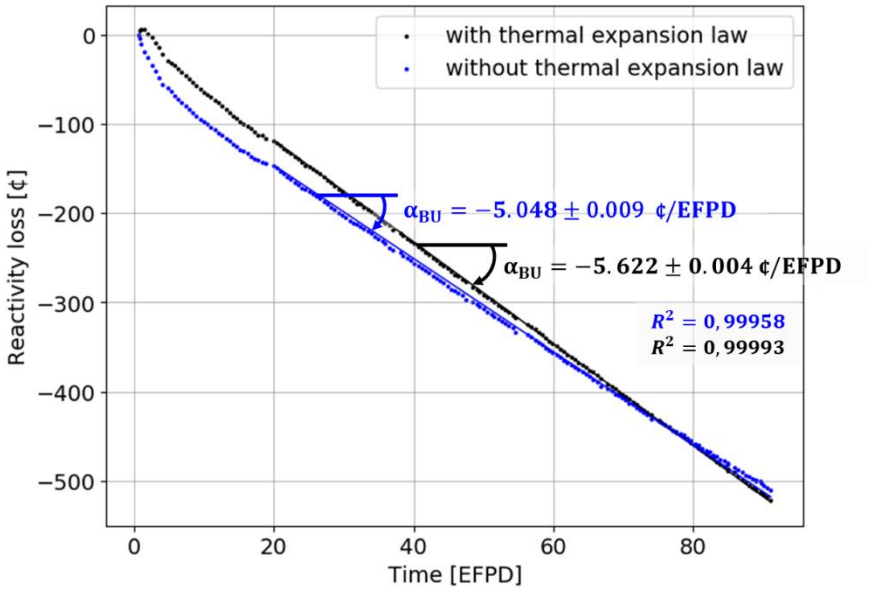

Figure 28. Reactivity loss of the cycle 42-115 with corrected rod bank driveline values in black and non-corrected values in blue.[15]

3.2.3. Former interpretation limitations

As was mentioned in the last subsection, the main limitation on changes in the rod bank driveline during the cycle is the lack of knowledge about the origin of this law and the related uncertainty.

For the control rod worth measurement, there are more steps and more assumptions involved:

- **Raw reactivity measurement**: For a given set of kinetic data, the reactivity computed from a changing counting rate depends on acquisition time, start of measurement and the specific parameters of the software used. Hence, the $\frac{\rho}{\beta}$ ratio conservation is not necessarily ensured.
- **Thermal expansion in "cold" state**: There is some thermal expansion even in the cold state (uniformly at 250°C – isothermal state) so that the axial step considered for each reactivity measurement is not exactly the instrumental position of the control rod.

[15] It has to be noted that the reactivity loss curves do not start at time $t = 0$. This is because the cycle report data were reported once the reactor was stable at high power. The early beginning of the cycle, with the different experimental tests including control rod measurement and some shuffling of subassemblies were not considered. Moreover, the time it takes for the temperatures of the structures to equilibrate involves inserting/extracting control rods, which produces apparent positive reactivity on the curve with driveline correction.

- **Interpolation between experimental points**: S-curve polynomial fitting reproduces the global control rod worth shape, but this does not fit the experimental values exactly.
- **Shadow-Effect coefficient**: The shadow-effect was considered as axially constant and identical disregarding the specificities of the weighting applied and the loading plan. This is a practical assumption for operation and safety purposes but too simplistic for a rigorous experimental validation. Each Phenix loading plan included specific experimental devices, which could interact with a control rod and lower or increase the individual weight of the interacting control rod. For cycle 42, eight in-core experimental devices were in the core including two devices with absorber materials. Those absorbing experimental devices influence the control rod worth and then the shadow-effect.
- **Conditions for using the experimental rod bank S-curve**: Rod bank worth has been experimentally evaluated for loading plan 42-114, at cold temperature. However, the rod bank has been used to compensate the reactivity loss under different conditions:
    - For loading plan 42-115: 3 subassemblies have been moved between 42-114 and 42-115, including an experimental device with absorbers.
    - At full power in hot temperature conditions
    - With fuel depletion and boron depletion for more than 80 days, which could potentially affect the control rod worth

3.2.4. Reinterpretation process

To determine an updated value for the reactivity loss coefficient with an associated experimental uncertainty, each limitation listed in the previous subsection is revisited with an exhaustive analysis.

The first step is to compute the different parameters needed for the reactivity loss coefficient:

- Shadow-effect function → $SE(z, \delta z_{RB})$
- Transmission function between loading plan 42-114 at cold temperature and loading plan 42-115 at hot temperature with depleted fuel to adapt the rod bank S-curve → $f_{TR}(z, t)$

The most accurate way to compute these coefficients is to rely on the reference neutronics calculation tool TRIPOLI-4® and an "*as realistic as possible*" Phenix model presented in Chapter 2 for the geometrical modeling and in Appendix D for calculation parameters. This allows the shadow-effect function to be calculated.

However, TRIPOLI-4® calculations are time consuming, therefore, for the transmission function f_{TR} that requires a large amount of calculations, the APOLLO3®-FR scheme presented in Chapter 2 and validated on a Phenix-like configuration for control rod worth.

Once each parameter is updated, the reinterpretation process can be done with previous experimental raw data actualized with the updated coefficients and the newly considered corrections (i.e. the thermal expansion correction during weight balancing, transmission function) as presented in Figure 29.

As this complex interpretation process relies on imperfectly known input data, the uncertainty due to input data must be quantified. To propagate the input data uncertainties to the reactivity loss coefficient, a standard Monte-Carlo method is used [52]. This involves performing the calculation process a large number of times with input data sampled according to their probability distribution (defined by their uncertainties and their types). The various quantities of interest for the calculations are stored, and statistical analysis of the stored samples provides the information needed to determine the uncertainty. In this case, the main quantities of interest are the points of the reactivity loss curve. The sampled input data concerned by the propagation on the global interpretation process are framed in red in Figure 29 and are sampled 100 000 times.

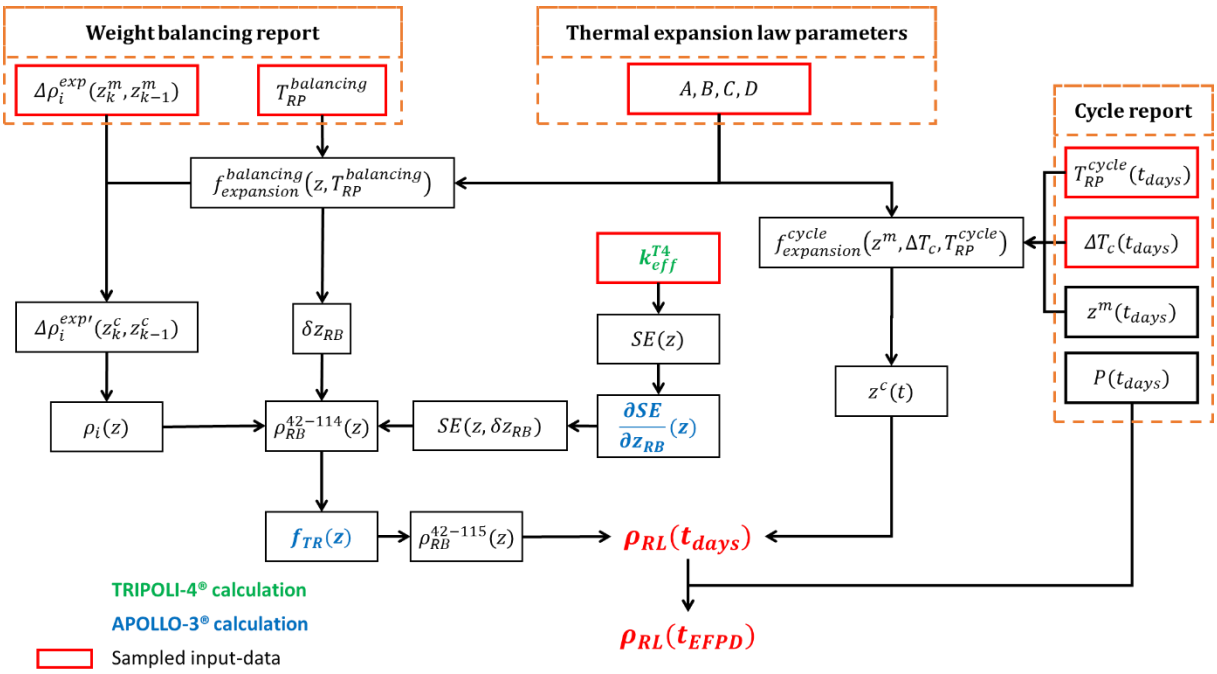

Figure 29. Global reinterpretation process of the experimental reactivity loss coefficient for cycle 42-115 of the Phenix reactor

In order to perform the statistical uncertainty propagation, the different input data uncertainties and distributions presented in Table VI, have been considered. To establish such characteristics, the following assumptions were made:

- For the thermal expansion law, no specific uncertainty values were associated with the coefficient A, B, C and D. In this work, they have been calibrated on the rod

shift in cold and hot state, available in a document where they have been calculated with an associated uncertainty. From the cold state value, the uncertainty value can be extracted to parameter D. With the hot state value, the uncertainty value can be extracted to parameters A and B (assuming that they are equal). Parameter C represents a given temperature reference, so has uncertainty of zero.

- For the temperature of the rotating plug during rod balancing ($T_{RP}^{balancing}$), which is constant during balancing, the value is not known for cycle 42-114. In other accessible Phenix rod balancing, this temperature was centered on a value within a discrepancy range of 2%. It is therefore considered that this temperature for cycle 42-114 is inside the $\pm$2% range with uniform distribution.
- For the temperature of the rotating plug during cycle (T_{RP}^{cycle}), the uncertainty is considered to be 2%, with a normal distribution. The rotating plug temperature was measured as an average of 10 different thermocouples. The uncertainty associated with each of these values is assumed to be 5%, with a normal distribution, and they are considered uncorrelated. Therefore, the uncertainty of the average is 2%, with the same distribution[16].
- For the sodium temperature rise of fissile subassemblies (ΔT_c), the value was computed by averaging the temperature rise of each of the fissile subassemblies (around 110 subassemblies). Each subassembly outlet temperature is measured with two thermocouples. As has been shown for Superphenix, the uncertainty for such measurements is large (20%) mainly because of the position of those thermocouples. However, as the average is calculated on the basis of 110 subassemblies, the propagated uncertainty (by considering that each measurement is not correlated with the others) on the ΔT_c is less than 2%, which is the value considered with a normal distribution.

Table VI. Input data considered for the uncertainty propagation of the reactivity loss coefficient

Input data	**Origin of the uncertainty**	**Probability distribution**	**Standard deviation or range**
$\Delta\rho_i^{exp}$ (Reactivity measurements)	Measurement	Normal distribution	0.50¢
k_{eff}^{T4}	Statistical uncertainty	Normal distribution	0.88¢
$T_{RP}^{balancing}$ (Rotating plug temperature during rod balancing)	Value unknown	Uniform distribution	$\pm$2%
ΔT_c (Fissile sodium temperature rise)	Measurement Position thermocouples	Normal distribution	2%

[16] $Var(\sum_n a_n X_n) = \sum_n a_n^2 \cdot Var(X_n)$ if the different random variables X_n are independent.

T_{RP}^{cycle} (Rotating plug temperature during cycle)	Measurement	Normal distribution	2%
A ($f_{expansion}$ parameter)	Calculation uncertainty quantification	Uniform distribution	±60%
B ($f_{expansion}$ parameter)	Calculation uncertainty quantification	Uniform distribution	±60%
C ($f_{expansion}$ parameter)	Formula assumption	-	0
D ($f_{expansion}$ parameter)	Calculation uncertainty quantification	Uniform distribution	±200%

3.3. Reinterpretation for cycle 42-115

The main task of the 42-115 reactivity loss reinterpretation is to compute parameters and functions needed with the TRIPOLI-4® code and the APOLLO3®-FR scheme. In this section, the process used to estimate the reactivity loss coefficient is described in detail and the different results presented.

3.3.1. Recalibration of the experimental reactivity measurement

The first step in the reinterpretation process is to correct the reactivity measurements using the kinetic data from that time. Ideally, this interpretation would require determining the reactivity with the new kinetic data and the new methods from the raw changing counting rate[17]. However, raw data are unavailable. Only interpreted reactivities during the rod balancing are available in the cycle report ($\Delta\rho_{\mathrm{i}}^{exp}$). Nevertheless, in another Phenix cycle (cycle 49), rod balancing had been carried out with two sets of kinetic data. The results provided the values measured for these two sets and the comparison between both ensured that the $\frac{\rho}{\beta}$ ratio was maintained[18]. Thus, these reactivity measurements can be considered independent of the kinetic data used, as long as they remain expressed in ¢.

Moreover, to consider the thermal expansion shift during rod balancing, the thermal expansion law should be applied, which gives:

$$\Delta\rho^{exp\prime}(z_k^c, z_{k-1}^c) = \Delta\rho^{exp}(z_k^m, z_{k-1}^m) \quad (3\text{-}6)$$

[17] By inverting the point kinetic equation presented in Appendix A.
[18] In a range of β_{eff} that covers the value of the β_{eff} computed by TRIPOLI-4® and APOLLO3® for the cycle 42

$$z_k^c = f_{expansion}\left(z_k^m, \Delta T_c = 0, T_{RP}^{balancing}\right) \quad (3\text{-}7)$$

The thermal expansion law variables $\left(\Delta T_c, T_{RP}\right)$ are available in the experiment report (with ΔT_c being equal to zero as no power is produced). For the parameters of this law (A, B, C and D), they have been calibrated on the rod shift in cold and hot state, available in a document where they have been calculated with an associated uncertainty.

3.3.2. Shadow-effect coefficient

The way to obtain the shadow-effect function with TRIPOLI-4® is to simulate the rod balancing and to build it with the following equation:

$$SE^{T4}(z_{T4}) = \frac{\rho_{RB}^{T4}(z_{T4}) - \sum_{i=1}^{6} \rho_i^{T4}(z_{T4})}{\sum_{i=1}^{6} \rho_i^{T4}(z_{T4})} \quad (3\text{-}8)$$

The different rod configurations computed by TRIPOLI-4® are not exactly the same as the experiment. This is mainly because experimental measurements of the individual S-curves were not performed for the same control rod drivelines. Hence, the shadow-effect coefficient would depend on the interpolation law used to interpolate between experimental points. To have a number of shadow-effect values independent of an interpolation law, it has been decided to compute the shadow-effect coefficient partially independently from the experiment:

- Extraction/insertion of individual control rods is always implemented with the same step of 10 cm. This then implies running of 67 multiplication factor calculations to obtain the shadow-effect function.
- The rest of the rod bank is positioned in the axial position given by the experiment report (i.e. the axial position recorded in the balancing report without the thermal expansion correction)

As one of the reinterpretation objectives is to take account of the control rod driveline shift due to thermal expansion during rod balancing, the thermal expansion law should be applied also to the rest of the rod bank. This shift is then named δz_{RB} and is governed by the thermal expansion law (illustrated in Figure 30).

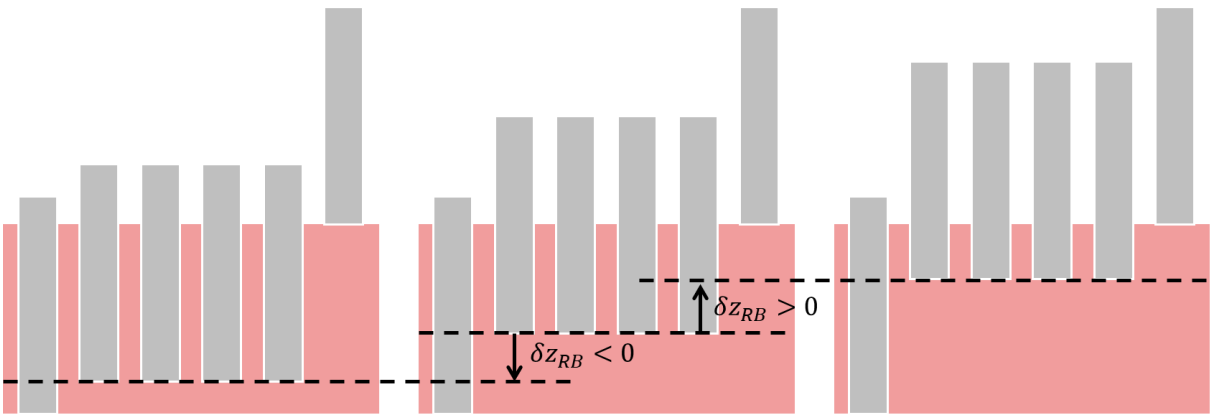

Figure 30. Illustration of the rod bank shift during rod balancing

To be able to compute the shadow-effect function for each rod bank displacement, the rod bank shift parameter is added to the parameters of the shadow-effect function. As the shifts involved are small compared to the extraction range (between -10 and 20 mm), it is considered that the development in Taylor series with a first-order assumption is sufficient to take account of the impact on the rod bank shift:

$$SE^{T4}(z, \delta z_{RB}) = SE^{T4}(z) + \frac{\partial SE}{\partial \delta z_{RB}}(z) \cdot \delta z_{RB} \quad (3\text{-}9)$$

To obtain the derivative of such a function, two additional calculations of the shadow-effect function have been made. As TRIPOLI-4® calculations are too costly, it has been preferred to consider the APOLLO3®-FR scheme to perform these calculations.

By computing the shadow-effect coefficient for TRIPOLI-4® and for APOLLO3®, the graph presented in Figure 31 is obtained (for a rod bank shift equal to zero).

Firstly, it may be noted that the computed shadow-effect is significantly different from the one used during operation and that it is not axially constant. Secondly, the APOLLO3® calculations are in good agreement (<2σ statistical uncertainty[19]) with the TRIPOLI-4® reference ones. This good accuracy gives confidence in the APOLLO3®-FR neutronics scheme for computation of the derivative towards the rod bank shift ($\frac{\partial SE^{AP3}}{\partial \delta z_{RB}}$) and the transmission function between the loading plan 42-114 and 42-115 (f_{TR}^{AP3}). Lastly, the form of the equation makes the SE coefficient highly sensitive to an axial position lower than 20 cm: the denominator and numerator of the SE coefficient formula tend to zero with the axial position, so a small statistical variation in that range has a large impact on the value Values for an axial position lower than 20 cm are therefore not reliable. Nevertheless, the shadow-effect is used only for the upper part of the core where this high sensitivity vanishes.

[19] The statistical uncertainty propagation of the k_{eff} values from TRIPOLI-4® has been carried through to the shadow effect by scoring the shadow effect function at each sampling. This method provided a distribution of points for the shadow effect, with the displayed uncertainty representing the standard deviation.

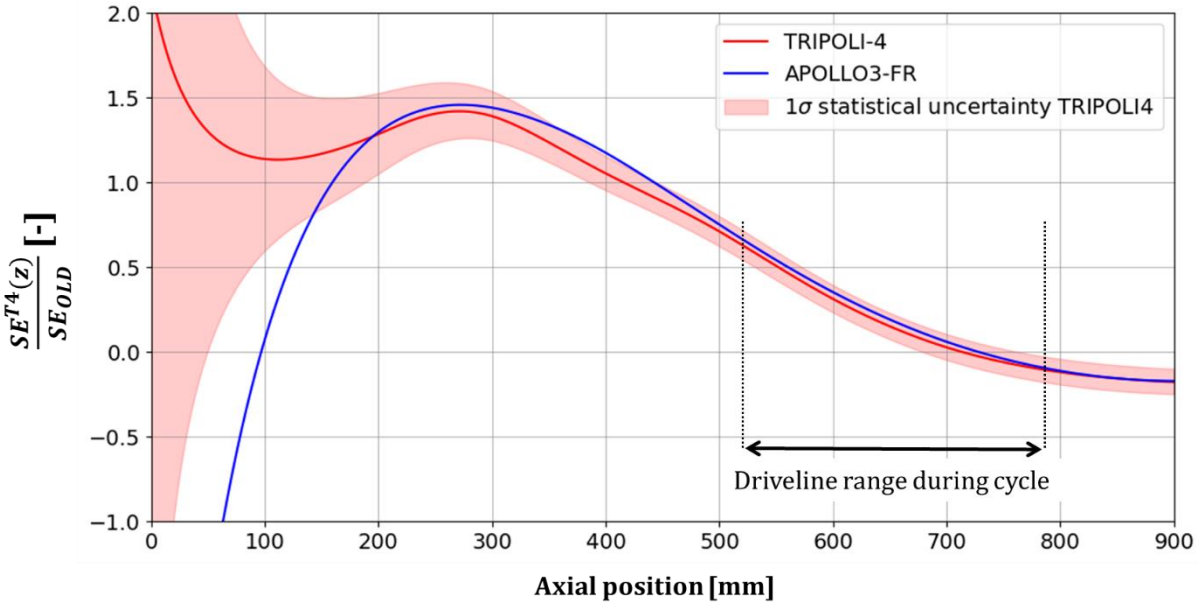

Figure 31. Shadow-effect coefficient computed by TRIPOLI-4® and APOLLO3®-FR (divided by the former constant value of the shadow-effect)

3.3.3. Determination of the rod bank S-curve and its derivative

With the corrected values of the reactivity measurements and the shadow-effect function, it is possible to determine the rod bank S-curve. However, the axial positions of the various experimental and calculated points are not necessarily aligned, as illustrated in Figure 32 for the individual S-curves.

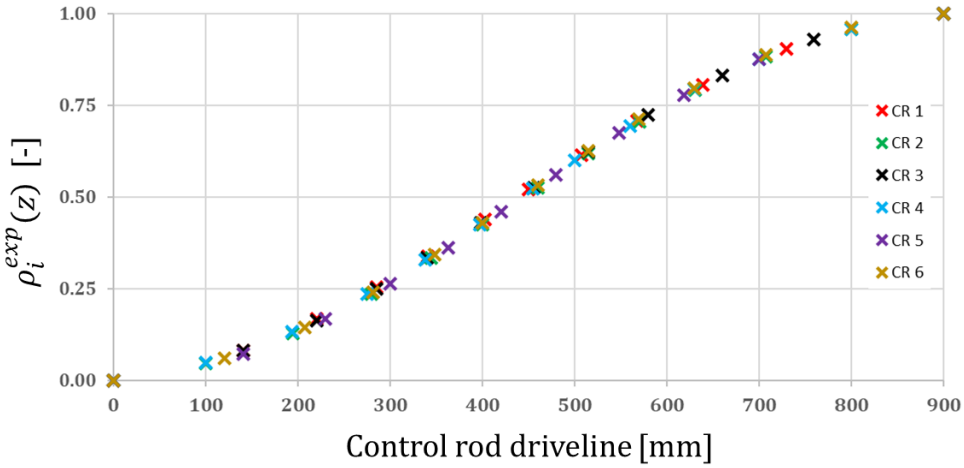

Figure 32. Experimental S-curves of each control rod of the rod balancing at the beginning of cycle 42

Hence, an interpolation model has to be used. Historically, a 5-degree polynomial is used to interpolate an S-curve. This ensures that there is a continuous function; nevertheless, it does not reproduce the experimental data samples exactly. The linear approximation

allows for reproduction of experimental points, but implies a constant piecewise function of the differential control rod worth (see Figure 33), which has a significant impact on the reactivity loss coefficient. Cubic spline [53], [54] allows for fittings the data and ensures that there is a continuous differential control rod worth curve with a more representative trend than the linear fit.

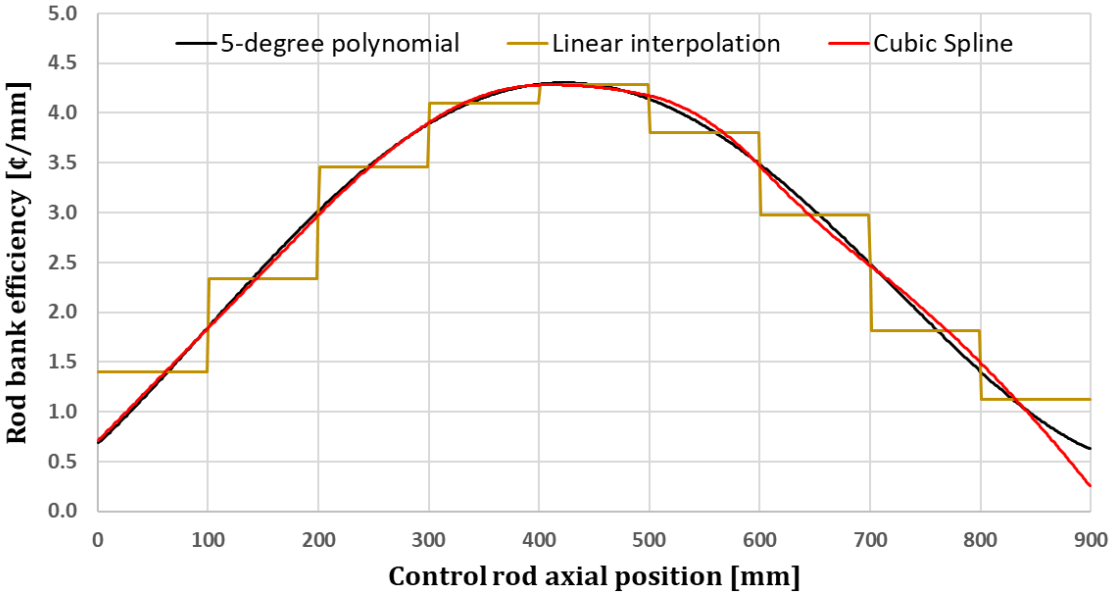

Figure 33. Impact of the interpolation model on the differential rod bank worth (TRIPOLI-4® calculation)

With the following formula:

$$\rho_{RB}^{exp}(z) = \left(1 + SE^{T4}(z, \delta z_{RB})\right) \cdot \sum_{i=1}^{6} \rho_i^{exp}(z) \qquad (3\text{-}10)$$

The experimental S-curve of the rod bank and the differential rod bank worth can be obtained (see Figure 34).

First, discrepancies between the TRIPOLI-4® calculations and the experimental values stay within the 3σ experimental uncertainty. For the latter, it is almost exclusively influenced by the statistical uncertainty of the TRIPOLI-4® calculations for the shadow-effect coefficient in the lower part of the core. In the upper part, the primary contribution comes from the uncertainty in the thermal expansion correction law. The uncertainty due to nuclear data can explain this discrepancy (green vertical bars in Figure 34 - between 3.5% and 3.9% on the differential rod bank worth); however, a modeling bias, particularly in the rod balancing calculation, which is not exactly the same as the experimental rod balancing, cannot be excluded.

To improve the validation of this aspect, further work on the thermal expansion law could be undertaken with modern tools, providing a better understanding of this law and its uncertainties. Consequently, the rod balancing could be performed under the same

conditions as the experiments and with more converged calculations for TRIPOLI-4®, reducing the statistical contribution via the shadow effect. Given that the discrepancy observed in the differential rod-bank worth between TRIPOLI-4® and the experimental results are similar for the rod bank and the individual control rod worth (Figure 35), it can be considered that this potential bias does not transfer through the shadow effect. Therefore, within the scope of this work, the experimental S-curve, obtained with the shadow effect calculated using TRIPOLI-4®, can be used with good confidence for the computation of the reactivity loss curve.

Second, the APOLLO3® curve is in good agreement with the TRIPOLI-4® calculation, especially in the upper part of the core, whereby the control rods are moving during the cycle. This is consistent with the comparison conducted on the shadow-effect coefficient and confirms the reliability of the quantities calculated by APOLLO3® in this experimental reinterpretation.

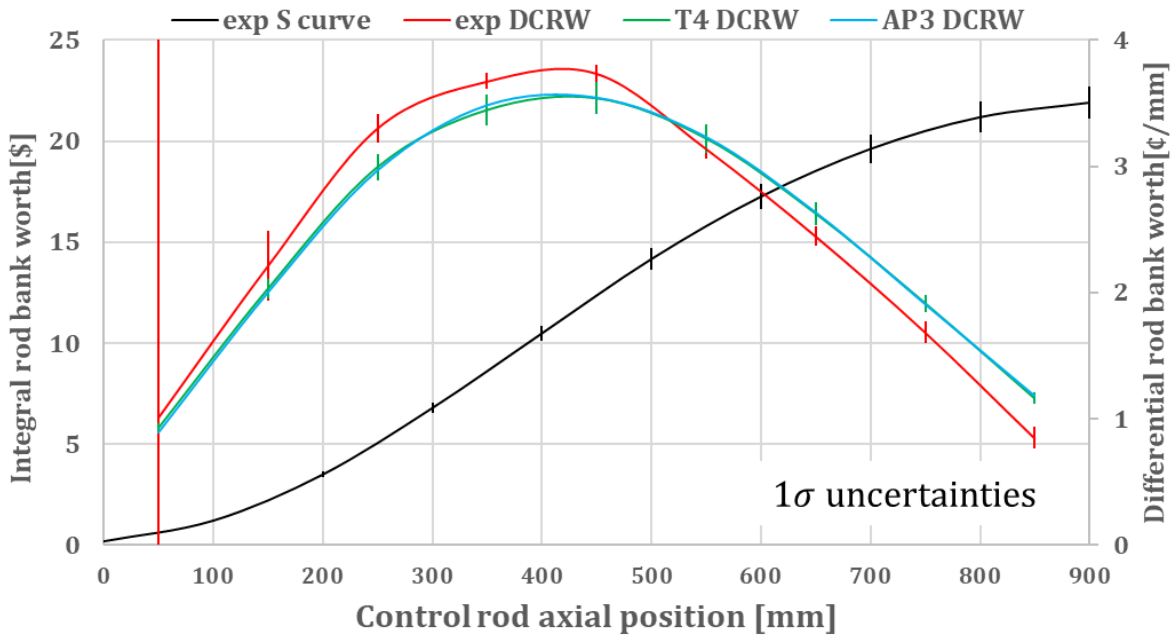

Figure 34. Experimental rod bank S curve with its differential worth compared to the TRIPOLI-4® and APOLLO3® calculations

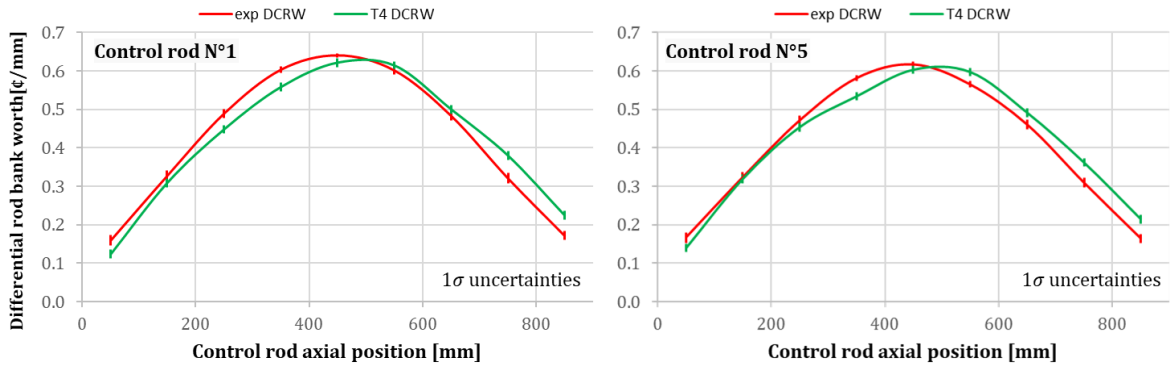

Figure 35. Experimental differential control rod worth curve compared to the TRIPOLI-4® calculation

3.3.4. Experimental reactivity loss curve

The reactivity loss can now be determined by updating the differential rod bank worth for cycle 42-115. However, the differential rod bank worth has been established experimentally only for cycle 42-114 and in cold state. Whereas this curve is used in hot state, with fuel depletion and a different loading plan as presented in the last section. To take those changes into consideration, a transmission function is multiplied with the differential control rod worth as follows:

$$\varepsilon_{RB}^{exp}(z) = \frac{d\rho_{RB}}{dz}(z) \tag{3-11}$$

$$\varepsilon_{RB}^{exp\prime}(z,t) = \varepsilon_{RB}^{exp}(z) \cdot f_{TR}(z,t) \tag{3-12}$$

$$f_{TR}^{AP3}(z,t) = \frac{\varepsilon_{115,Hot,BOC}^{AP3}(z)}{\varepsilon_{114,Cold,BOC}^{AP3}(z)} \cdot \left(\frac{\frac{\varepsilon_{115,Hot,EOC}^{AP3}(z)}{\varepsilon_{115,Hot,BOC}^{AP3}(z)} - 1}{T_{cycle42-115}} t + 1 \right) \tag{3-13}$$

Where:

- ε_{RB}^{exp} : Reinterpreted value of the differential rod bank worth (red curve in Figure 34)
- $\varepsilon_{c}^{exp\prime}$: Reinterpreted value of the differential rod bank worth corrected by the transmission function
- $T_{cycle42-115}$: Irradiation time of cycle 42-115

Each function has been computed with the APOLLO3®-FR scheme by computing the S-curve (only for the range concerned during irradiation) and their ratios are shown in Figure 36 :

- 42-114 at cold temperature at the beginning of the cycle ($\varepsilon_{114,Cold,BOC}^{AP3}(z)$)
- 42-115 at hot temperature at the beginning of the cycle ($\varepsilon_{115,Hot,BOC}^{AP3}(z)$)

- 42-115 at hot temperature at the end of the cycle ($\varepsilon^{AP3}_{115,Hot,EOC}(z)$)[20]

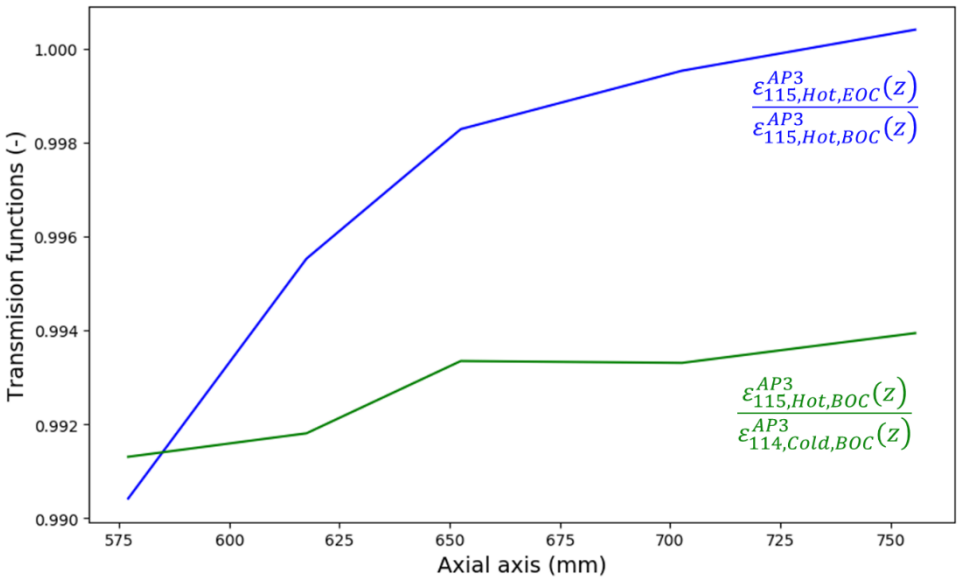

Figure 36. Two main components of the transmission function evolution through axial axis

These transmission functions have only been calculated with APOLLO3®-FR and not with TRIPOLI-4®. As Figure 34 exhibits, APOLLO3®-FR is in good agreement with TRIPOLI-4® and is able to reproduce the S-curve of this Phenix model with a negligible numerical bias. It is therefore assumed that the numerical bias due to the deterministic scheme for the transmission function is negligible.

By applying the new differential rod bank worth formula in the reactivity loss equation, the reactivity loss curve is obtained:

$$\rho_{BU}(t) = \int_{u=0}^{u=t} -\varepsilon^{exp}_{RB}\left(z^{c}_{RB}(u)\right) \cdot f^{AP3}_{TR}(z^{c}_{RB}(u), u)du \quad (3\text{-}14)$$

$$z^{c}_{RB}(t) = f_{expansion}\left(z^{m}_{RB}(t), \Delta T_c(t), T^{cycle}_{RP}(t)\right) \quad (3\text{-}15)$$

Which gives the following reactivity loss curve (Figure 37) when using the reinterpreted data:

[20] It has to be noted that this curve has been computed with the different depletion calculations on the cycle 42-115 performed and further explained in the next chapter. This differential control rod worth takes into account the boron depletion inside the control rods and the fuel depletion of the fissile material during the cycle.

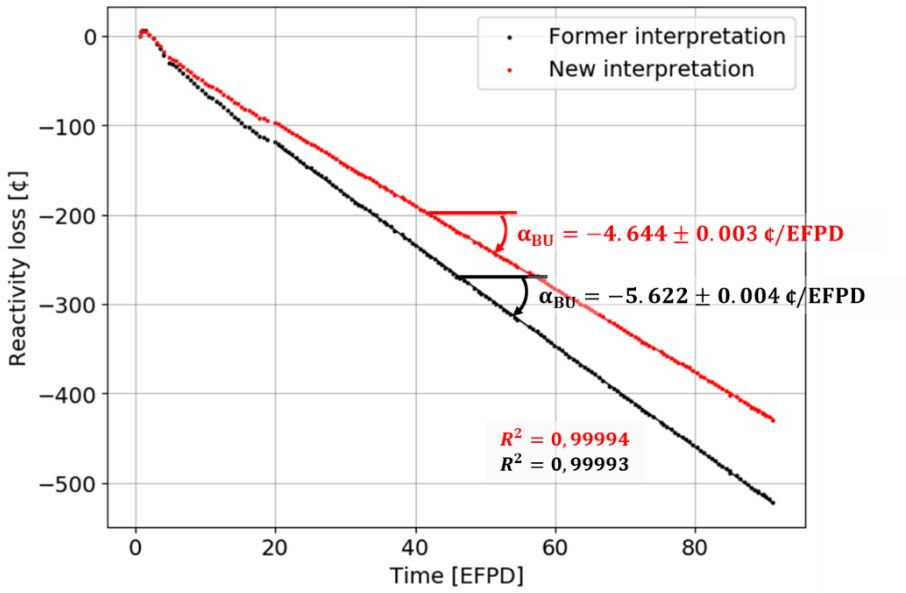

Figure 37. Reinterpretation of the reactivity loss of the cycle 42-115

By isolating each step of the reinterpretation process, the individual associated impact is quantified and described in Table VII. As can be seen, the update process has a significant impact on the reactivity loss coefficient (-17.39%).

This difference is mainly due to the new shadow-effect coefficients (-21.55%) that were significantly different from former considerations as shown in Subsection 3.3.2.

The thermal expansion correction law has an opposed strong impact with 11.37% that was considered in the former analysis for thermal expansion during irradiation and 2.37% during rod balancing in cold state that is newly considered (13.70% in total).

For the remaining effect studied, their impact is much smaller with -0.67% for the transmission function introduction and +0.47% for the interpolation method.

Table VII. Impact of the different input parameter on the reactivity loss coefficient

Input parameter	α_{BU}^{n} **[¢/EFPD]**	$\frac{\lvert\alpha_{BU}^{n}\rvert-\lvert\alpha_{BU}^{n-1}\rvert}{\lvert\alpha_{BU}^{0}\rvert}$ **[%]**
Raw interpretation without any correction	-5.048	**-**
Thermal expansion of the CR driveline during cycle (former interpretation)	-5.622	**11.37**
Polynomial 5 → Cubic spline (for interpolation)	-5.646	0.47
Actualization of the shadow effect coefficient	-4.558	**-21.55**

Thermal expansion of the CR driveline during rod balancing	-4.678	2.37
Transmission function	**-4.644**	-0.67

3.3.5. Uncertainty propagation

By applying the Monte-Carlo method presented in Figure 29 for 100,000 samples, a distribution of output values is obtained for each point of the reactivity loss, as illustrated in Figure 38. As the input data distributions are a mix of Gaussian and uniform distributions, the output data distributions have a specific distribution in between. To characterize the difference with the normal distribution, the skewness and the excess of kurtosis are used [55]. Overall, skewness is low for the points on the reactivity loss curve for the time range of interest (20 EFPD to EoC). This indicates that the distribution remains symmetrical around the mean value.

The excess of kurtosis represents the “flatness“ of the distribution compared to a normal distribution. Its value is negative if the distribution is flatter than the normal distribution and tends to a normal distribution (excess of kurtosis of -1.2) and vice versa. The trend of reactivity loss distributions exhibits negative excess of kurtosis due to the uniform uncertainty distributions of certain parameters. This excess is particularly high at the beginning of the cycle, with the temperature equilibrium of structures causing significant perturbations in the control rod driveline, especially where the differential rod bank worth is high. With the normal component from the shadow effect, the distribution becomes less uniform, but the excess of kurtosis remains between -0.2 and -0.6 (see Figure 39).

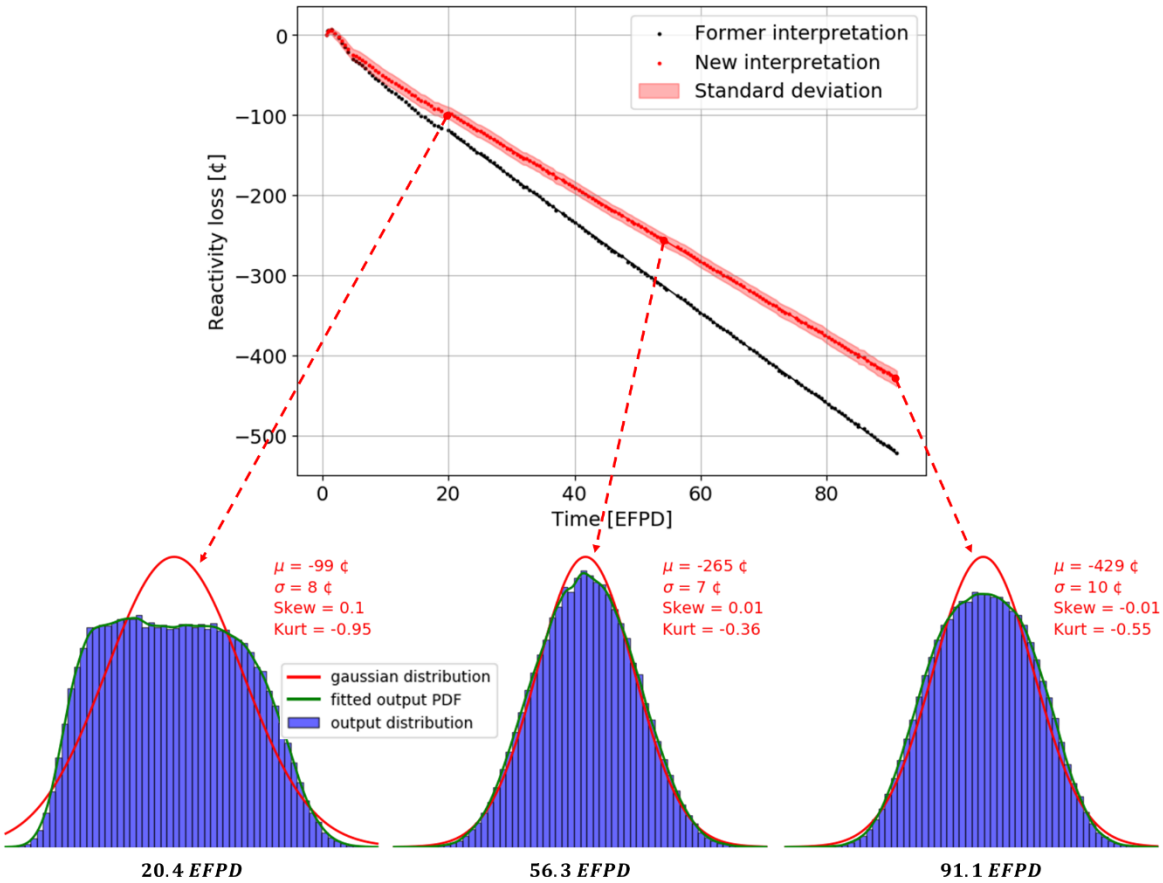

Figure 38. Reinterpretation of the reactivity loss of cycle 42-115 with the propagated uncertainties. (μ Being the mean, σ the standard deviation, Skew the skewness and Kurt the excess of kurtosis)

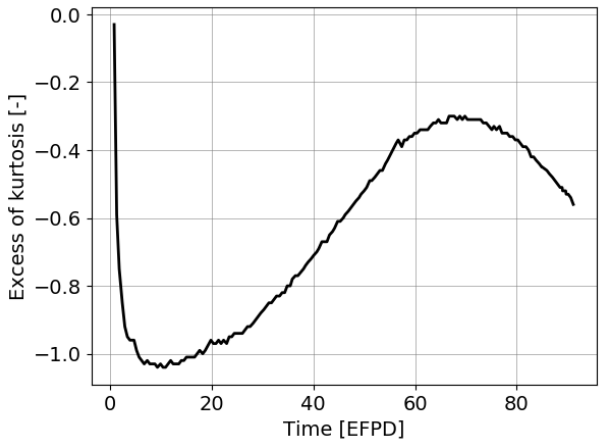

Figure 39. Evolution of the excess of kurtosis of the sampled output reactivity loss

To compute α_{BU}, the *curve_fit* [56] function from the python *scipy.optimize* package is used. This function uses non-linear least squares to fit a given function (in this case a

linear function) with input data. With this tool, the uncertainty obtained on the reactivity loss coefficient when considering the uncertainties of experimental data is **0.74%** at $\mathbf{1\sigma}$.

The first and the largest contributor to uncertainty is the set of parameters in the thermal expansion formula (**0.68%**). This impact is explained by the fact that it is an input to every step for determining the reactivity loss curve and mainly on the rod bank driveline during cycle.

The second component of the uncertainty comes from the shadow-effect computed with TRIPOLI-4® (**0.23%**). This last uncertainty is due to the statistical uncertainty associated with the multiplication factors computed by TRIPOLI-4® to determine this coefficient. For this parameter, the uncertainty due to nuclear data has not been propagated from the multiplication factors to $SE(z)$. It is assumed that this uncertainty is negligible due to the similarity between the different S-curves. Thus, a perturbation would influence the S-curves in the same way, which would not change their ratio (the ratio being the shadow-effect).

The initial experimental uncertainty due to the reactivity measurement has a smaller impact (**0.093%**), as well as other variables of the thermal expansion law that almost vanish quadratically with the impact of the main contributors. Table VIII summarizes the different contributions of each input data.

To improve the experimental uncertainty, future work could be envisaged to reduce the statistical uncertainty of the shadow-effect. This would require a certain amount of computational effort, but is currently the most affordable way, as it does not require any additional research work. Also, further work with modern system tools could potentially provide a better understanding and estimation of the thermal expansion law in order to reduce the main impact of this contributor.

Table VIII. Uncertainty propagation (1σ) of different sets of input data for the reactivity loss coefficient of the Phenix cycle 42-115

Input data	$\sigma_{\alpha_{BU}}$ [%]
A, B, C, D	0.677
$SE(z)$	0.236
T_{RP}^{cycle}	0.119
$\Delta\rho_i^{exp}$	0.092
ΔT_c	0.024
$T_{RP}^{balancing}$	0.004

Total	**0.747**

This standard deviation value for the reactivity loss coefficient, commonly equated with uncertainty, does not, however, provide information about its distribution. The distribution, like the sampled reactivity loss, should lie between a normal and uniform distribution. For uniform distributions, the standard deviation is not a statistical measure that accurately characterizes the associated uncertainty. Therefore, the concept of extended uncertainty and coverage factors could be used [57]. This involves determining the standard deviation of an equivalent normal distribution (i.e equivalent in terms of level of confidence, which is 68.27% for 1σ). For instance, with an initial uniform distribution, the coverage factor to obtain an equivalent Gaussian distribution in terms of extended uncertainty for a level of confidence of 68.27% is 1.2. In this manuscript, the different coverage factors have not been computed but could be in further work following different methods [58]. Meanwhile, a larger conservative uncertainty of **1.5%** has been considered.

During the interpretation process for the quantification of the reactivity loss coefficient and its uncertainty, the power of the reactor is not a direct parameter to be considered. However, its value is necessary for the normalization of this coefficient and for defining the time unit: Equivalent Full Power Day. The change in power is available in the cycle report. The power was a value calculated by the core management code based on the temperature rise of the sodium in fissile subassemblies, the flow rate and the pump outlet temperature. Uncertainties associated with these values are poorly known. An uncertainty of **3%** based on the various sources of information that have been collected is considered and thus represents the main uncertainty of the reactivity loss coefficient. Although core power has a first order impact on reactivity loss, previous interpretations did not take into account this kind of uncertainties. In the present study, it has been chosen to include such uncertain parameter in the total uncertainty. Discussion will be made on the rightness of such assumption in the section devoted to assimilation process.

Finally, the exhaustive reinterpretation of the reactivity loss of Phenix cycle 42 and the uncertainty propagation associated with the different input data has allowed for determination of an experimental value of **-4.644 ± 0.156 ¢/EFPD**.

3.4. Conclusion

The analysis of the 42-115 Phenix cycle reactivity loss relies on the experimental determination of the control rod worth performed in cycle 42-114. To determine the control rod worth experimentally, a rod balancing experiment was carried out. The rod bank worth was then obtained through the so-called shadow-effect coefficient. With the reconstructed rod bank worth, the reactivity loss curve was assessed using changes in the rod bank driveline during the cycle, which had to be corrected with a phenomenological

law to take account of the structural thermal expansion of the core. However, this method suffers from certain limitations that significantly bias the experimental measurements:

- Shadow-effect coefficient was considered axially constant and the same for all irradiation cycles.
- Structural thermal expansion wasn't considered for the rod balancing

To overcome these limitations, the different parameters have been computed with the reference neutronics computational tool TRIPOLI-4® with a Phenix model as close as possible to the experiment in terms of isotopic content and geometries. Different parameters are revisited and some irrelevant assumptions that were considered in the former interpretation are lifted (as thermal expansion during rod balancing). With this new approach, the reactivity loss curve changes from **-5.622 ¢/EFPD** to **-4.644 ¢/EFPD.**

For this analysis, the uncertainty due to the different input data or unknown data has been propagated to the reactivity loss coefficient with a Monte-Carlo simulation to determine a conservative value of the experimental uncertainty associated with this reinterpretation. This gives an experimental uncertainty on the reactivity loss coefficient of **3.35%** composed (quadratically) of **3%** due to the power normalization and **1.5%** due to the input data of the reinterpretation process.

This reinterpretation has made it possible to increase the confidence attributed to the experimental value of the reactivity loss coefficient of Phenix cycle 42 and to use it for validation purposes for calculation schemes such as the APOLLO3®/MENDEL scheme.

Chapter 4. APOLLO3®/MENDEL calculation

Chapter 4. APOLLO3®/MENDEL calculation 97
4.1. Introduction 98
4.2. Calculated 42th Phenix cycle reactivity loss 98
4.2.1. Temporal mesh 99
4.2.2. In-core experiment modeling 100
4.2.3. Control rod extraction 101
4.2.4. Control rod depletion 102
4.2.5. Multiphysics coupling 104
4.2.6. Best-Estimate result 107
4.2.7. Experimental validation of the APOLLO3®/MENDEL scheme 109
4.3. APOLLO3®/MENDEL Bias decomposition and uncertainty quantification 110
4.3.1. MENDEL numerical bias 110
4.3.2. Bias induced by geometrical assumptions 110
4.3.3. Bias induced by PROJERIX initialization 112
4.3.4. Neutronics scheme deterministic bias 112
4.3.5. Uncertainty due to power normalization 113
4.3.6. Uncertainties coming from nuclear data 113
4.3.7. Uncertainty due to delayed neutron fraction 114
4.3.8. Biases and uncertainties induced by Multiphysics coupling 114
4.4. Conclusion 115

Summary - In this chapter, the advanced modeling capabilities enabled by the APOLLO3®/MENDEL scheme are tested, incorporating fuel performance coupling at the core scale with GERMINAL V2. This approach made it possible to determine the Best-Estimate value of the complete scheme, using the experimental value calculated in the previous chapter. The results show that the calculation is very closely aligned with the experiment (C/E = 1.0013). A breakdown of the remaining modeling biases has been undertaken, but specific sensitivities are needed in order to obtain an accurate quantification and consolidation of the results.

Objectives

- Incremental improvement in modeling fidelity to break down the different contributions to reactivity loss made by individual modeling assumptions
- Estimation of the remaining biases of the modeling

Highlights

- Best-Estimate value with APOLLO3®/MENDEL/GERMINAL V2 for Phenix cycle 42 :- $\mathbf{4.650\ ¢/EFPD}\ |\frac{C}{E} - \mathbf{1} = +\mathbf{0.13}\%$
- In-core experiment modeling, control rod extraction, control rod depletion, evolving temperature map and fission gas migration all have a significant impact on reactivity loss

- Sensitivities specific to reactivity loss are needed in order to estimate numerical bias and nuclear data uncertainty

4.1. Introduction

With the new interpreted experimental value and its uncertainty, it is now possible to perform an experimental validation of the APOLLO3®/MENDEL scheme on the 42nd Phenix cycle. The main improvement with such a scheme is the possibility of performing fuel depletion calculation with multiphysics considerations (fuel performance) as was shown in the second chapter. Before considering contributions from other physics, it is preferable to ensure that all assumptions associated with single-physics problem (neutronics alone, in this case) are well managed and/or no longer required. The first step with the APOLLO3®-FR scheme for fresh fuel has been discussed in the second chapter. However, fuel depletion in operation condition implies some specific computational features for the core calculation, which will be addressed incrementally in the first section. The question of the remaining bias and uncertainty due to the different input data of the calculation will then be discussed.

4.2. Calculated 42th Phenix cycle reactivity loss

To move towards high-fidelity modeling and using multiphysics coupling as presented in the second chapter, the impact of the following item/parameter has to be studied:

- Temporal mesh
- In core experiments (DCC) modeling (see Figure 40)
- Control rod movement
- Control rod depletion
- Temperature map over time
- Fission gas migration coefficient map

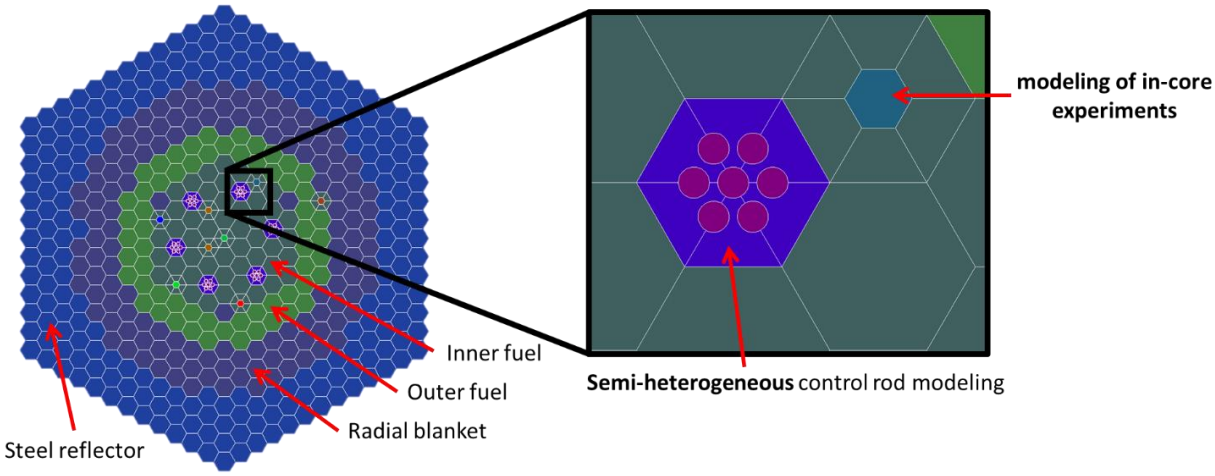

Figure 40. APOLLO3® modeling of the 42nd Phenix cycle

By incrementally adding the modeling approaches listed above, it is possible to evaluate their impact on the reactivity loss and on the isotopic composition to assess possible compensations.

4.2.1. Temporal mesh

In fuel depletion calculation with the quasi-static hypothesis, the temporal mesh must be chosen in order to respect the underlying constant flux assumption during a time-step. To study the influence of the time-step for the 42nd Phenix cycle, several fuel depletion calculations have been made for multiple time-steps: 90 days (direct BoC→EoC depletion) and different combinations of steps of 20 days – 10 days – 5 days. Results show that the influence of the time-step is apparently negligible for the reactivity loss coefficient (0.4 ¢ discrepancy for total reactivity loss, between the BoC and EoC rod bank driveline, between the four different cases).

However, looking at the ^{239}Pu consumption discrepancy between each case (see Figure 41), it can be seen that for the 1-time step calculation, apparently good results on reactivity loss can be explained by a compensation between the internal and the external regions of the core. This compensation is significantly lower for the other cases with intermediate time-step. It makes it possible to show that a 20-day time-step is sufficient for a fuel depletion problem in an SFR like Phenix (for isotopic composition and reactivity loss).

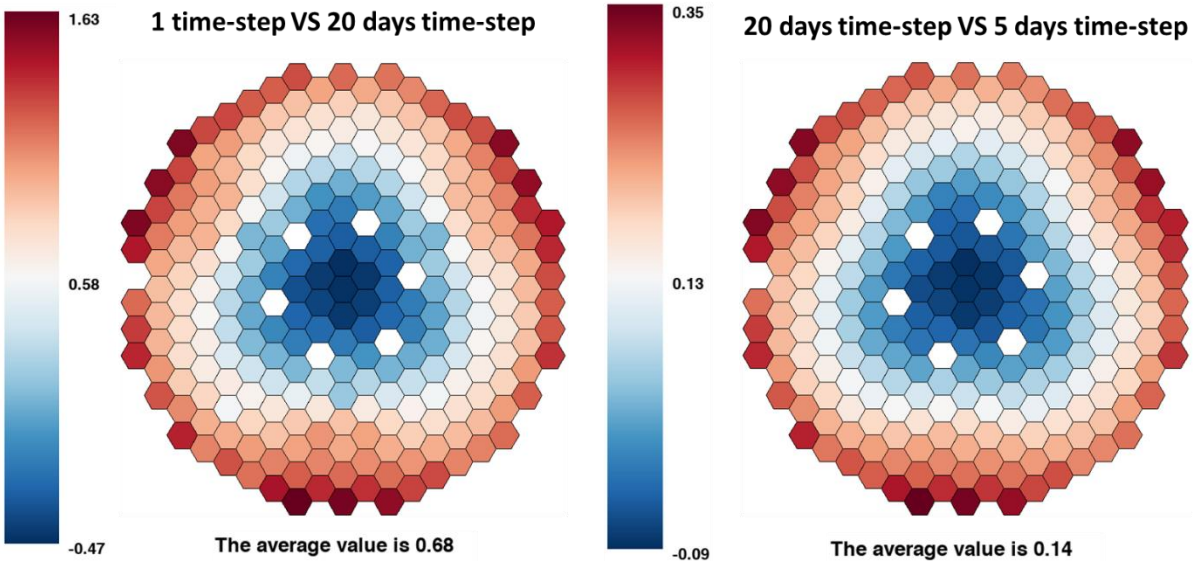

Figure 41. Discrepancy map (in percent) of the ^{239}Pu consumption at mid-height of the core for between 1 time-step against 20-day time-step depletion calculation (left) and between 20-day against 5-day time-step (right)

The discrepancy on ^{239}Pu consumption between two cases i and j is expressed as follows:

$$D_{ij,map}^{^{239}Pu} = \frac{N_{i,EOC}^{^{239}Pu}(\vec{r}) - N_{i,BOC}^{^{239}Pu}(\vec{r})}{N_{j,EOC}^{^{239}Pu}(\vec{r}) - N_{j,BOC}^{^{239}Pu}(\vec{r})} - 1 = \frac{\Delta N_i^{^{239}Pu}(\vec{r})}{\Delta N_j^{^{239}Pu}(\vec{r})} - 1 \quad (4\text{-}1)$$

The ^{239}Pu consumption discrepancy is preferred to the final isotopic composition discrepancy to avoid scaling effect due to inhomogeneous isotopic composition between the different subassemblies, especially between fissile and fertile.

4.2.2. In-core experiment modeling

For the 42nd Phenix cycle, eight experimental devices were present inside the core in DCC-like subassemblies. Those experiments were of three different types: fuel, absorbers and structural materials. Failure to consider those in-core experiments (as in the PROJERIX case) may impact the fuel material balance that can contribute to the reactivity loss. Also, failure to consider these absorbing materials can significantly influence its surroundings. By adding these in-core experimental devices, the reactivity loss coefficient is slightly impacted by -0.04%.

The discrepancy map of ^{239}Pu consumption between the case with and without in-core experiments (Figure 42) shows a large impact of in-core experiments on its surroundings with opposing impact for absorbing and fuel experiments. This almost symmetrical effect (depending on how in-core experiments have been positioned inside the core) implies an apparent zero effect on the reactivity loss coefficient generated by compensation on isotopic compositions. **For fuel depletion purposes, in-core experiment modeling should and will be considered to avoid hidden compensations**.

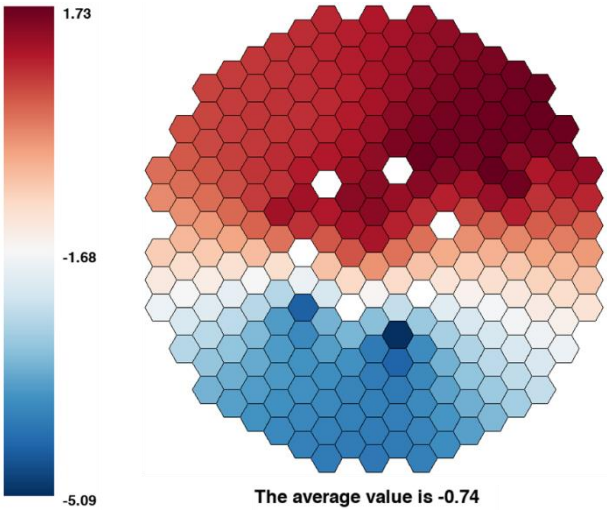

Figure 42. Discrepancy map (in percent) at mid-height of ^{239}Pu consumption between of considering in-core experiment modeling

4.2.3. Control rod extraction

During an irradiation cycle, the reactivity loss is compensated at any time by control rod extraction. This extraction imposes a forced spatial redistribution of the flux that can lead to local reaction rate underestimation/overestimation (different power map) if it is not taken into consideration.

Compared to the previous hypotheses studied, control rod movement implies a change in the geometry at each time-step. For this change to be made, all isotopic compositions depleted after the time step are stored in a database and dumped into the new geometry. Theoretically, if the control rod axial position follows the actual experimental one, the multiplication factor computed would be almost identical at all steps as it is the sum of the reactivity loss due to fuel depletion and the reactivity gains with the control rod extraction. To break down both phenomena, three multiplication factors are computed at each step. The first at the beginning of the step; the second in the same geometry after fuel depletion (difference between both gives the reactivity loss of the time step); the third with the depleted isotopic composition in the new geometry (difference between the two last one gives the control rod worth).

By focusing on the discrepancy map of ^{239}Pu consumption for different axial position in the core, it can be seen that the redistribution effect affects the entire core radially and axially (see Figure 43). In this case, depletion with evolving control rod driveline (hereinafter Case 1) is compared with a depletion calculation performed with control rod at EoC axial position (maximum extraction during the cycle, hereinafter Case 2).

In Case 1, control rods are consistently lower than in Case 2. It implies that the neutron flux is redistributed to the bottom of the core so that the ^{239}Pu consumption is higher in this zone, whereas the opposite occurs in the upper region (see Figure 43). However, they do not compensate each other so that there is a global ^{239}Pu under-consumption in case 2 (static control rod at EoC axial position). This difference in ^{239}Pu consumption (and other isotopes not presented here) implies a difference in the reactivity loss coefficient of +0.74% (when going from static control rod to moving control rod).

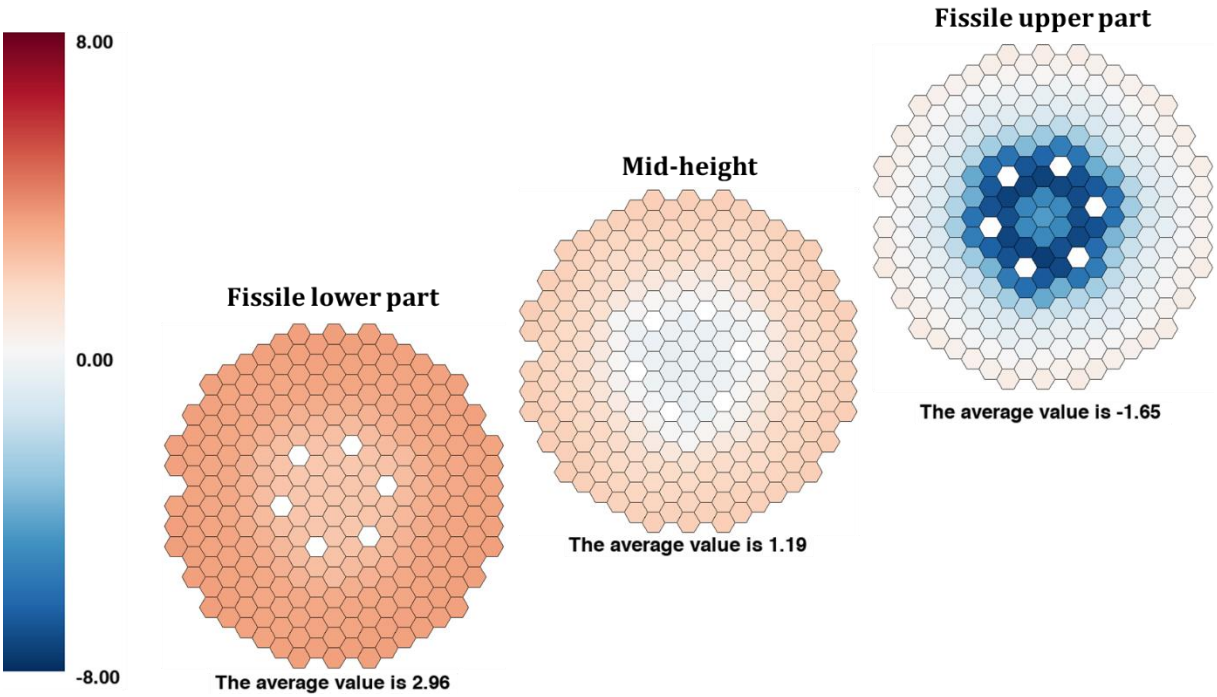

Figure 43. Discrepancy map (in percent) at three axial positons of ^{239}Pu consumption of considering control rod extraction during cycle compared to a calculation with control rod at EoC axial position

By positioning the control rods in the static case at an average axial position (in relation to the entire cycle) instead of the EoC position, the difference in consumptions vanishes and the discrepancy on the reactivity loss coefficient drops to +0.25%. Hence, the depletion calculation with static control rod is able to correctly model isotopic evolution. In other words, moving the control rod during fuel depletion is not required to simulate this phenomenon accurately, if the axial position maintains the average position. However, the static control rod induces a remaining bias of +0.25% on the reactivity loss coefficient so the **moving control rod should and will be used for reactivity loss calculation purpose**.

4.2.4. Control rod depletion

The control rod extraction modeling makes it possible to ensure that the control rods have reproduced the correct neutron flux to its neighboring rods at each time-step. It then allows consideration of the ^{10}B depletion (see Figure 44 for the depletion chain) in the correct depletion conditions (i.e. the irradiated axial proportion of the control rod is the experimental one at each time-step). It should be noted that absorbing experimental devices with ^{10}B are also concerned by this depletion.

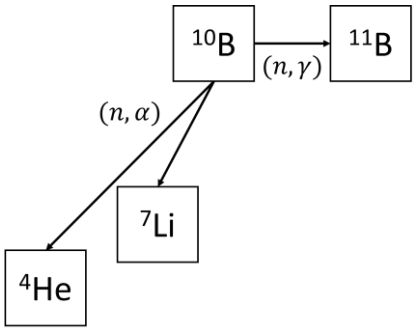

Figure 44. ^{10}B depletion chain

The impact on the reactivity loss coefficient is significant and larger than other parameters considered (-1.76%). When ^{10}B depletion occurs, the global absorbing material decreases, which has a direct effect on the multiplication factor. Moreover, as the B_4C is enriched at 48% in ^{10}B, the control rod worth and then the effect on the flux does not significantly change when the enrichment decreases by a few percent. It explains why the isotopic composition is slightly affected by this modeling consideration, as the Figure 44 shows it.

The control rod worth goes from 486.7 ¢ without ^{10}B depletion to 484.6 ¢ with a final enrichment of about 46% in the most irradiated areas[21]. For cycle 42, the impact of the boron chain is the sum of the control rod impact and the absorbing in-core devices. With the control rod worth difference, the isolated impact of the control rod could be estimated to -0.5%, the rest being due to in-core device boron depletion (which also has a larger impact on its surroundings than the control rods). Hence, ^{10}B depletion in control rods (and devices containing significant amount of boron as shown in Figure 45) is an important parameter to consider for reactivity loss studies but not necessarily for isotopic composition analysis. **Therefore, for the best estimate modeling of the reactivity loss coefficient, boron depletion will be considered**

[21] It is with this depleted configuration that $\varepsilon_{115,Hot,EOC}^{AP3}$ was calculated in Equation (3-13) of Chapter 3, which allows accounting for the evolution of the core and control rods in the rod bank worth used to determine the experimental reactivity loss.

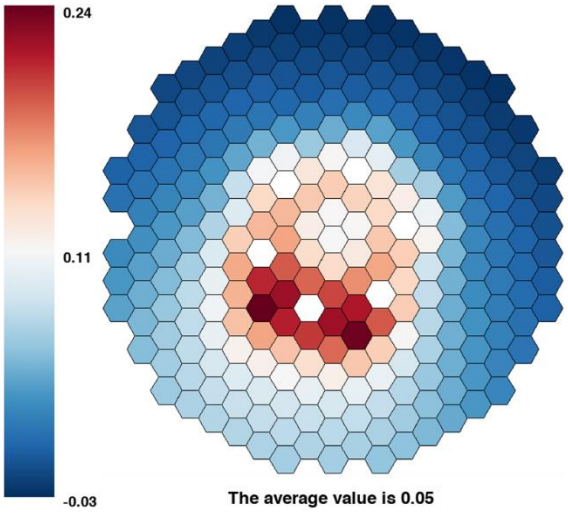

Figure 45. Discrepancy map (in percent) of ^{239}Pu consumption with and without consideration of the ^{10}B depletion chain (for the control rods and in-core absorbing experiments). Axial position: upper part of the fissile zone, axial position concerned with facing control rod during the cycle

4.2.5. Multiphysics coupling

The previous modelling approaches have highlighted the impact of neutronics assumptions accessible for the APOLLO3®/MENDEL scheme. The next step is to couple GERMINAL V2 to the fuel depletion calculation. During irradiation, high fluxes and high temperatures will induce significant fuel restructuring, which changes the heat transfer between the cladding and the pellet, which in turn affects the fuel temperature and therefore the reactivity, via the Doppler Effect. In addition, restructuring causes fission gases such as Xenon and Krypton to migrate out of the pellet into the plenums, which decreases the total absorption and then the reactivity. To take account of the temperature map and leakage coefficient map and its evolution over time, one average pin is considered per subassembly (around hundred pins considered) and both maps are updated at each depletion time-step.

First, introducing Fission Gas leakage has an impact of -0.35% on the reactivity loss. Like the control rod depletion, the impact of FG leakage is only on the total absorption and does not exhibit any effect on the neutron spectrum and the spatial flux redistribution through irradiation. Therefore, the impact on the isotopic composition is negligible. In the Phenix case, fission products have a second-order impact on the reactivity loss as it is mainly driven by heavy nuclei depletion. In another reactor concept where fission products would have been a prime impact (for instance self-breeder[22] reactor designs), the impact of fission gas leakage could be more significant. Former computational tools integrated

[22] Capable of regenerating the quantity of fissile material directly within the fissile zone essential. This implies a very low, if not zero or even positive, reactivity loss, which will therefore place much greater importance on the amount of purely absorbing materials, such as fission products (FPs).

the fission gas leakage into the lumped fission yield. Incorporation of such leakage into a lumped fission yield is no longer possible in new methodologies based on evaluated data. Thus, coupling for fission gas release is important to consider for reactivity loss calculations.

Then, coupling of the temperature map produces a different initial flux distribution also with a different behavior over time for the flux redistribution. It can be seen in Figure 46 as the local power discrepancy in BoC state has a different pattern than the one in EoC state. The order of magnitude of the power redistribution due to the coupling stays relatively low (below 1%). However, the temperature map and its evolution induces a local overestimation/underestimation of around 2% for the ^{239}Pu consumption depending on the zone (see Figure 47). Moreover, the discrepancy in the reactivity loss coefficient is about -0.55%.

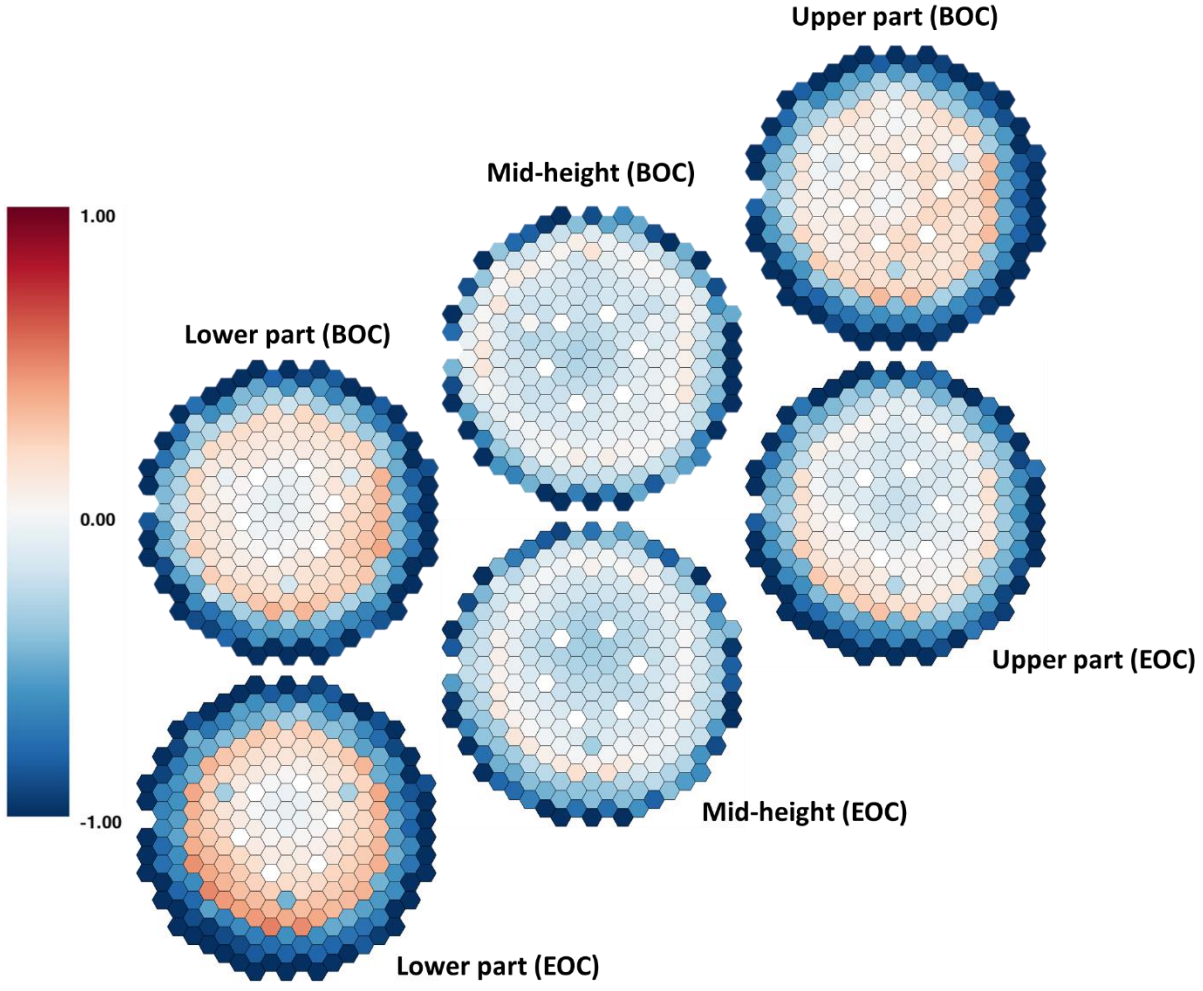

Figure 46. Local power discrepancy map (in percent) with different levels of consideration of multiphysics coupling with GERMINALV2 during fuel depletion (in BoC and EoC state)

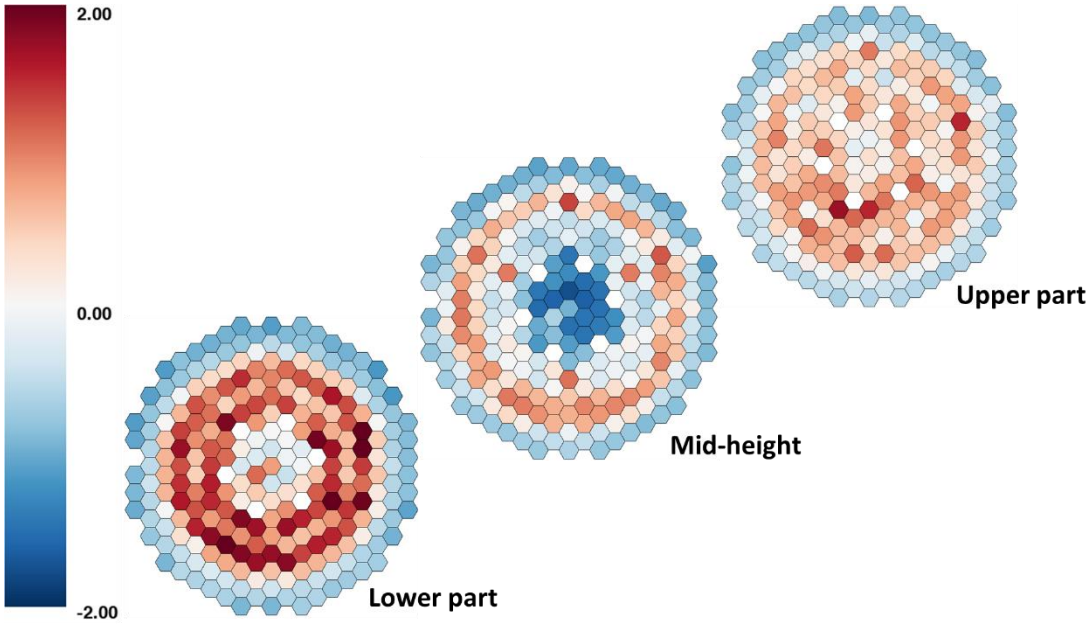

Figure 47. Discrepancy map (in percent) at several levels of ^{239}Pu consumption with consideration of multiphysics coupling with GERMINALV2 during fuel depletion

As has been shown in Section 2.4 in Chapter 2 two main mechanisms are involved when coupling the neutronics calculation with the temperature:

- The initial discrepancy between the computed Doppler feedback[23] with GERMINAL V2 and without coupling
- The evolution over time of the total Doppler feedback (considered as constant with a uniform and constant average temperature)

To distinguish between both mechanisms, another calculation has been performed with a constant temperature map computed only at BoC state (called *soft coupling*). It allows the initial Doppler feedback to be obtained and considered as constant over time. By comparing the non-coupled case with this latter one, the first item of the list presented above can be obtained (in first order) and by comparing the soft coupling with the full coupling, it is possible to estimate the influence of the evolving Doppler feedback over time.

Following this methodology, it can be seen that the discrepancy in Figure 47 for the ^{239}Pu consumption, between a fully coupled case and a non-coupled case is mainly due to the initial temperature map (see Figure 48). The remaining changes in temperature during the cycle are sufficiently small to have a negligible impact on the isotopic composition.

The initial discrepancy in the temperature map produces cross-section changes that will perturb the reaction rates and especially reaction rate ratios that lead the isotopic

[23] The total Doppler feedback is the integral reactivity worth between the cold state and the hot state.

consumption (or production). By imposing a global uniform temperature, the local temperature discrepancy will automatically induce locally different reaction rate ratios. Nevertheless, the different biases tend to cancel each other out globally so that integral coefficients such as multiplication factors are conserved.

In the case studied, the average temperature does not allow fitting of the global Doppler feedback. The discrepancy between the soft coupling case and the non-coupled case for the reactivity loss coefficient is +0.17%. This discrepancy could be reduced to zero with a properly chosen average temperature. However, even if the rate of temperature change over the cycle is small, Doppler feedback is significantly changed to induce a discrepancy between the soft coupling and the full coupling of about -0.73%. An average temperature cannot properly reproduce the reactivity loss coefficient. **Therefore, a full coupling calculation is needed for reactivity loss whereas a soft coupling is sufficient for fuel depletion.**

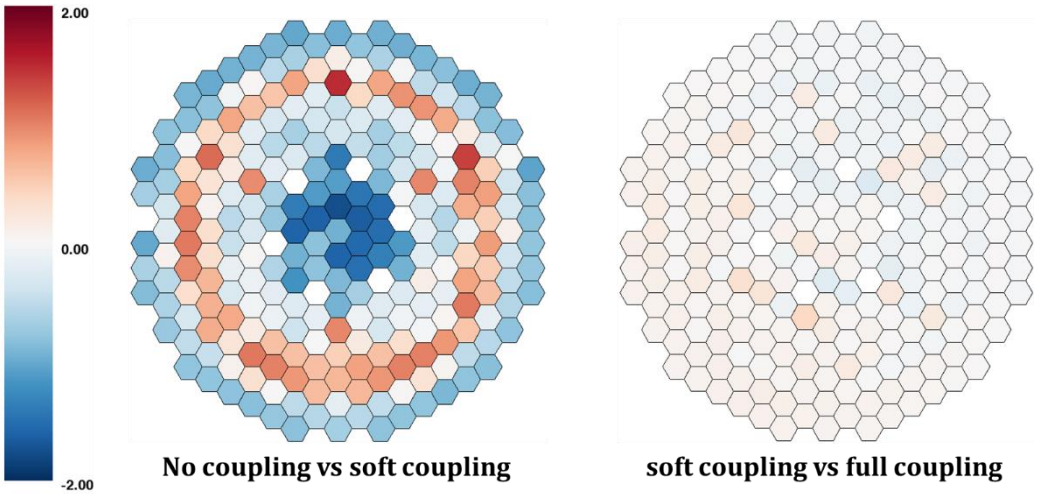

Figure 48. Discrepancy map (in percent) at mid height of ^{239}Pu consumption with consideration of different coupling methodologies

4.2.6. Best-Estimate result

The Best-Estimate value is obtained for the APOLLO3®/MENDEL scheme by taking into account previous recommendation on the listed items. For cycle 42-115, Best-Estimate approach leads to a reactivity loss coefficient of **-4.650 ¢/EFPD** (-0.13% discrepancy with the experiment within the uncertainty range) for a total reactivity loss of **460.4 ¢.** The following table summarizes contributions of the different modeling considerations for a fuel depletion calculation in operation condition.

Table IX. Reactivity loss of cycle 42-115 depending on the fidelity of the modeling

Removed assumptions	Reactivity loss [¢]	Reactivity loss coefficient [¢/EFPD]
1 time-step depletion (no ICE, CR at EOC height)	-469.4	-
20 days time-step (no ICE, CR at EOC height)	-469.7	-4.743
10 days time-step (no ICE, CR at EOC height)	-469.8	-4.742 (-0.03%)
5 days time-step (no ICE, CR at EOC height)	-469.8	-4.741 (-0.02%)
+ in-core experiments	-469.7	-4.739 (-0.04%)
+ control rod extraction (compared to CR driveline at EOC)	-475.0	-4.773 (+0.74%) (+0.25% for average driveline)
+ control rod depletion (^{10}B depletion chain)	-466.7	-4.692 (-1.76%)
+ temperature map (GERMINAL V2 + soft coupling)	-466.9	-4.700 (+0.17%)
+ temperature map (GERMINAL V2 + full coupling)	-462.4	-4.666 (-0.73%)
+ FG migration map (GERMINAL V2 + full coupling) **Best-Estimate**	**-460.4**	**-4.650** (-0.35%)

This global reactivity loss comes at 72.4% from heavy nuclei, 27.0% from fission products and 0.6% from "structural" elements (mainly ^{16}O from the fuel oxide and the ^{23}Na from the coolant). By breaking down the reactivity loss to each isotope with the Standard Perturbation Theory[24] (SPT – see Figure 49), it can be seen that ^{239}Pu mainly drives the reactivity loss (-373 ¢), far ahead of the second most important isotope, the ^{238}U (+35 ¢). MOX and fertile blankets are composed of depleted uranium, yet the ^{235}U has a significant impact on the reactivity loss (2nd negative contribution with -25 ¢). It has to be noted that, even if it is a fissile isotope, ^{241}Pu mass balance has a positive contribution. It is because Phenix reactor produces more ^{241}Pu than it consumes (which is not the case for ^{239}Pu in the fissile zone and ^{235}U).

[24] Decomposition of reactivity described in Equation (5-2) of the following chapter, where the direct flux is calculated in the BoC configuration and the adjoint flux in the EoC configuration.

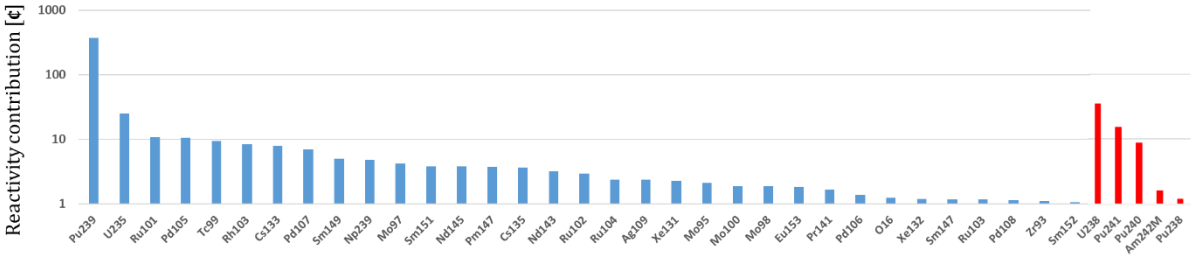

Figure 49. Reactivity contribution to the reactivity loss between BoC and EoC for each isotope (contribution $> 1¢$). Contribution in blue are negative and in red for positive contribution.

4.2.7. Experimental validation of the APOLLO3®/MENDEL scheme

At this stage, the experimental value of the reactivity loss coefficient for 42nd Phenix cycle has been reinterpreted and offers a reliable value with its associated uncertainty. The best-estimate modeling with APOLLO3®/MENDEL of this cycle allows a computed value reasonably consistent with the experiment:

$$\frac{C}{E} = 1.0013 \ , \frac{\Delta E}{E} = 0.0335$$

The reactivity loss obtained with APOLLO3®/MENDEL is the result of contributions from all the parameters involved in the scheme (nuclear data, technological data, solver parameters, meshes, etc.). Thus, the good agreement with the experiment is the result of all associated biases. However, this single value does not allow to conclude the actual accuracy of the scheme. If applied to a different reactor, the biases could potentially be different and thus no longer compensate. To make the best use of the experimental value and be able to associate a level of confidence with the calculation, the biases and uncertainties must be quantified (ΔC).

To do so, usually, a comparison with a reference calculation (numerical validation) is added to the experimental validation (C/E) which implies that the rest of the discrepancy with the experiment is caused by the input data (nuclear data, technological data, etc.). In addition, an uncertainty quantification is performed in order to separate the different types of uncertainty and estimate whether the lack of knowledge regarding the input data is able to explain the discrepancy with the experiment. This global methodology is called VVUQ (Verification, Validation and Uncertainty Quantification) and allows for quantification of the reliability of a computational tool prediction.

For fuel depletion and reactivity loss, a reference calculation is not easily accessible, as detailed in the first chapter and especially when a multiphysics coupling is needed. Therefore, the estimation of the different numerical biases and uncertainties should be determined by using another method.

4.3. APOLLO3®/MENDEL Bias decomposition and uncertainty quantification

In order to perform such bias decomposition and uncertainty quantification for the Phenix reactivity loss with the APOLLO3®/MENDEL deterministic scheme, all the assumptions and sources of uncertainties should be listed:

- Bias induced by MENDEL
- Bias induced by geometrical assumptions
- Bias induced by isotopic composition initialization from PROJERIX
- Bias induced by the APOLLO3®-FR neutronics scheme
- Bias induced by assumptions related to the coupling with GERMINAL V2
- GERMINAL V2 input data and parameters uncertainty
- Power uncertainty used to normalize the neutron flux
- Delayed neutron fraction uncertainty used to obtain the calculated value in ¢
- Nuclear data uncertainty

The purpose of this section will then be to address the bias and uncertainties listed above and to estimate it if possible.

4.3.1. MENDEL numerical bias

The MENDEL numerical bias can be divided into two different parts.
The first one is the purely numerical bias of solving the Bateman equation system with a Runge-Kutta scheme. This can be considered as negligible as this type of equation does not need a specific modeling hypothesis compared to the Boltzmann equation.

The second one is the bias of considering only a partial set of heavy-nuclei (32) and fission product (141) instead of every possible isotope. As this depletion chain has been developed and optimized specifically for SFR reactivity loss purpose [8] this bias can be considered as negligible.

4.3.2. Bias induced by geometrical assumptions

For a power reactor like Phenix, global temperature conditions of structures (that defined their size and then the geometry of the core) stay constant during irradiation if the power is stable. However, the full power dimensions are not known precisely, which induces a bias due to the modeling of a given state (for instance a bias on the multiplication factor). This bias for a given geometry is considered as constant over time as the power is constant during irradiation. It can legitimately be accepted that, to first order, a bias in the

geometry of structures has the same impact on the reactivity throughout the cycle. Then, as the reactivity loss is a difference between two states, the bias offsets itself.

During irradiation, the fuel behavior will induce different changes:

- Change in the fissile column height due to pellet restructuring
- Change in the cladding height due to swelling and changes in its temperature
- Change in the radial dimension of the pellet due to pellet restructuring
- Reduction of the sodium quantity inside the subassembly as pins have expanded radially

The length of the fissile column can affect the neutron spectrum and the leakage rate. By analyzing the fissile column length evolution for each subassembly (GERMINAL output), the average change between BoC and EoC is between -0.16% and +0.06% of the initial cladding height, which is less than one millimeter. In a fast spectrum reactor, the mean free path is of the order of a few centimeters. Hence, it can be considered that such small dimension changes will not induce significant changes in the axial leakage rate or flux spectrum nor in the reactivity loss coefficient, therefore.

The cladding height depends on the cladding temperature. By expanding, the total amount of steel facing fissile fuel decreases (fissile fuel has an axial expansion significantly lower than the cladding) and therefore so does the related absorbing and scattering contribution. In [34], the impact of such a parameter has been estimated for the Superphenix reactor. Its value is around 0.072 pcm/°$C_{cladding}$. During cycle 42, the cladding temperature change is around 5 °C between EoC and 20 EFPD (the range used to compute the reactivity loss coefficient). By considering a similar reactivity impact of this phenomenon for the Phenix reactor, an effect below 0.04% would be obtained on the reactivity loss coefficient.

For fast spectrum, the mean free path is several orders of magnitude higher than the dimension changes involved in the radial pin expansion. Consequences on the flux can then be considered as negligible (for a constant mass of heavy nuclei).

When radially expanding, the pins remove a sodium quantity from the hexagonal tube. For cycle 42, this reduction rate is around -0.003%$_{Na23}$/days. The sensitivity to the sodium quantity for the beginning of cycle 42 is around -3 pcm/%$_{Na23}$ which gives an estimated impact of around 0.06% on the reactivity loss coefficient.

Finally, the constant geometry hypothesis can be considered as acceptable for a fuel depletion purpose, as the geometry changes during irradiation have a negligible impact (< 0.1%) on the reactivity loss coefficient.

4.3.3. Bias induced by PROJERIX initialization

As explained in the 2.2.1.1 subpart, the initial isotopic composition is initialized from a previously calculated database. The actual bias on the isotopic composition is not known. Nevertheless, the PROJERIX database has been validated against reactor's reactivity for each beginning of cycle. The main isotopes from the Uranium-Plutonium depletion chain are strongly related to each other in a Boltzmann/Bateman coupled problem. The reactivity validation then makes it possible to consider that the initial bias of the PROJERIX database is limited. Moreover, a comparison has been made for the 48th cycle reactivity loss coefficient between a calculation initialized with the PROJERIX database and a calculation initialized with isotopic composition computed with the APOLLO3®/MENDEL scheme from cycle 42. Between them, most of the fuel present in the 42nd cycle has been replaced so that at the beginning of cycle 48, the core is practically free from the PROJERIX bias. This comparison led to a discrepancy of 0.2% between both reactivity loss coefficients. This value is in the order of magnitude of some modeling consideration estimated in the last subsection but stays relatively low so it provides promising insight on the current analysis. Further work with modern tools and new methodologies could potentially provide a better knowledge about the isotopic composition bias at the beginning of the cycle.

4.3.4. Neutronics scheme deterministic bias

To estimate the neutronics scheme bias, the same study as the one conducted on the Phenix-Like model, has been done by comparing APOLLO3® with TRIPOLI-4® for cycle 42 (in BoC state). The differences between the Phenix-Like configuration and this configuration are the temperatures (hot in this case), that each part of each subassembly has its own Burn-Up (with a unique heavy nuclei distribution and fission product instead of identical fresh fuel) and there are eight in-core devices.

Results are presented in the Table X. Discrepancies are larger in this case than in the Phenix-Like configuration (increased from 0.11% for ^{238}U Capture in the internal core for Phenix-like to 1.61%).

Table X. Discrepancy between APOLLO3® and TRIPOLI-4® on global reaction rates for each media of the BOC configuration of Phenix cycle 42 (control rod in the EOC position)

AP3/T4 – 1 $(\mathcal{D}_\tau^m)$ [%]	^{238}U		^{239}Pu		^{240}Pu		^{241}Pu	
	(n,γ)	(n,f)	(n,γ)	(n,f)	(n,γ)	(n,f)	(n,γ)	(n,f)
C1	**1.61**	-2.35	2.35	**0.58**	2.21	-0.33	0.29	0.69
C2	0.39	-3.09	1.05	**-0.35**	0.81	-1.10	-0.92	-0.31
FCAI	-0.31	-2.43						
FCAS	-1.77	-3.77						
FCR	1.47	-1.02						

These biases will propagate to the isotopic composition at the end of the time-step, which will in turn affect the neutron flux etc., until the end of irradiation. They act as a perturbation on the reactor system (on the reaction rates). In this paradigm, where a bias is a perturbation, the question of its propagation to quantify its impact on a given quantity of interest can rely on the perturbation theory. With such theory, the sensitivities (normalized local derivatives) can be obtained and, once done, easily provide the propagated bias with the simple following formula (considering a constant bias over time and a first order approximation of the reactivity loss around the calculated point):

$$\mathcal{D}_{\alpha}^{AP3FR} = \sum_{m} S_{\tau,m}^{\alpha} \mathcal{D}_{\tau}^{m} \tag{4-2}$$

$$S_{p}^{R} = \frac{p}{R}\frac{dR}{dp} \tag{4-3}$$

With $S_{\tau,m}^{\alpha}$, the sensitivity to the reactivity loss coefficient of the reaction rate τ in the subdomain m. $\mathcal{D}_{\tau}^{m}$, the initial bias on the reaction rate τ in the subdomain m. And $\mathcal{D}_{\alpha}^{AP3FR}$ the propagated bias on the reactivity loss coefficient when the fuel depletion is performed with an initial and constant bias $\mathcal{D}_{\tau}^{m}$.

With the same idea, the initial bias due to initial isotopic composition could be propagated to the reactivity loss if initial biases were known:

$$\mathcal{D}_{\alpha}^{N_i^0} = \sum_{m} S_{N_i^0,m}^{\alpha} \mathcal{D}_{N_i^0}^{m} \tag{4-4}$$

4.3.5. Uncertainty due to power normalization

At each time-step of the irradiation calculation, the neutron flux is normalized with the power in order to compute the reaction rates and then the isotopic composition of the following time-step. This power is taken from the cycle report and is the same used to define the EFPD in the experimental chapter. To compute the sensitivity of the reactivity loss to the power, the power has been increased by 1%. It gives a discrepancy in the reactivity loss coefficient of 0.919%. This sensitivity would give a reactivity loss coefficient uncertainty of 2.76%, with a 3% power uncertainty. Such an uncertainty value for the experimental power implies that part of the C/E could be explained by a bias on the power considered.

4.3.6. Uncertainties coming from nuclear data

To quantify the nuclear data uncertainty, the variances and covariances of the different nuclear data needed to compute the reactivity loss must be propagated. These covariances for the energy mesh (33 groups) considered in this study are accessible for JEFF 3.1.1 in a covariance matrix called COMAC V1 [59].

A Monte-Carlo method to propagate such uncertainties, like the one used to quantify the reactivity loss experimental uncertainty in subsection 3.3.5, is not accessible. The number of parameters to consider, with a substantial computational time for the reactivity loss coefficient, would make the calculation prohibitive.

However, it is possible to consider the nuclear data uncertainty as a perturbation with its own probability distribution applied at the beginning of irradiation that propagates during irradiation and thus on the reactivity loss coefficient. Then, with the reactivity loss sensitivities to nuclear data and first-order approximation, it is possible to express nuclear data uncertainty using the following simple formula (see Appendix F for more details):

$$\Delta\alpha_{\mathrm{BU}}^{ND} = \sqrt{S_\alpha^T \cdot M \cdot S_\alpha} \tag{4-5}$$

4.3.7. Uncertainty due to delayed neutron fraction

Since the experimental reactivity loss coefficient is expressed in ¢ rather than *pcm*, it is essential to calculate the effective delayed neutron fraction (β_{eff}) for the configuration used. To achieve this, the reference calculation code TRIPOLI-4® with the IFP method [60] was utilized during the calculations performed in the previous chapter for the shadow-effect coefficient. The final β_{eff} of the Phenix model is then obtained by averaging the overall set. This actualization gives a delayed neutron fraction 5.43% inferior to the old one with an associated statistical uncertainty of 1%. The total uncertainty of the β_{eff} should include the uncertainty due to nuclear data.

To compute the nuclear data uncertainty of the β_{eff}, the APOLLO3®-FR scheme has been used with the methodologies presented in [61]. It gives an uncertainty of 2.46%. Nevertheless, this method does not consider the uncertainty due to delayed neutron spectra. For this first one and based on the work carried out in [62] the order of magnitude of this sensitivity is considered to be around 1%. This gives a total uncertainty of 2.84%.

4.3.8. Biases and uncertainties induced by Multiphysics coupling

As explained in part 2.1.3.1, GERMINALV2 has been chosen alone, instead of a more complex modeling (for instance a dedicated tool for thermal-hydraulic and 3D modeling of the pin for fuel performance computation), because it is considered that only fuel performance is significantly affected during irradiation. The total impact from multiphysics, compared to a non-coupled case, has been quantified to -0.9%. As the code has been specifically validated experimentally with the Phenix feedback, it can be considered as a first approximation that the GERMINAL bias propagated to the reactivity

loss coefficient would be a fraction of 0.9%. With such consideration, the bias induced by multiphysics assumptions would be negligible.

Alternatively, to approach such bias and uncertainty quantitatively, due to GERMINAL input data and parameters, it could be remembered that the multiphysics coupling for reactivity loss in the hypothesis range used in this work, is affecting only the cross-sections via the temperature at each time-step like a perturbation (and respectively the FG release as a local isotopic composition perturbation). Hence, reactivity loss sensitivities could be used to mimic the neutronics response of temperature changes. Going further would require addressing a number of technical details and methodological questions that are beyond the scope of this thesis but should be addressed in the short and medium term in order to assess modern tools with multiphysics coupling capabilities.

4.4. Conclusion

Modern computation tools as APOLLO3® allows for significantly increasing the modeling fidelity by removing the commonly used hypothesis and being more easily coupled with other SCTs. In this chapter, fidelity has been gradually increased for the fuel depletion calculation by removing each hypothesis attainable up to the multiphysics aspect with the reference fuel performance code GERMINAL V2. It allowed for calculation of a **Best-Estimate** value for the reactivity loss coefficient for the 42nd Phenix cycle of **-4.650 ¢/EFPD (+0.13% discrepancy with the experiment)**.

Following this methodology, and studying the impact of these hypotheses on the reactivity loss along with the isotopic composition, it has been possible to identify modeling requirements depending on the desired accuracy and the purpose of the study as presented in the following table:

Table XI. Modeling parameter guidelines for fuel depletion calculation

	Reactivity loss	Isotopic composition
In-core experiments modeling	Yes	Yes
Control rod extraction modeling	Yes	Yes
Control rod depletion modeling	Yes	No
Multiphysics coupling (temperature map) - soft	No	Yes
Multiphysics coupling (temperature map) - full	Yes	No
Multiphysics coupling (fission gas leakage)	Yes	No

Moreover, the sole comparison of the best-estimate value with the experiment is not sufficient to conclude on the accuracy and predictability of such scheme. Current VVUQ methodology requires the quantification and discrimination of the numerical biases due to calculation assumption and uncertainties due to input data. The lack of reference calculation for complex coefficients, such as reactivity loss, imply an additional work of listing and estimating all input data and assumptions concerned. With the different results

obtained with the best-estimate calculation and with physical consideration, **it has been possible to estimate part of the biases as negligible**. For the rest, the different biases may be seen through the perturbation theory perspective and may, with the reactivity loss sensitivities, allow for estimation of their impact.

However, standard perturbation tools (in neutron physics) are able to compute sensitivities for one state or a state perturbation where the two states are independent. In the reactivity loss context, all the different states are coupled by the Boltzmann and Bateman equations. Hence, a specific formalism able to model such coupling is needed. This formalism has been implemented in APOLLO3® and will be detailed in the next chapter.

Chapter 5. Boltzmann/Bateman coupled sensitivities

Chapter 5. Boltzmann/Bateman coupled sensitivities 117
5.1. Introduction 118
5.2. Reactivity loss sensitivity theory 118
5.2.1. Standard Perturbation Theory 118
5.2.2. Depletion Perturbation Theory 120
5.2.3. Computational scheme for coupled sensitivities 123
5.2.4. Limitations for power reactor experimental application 127
5.3. Partial adjoint depletion implications: application to a fuel sub-assembly 128
5.3.1. Fully backtrack sensitivities 129
5.3.2. Partial consideration of the irradiation history 131
5.3.3. Nuclear data uncertainty 133
5.4. Application to the 42th Phenix cycle 137
5.4.1. Reactivity loss sensitivities as a tool for analysis 137
5.4.2. Reactivity loss uncertainty due to nuclear data and its limitations in operation condition 140
5.4.3. APOLLO3®/MENDEL decomposition bias with coupled sensitivities 142
5.5. Conclusion 144

Summary – In this chapter, the coupled Boltzmann/Bateman sensitivities are presented, along with the corresponding calculation scheme with APOLLO3®/MENDEL. The current limitations of its implementation in APOLLO3® have been studied in a simple and controlled case of an infinite lattice subassembly, revealing that the calculated sensitivities with this limitation tend to be overestimated by 20% for the captures and fissions of heavy nuclei at the relevant burnups. The contribution of this formalism is significant compared to the standard perturbation theory. The calculation of these sensitivities on a core scale provides an additional tool for analyzing the physics of irradiation phenomena. This approach has enabled estimation of the APOLLO3®/MENDEL scheme biases as less than 1% on the reactivity loss coefficient, and the contribution of uncertainties due to nuclear data as 6.943%. Given the experimental uncertainty and the numerical bias with values much lower than the uncertainty due to nuclear data, it is possible to foresee the data assimilation using this Phenix cycle reactivity loss.

Objectives

- Computation of these sensitivities for the reactivity loss of Phenix cycle 42
- Quantification of the nuclear data uncertainty associated with the Best-Estimate Value
- Estimation of the remaining bias of the Best-Estimate modeling

Highlights

- The nuclear data uncertainty for the reactivity loss of the Phenix cycle 42 is estimated as 6.943% for the JEFF 3.1.1 library, and 6.856% for nuclear data already contained in COMAC V1/ 1.094% for the newly introduced ones
- The "last-cycle" hypothesis considered in computation of such sensitivities tends to overestimate sensitivities of heavy nuclei capture and fission
- The APOLLO3®/MENDEL scheme bias is estimated as less than 1% on the reactivity loss coefficient

5.1. Introduction

Knowledge of a phenomenon's sensitivities to a certain number of input data is an especially effective tool for understanding the underlying physics and the various contributors, making analysis significantly easier. Moreover, as it has been shown in the previous chapter, sensitivities are helpful to quantify and estimate respectively the uncertainties due to input data and biases. However, the formalisms traditionally used for reactivity differences are limited in the context of reactivity loss during irradiation because only the contribution of the transport equation is considered. In a fuel depletion calculation, the coupled Boltzmann/Bateman system increases the number of possible contributors and requires a specific formalism, which will be detailed along with the limitations of the standard formalism in the first section. The application to an operational reactor involves several difficulties concerning the consideration of irradiation history. The impact of not accounting for the full irradiation history will be studied using a simple, well-managed subassembly case in the second section. Ultimately, calculation of coupled Boltzmann/Bateman sensitivities for Phenix cycle 42 in the third section will allow different contributing factors to be quantified. This will make it possible to estimate the APOLLO3®/MENDEL scheme's bias and quantify the uncertainty associated with nuclear data.

5.2. Reactivity loss sensitivity theory

The most straightforward way to compute sensitivities is to directly perturb each parameter individually, to observe the impact on the quantity of interest, which will directly provide the sensitivities. However, this brute force approach suffers from the same limitations as the Monte Carlo uncertainty quantification, making it inapplicable for reactivity loss.

Nevertheless, in neutron physics, the Boltzmann equation has an adjoint formulation that allows sensitivities to be obtained for every parameter, through perturbation theory.

5.2.1. Standard Perturbation Theory

The purpose of the Standard Perturbation Theory (SPT) is to express the perturbation of an operator's parameter of a given state on the multiplication factor. The multiplication factor depends on the neutron flux, the adjoint neutron flux and the operator of the Boltzmann equation (2-3):

$$k = \frac{\langle \phi^*, \mathcal{F}\ \phi \rangle}{\langle \phi^*, \mathcal{B}\ \phi \rangle} \tag{5-1}$$

With <> the integration over the phase space of the stationary Boltzmann equation (angular, energetic, and spatial variables).

By using a first linear approximation, the perturbation of a Boltzmann operator's parameter on the reactivity could be expressed as:

$$d\rho = \frac{dk}{k^2} = -\frac{< \phi^*, \left(\boldsymbol{d\mathcal{B}} - \frac{\boldsymbol{d\mathcal{F}}}{k}\right)\phi >}{< \phi^*, \boldsymbol{\mathcal{F}}\,\phi >} \tag{5-2}$$

With ϕ and ϕ^* governed respectively by the direct Boltzmann equation (2-3) and the adjoint Boltzmann equation [63]:

$$\left(\boldsymbol{\mathcal{B}}^* - \frac{\boldsymbol{\mathcal{F}}^*}{k}\right)\phi^* = \mathcal{H}^*\phi^* = 0 \tag{5-3}$$

With $\mathcal{H}^*$ the adjoint transport operator. The adjoint equation has the same form as the direct one with $-\nabla\cdot\vec{\Omega}$ instead of $\nabla\cdot\vec{\Omega}$ for the advection operator and a $\left(E \to E', \vec{\Omega} \to \vec{\Omega}'\right)$ dependency instead of $\left(E' \to E, \vec{\Omega}' \to \vec{\Omega}\right)$. This similar form with the direct formulation allows a transport solver such as MINARET to solve the adjoint problem.

The reactivity loss of a given cycle is the difference between reactivity at the end of the cycle (ρ_{EOC}) and at the beginning of the cycle (ρ_{BOC}):

$$\Delta\rho = \rho_{EOC} - \rho_{BOC} \tag{5-4}$$

Then, the perturbation of the difference can be expressed as follow:

$$d\Delta\rho = d\rho_{EOC} - d\rho_{BOC} \tag{5-5}$$

Hence, it is possible to directly obtain the sensitivities for a reactivity change to every isotope-reaction couple with equations (5-4) and (5-2) :

$$S_p^{\rho_B-\rho_A} = \frac{p}{\rho_B-\rho_A}\left(\frac{< \phi_A^*, \left(\frac{\boldsymbol{\partial\mathcal{B}_A}}{\boldsymbol{\partial p}} - \frac{1}{k_A}\frac{\boldsymbol{d\mathcal{F}_A}}{\boldsymbol{dp}}\right)\phi_A >}{< \phi_A^*, \boldsymbol{\mathcal{F}_A}\,\phi_A >} - \frac{< \phi_B^*, \left(\frac{\boldsymbol{\partial\mathcal{B}_B}}{\boldsymbol{\partial p}} - \frac{1}{k_B}\frac{\boldsymbol{\partial\mathcal{F}_B}}{\boldsymbol{\partial p}}\right)\phi_B >}{< \phi_B^*, \boldsymbol{\mathcal{F}_B}\,\phi_B >}\right) \tag{5-6}$$

Which can be expressed as the difference between the sensitivities of the two states being compared, as follows:

$$S_p^{\Delta\rho} = \frac{1}{\Delta\rho}\left(\frac{S_p^{k_B}}{k_B} - \frac{S_p^{k_A}}{k_A}\right) \tag{5-7}$$

This formalism is called Equivalent Generalized Perturbation Theory (EGPT) [64]. However, this formalism with SPT sensitivities for both states A and B can be used only if the reactivity worth considered only has dependencies with nuclear data, neutron flux and adjoint neutron flux (i.e. $R(p, \phi, \phi^*)$). For instance, control rod worth between a fully inserted case and a fully withdrawn case. It depends only on the neutron flux, as the

extraction movement of the control rod is not related to the parameters of the control rod worth[25].

This statement is not adapted to the fuel depletion problem. The reactivity loss is induced by isotopic composition changes related to the neutron flux (which is also influenced by the changing isotopic composition). This implies that the reactivity loss depends on the neutron flux, the adjoint neutron flux and the isotopic composition. The EGPT formalism is then not sufficient to approach such a problem and a specific formalism is required that would be able to address a $R(p, \phi, \phi^*, \boldsymbol{N})$ quantity of interest: the coupled Bateman/Boltzmann sensitivities.

5.2.2. Depletion Perturbation Theory

The coupled Bateman/Boltzmann sensitivities from the Depletion Perturbation Theory (DPT), have been established by Gandini [65], Williams [66] and generalized by Takeda and Umano [67] (where the following mathematical development and notations have been taken). These consider the direct and the indirect terms affected by a nuclear data change on an R quantity of interest that depends on $\boldsymbol{N}$, ϕ and ϕ^*:

$$S_p^R = \frac{p}{R}\frac{dR}{dp} = \frac{p}{R}\left(\frac{\partial R}{\partial p} + \frac{\partial R}{\partial \boldsymbol{N}}\frac{d\boldsymbol{N}}{dp} + \frac{\partial R}{\partial \phi}\frac{d\phi}{dp} + \frac{\partial R}{\partial \phi^*}\frac{d\phi^*}{dp}\right) \tag{5-8}$$

If this formula is applied to a quantity in the EoC state, with quasi-static assumption and I time-step for the fuel depletion calculation, the final sensitivity depends on every intermediate $\boldsymbol{N}$, ϕ and ϕ^* computed at each time-step:

$$R = \int_0^{t_I} \mathrm{d}t\langle \mathrm{R}\rangle \tag{5-9}$$

$$\begin{aligned} \mathrm{S_p^R} = {} & \left\{\frac{\mathrm{p}}{\mathrm{R}}\left[\int_0^{t_I}\langle\frac{\partial \mathrm{R}}{\partial \mathrm{p}}\rangle\,\mathrm{dt}\right]\right. \\ & + \int_0^{t_I}\langle\frac{\mathrm{d}\mathbf{N}}{\mathrm{dp}}\frac{\partial \mathrm{R}}{\partial \mathbf{N}}\rangle\,\mathrm{dt} + \sum_{i=1}^{I}\langle\frac{\mathrm{d}\phi_i}{\mathrm{dp}}\int_0^{t_I}\frac{\partial \mathrm{R}}{\partial \phi_i}\mathrm{dt}\rangle + \sum_{i=1}^{I}\langle\frac{\mathrm{d}\phi_i^*}{\mathrm{dp}}\int_0^{t_I}\frac{\partial \mathrm{R}}{\partial \phi_i^*}\mathrm{dt}\rangle \\ & \left. + \langle\frac{\mathrm{d}\mathbf{N}_I}{\mathrm{dp}}\frac{\partial \mathrm{R}}{\partial \mathbf{N}_I}\rangle + \langle\frac{\mathrm{d}\phi_I}{\mathrm{dp}}\frac{\partial \mathrm{R}}{\partial \phi_I}\rangle + \langle\frac{\mathrm{d}\phi_I^*}{\mathrm{dp}}\frac{\partial \mathrm{R}}{\partial \phi_I^*}\rangle\right\} \end{aligned} \tag{5-10}$$

Where the direct term from the perturbation theory appears as the first term, and the remaining terms are the indirect ones used to model the depletion constraints. To express and compute indirect terms, new quantities are introduced.

[25] Such formalism has been used to compute the sensitivities of the differential control rod worth and the related nuclear data uncertainties presented in Figure 34 in Chapter 3.

First, an integral parameter P_i^*, also called adjoint power, is defined as follows for every time-step:

$$P_i^* = \begin{cases} \dfrac{\langle \phi_i \dfrac{\partial R}{\partial \phi_i} \rangle}{P_i} & \text{if } \mathrm{t_i} = \mathrm{t_I} \\ \dfrac{\langle \int_{t_i}^{t_{i+1}} dt N^* \mathcal{T} N \rangle + \langle \int_{t_i}^{t_{i+1}} dt \phi_i \dfrac{\partial R}{\partial \phi_i} \rangle}{P_i} & \text{else} \end{cases} \quad (5\text{-}11)$$

With $\mathcal{T}$ being the flux dependent component in the matrix evolution ($\mathcal{A} = \mathcal{T}(\phi) + \mathcal{D}$) and the other component being decays.

Then, a function Γ_i, also called forward importance function is defined as follow:

$$\mathcal{H}_i \Gamma_i = \begin{cases} -\dfrac{\partial R}{\partial \phi_i^*} & \text{if } \mathrm{t_i} = \mathrm{t_I} \\ -\int_{t_i}^{t_{i+1}} dt \dfrac{\partial R}{\partial \phi_i^*} & \text{else} \end{cases} \quad (5\text{-}12)$$

With $\mathcal{H}$ the transport operator ($\mathcal{H}_i \phi_i = 0$).
Then, a function Γ_i^*, also called adjoint importance function, is defined as follows:

$$\mathcal{H}_i^* \Gamma_i^* = \begin{cases} P_i^* \kappa \sigma_{fc} N_i - \dfrac{\partial R}{\partial \phi_i} & \text{if } \mathrm{t_i} = \mathrm{t_I} \\ -\int_{t_i}^{t_{i+1}} dt \left\{ \dfrac{\partial R}{\partial \phi_i} + N^* \dfrac{\partial \mathcal{A}}{\partial \phi_i} N \right\} + P_i^* \kappa \sigma_{fc} N_i & \text{else} \end{cases} \quad (5\text{-}13)$$

With N^*, the adjoint isotopic vector also introduced and governed by the adjoint Bateman equation:

$$-\frac{\partial}{\partial t} N^* = \mathcal{A}_i^* N^* + \left[\frac{\partial R}{\partial N}\right] = (\mathcal{T}_i^* + \mathcal{D}^*) N^* + \left[\frac{\partial R}{\partial N}\right] \quad (5\text{-}14)$$

With an initial value at the end of irradiation considered as:

$$N_I^* = \left[\Gamma_I^* \frac{\partial \mathcal{H}_I}{\partial N_I} \phi_I + \Gamma_I \frac{\partial \mathcal{H}_I^*}{\partial N_I} \phi_I^* + \frac{\partial R}{\partial N_I} - P_I^* \kappa \sigma_{fc} \phi_I \right] \quad (5\text{-}15)$$

With [ ] being the summation over energy groups and $\mathcal{A}^*$ being the adjoint Bateman operator (which is the transpose of the Bateman operator).

Unlike the isotopic composition vector, N^* is not continuous over the irradiation time so that there is a "jump condition" between the different time-steps, which needs to respect the following formula:

$$N_{i^-}^* = N_{i^+}^* + \left[\Gamma_i^* \frac{\partial \mathcal{H}}{\partial N_i} \phi_i \right] + \left[\Gamma_i \frac{\partial \mathcal{H}^*}{\partial N_i} \phi_i^* \right] - \left[P_i^* \kappa \sigma_{fc} \phi_i \right] \quad (5\text{-}16)$$

With such considerations, an equivalence between the (5-10) equation and the following one, where all the different components are known, could be established:

$$S_p^R = \frac{p}{R}\left\{\sum_{i=1}^{I}\langle\int_{t_i}^{t_{i+1}} dt\frac{\partial R}{\partial p}\rangle + \sum_{i=1}^{I}\langle\int_{t_i}^{t_{i+1}} dt\boldsymbol{N}^*\frac{\partial \mathcal{A}_i}{\partial p}\boldsymbol{N}\rangle + \sum_{i=1}^{I}\langle\Gamma_i^*\frac{\partial \mathcal{H}_i}{\partial p}\phi_i\rangle + \sum_{i=1}^{I}\langle\Gamma_i\frac{\partial \mathcal{H}_i^*}{\partial p}\phi_i^*\rangle - \sum_{i=1}^{I}P_i^*\langle\frac{\partial \kappa\sigma_{fc}}{\partial p}\boldsymbol{N_i}\phi_i\rangle\right\} \quad (5\text{-}17)$$

In this final expression of the sensitivity for a given quantity of interest (that depends only on $\boldsymbol{N}$, ϕ and ϕ^*) the first term is the direct one, the second is called the **B**ateman term, the third and fourth are the **F**lux term and the last one the **P**ower term. This formula is for global sensitivity. To obtain local sensitivities (i.e. each geometrical subdomain m for a given energy group g) the integration over the all phase space $\langle\ \ \rangle$ could be replaced with local integration $\langle\ \ \rangle_{m,g}$.

In the case of reactivity loss analysis, the quantity of interest at the end of irradiation is the multiplication factor ($R = k_I$). The direct term of the sensitivity is then:

$$S_p^{k_I,SPT} = \frac{p}{k_I}\sum_{i=0}^{I-1}\langle\int_{t_i}^{t_{i+1}} dt\frac{\partial R}{\partial p}\rangle = \frac{p}{k_I}\frac{\partial k_I}{\partial p} \quad (5\text{-}18)$$

And equations from (5-11) to (5-15) are simplified:

- $\frac{\partial k_I}{\partial \phi_i} = \frac{\partial k_I}{\partial \phi_i^*} = 0$ for $i = 0$ to $i = I$
- $\frac{\partial k_I}{\partial N} = 0$
- $\frac{\partial k_I}{\partial N_i} = 0$ for $i = 0$ to $i = I - 1$
- $\Gamma_i = 0$ for $i = 0$ to $i = I$

Which leads to $P_I^* = \Gamma_I = \Gamma_I^* = 0$ and $N_I^* = \frac{\partial k_I}{\partial N_I}$ for the final time t_I. Considering the rest of the time-step, the different adjoint quantities need to respect the following equations:

$$P_i^* = \frac{\langle\int_{t_i}^{t_{i+1}} dtN^*\mathcal{T}_i N\rangle}{P_i} \quad \text{Adjoint power equation} \quad (5\text{-}19)$$

$$\mathcal{H}_i^*\Gamma_i^* = P_i^*\kappa\sigma_{fc}N_i - \int_{t_i}^{t_{i+1}} dtN^*\frac{\partial \mathcal{A}_i}{\partial \phi_i}N \quad \text{Generalized adjoint importance equation} \quad (5\text{-}20)$$

$$N_{i^-}^* = N_{i^+}^* + \left[\Gamma_i^* \frac{\partial \mathcal{H}}{\partial N_i}\phi_i\right] - \left[P_i^* \kappa \sigma_{fc} \phi_i\right] \qquad \text{Jump condition} \qquad (5\text{-}21)$$

Moreover, for the adjoint composition vector during each time-step:

$$-\frac{\partial}{\partial t}N^* = \mathcal{A}_i^* N^* = (\mathcal{T}_i^* + \mathcal{D}^*)N^* \qquad \text{Adjoint Bateman equation} \qquad (5\text{-}22)$$

The initialization of the adjoint isotopic vector depends on an EoC multiplication factor. The value of this vector therefore cannot be known during the direct depletion calculation. This also applies to P_i^* and Γ_i^*, as they depend on N^*. Hence, after the direct depletion calculation to obtain the quantity of interest, a backward adjoint depletion calculation, following a specific scheme, should be used, as described in the next subsection.

5.2.3. Computational scheme for coupled sensitivities

The first main step is to compute the final multiplication factor. This procedure is performed by the APOLLO3®/MENDEL deterministic scheme presented in 2.1.4 subsection.

Once computed, the sensitivity calculation loop begins by initializing the sensitivity vector with the direct term. By using the (5-2) equation with (5-18), the following can be obtained:

$$S_p^{k_I,SPT} = -pk_I \frac{< \phi_I^*, \frac{\partial \boldsymbol{\mathcal{H}_i}}{\partial \boldsymbol{p}} \phi_I >}{< \phi_I^*, \boldsymbol{\mathcal{F}_I}\, \phi_I >} = -k_I \frac{< \phi_I^*, \boldsymbol{\mathcal{H}_I^p} \phi_I >}{< \phi_I^*, \boldsymbol{\mathcal{F}_I}\, \phi_I >} \qquad (5\text{-}23)$$

With $\boldsymbol{\mathcal{H}^p}$ being the Boltzmann operator, considering only the terms where p appears. It is possible to do so if the parameter p is involved linearly in the operators, which is the case for nuclear data (cross-sections) in the Boltzmann equation. The sensitivities require the adjoint neutron flux at this step, so an adjoint Boltzmann calculation must be carried out upstream.

Then the adjoint isotopic composition has to be initialized. As the dependency in regard to an isotopic composition is the same as the dependency in regard to the cross-sections in the Boltzmann equation, the SPT formula (5-2) can be used with N_I as a parameter:

$$N_I^* = \frac{\partial k_I}{\partial N_I} = -k_I^2 \frac{< \phi_I^*, \frac{\partial \boldsymbol{\mathcal{H}_I}}{\partial \boldsymbol{N_I}} \phi_I >}{< \phi_I^*, \boldsymbol{\mathcal{F}_I}\, \phi_I >} \qquad (5\text{-}24)$$

After initialization at time t_I, backward depletion must be applied to the adjoint composition from t_I to t_{I-1} with the adjoint Bateman equation (5-22). The adjoint Bateman operator used to solve this step must be the adjoint of the Bateman operator (i.e. its transpose) used during the direct depletion of the given time-step, i.e. the one with ϕ_{i-1}. For the depletion matrix, only the scalar flux is needed. It is therefore possible to store it in memory from the direct calculation, in order to save a flux calculation during the process. As the form is similar to the forward Bateman equation, the MENDEL solver can handle such backward depletion. At the end of this depletion step, the adjoint composition vector before the discontinuity is obtained: $N^*_{I-1^+}$.

To continue the backward depletion calculation, the jump condition at t_{I-1} must be respected but knowledge of the adjoint power and the generalized importance is needed. First, both need integration over time data during the backward depletion, respectively:

$$\int_{t_{i-1}}^{t_i} dt N^* \mathcal{A}_{i-1} N$$

$$\int_{t_{i-1}}^{t_i} dt N^* \frac{\partial \mathcal{A}_{i-1}}{\partial \phi_{i-1}} N$$

These integrals are computed numerically by subdividing the depletion step and by using the trapezoidal rule. At the end of the depletion step, it allows the value of the adjoint power to be obtained using the (5-19) formula and the source of the generalized adjoint importance equation (5-20) to be obtained, which needs to be solved to determine Γ^*_{I-1}.

The MINARET solver has been developed to solve the transport equation with a non-null source term, so it can compute the adjoint generalized importance. However, this problem has an infinite number of solutions of the form $\Gamma^*_i + b\phi^*_i$. If an additional orthogonal condition between the adjoint generalized importance and the fission source is imposed[26] ($\langle \Gamma^* + b\phi^*, -\mathcal{F}\phi \rangle = 0$), the value of b can be computed as follows [68]:

$$b = -\frac{\langle \Gamma^* \rangle}{\langle \phi^*, \mathcal{F}\phi \rangle} \tag{5-25}$$

It has to be noted that this step is very RAM-intensive (and time-consuming) as it requires computation and storage of three angular functions (angular neutron flux, angular adjoint neutron flux and adjoint generalized importance).

[26] This specific condition, further explained in [15], comes from the Generalized Perturbation Theory and allows a term to be eliminated in the variation of k in the expression of the GPT functional.

After the unequivocal determination of the generalized adjoint importance, the $N^*_{I-1^-}$ after jump condition can be determined and the sensitivity contribution of the given time-step $\left(\boldsymbol{S_p^{k_I,BPF_i}}\right)$ can be added to the sensitivity vector initialized at time t_I:

$$\boldsymbol{S_p^{k_I,BPF_i}} = \frac{1}{k_I}\left\{\left\langle \int_{t_i}^{t_{i+1}} dt \boldsymbol{N}^* \mathcal{A}_i^p \boldsymbol{N}\right\rangle + \left\langle \Gamma_i^* \mathcal{H}_i^p \phi_i\right\rangle - P_i^* \left\langle p \frac{\partial \kappa\sigma_{fc}}{\partial p} \boldsymbol{N_i} \phi_i\right\rangle\right\} \tag{5-26}$$

This process can be iterated until t_0 to obtain the coupled Boltzmann/Bateman sensitivity of the final multiplication factor $\left(\boldsymbol{S_p^{k_I,DPT}}\right)$, with the parameter p being all the parameters involved in the Bateman operator (fission yields, decay constants and branching ratios), in the $\kappa\sigma_{fc}$ terms (fission energy release and capture energy release) and in the Boltzmann operator (cross-sections). Moreover, the N_0^*- obtained, represents the impact of the initial isotopic composition of each of the isotopes c on the final multiplication factor $\left(\frac{dk_I}{dN_{0_c}}\right)$. With its value, the sensitivities to the initial isotopic compositions can be defined as follows:

$$S_{N_{0_c}}^{k_I,DPT} = \frac{N_{0_c}}{k_I} N_{0_c^-}^* \tag{5-27}$$

The general scheme of all direct and adjoint depletion with production of sensitivities is described in Figure 50. This methodology has been developed and validated against direct parameter perturbation based on the [69] benchmark for LWR and FR cells, upstream of the PhD.

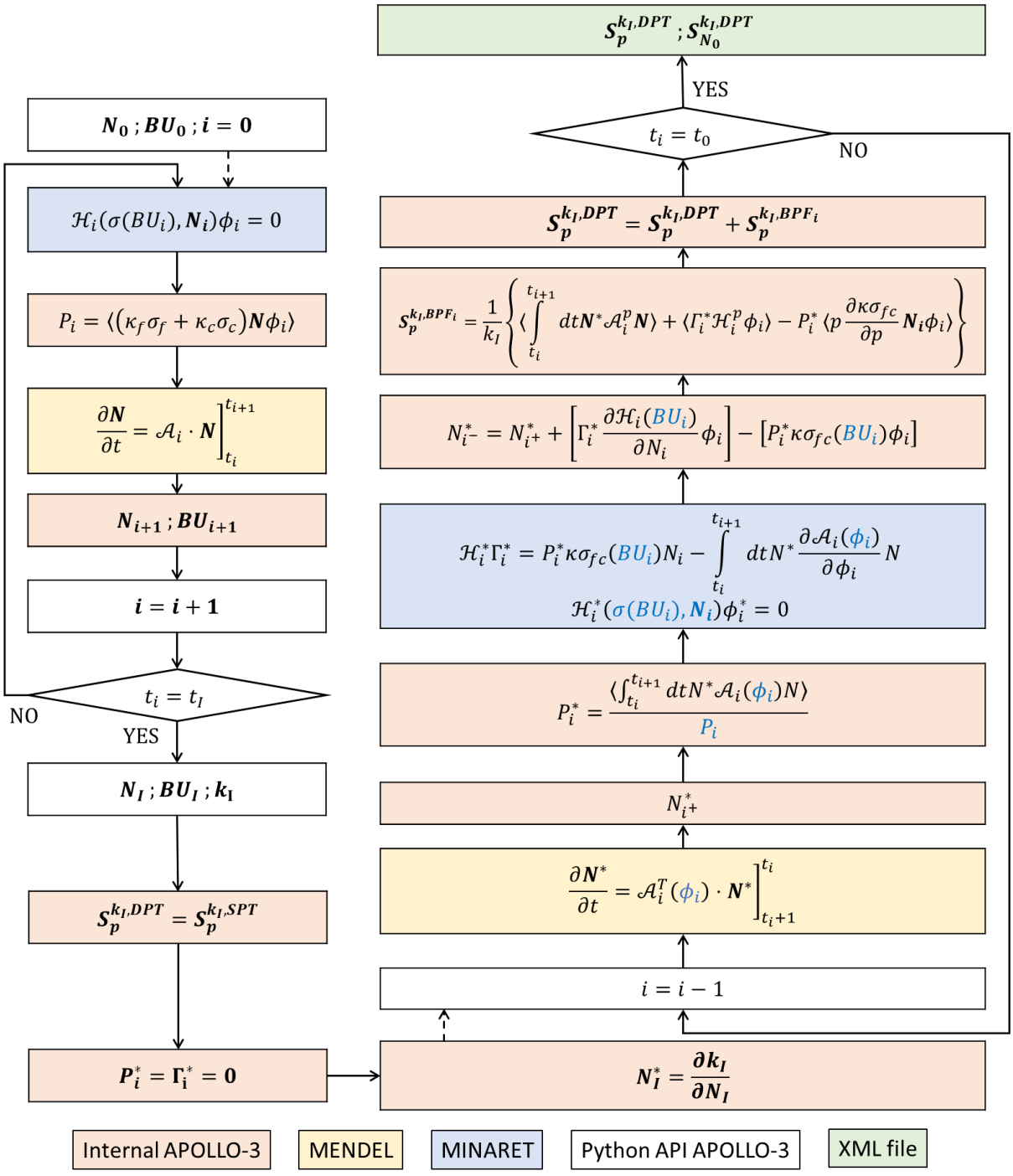

Figure 50. General scheme for direct and adjoint depletion calculation for DPT sensitivity calculation with APOLLO-3®

With this global scheme, sensitivities of the targeted multiplication factor to a nuclear data perturbation starting at time t_0 are obtained. To compute the sensitivity to the same perturbation of the reactivity loss coefficient between two states bounded by fuel depletion, the EGPT can be used as follows:

$$S_p^{\mathrm{RL,DPT_{A\to B}}} = \frac{1}{\rho_B - \rho_A}\left(\frac{S_p^{k_B, DPT_{B\to t_0}}}{k_B} - \frac{S_p^{k_A, DPT_{A\to t_0}}}{k_A}\right) \quad (5\text{-}28)$$

By considering sensitivities from DPT for A and B, all the dependencies in ϕ, $\phi^*$and N are already considered, and considered in the same way (i.e. from t_0 where the perturbation to a parameter starts), so that they can be considered as independent of each other. If the perturbation starts at $t_0 = t_A$, the k_A DPT sensitivity is equivalent to the SPT sensitivity.

However, if $t_0 < t_A$, the backward depletion should be performed until the time where the input data is supposed to be perturbed. For a power reactor, with load management and subassembly shuffling, the beginning of irradiation is not the same for each subassembly (as illustrated in Figure 51). Moreover, the geometry changes with each cycle and *new* subassemblies appear, which can complexify the adjoint depletion.

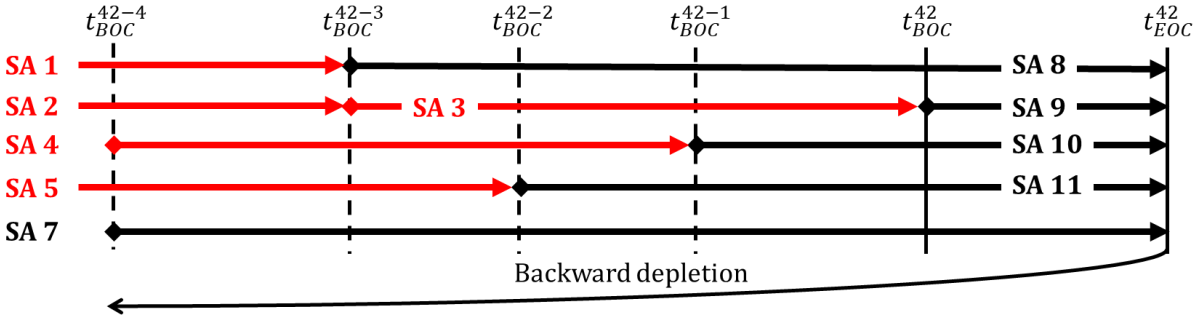

Figure 51. Illustration of backward depletion for power reactor for an initialization at time t_{EOC}^{C} (end of cycle of the cycle C). Black arrows represent the irradiation history of the subassembly present in the cycle C. Red arrows represent the irradiation history of other subassemblies that have common in-core irradiation time with subassemblies in black

5.2.4. Limitations for power reactor experimental application

The DPT sensitivity calculation requires intensive computational power during the adjoint depletion by propagating through time the adjoint isotopic composition vector that is specific to the end of cycle configuration. In a power reactor, the loading plan management implies changing the geometrical configurations of the core. This kind of change would then require projecting N^* into other configurations to continue the adjoint depletion between cycles (described in detail in Appendix H). This type of projection is not achievable yet, but further development in APOLLO-3® could make these projections feasible by being able to interact via the python APOLLO-3® API with the adjoint isotopic composition vector.

Meanwhile, it is possible, as a first approximation, to consider backtracking only from B to A for the coupled sensitivity of the final state B and to compare it with SPT sensitivity of state A as if the perturbation were applied to state A rather than an earlier state (hereinafter referred to as Last Cycle –LC– sensitivities):

$$S_p^{\mathrm{RL,LC_{A\to B}}} = \frac{1}{\rho_B - \rho_A}\left(\frac{S_p^{k_B,DPT_{B\to A}}}{k_B} - \frac{S_p^{k_A,SPT_A}}{k_A}\right) \tag{5-29}$$

The underlying assumption is that the initial isotopic composition of state A is not sensitive to a nuclear data perturbation (i.e. the initial isotopic composition is perfectly known). To propagate a discrepancy between two codes, which starts with the same isotopic composition, this hypothesis is completely valid.

However, for nuclear data uncertainty quantification where the perturbation starts at the beginning of irradiation, the validity of this hypothesis is not guaranteed. To study the impact of such an assumption on the reactivity loss sensitivities, a simple case where it is possible to fully backtrack in time during the adjoint isotopic composition has been studied.

5.3. Partial adjoint depletion implications: application to a fuel sub-assembly

Being able to fully backtrack in time in a simple case implies that it is possible to manage the full irradiation range in a single simple and representative configuration. The Phenix subassembly model considered in section 2.4 for the multiphysics analysis provides the necessary conditions for such a study. For this work, only the 5 MW during 600 days without multiphysics coupling case is considered.

To study the impact of considering a partial irradiation history for the adjoint depletion, the 600 days are divided into 7 irradiation steps with the following boundaries: [0, 20, 100, 200, 300, 400, 500, 600]. From these boundaries, the given sensitivities will be computed (c being the index of the time boundaries in the above list):

- $S_p^{k_c,DPT_{c\to 0}}$
- $S_p^{k_c,DPT_{c\to c-1}}$
- $S_p^{k_c,SPT}$

It will allow a comparison of the Fully Backtracked reactivity loss sensitivities formalism (FB):

$$S_p^{\mathrm{RL,FB_{c-1\to c}}} = \frac{1}{\rho_c - \rho_{c-1}}\left(\frac{S_p^{k_c,DPT_{c\to 0}}}{k_c} - \frac{S_p^{k_{c-1},DPT_{c-1\to 0}}}{k_{c-1}}\right) \tag{5-30}$$

With the partial ones (LC):

$$S_p^{\mathrm{RL,LC_{c-1\to c}}} = \frac{1}{\rho_c - \rho_{c-1}}\left(\frac{S_p^{k_c,DPT_{c\to c-1}}}{k_c} - \frac{S_p^{k_{c-1},SPT_{c-1}}}{k_{c-1}}\right) \quad (5\text{-}31)$$

And with the ones without coupling (EGPT+SPT):

$$S_p^{\mathrm{RL,SPT_{c-1\to c}}} = \frac{1}{\rho_c - \rho_{c-1}}\left(\frac{S_p^{k_c,SPT}}{k_c} - \frac{S_p^{k_{c-1},SPT}}{k_{c-1}}\right) \quad (5\text{-}32)$$

Initially, the most sensitive isotope-reaction pairs for the reactivity loss will be identified and the different contributions between the different terms of the new formalisms will be described in detail. Then, the fully backtracked sensitivities will be compared to the last-cycle ones to determine how they are affected when ignoring past irradiations. Finally, the nuclear data uncertainty will be propagated for both considerations (FB and LC).

5.3.1. Fully backtrack sensitivities

First, the FB formalism (see equation (5-30)) is applied for a hundred-day reactivity loss at a representative burnup (with regards 42nd Phenix cycle). Table XII is obtained for the 21 main contributors. In these 21 contributors:

- 5 contributors (κ_f and fission yield γ) are newly introduced by the DPT;
- 6 contributors with a direct term are significantly affected by the DPT (capture and fission);
- 10 contributors are negligibly affected by the DPT formalism (fission spectrum χ, neutron multiplicity ν, elastic and inelastic scattering).

In a Phenix-like subassembly case analysis, the reactivity loss is mainly sensitive to the reactions of the Uranium-Plutonium chain (^{238}U, ^{239}Pu, ^{240}Pu and ^{241}Pu).
The ^{239}Pu fission has the biggest contributions on each term when considered individually, but they tend to cancel each other out as the physics behind them is opposed:

- **-0.633 %/% for the direct term**. This value reflects the lower impact of the ^{239}Pu fission at the end of irradiation compared to the beginning due to flux redistribution.
- **+1.842 %/% for the Bateman term**. This value reflects the disappearance term of the ^{239}Pu in the Bateman equation. An increase in ^{239}Pu fission increases the ^{239}Pu disappearance and then accentuates the reactivity loss. The same reasoning can be applied to the ^{238}U capture and this explains why its Bateman term is about -1.376 %/%.
- **-0.671 %/% for the Power term**. This value reflects the contribution of this reaction in the flux normalization. Increasing the ^{239}Pu fission reduces the flux normalization constant. Then, reaction rates are reduced for every

isotope, which in turn reduces the reactivity loss as the ^{239}Pu net loss is reduced. This phenomenon is the same for the fission energy release parameter (^{239}Pu κ_f).

- **0.001 %/% for the flux term**. This value is almost negligible for every isotope-reaction pair in that case. It reflects the impact on the flux redistribution (energetically).

For the ^{238}U capture, the contribution is low for the multiplication factor and in the power normalization. Hence, its sensitivity is practically represented only by the Bateman term (see the left subfigure of Figure 52), which is not cancelled by other terms as in the case of the ^{239}Pu fission (see the right subfigure of Figure 52). This specificity implies that the ^{238}U capture is the largest contribution in the reactivity loss sensitivity. The change in order of magnitude and sign, going from a secondary contribution with the direct term to the main contributor with the DPT formalism, demonstrates the importance of considering this latter one for depletion phenomena.

Table XII. Contributors to the most important coupled Boltzmann/Bateman sensitivities (FB) for the reactivity loss between 300 days (37 GWd/t$_{C1}$) and 400 days (49 GWd/t$_{C1}$)

Sensitivities [%/%]	Direct Term (SPT)	**B**ateman	**P**ower	**F**lux	**Total**
^{238}U (n,γ)	0.156	-1.376	-0.021	0.001	-1.241
^{239}Pu κ_f	-	-	-0.672	-	-0.672
^{239}Pu (n,f)	-0.633	1.842	-0.671	0.001	0.539
^{239}Pu $\chi-\nu$	-0.465	-	-	0.000	-0.465
^{239}Pu (n,γ)	-0.022	0.345	-0.006	0.000	0.316
^{241}Pu $\chi-\nu$	-0.197	-	-	0.000	-0.197
^{240}Pu $\chi-\nu$	-0.197	-	-	0.000	-0.197
^{238}U (n,f)	-0.103	0.024	-0.087	0.000	-0.165
^{240}Pu (n,f)	-0.152	0.053	-0.057	0.000	-0.155
^{240}Pu (n,γ)	0.050	-0.192	-0.002	0.000	-0.144
^{16}O (n,n)	0.135	-	-	0.000	0.135
^{238}U $\chi-\nu$	-0.119	-	-	0.000	-0.119
^{238}U κ_f	-	-	-0.087	-	-0.087
^{238}U (n,n')	0.071	-	-	0.000	0.071
^{240}Pu κ_f	-	-	-0.057	-	-0.057
^{241}Pu κ_f	-	-	-0.048	-	-0.048
^{239}Pu:^{105}Ru γ	-	0.047	-	-	0.047

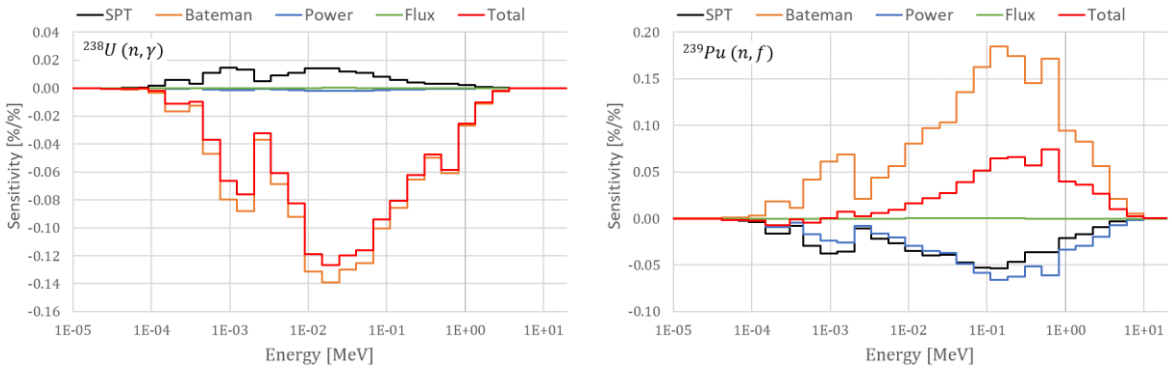

Figure 52. 33g profile of the different term composing the FB sensitivities for the reactivity loss between 300 days and 400 days of irradiation at 5 MW for ^{238}U (n, γ) (left) and ^{239}Pu (n, f) (right)

5.3.2. Partial consideration of the irradiation history

When considering only the last 100-day history for the adjoint depletion rather than the full irradiation history (see equation (5-31)), a difference between the LC and the FB formalism in the order of magnitude of tens of percent for the main contributors is observed (see Table XIII). Such partial consideration has already been briefly discussed in [70] (reactivity loss of large liquid-metal fast breeder reactor with 2D-RZ modeling) and the same trends were observed regarding the sensitivity norm increase for main heavy nuclei reaction.

Table XIII. Comparison of the reactivity loss sensitivities computed with FB and LC for the irradiation between 300 days (37 GWd/t$_{C1}$) and 400 days (49 GWd/t$_{C1}$) at 5 MW

	$S^{RL,FB_{400\to300}}$ [%/%]	$S^{RL,LC_{400\to300}}$ [%/%]	$\frac{S^{RL,FB_{400\to300}}}{S^{RL,LC_{400\to300}}} - 1$ [%]
^{238}U (n,γ)	-1.241	-1.358	9.5
^{239}Pu κ_f	-0.672	-0.758	12.8
^{239}Pu (n,f)	0.539	0.639	18.5
^{239}Pu (n,γ)	0.316	0.409	29.3
^{238}U (n,f)	-0.165	-0.185	11.6
^{240}Pu (n,f)	-0.155	-0.174	12.4
^{240}Pu (n,γ)	-0.144	-0.215	49.0
^{238}U κ_f	-0.087	-0.098	12.6
^{240}Pu κ_f	-0.057	-0.064	12.2
^{241}Pu κ_f	-0.048	-0.053	12.1
^{239}Pu:^{105}Ru γ	0.047	0.047	-0.9

By generalizing the comparison with the rest of the 150 main contributors (see Figure 53 where the difference through time between LC and FB sensitivities has been evaluated

and displayed by sensitivity terms and isotope types), the discrepancy tends to increase with time, but with a different behavior depending on their reaction types:

- For the Bateman term of heavy nuclei capture and fission (top left and top right subfigures in Figure 53), LC sensitivities tend to be overestimated. The discrepancy increases with time within a wide range of rates but in a similar trend.
- For fission and capture energy release (bottom left in Figure 53), which is also the power term of heavy nuclei capture and fission, LC sensitivities are also overestimated compared to FB ones. There is a trend for these terms similar to the Bateman term of heavy nuclei, but within a smaller range. It is explained in that case by the adjoint power that is an integral parameter (i.e. the same for every input parameter). In the Bateman term, the adjoint quantity is specific to each isotope and each evolving subdomain of the geometry.
- For fission yields (bottom right in Figure 53), in contrast, LC globally underestimates the sensitivities. The trends between the different fission yields are similar and the discrepancy tends to saturate with time for most of them.
- For fission product capture, it can be considered that LC sensitivities are similar to FB sensitivities, as all discrepancies are between -1.5% and +0.6%.

Finally, last-cycle sensitivities are able to represent the different specific terms related to the reactivity loss compared to the SPT formalism. However, they are significantly different from FB sensitivities when the irradiation history increases. For a representative Phenix cycle reactivity loss, this implies around 20% overestimations for the main capture and fission reactions and an underestimation of around -10% for the main fission yields.

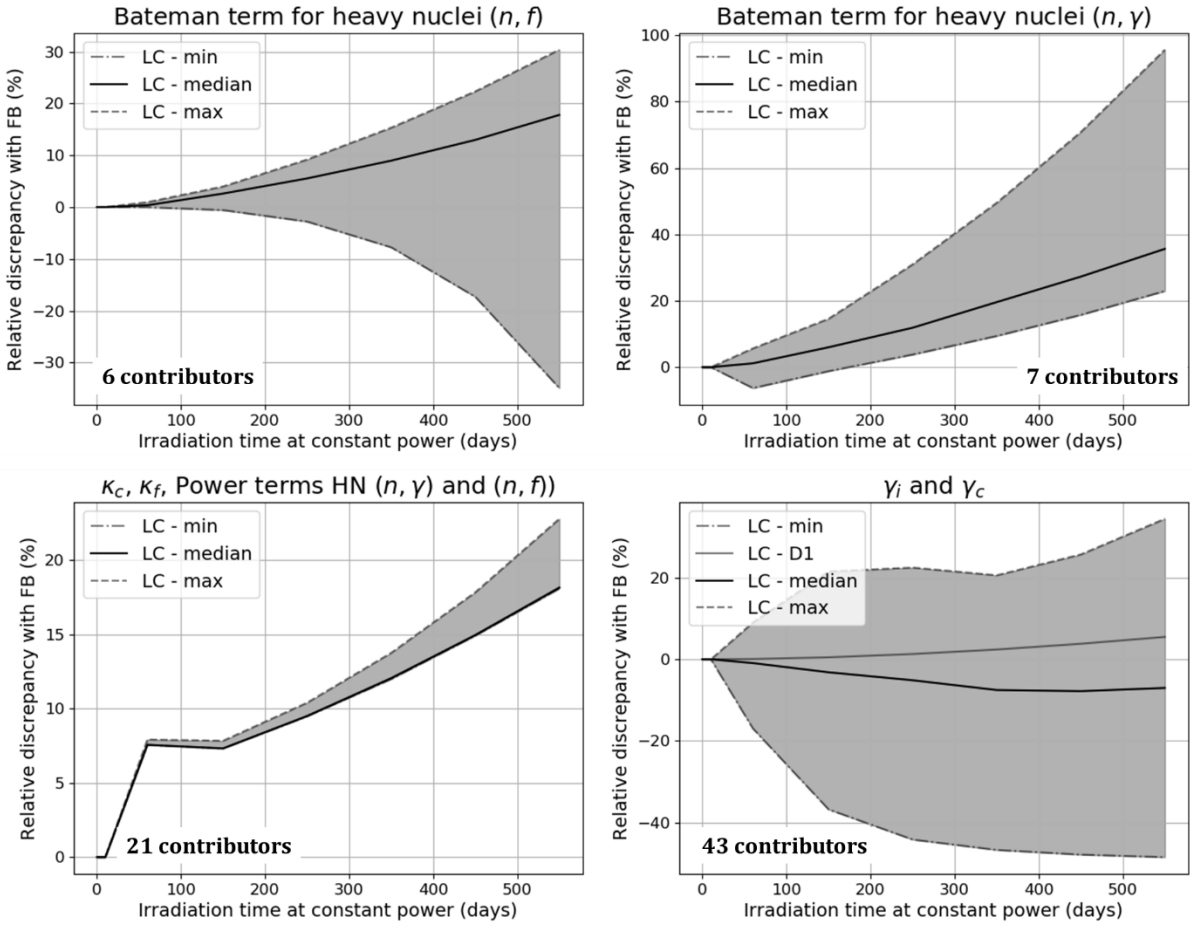

Figure 53. Discrepancy between LC/FB sensitivities of the first 150 contributors depending on their reaction types and sensitivity terms. D1 meaning the 1st decile

Regarding the similar trends of the biases for the different reactions, an ad-hoc burnup-based correction could be imagined in order to rebuild the missing irradiation history in the LC formalism. Meantime, using LC sensitivities instead of FB to calculate reactivity loss sensitivities for the cycle 42 of the Phenix reactor should induce a bias of this order.

5.3.3. Nuclear data uncertainty

With the sensitivity vector computed in the last subsection and with the "sandwich" formula (4-5), the uncertainty due to nuclear data on reactivity loss can be estimated. Considering the COMAC V1 covariance matrix, the Table XIV displays the uncertainty in regards of an isotope-reaction pair computed with correlations. First, it can be seen that the total nuclear data uncertainty on the reactivity loss coefficient is almost constant with time (small increase over time).

Then, the uncertainty is mainly driven by three isotope-reaction pairs that represent 94% of the uncertainty: ^{238}U capture, ^{240}Pu fission and capture. The ^{238}U capture is the main contributor largely because its sensitivity is particularly high (around -1.2 %/%) in the

reactivity loss context. However, the ^{240}Pu fission and capture were respectively in the 6th and 7th rank in terms of sensitivity contribution. This switch in ranking between ^{240}Pu and ^{239}Pu isotopes can be explained by two contributions:

- Uncertainty of ^{240}Pu capture and fission are higher than ^{239}Pu uncertainties as shown in Figure 54;
- Additionally, ^{240}Pu capture and fission are correlated in COMAC V1 whereas ^{239}Pu capture and fission show anti-correlation. These correlations induce an additional uncertainty for the ^{240}Pu capture and fission and mitigate the ^{239}Pu capture and fission uncertainty.

Table XIV. Uncertainty on reactivity loss due to nuclear data for diverse irradiation time with FB sensitivities and the COMAC V1 covariance Matrix

%	^{238}U (n,γ)	^{240}Pu (n,f)	^{240}Pu (n,γ)	^{239}Pu (n,f)	^{239}Pu (n,γ)	^{238}U (n,n')	^{99}Tc (n,γ)	^{238}U (n,f)	^{241}Pu (n,γ)	^{150}Nd (n,γ)	TOTAL
100_200	4.23	2.16	1.70	0.65	0.80	0.69	0.56	0.53	0.47	0.36	**5.34**
200_300	4.34	2.12	1.68	0.73	0.76	0.67	0.55	0.51	0.48	0.40	**5.41**
300_400	4.45	2.07	1.66	0.81	0.71	0.66	0.55	0.49	0.49	0.44	**5.48**
400_500	4.53	2.01	1.62	0.87	0.66	0.65	0.54	0.47	0.50	0.48	**5.52**
500_600	4.60	1.93	1.58	0.93	0.60	0.63	0.54	0.45	0.50	0.52	**5.55**

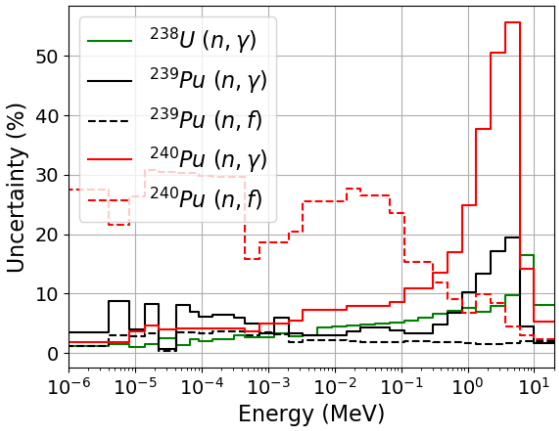

Figure 54. JEFF 3.1.1. uncertainty of the main contributors to the reactivity loss uncertainty

By considering, the sensitivities computed with the partial backtracking (LC), the three main contributors stay the same but the order is changed for some of the secondary contributors as shown in Table XV in the blue columns. Moreover, the trends with irradiation are significantly different. As the discrepancy in sensitivities increases with time between LC and FB, the uncertainty of the contributors rises constantly with irradiation. This implies that the slow variations with time for the total uncertainty is replaced by an increasing uncertainty in irradiation. Nevertheless, by increasing the discrepancy in sensitivities with time for capture and fission of heavy nuclei, such an

approach is a conservative one in the present case (but it raises the question of its generalization to other designs or extension at core scale).

Table XV. Reactivity loss nuclear data uncertainty for different irradiation time with LC sensitivities and the COMAC V1 covariance Matrix

%	^{238}U (n,γ)	^{240}Pu (n,f)	^{240}Pu (n,γ)	^{239}Pu (n,γ)	^{239}Pu (n,f)	^{238}U (n,n')	^{241}Pu (n,γ)	^{99}Tc (n,γ)	^{238}U (n,f)	^{150}Nd (n,γ)	TOTAL
100_200	4.19	2.31	1.90	0.88	0.62	0.68	0.49	0.56	0.57	0.36	**5.45**
200_300	4.51	2.38	2.09	0.91	0.76	0.67	0.54	0.55	0.56	0.40	**5.82**
300_400	4.87	2.46	2.30	0.94	0.91	0.66	0.58	0.55	0.55	0.45	**6.24**
400_500	5.25	2.53	2.52	0.97	1.07	0.66	0.63	0.54	0.54	0.50	**6.69**
500_600	5.67	2.61	2.75	1.00	1.24	0.65	0.69	0.53	0.52	0.55	**7.18**

The COMAC V1 covariance matrix does not cover all the fission product range considered in the depletion chain (in Appendix G is presented each of the isotope-reaction pairs contain in COMAC V1). For them, the hypothesis used in [8] of considering 20% uncertainty for the full energy range of the missing fission product without correlation, is used here and will be called ***FP20***.

This covariance matrix does not cover the nuclear data related to fuel depletion as well, for instance, fission energy release, capture energy release, fission yield, decay constant and branching ratio. For these, the following considerations are taken:

- Fission Yield ($\boldsymbol{\gamma}$): JEFF 3.1.1 uncertainties. To determine correlations, the SANDY code developed at the Belgian nuclear research center SCK-CEN [71] has been used with a methodology and input data provided by Luca Fiorito [72], [73]. It uses JEFF 3.1.1 fission yield data and a Generalized least squares method with five conservation laws/constraints (mass, charge, etc.) further explained in [72].
- Fission energy release ($\boldsymbol{\kappa_f}$): JEFF 3.1.1 uncertainties for ^{238}U, ^{235}U, ^{239}Pu, ^{240}Pu, ^{241}Pu and ^{241}Am without correlations
- Capture energy release ($\boldsymbol{\kappa_c}$): no uncertainties and no correlations
- Branching Ratio ($\boldsymbol{B}$): JEFF 3.1.1 uncertainties with no correlations
- Decay constant ($\boldsymbol{\lambda}$): JEFF 3.1.1 uncertainties with no correlations
- Missing Heavy nuclei (***HN20***): 20% uncertainties with no correlations

The total uncertainty of these new contributors ($\gamma, \lambda, B, \kappa_f$) is about 1.24% (from 1.20% at BoI to 1.28% at EoI). As this is added quadratically, the total uncertainty is increased only slightly. However, updated COMAC V1 brings new significant contributors (see the red rows in Table XVI) that change the contribution order. Regarding the missing fission products and heavy nuclei, their contribution has a minimal impact (0.24%) mainly composed of ^{105}Pd (n,γ) and ^{101}Ru (n,γ) respectively ranking at 44 and 47 of all the contributors (43 first contributors represent 99.2% of the total uncertainty). Thus, the lack of covariances for these isotopes leads, in the Phenix reactor case, to a residual bias

in uncertainty quantification. However, for another SFR where the contribution of fission products to reactivity loss is more significant, this lack of knowledge could result in a larger bias. For this possibility, future work could focus on systematically determining and incorporating the missing fission product covariances (mainly ^{105}Pd (n,γ) and ^{101}Ru (n,γ)) into covariance matrices.

Table XVI. Uncertainty on reactivity loss due to nuclear data between 300 days and 400 days of irradiation at 5 MW with the updated COMAC V1 (for the main contributors representing 99% of the total uncertainty)

	FB Sensitivity [%/%]	FB Uncertainty [%]	LC
TOTAL		5.619	6.364
^{238}**U** (n,γ)	-1.2409	4.448	4.872
^{240}**Pu** (n,f)	-0.1551	2.070	2.461
^{240}**Pu** (n,γ)	-0.1441	1.659	2.300
^{239}**Pu** (n,γ)	0.3161	0.708	0.936
^{239}**Pu** (n,f)	0.5393	0.807	0.912
^{238}**U** (n,n')	0.0711	0.656	0.661
^{239}**Pu:**^{101}**Ru** γ	0.0468	0.594	0.587
^{239}**Pu:**^{107}**Pd** γ	0.0304	0.571	0.584
^{241}**Pu** (n,γ)	0.0343	0.485	0.583
^{99}**Tc** (n,γ)	0.0219	0.547	0.546
^{238}**U** (n,f)	-0.1655	0.494	0.546
^{150}**Nd** (n,γ)	0.0014	0.437	0.448
^{239}**Pu** κ_f	-0.6692	0.367	0.414
^{239}**Pu:**^{153}**Sm** γ	0.0095	0.433	0.397
^{239}**Pu** χ	-0.4653	0.285	0.285
^{240}**Pu** χ	-0.1966	0.273	0.273
^{149}**Sm** (n,γ)	0.0107	0.262	0.257
^{238}**U:**^{135}**I** γ	0.0020	0.252	0.231
^{239}**Pu:**^{109}**Ag** γ	0.0106	0.213	0.216
^{148}**Sm** (n,γ)	0.0003	0.209	0.210
^{154}**Sm** (n,γ)	0.0004	0.194	0.194
^{238}**U:**^{99}**Mo** γ	0.0052	0.188	0.181
^{241}**Pu** χ	-0.1967	0.169	0.169
^{133}**Cs** (n,γ)	0.0196	0.165	0.166
^{239}**Pu:**^{133}**Xe** γ	0.0365	0.172	0.151
^{238}**U:**^{149}**Pm** γ	0.0036	0.132	0.149
^{107}**Pd** (n,γ)	0.0161	0.149	0.148

5.4. Application to the 42th Phenix cycle

In order to compute sensitivity to the 42nd Phenix cycle reactivity loss, two sets of sensitivities have been computed for multiplication factor with the use of the depletion perturbation theory. One at the end of the cycle (i.e. 91 EFPD) and the other one after the neptunium effect at 20 EFPD with the following considerations:

- Both adjoint depletions have been made until the beginning of cycle (0 EFPD)
- Static geometry with control rods at the end of cycle position
- 20 days time steps
- In-core device modeled
- Evolving temperature map computed by GERMINAL V2

Such calculation scheme imply to perform six flux calculations for the direct depletion (14 with the coupling with GERMINAL V2) and six adjoint generalized importance calculations for the adjoint depletion[27]. One flux calculation requires 60 GB RAM memory for an associated calculation time around two hours on a standard working station. Moreover, between the different power steps, the code needs to manage different fields to build the source of the generalized importance equation, compute the different terms of the sensitivities, etc. As the core model contains around 5500 depleting subdomains, these "intermediate" steps represent 2/3 of the total computational time and a large RAM memory usage. Globally, it took around a hundred hours to perform an adjoint depletion from the end-of-cycle to the beginning and the RAM memory usage reached 450 GB.

5.4.1. Reactivity loss sensitivities as a tool for analysis

Using EGPT approximation, coupled sensitivities for reactivity loss of the Phenix cycle 42 can be estimated. These sensitivities and the associated terms allow the various competing phenomena occurring in the reactor to be investigated and quantified, along with their impact on the reactivity loss coefficient (i.e. differential response to the same perturbation between the end and the beginning of cycle multiplication factors).

First, as seen in Figure 55, a spatial redistribution of the neutron flux is observed (decrease in C1 and increase in C2 and fertiles) as well as changes in the neutron spectrum (softening in C1 and C2 and hardening of the flux in fertiles, see Figure 56) during the cycle. These changes directly impact the reactivity loss coefficient as sensitivity to the multiplication factor changes.

[27] With an additional adjoint and direct flux (so three angular functions in total) for the determination of a unique solution to the equation (5-25).

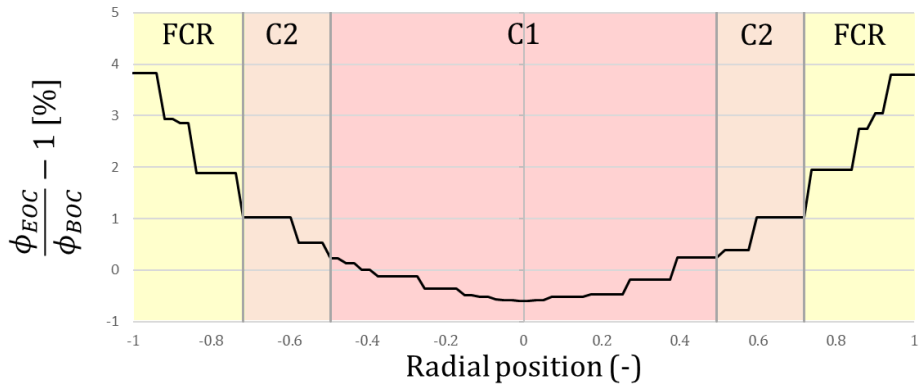

Figure 55. Radial flux redistribution at mid-height between the end and the beginning of the Phenix cycle 42

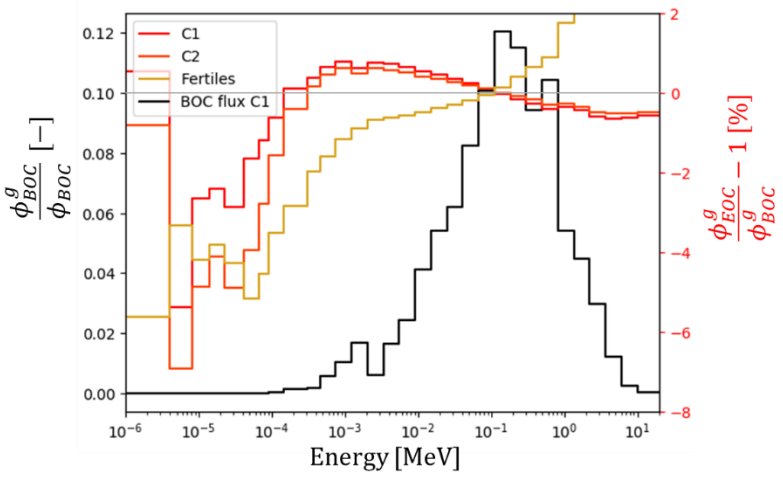

Figure 56. Flux spectrum changes between the end and the beginning of the Phenix cycle 42 for different media

For instance, considering the ^{238}U (n,γ) nuclear reaction, a local increase in neutron capture will tend to decrease the neutron flux locally and thus reduce the multiplication factor. In the C1 medium the scalar flux decreases locally with time (see Figure 55), so that the same perturbation on the ^{238}U (n,γ) cross-section will have a lower impact than at BoC. The ^{238}U (n,γ) sensitivity to the multiplication factor decreases with time so its sensitivity for the reactivity loss (its derivative) is negative, varying inversely with C2 where the scalar flux increases. This will imply an increasing sensitivity to the multiplication factor with time, which leads to a positive sensitivity to the reactivity loss (direct terms of the two first rows of Table XVII).

This simple reasoning does not take account of the other contributors due to the spectrum change neither the complex spectrum change due to any perturbation, but it does illustrate the phenomenon that can be highlighted by perturbation theory (direct column in Table XVII). Nevertheless, as presented in previous sections, other phenomena are also affecting the reactivity loss coefficient.

The main contributor for reactivity loss in Phenix cycle 42 is the changes over time in ^{239}Pu's net balance with time in the C1 medium (more generally changes in fissile material). Even if C1 and C2 are almost equally involved in power generation, the higher enrichment in C2 subassemblies leads to a ^{239}Pu-"burner" behavior. At the beginning of the cycle, the reaction rate ratio between ^{238}U capture and ^{239}Pu absorption is around 0.5 for C2. In C1, this ratio rises to 0.7 so that the ^{239}Pu is better regenerated, which strongly links the ^{238}U and ^{239}Pu in this zone. As ^{239}Pu has the largest impact on the multiplication factor for C1 compared with C2, ^{238}U capture and ^{239}Pu absorption will have a larger impact on the reactivity loss coefficient in C1 than in C2 (the sensitivity to the ^{238}U and ^{239}Pu isotopes are 2.5 times larger in C1 than in C2, see Table XVIII).

This effect is quantified by the Bateman term in the DPT formalism and can be seen for ^{238}U (n,γ) and ^{239}Pu (n,f) in C1 and C2 in Table XVII.

Table XVII. 42nd Phenix cycle reactivity loss one group sensitivities integrated over the different media and BPF terms

Sensitivity [%/%]		Direct (SPT)	**B**ateman	**P**ower	**F**lux	**Total**
^{238}U (n,γ)	C1	-0.025	-1.141	-0.007	0.000	-1.173
	C2	0.071	-0.370	-0.005	0.000	-0.304
	Fertiles	0.150	-0.247	-0.016	0.000	-0.113
^{239}Pu (n,f)	C1	-0.035	1.477	-0.315	0.000	1.127
	C2	-0.314	0.655	-0.290	0.000	0.051
	Fertiles	-0.283	0.022	-0.039	0.000	-0.300
^{239}Pu (n,γ)	C1	-0.046	0.305	-0.003	0.000	0.257
	C2	0.004	0.124	-0.002	0.000	0.125
	Fertiles	0.026	0.007	-0.001	0.000	0.033

Table XVIII. BoC multiplication factor sensitivities to the isotopic composition integrated over the different media (computed with SPT)

Sensitivity [%/%]	^{238}U	^{239}Pu	^{240}Pu	^{241}Pu	Other HN	FP
C1	-0.080	0.293	0.015	0.021	0.007	-0.016
C2	-0.028	0.186	0.012	0.013	0.003	-0.007
Fertiles	-0.015	0.009	0.000	0.000	0.003	0.000

Furthermore, while Bateman's term sees the impact of a perturbation via local reaction rate ratios, the Power term sees the impact of a perturbation via the reaction rates involved in power normalization. Since the power generated in C1 and C2 is practically identical, a perturbation on a fission cross-section or a fission kerma applied in C2 is approximately identical to C1. Thus, an increase in the fission cross-section of ^{239}Pu, for example in C2, implies a lower normalization constant, which therefore decreases the flux norm and the reaction rates throughout the core. As a reduction in the overall reaction

rates results in losing less fissile material, this implies that less reactivity is lost (negative contribution).

With all the terms, it is possible to understand that the impact of a perturbation in the fission cross-section of ^{239}Pu in C2, which seems to be negligible, is actually due to local and global compensations with C1. This can be used to illustrate and quantify the interdependencies between the different regions of the core during fuel depletion in regard to the reactivity loss.

The limitations of the SPT for fuel depletion analyses were known in the past and integrated parameters were produced to provide comprehensive analyses of the various phenomena occurring during fuel depletion. They include, for instance, coupling coefficients between different media, breeding gain coefficient, ^{239}Pu equivalent quantity among others [43]. The main limitations of such coefficients are that coupled terms between phenomena are hardly taken into account. DPT sensitivities therefore offers a generalization, in a single formalism, of the different phenomena affecting a given quantity of interest and their coupled terms. In the DPT formalism, the weights of these coupled terms are integrated into the "flux term" via the generalized importance equation.

It represents how much a nuclear data perturbation would affect the direct depletion calculation, which would, in return, affect the spectrum redistribution. In this reactivity loss studied here, this term is negligible (see Table XVII). This means that the spectrum change (energy redistribution) presented in Figure 56 would not be significantly impacted by an initial perturbation on nuclear data that would be transmitted in the isotopic composition during the fuel depletion process. It could be explained by a relatively constant spectrum with depletion at core scale (contrary to LWR for which spectrum changes with ^{239}Pu build-up).

Finally, the understanding of the different phenomena involved in the Phenix reactor could be provided by an integral coefficient computed with direct calculation, as they are not significantly coupled. The depletion perturbation theory, by generalizing such a coefficient, also contributes to an understanding of the different mechanisms involved and to quantification of the different contributors and their interactions, which were hardly accessible before. It therefore allows the quantification of the nuclear data uncertainty to be approached with confidence.

5.4.2. Reactivity loss uncertainty due to nuclear data and its limitations in operation condition

With sensitivities presented in Table XIX and the COMAC V1 covariances matrix, the total JEFF 3.1.1 nuclear data uncertainty for the Phenix reactivity loss can be quantified and is estimated at 6.94%. Beside covariances from the cross-section included in COMAC V1,

other nuclear data have to be considered for the reactivity loss uncertainty, such as fission yield, energy release, decay constant and branching ratio. In the Phenix reactor, the reactivity loss is mainly caused by heavy nuclei so that the main contributors to the uncertainty are due to heavy nuclei (see Table XX). However, some fission yield values such as ^{239}Pu:^{107}Pd and ^{239}Pu:^{101}Ru are among the top ten contributors. Thus, systematically incorporating this type of data into the covariance matrices would lead to a more consistent estimation of the uncertainty.

Table XIX. Sensitivity and nuclear data uncertainty with COMAC V1 for the 42nd Phenix cycle reactivity loss (contribution separated in BPF terms[28])

	RL SA C1 300→400	Reactivity loss Phenix cycle 42					
	LC Sensitivity [%/%]	1 group Sensitivity [%/%]					Uncertainty [%]
		Direct (SPT)	**B**ateman	**P**ower	**F**lux	Total	
^{238}U (n,γ)	-1.358	0.196	-1.765	-0.028	0.000	**-1.579**	**5.666**
^{240}Pu (n,γ)	-0.215	0.039	-0.254	-0.002	0.000	**-0.216**	**2.261**
^{240}Pu (n,f)	-0.174	-0.153	0.050	-0.056	0.000	**-0.157**	**2.247**
^{239}Pu (n,f)	0.639	-0.632	2.163	-0.646	0.000	**0.879**	**1.295**
^{239}Pu (n,γ)	0.409	-0.016	0.438	-0.006	0.000	**0.408**	**0.848**
^{238}U (n,n')	0.071	0.087	-	-	0.000	**0.087**	**0.795**
^{238}U (n,f)	-0.185	-0.133	0.018	-0.107	0.000	**-0.219**	**0.652**
^{241}Pu (n,γ)	0.041	0.005	0.034	0.000	0.000	**0.038**	**0.558**
^{239}Pu:^{107}Pd γ	0.031	-	0.027	-	-	**0.027**	**0.507**
^{239}Pu:^{101}Ru γ	0.046	-	0.040	-	-	**0.039**	**0.499**
^{99}Tc (n,γ)	0.022	0.021	-0.002	0.000	0.000	**0.019**	**0.471**
^{150}Nd (n,γ)	0.001	0.001	0.000	0.000	0.000	**0.001**	**0.417**
^{239}Pu:^{153}Sm γ	0.009	-	0.008	-	-	**0.008**	**0.364**
^{239}Pu χ	-0.465	-0.490	0.000	0.000	0.000	**-0.493**	**0.349**
^{239}Pu κ_f	-0.755	-	-	-0.623	-	**-0.623**	**0.327**
^{240}Pu χ	-0.197	-0.188	-	-	0.000	**-0.187**	**0.284**
^{240}Pu (n,n')	0.006	0.005	-	-	0.000	**0.005**	***i*0.272**
^{238}U:^{135}I γ	0.002	-	0.002	-	-	**0.002**	**0.226**
^{148}Sm (n,γ)	0.0003	0.0003	0.0000	0.0000	0.0000	**0.0003**	**0.208**
^{149}Sm (n,γ)	0.011	0.012	-0.003	0.000	0.000	**0.008**	**0.205**

[28] It should be noted that the different terms B, P, and F are not obtained by storing them individually (which is not possible yet with APOLLO3®) when generating sensitivities, but rather by performing three separate adjoint evolutions. The first evolution considers only the Bateman terms, the second includes both the Bateman and Power terms, and the final evolution incorporates all terms. Each individual term is then derived from the differences between these results. This method provides an approximation of the different terms, which means their sum may not necessarily equal the total sensitivity (calculated more accurately). However, as can be observed, this approach remains a very good approximation, offering valuable insights into the various phenomena for physical analysis.

^{239}Pu:^{109}Ag γ	0.011	-	0.009	-	-	**0.009**	**0.186**
^{238}U:^{99}Mo γ	0.005	-	0.005	-	-	**0.005**	**0.177**
^{241}Pu χ	-0.197	-0.172	-	-	0.000	**-0.169**	**0.174**

Table XX. Uncertainty breakdown of the 42nd cycle Phenix reactivity loss depending on the type of nuclear data

Nuclear data	Uncertainty [%]
COMAC V1	**6.943**
Former COMAC V1	6.856
FP20	*0.191*
HN20	*0.067*
γ	1.019
$B - \lambda$	0.016
κ_f	0.343

As has been seen in the previous section, choosing not to consider the irradiation history has an impact on the sensitivities that needs to be addressed. In the 42nd cycle only 1/6 of fissile subassemblies are fresh fuel at BoC, with the remaining ones having been irradiated already with various SA irradiation histories. Hence, the computed sensitivities are between the last-cycles (LC) and fully backtracked (FB) configurations depending on the subassembly. If the global initial burnup and the burnup variation in cycle 42 are compared with the subassembly case, this reactivity loss cycle is similar to the subassembly reactivity loss between 300 days and 400 days.

The core configuration is significantly more complex than a subassembly in an infinite lattice. With two types of fuel, fertile blankets, in-core devices, control-rods, etc. Yet, both sets of sensitivities are in the same order of magnitude as shown in Table XIX and globally maintain the same order and ratios between the different contributors. In the subassembly case studied, it has been seen that sensitivities with partial backtracking were overestimated for heavy nuclei. Knowing the similarities between sensitivities of both cases, it is assumed, as a first approximation, that the conservativeness regarding heavy nuclei is conserved. With such an assumption, the uncertainty due to nuclear data for the reactivity loss coefficient of cycle 42 can be considered as conservative, but calls for confirmation of this result with fully backtracked sensitivities or more detailed studies on the origin of the bias between LC and FB sensitivities.

5.4.3. APOLLO3®/MENDEL decomposition bias with coupled sensitivities

In the section of Chapter 4 related to bias decomposition, the APOLLO3®/MENDEL scheme bias has been estimated and summarized for the main isotope-reaction pairs in Table X.

Firstly, to propagate the initial bias on the reaction rates to the reactivity loss coefficient, the Boltzmann/Bateman coupled sensitivities can be used. Sensitivities to the reaction rates are required to perform such propagation. However, only cross-sections sensitivities are available. Both are not equivalent, as a change in cross-section would induce a flux redistribution and a spectrum change, which would also affect the reaction rates. In subsection 5.4.1, it has been shown that the neutron spectrum and the flux are slightly affected during irradiation, as evidenced by a negligible flux term in the coupled Boltzmann/Bateman sensitivities. Hence, to the first order, cross-section sensitivities can be considered equivalent to reaction rate sensitivities for performing such bias propagation in this case.

Secondly, biases on the reaction rates have been estimated with TRIPOLI-4® based on the same isotopic compositions. Therefore, the propagation of this bias must be carried out as if isotopic compositions were perfectly known. This assumption was the one made with the "last-cycle" sensitivities. Table XXI summarized the LC sensitivities per medium, which will propagate the biases of Table X.

Thirdly, using sensitivities to propagate the initial reaction rate biases with the formula (4-2) implies a consideration that the bias is constant during irradiation. As the flux spectrum of the Phenix reactor is only slightly sensitive to fuel depletion, it may be considered with confidence that the bias should be affected negligibly.

Finally, it provides a propagated bias on the reactivity loss coefficient of -0.83%. It means that if the APOLLO3®-FR scheme is improved, so that the discrepancy with TRIPOLI-4® vanishes, the reactivity loss coefficient would be +0.83% higher. This would give a C/E of around +0.96% instead of +0.13%.

Table XXI. Reactivity loss sensitivity per fissile/fertile medium of the main isotope-reaction pairs for cycle 42

$S_\alpha^{\sigma,m}$ [%/%]	^{238}U		^{239}Pu		^{240}Pu		^{241}Pu	
	(n,γ)	(n,f)	(n,γ)	(n,f)	(n,γ)	(n,f)	(n,γ)	(n,f)
C1	-1.160	-0.057	0.250	1.118	-0.162	-0.071	0.026	0.041
C2	-0.299	-0.078	0.123	0.053	-0.054	-0.084	0.012	-0.017
FCAI	-0.024	-0.014	0.009	-0.066	0.000	-0.001	0.000	0.000
FCAS	-0.002	-0.001	0.000	-0.005	0.000	0.000	0.000	0.000
FCR	-0.087	-0.067	0.023	-0.229	0.000	-0.001	0.000	0.000

The propagated bias is in the same order of magnitude of other important modeling parameter as the multiphysics coupling (subsection 4.2.5) or control rod depletion (subsection 4.2.4). It therefore remains relatively small compared to the experimental uncertainty. However, in the context of VVUQ of SCTs towards fuel depletion, the difference observed in the biases between the reactor under operating conditions and the

Phenix-like configuration must be investigated (quantifying the impact of all the differences with the Phenix-like model: heterogeneous MOX fuel, in-core experiments, hot temperature, etc).

Moreover, the quantification of the APOLLO3®/MENDEL bias is possible using Boltzmann/Bateman coupled sensitivities. Yet, these sensitivities are calculated using the same tools, the same biases and in a configuration that has been identified in Chapter 4 as leading to biases during fuel depletion (static control rod). This, a fortiori, necessarily implies a bias in sensitivities that can hide compensations. The sensitivity of these sensitivities to scheme bias is a question that will need to be addressed in future in-depth work and validation. However, given the similar results with the subassembly case, which represents less complex conditions for the calculation scheme, it can be considered that the impact of the different biases seems sufficiently low to conserve the trends and the order of magnitude.

5.5. Conclusion

A deeper understanding of the reactivity loss (or any quantity of interest occurring during irradiation) requires a specific formalism called Depletion Perturbation Theory, which has been presented with the related computational scheme to perform such a calculation using APOLLO3®/MENDEL.

This formalism provides additional tools to assist in comprehending the different phenomena and to quantify their impact on the reactivity loss with sensitivities to nuclear data. These sensitivities have allowed estimation of the numerical bias of the APOLLO3®/MENDEL scheme, which remains controlled below 1%. It has also been possible to estimate the JEFF 3.1.1 nuclear data uncertainty for the reactivity loss of Phenix cycle 42, which is 6.94% compare to 1.97% for previous estimation without the depletion perturbation theory.

Using these sensitivities in operation condition with the current implementation of the method has been identified as having limitations regarding the irradiation history, which cannot be taken into account. This limitation has been quantified on a simplified case for a Phenix subassembly. In this configuration, not considering the irradiation history resulted in an overestimation of the heavy nuclei capture and fission sensitivities and an underestimation of the fission yield ones. This produced a conservative nuclear data uncertainty quantification for the heavy nuclei that represent the great majority of the uncertainty in JEFF 3.1.1. Given the similarities between the subassembly case and the core case, the conservatism can be extended to the experimental core condition studied. Therefore, 6.94% can be considered as a conservative value for the nuclear data uncertainty of the 42nd cycle Phenix reactivity loss.

The analysis of the reactivity loss of Phenix cycle 42 with APOLLO3®/MENDEL has shown that the uncertainty due to JEFF 3.1.1 nuclear data was significantly greater than the experimental uncertainty and the numerical bias. The main challenge therefore lies in reducing the uncertainty of the nuclear data. However, reducing the uncertainty of such a general-purpose database is technically and experimentally costly. Since the nuclear database used is not the most recent one, future work could be conducted with new libraries such as JEFF 4 to assess the associated uncertainty reduction. In the meantime, since the Phenix reactivity loss experimental uncertainty is lower, it could be investigated with the aim of using this information to constrain and reduce the nuclear data uncertainty through data assimilation.

Chapter 6. Integral data assimilation perspectives

Chapter 6. Integral data assimilation perspectives 146
6.1. Introduction 147
6.2. Data assimilation principles 148
6.3. Synthesis of data assimilation input data for Phenix reactivity loss 149
6.4. Data assimilation based on the Phenix reactivity loss 151
6.4.1. C/E influence on IDA 155
6.4.2. Influence of considering biased sensitivities 156
6.4.3. Prior covariances impact on IDA 158
6.5. Application of posterior nuclear data to other experiments 161
6.6. Conclusion 166

Summary - Data assimilation based on the Phenix cycle reactivity loss coefficient can help to reduce this uncertainty and provide nuclear data in line with this experiment. An exploratory exercise was then undertaken using a simple model to identify the main trends of such a process. The main impact of data assimilation with the Phenix reactivity loss experiment is to reduce the uncertainty via new correlations (low corrective factors and low variance reduction). To perform data assimilation process with the Phenix reactivity loss information, posterior nuclear data and covariances have been applied and produced with a set of other experiments available with various representativities. This has shown that no inconsistencies with posterior C/E and uncertainties were produced and that the potential use of such experiments for the production of engineering libraries should be studied in depth in a dedicated work with larger experimental databases and more advanced methods.

Objectives

- Study the behavior of nuclear data assimilation with the reactivity loss information
- Determination of the potential of such an exercise for innovative concepts today

Highlights

- Uncertainty reduction bring mainly by new correlations
- Reactivity loss can provide a new type of information for engineering library

6.1. Introduction

In the previous chapter, the uncertainty due to nuclear data of reactivity loss was estimated to be around 7%. In a design approach, this uncertainty level regarding the reactivity loss coefficient implies having the same uncertainty for the cycle duration, the amount of fissile material required at the beginning of the cycle, and the weight of the control rod used to compensate for the reactivity loss. As any change in fuel content may also change the values of core feedback coefficients, this uncertainty level have a significant impact on both the reactor techno-economically along with its safety. Thus, reducing the uncertainty coming from nuclear data is therefore of prime interest to comply with forseen margins associated with these different aspects.

The production of general-purpose libraries is a process that requires heavy efforts in a (very) wide variety of energy domains, isotopes, and reactions, as well as theoritcal nuclear models. Moreover, even today, some reactions may still exibit deficiencies, as it is the case for the JEFF 3.1.1 data for ^{235}U (n,γ) [74]. Thus, the time needed to detect inconsistencies in nuclear data, combined with the time needed to create and produce new experiments (with a limited number of facilities), implies a slow deployment of new general-purpose libraries and, therefore, a slow reduction in nuclear data uncertainties for neutronics coefficients, including reactivity loss. Currently, joint efforts have been made to identify the needs in terms of uncertainties requirements [75] and for prioritizing some specific nuclear data to be improved [76] to accelerate and optimize this process.

In parallel and in support to this prupose, integral experiments in well-managed conditions (mainly critical experiment as JEZEBEL for instance) are often used to gain feedback on nuclear data. In addition, it can potentially help to constrain the nuclear data to reduce their uncertainties through integral data assimilation when the nuclear data uncertainty is larger than every other sources of uncertainty.

The use of integral data in a Bayesian frame is manyfold. Inherent feedback on nuclear data can help identifying inconsistencies in order to focus on new experiment designs in order to specifically target some isotopes and reactions in the desired energy range. It can be used to calibrate covariance data for design purpose or alternatively create an adjusted nuclear data library as it was done in the past for the Superphenix reactor with ERALIB1 [77]. This latter case is not the mainstream solutions nowadays as designs studies are still investigating core concepts for GEN-IV reactors items. The present study aims to see how reactivity loss data from Phenix reactor can be used to improve knowledge on nuclear data from a general point of view. The use of Boltzmann/Bateman coupling gives rise of additional nuclear data related to depletion and a first glance of what it means for data assimilation is proposed.

6.2. Data assimilation principles

A data assimilation process based on an integral experiment aims to find the combination of input parameters, along its covariances, that fit with the experimental distribution (average value and standard deviation):

$$\frac{C(p_{posterior})}{E} = 1 \tag{6-1}$$

$$\Delta C_{ND}^{posterior} = \sqrt{S^T M^{posterior} S} \leq \Delta E \tag{6-2}$$

With $p_{posterior}$ the set of parameters that allow for obtaining of the correct computed value after data assimilation, $M^{posterior}$ the covariance matrix that allows nuclear data uncertainty after data assimilation equals to the experimental value. However, this process needs to meet the physical constraints behind the different parameters. In other words, the input data cannot be freely changed and the process must follow the initial correlations between the parameters, as quantified in the *a priori* covariance matrix (M^{prior}). To adjust the a priori parameter to the experimental distribution and incorporate the knowledge of the new experimental data into the input data, the main classical way is to use Bayesian inference [78]. This method consists of considering the Bayes theorem as a starting mathematical paradigm:

$$p_r(\vec{x}|\vec{y}, U) = \frac{p_r(\vec{x}, U) \cdot p_r(\vec{y}|\vec{x}, U)}{\int p_r(\vec{x}, U) \cdot p_r(\vec{y}|\vec{x}, U) d\vec{x}} \tag{6-3}$$

With $p_r(\vec{x}, U)$, the distribution of the computed value with the parameters $\vec{x}$ knowing the *a priori* knowledge U (prior distribution); $p_r(\vec{y}|\vec{x}, U)$, the likelihood representing the probability that the *a priori* computed distribution fits with the added experimental set $\vec{y}$; and $p_r(\vec{x}|\vec{y}, U)$ the distribution of the computed value knowing the broader experimental set composed of U and $\vec{y}$ (posterior distribution). This can be summarized as follows:

$$posterior \propto prior \cdot likelihood \tag{6-4}$$

To determine the *a posteriori* distribution, various methods exist, depending on the types of data considered, set out in [78] for the nuclear data scope. In this work, the adjusted data are the JEFF 3.1.1 nuclear data used for the integral experiment calculation (33g cross-sections, fission yields, fission energy release, decay constant and branching ratio) with their uncertainties described by the "updated" COMAC V1 presented in the last chapter. This exercise is therefore limited to a deterministic algorithm based on the Generalized Least Square methodology (GLS) which consists of minimizing the following cost function [79]:

$$\chi^2_{GLS} = \left(\vec{p} - \vec{p}_{prior}\right)^T M^{-1} \cdot \left(\vec{p} - \vec{p}_{prior}\right) + \left(\vec{C}(\vec{p}) - \vec{E}\right)^T \cdot M_E^{-1} \cdot \left(\vec{C}(\vec{p}) - \vec{E}\right) \quad (6\text{-}5)$$

With a first order approximation for the computed value (i.e. with sensitivities):

$$C(p_1, p_2, \dots, p_N) = C_{prior} \cdot \left(1 + \sum_{i \in [i,N]} S^C_{p_i} \frac{p_i - p_{i,prior}}{p_{i,prior}}\right) \quad (6\text{-}6)$$

The underlying assumption in considering this cost-function is that the prior and likelihood distributions follow the normal distribution (maximum Shannon entropy principle [80]) and that the resulting posterior distribution can be approximated to a normal distribuion if χ^2_{GLS} is minimal (Laplace approximation [81]).

To determine the posterior distribution, the cost-function should therefore be minimized. To achieve this, the CONRAD code is used [82]. This code has mainly been developed for nuclear data evaluation based on experimental data and theoretical nuclear models. In a model called 'IDA_model', it is possible to use the generalized chi-square minimization features of CONRAD with sensitivities for integral data assimilation. The minimization is then performed with the following equations (fully developed in [79]):

$$M^{post} = \left[M^{prior^{-1}} + G^{C^T} \cdot M_E^{-1} \cdot G^C\right]^{-1} \quad (6\text{-}7)$$

$$\vec{p}_{post} = \vec{p}_{prior} + M^{post} \cdot \ G^{C^T} \cdot M_E^{-1} \cdot \left[\vec{E} - \vec{C}\left(\vec{p}_{prior}\right)\right] \quad (6\text{-}8)$$

$$G^C_p = \frac{\partial C}{\partial p} = \frac{C}{p} S^C_p \quad (6\text{-}9)$$

With M_E , the experimental covariance matrix (i.e. experimental uncertainties and covariances of the different integral experiments considered for IDA).

6.3. Synthesis of data assimilation input data for Phenix reactivity loss

In the last section, a brief presentation of the formalism used for IDA with CONRAD was presented. To perform such a process for the Phenix reactivity loss as an integral experiment, the following data are required:

- **Integral experimental value with its associated uncertainty**: In Chapter 3, the experimental value of the 42nd Phenix cycle reactivity loss has been reinterpreted using modern tools. The updated value is then estimated to **-4.644 ¢/EFPD** and the uncertainty associated with this value is **1.5%** without considering the power uncertainty. The uncertainty for the power

needed for the normalization process is not well known but a **conservative value of 3%** has been considered, which brings the uncertainty to **3.35%.** This assumption will be discussed in the following sub-sections.

- **Prior calculated value**: In Chapter 4, the best estimate modeling of the 42nd Phenix cycle reactivity loss gives **-4.650 ¢/EFPD** (**+0.13%** compared with the experimental value). The main bias identified in the modeling is from the APOLLO3®/MENDEL deterministic scheme, which has been quantified around **-0.83%**.
- **Sensitivities related to the phenomenon**: Sensitivities related to reactivity loss follow a specific formalism (DPT), presented in Chapter 4. However, in operation condition of Phenix cycles and the current implementation in APOLLO3®, the previous irradiation history cannot be taken into account. Only "last-cycle" sensitivities have been evaluated but the different bias of such an approach has been estimated. Moreover, to compare the calculation with the experiment, it was necessary to calculate the β_{eff}, which also depends on nuclear data. These sensitivities due to nuclear data must therefore be included in the sensitivity vector of the calculated value (described in Appendix I). In addition, the calculated value also depends on the core power level for the flux normalization so that the calculation has its own sensitivity to this parameter. The sensitivity has been quantified (**0.919 %/%**) and is added to the sensitivity vector.
- **Prior covariance matrix**. For the nuclear data library JEFF 3.1.1 used in this work, the related covariance matrix is named COMAC V1. In subsection 5.3.3, it has been shown that some isotope-reaction pairs are not represented in this previous version of such matrix. Hence, new variances and associated correlations have been added to this covariance matrix (power uncertainty and data related to depletion chain).

The first exercise is to perform an integral data assimilation to get the trends for corrective factors, posterior uncertainties and correlations. However, for the IDA process to be reliable, the input data should also be reliable. A sensitivity analysis will therefore be carried out to study the impact of the different limitations on reactivity loss sensitivities (LC instead of FB) and a biased prior computed value (APOLLO3®/MENDEL scheme bias). Additionally, the impact of correlations on the covariance matrix is investigated, in order to analyze its sensitivity to the IDA.

Moreover, the impact of the posterior corrective factors and covariances could be assessed on other integral coefficients from other experiments to quantify the uncertainty reduction from reactivity loss assimilation.

6.4. Data assimilation based on the Phenix reactivity loss

Before performing the data assimilation process with CONRAD, the input nuclear data must be selected. The total number of isotope-reaction pairs contained in the COMACV1 covariance matrix is 3516 for a total number of parameters of 36759. As the determination of the posterior covariance matrix requires a matrix inversion, the simulation time becomes prohibitive for this number of parameters. For this first stage, the 80 main contributors to total uncertainty (99.9% of total uncertainty) are retained, which gives 1678 parameters to be adjusted. As uncertainty on core power was introduced in the experimental value, this parameter is also identified as "uncertain" and is to be taken into account in the assimilation process.

As the calculation discrepancy with experiment is significantly smaller than the experimental uncertainty, the corrective factors obtained from the data assimilation are negligible. The main relevant corrections for the main contributors for multi-group cross-sections are below 0.356%, as shown in Table XXII for ^{240}Pu (n,γ), ^{240}Pu (n,f), ^{238}U (n,n') and ^{238}U (n,γ) and are significantly lower than the initial uncertainty.

In Table XXII, it is shown that the largest corrective factors are obtained for secondary contributors ^{148}Sm (n,γ), ^{150}Nd (n,γ), ^{154}Sm (n,γ) and ^{114}Cd (n,γ), which have a negligible impact on the discrepancy with the experiment. However, these corrective factors occur in energy groups where the uncertainty rises up to more than 1000%.

Table XXII. Corrective factors and uncertainty reductions obtained with data assimilation of the Phenix reactivity loss

	Largest multigroup corrective factor [%]	Posterior uncertainty [%] (for the energy group with the largest uncertainty reduction)	Prior uncertainty [%]
^{240}Pu (n,γ)	0.356	51.7	55.6
^{240}Pu (n,f)	0.170	25.9	27.7
^{238}U (n,n')	0.084	10.7	11.8
^{238}U (n,γ)	0.060	6.7	7.5
^{148}Sm (n,γ)	1.383	2836	2837
^{150}Nd (n,γ)	1.308	1338	1340
^{154}Sm (n,γ)	0.772	1890	1891
^{114}Cd (n,γ)	0.462	2877	2877
^{238}U:^{135}I γ	0.068	128	128
^{239}Pu:^{153}Sm γ	0.039	45.3	45.4
Power	0.019	2.8	3

Data assimilation based on the Phenix reactivity loss mainly affects the uncertainty of ^{240}Pu capture, ^{240}Pu fission, ^{238}U capture and ^{238}U inelastic, resulting in approximately 6% reduction in initial uncertainty for the most sensitive cross-sections (see Table XXII). The power, included as a fitted parameter, also shows impacts of a similar magnitude as the main nuclear data contributors. Nevertheless, the variance reduction associated with these isotope-reaction pairs (and power) contributes minimally to the overall uncertainty reduction. The primary mechanism by which the data assimilation process reduces uncertainty has been through generating additional correlations.

Figure 57 illustrates the prior correlation matrix (left subfigure) and the impact of data assimilation (difference between the posterior and prior correlations) for the seven main isotope-reaction pairs. It introduces additional correlations ranging between -0.3 and 0.2. They are almost homogeneously distributed between the main contributors (as shown in the right subfigure of Figure 57), including isotope-reaction pairs that were already *a priori* correlated, such as capture, fission and inelastic reactions of ^{238}U. For these initial cross-correlation, in most of the cases, IDA reduces them.

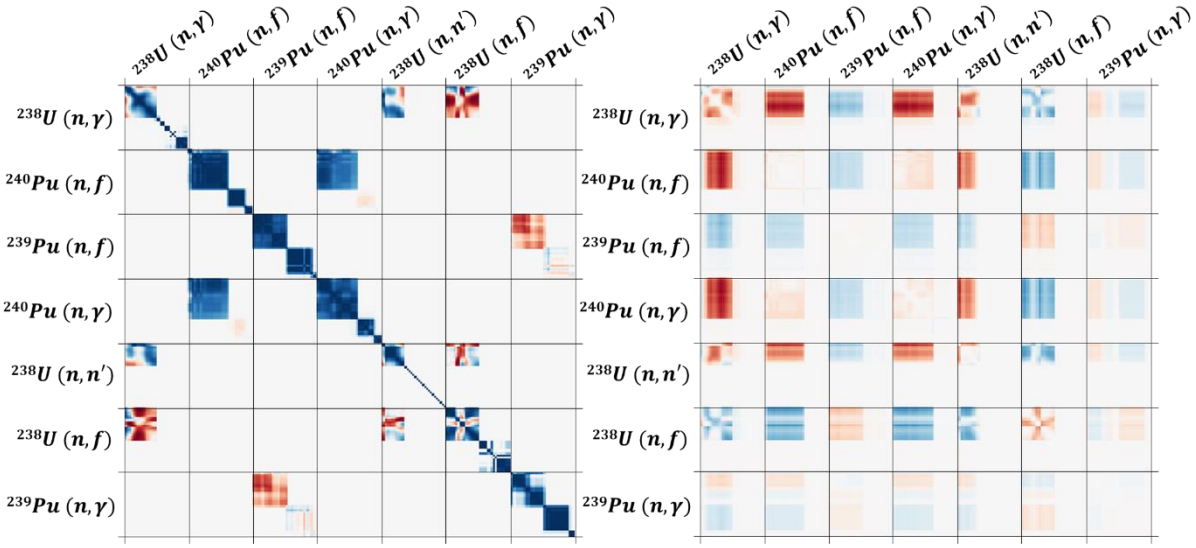

Figure 57. Prior correlation matrix (left) and the differences between posterior and prior correlations (right) for the most impacted isotope-reaction pairs when performing IDA with the Phenix reactivity loss and COMAC V1

These new correlations produce negative contributions in the uncertainty distribution as Figure 58 shows. As the ^{238}U (n,γ) is by far the most important contributor to the uncertainty, the assimilation process tends to correlate this reaction with the most important secondary contributors (^{240}Pu, ^{239}Pu and other ^{238}U reactions). Moreover, it also leads to correlate with isotope-reaction pairs with a lower contribution (below ^{239}Pu (n,γ) in Figure 58). For instance, ^{239}Pu:^{107}Pd fission yield and ^{239}Pu κ_f, which are *a priori* unrelated (at the nuclear data production step so at the microscopic scale).

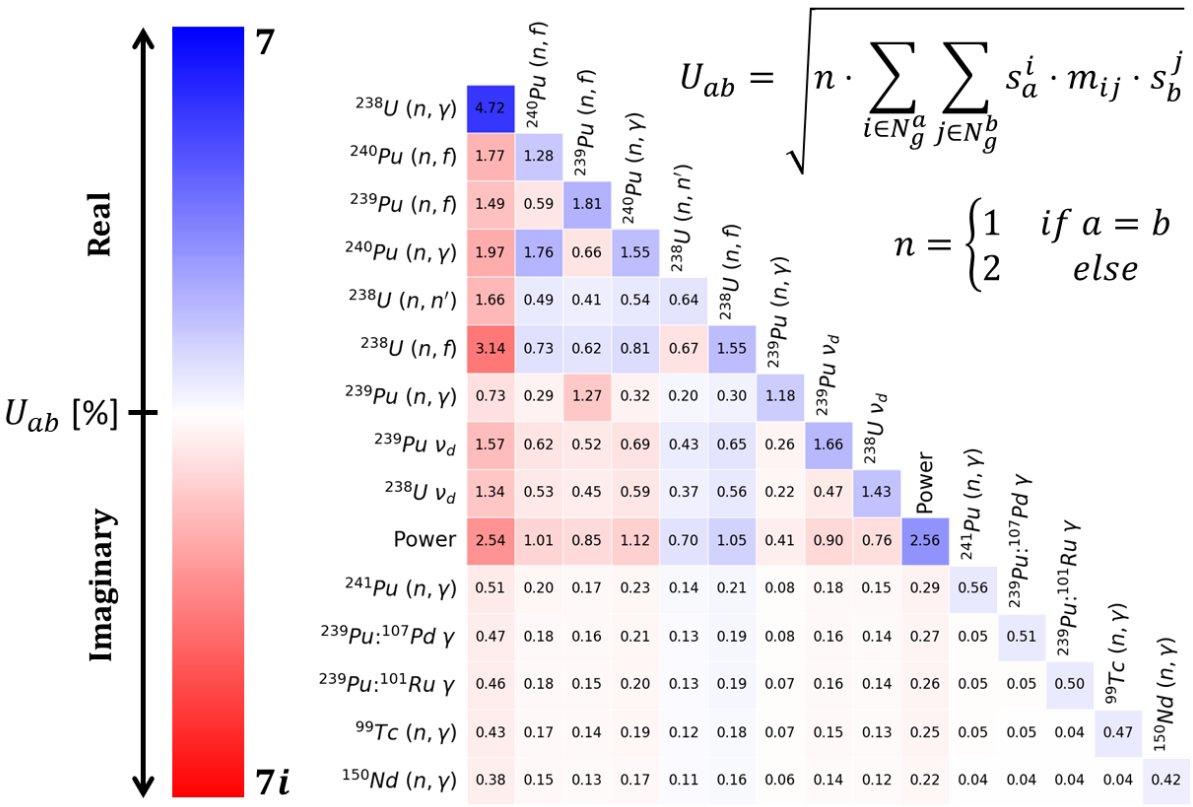

Figure 58. Posterior uncertainty distribution between the different isotope-reaction pairs when performing IDA with the Phenix reactivity loss and COMAC V1 (and by considering the power as uncertain)

Morover, the calculation has been performed with the power as an uncertain parameter in the calculation. The data assimilation process has therefore produced correlations between nuclear data and the power parameter (between -0.2 and +0.2) that have a meaning only in the mathematical framework of data assimilation.

To study the impact of considering power as an uncertain parameter, the same data assimilation process was performed without accounting for power uncertainty (both in the experiment and calculation sides). Not considering power, firstly by reducing experimental uncertainty, tends to increase the uncertainty reduction in nuclear data. Secondly, by eliminating a significant contributor, the uncertainty reduction applies to fewer assimilation parameters. This increases the uncertainty reduction and the generation of correlations between the remaining parameters, as depicted in the top right and bottom subfigures of Figure 59. Since uncertainty reduction was primarily achieved through correlations, its impact is predominantly carried by them (correlations change within -0.3 and +0.2 when power is considered in assimilation, compared to -0.5 and 0.3 when it is not).

Regarding corrective factors, a similar rationale applies. By removing a sensitive parameter, the discrepancy between calculation and experiment is minimized by

increasing corrective factors for other parameters, as illustrated in the upper left subfigure of Figure 59 for the ^{240}Pu (n,γ). For the latter, corrective factors remain small compared to the initial uncertainty. However, correlations are significantly affected and the question of considering the power as uncertain or not in the assimilation process, remains. Future work should focus on conducting data assimilation with more sophisticated models and techniques, such as marginalization of nuisance parameters for power [83].

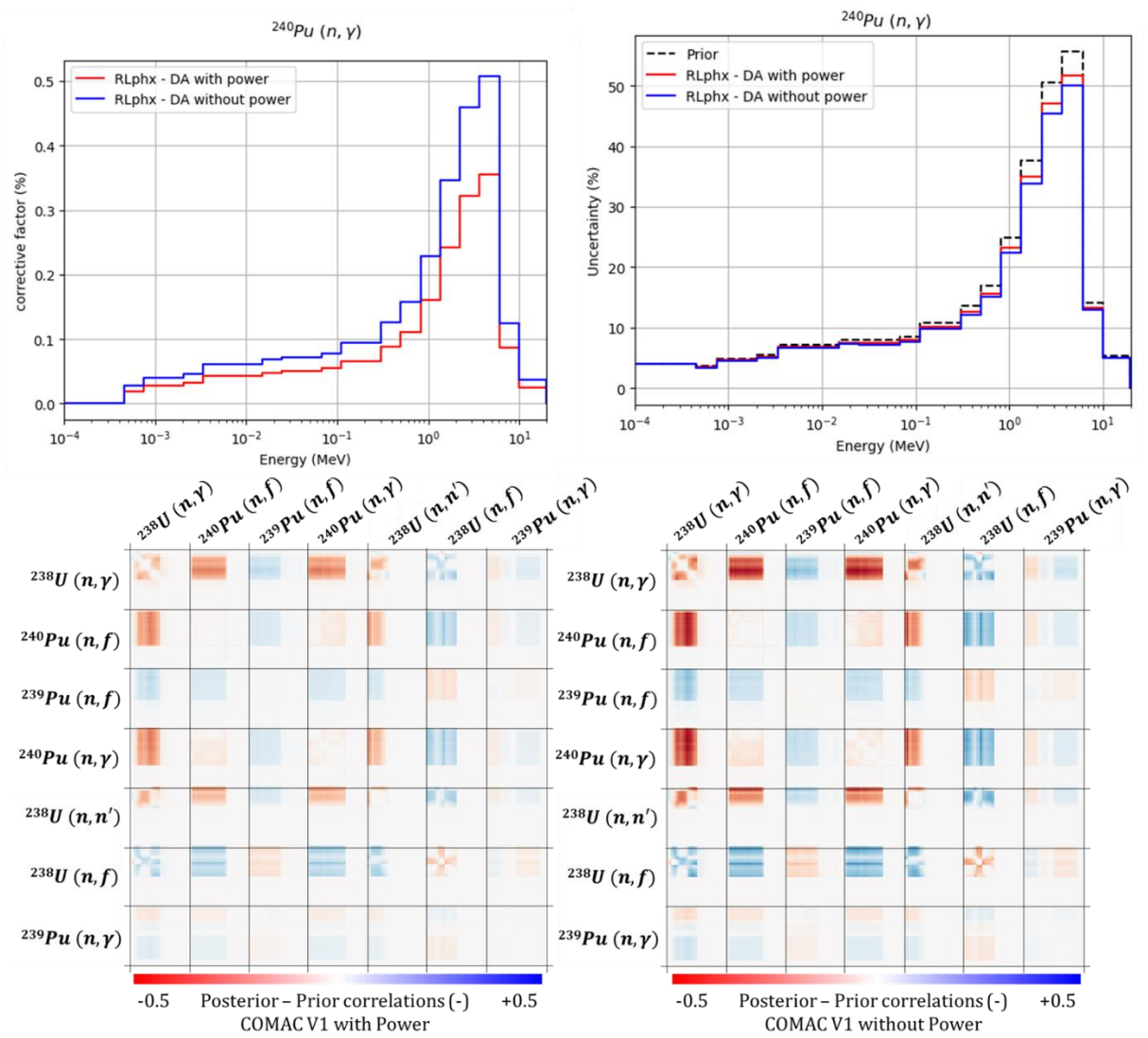

Figure 59. Comparison on data assimilation main results when the power is considered as uncertain or not

These new correlations characterize the Phenix reactivity loss information assimilated by the JEFF 3.1.1 cross-sections. The physical meaning of such correlations outside of the reactivity loss framework, in terms of actually improving nuclear data at the evaluation step, is complicated to apprehend and would require a high degree of confidence in the covariance matrix. Following the conclusion of the report "Investigation of Covariance Data in General Purpose Nuclear Data Libraries" [84], this question is still under vigorous debate and the scope of this work cannot pretend to contribute to this discussion.

However, these posterior values could be used for a specific reactor purpose by producing an adjusted nuclear data library to use "as it is". This perspective will be addressed in the next section but first and foremost, the limitations of the input data used for the data assimilation should be addressed.

6.4.1. C/E influence on IDA

It has been seen that corrective factors are slightly affected due to the low discrepancy with the experiment, compared to the experimental uncertainty. Also, the APOLLO3®/MENDEL bias has been estimated at -0.83% on the reactivity loss coefficient, which would give in an "unbiased" calculation, a C/E of +0.96%. In order to asses this impact on corrective factors and covariances, this C/E value is considered with the same sensitivities for IDA.

With such a modification, the same trend for corrective factors presented in Table XXII is obsevered but with opposite sign and values that are 7 times larger (because the discrepancy with the experiment is 7 times larger). Figure 60 shows the new posterior corrective factors and uncertainties for the four main isotope-reaction affected and it can be seen that the corrective factors remain largely smaller to the uncertainty. Globally, in the 80 main contributors adjusted, corrective factors remain small (only seven contributors have a corrective factor superior to 1%) and negligible compared to the prior and posterior uncertainty, including newly introduced nuclear data as fission yields and fission energy release.

The physics of the reactivity loss imply that the sensitivities between isotopes in the Uranium-Plutonium chain are successively opposed:

- ^{238}U (n,γ) and (n,f) integrated sensitivities: -2.05 %/%
- ^{239}Pu (n,γ) and (n,f) integrated sensitivities: +1.47 %/%
- ^{240}Pu (n,γ) and (n,f) integrated sensitivities: -0.33 %/%
- ^{241}Pu (n,γ) and (n,f) integrated sensitivities: +0.04 %/%

These types of sensitivities with several main contributors can potentially hide compensations during the adjustment process, which would lead to non-physical cross-section increases of both opposed isotope-reaction pairs. In that case, ^{239}Pu cross-sections are negligibly affected so that the ^{238}U and ^{240}Pu corrective are not overestimated to compensate for a ^{239}Pu cross-section change.

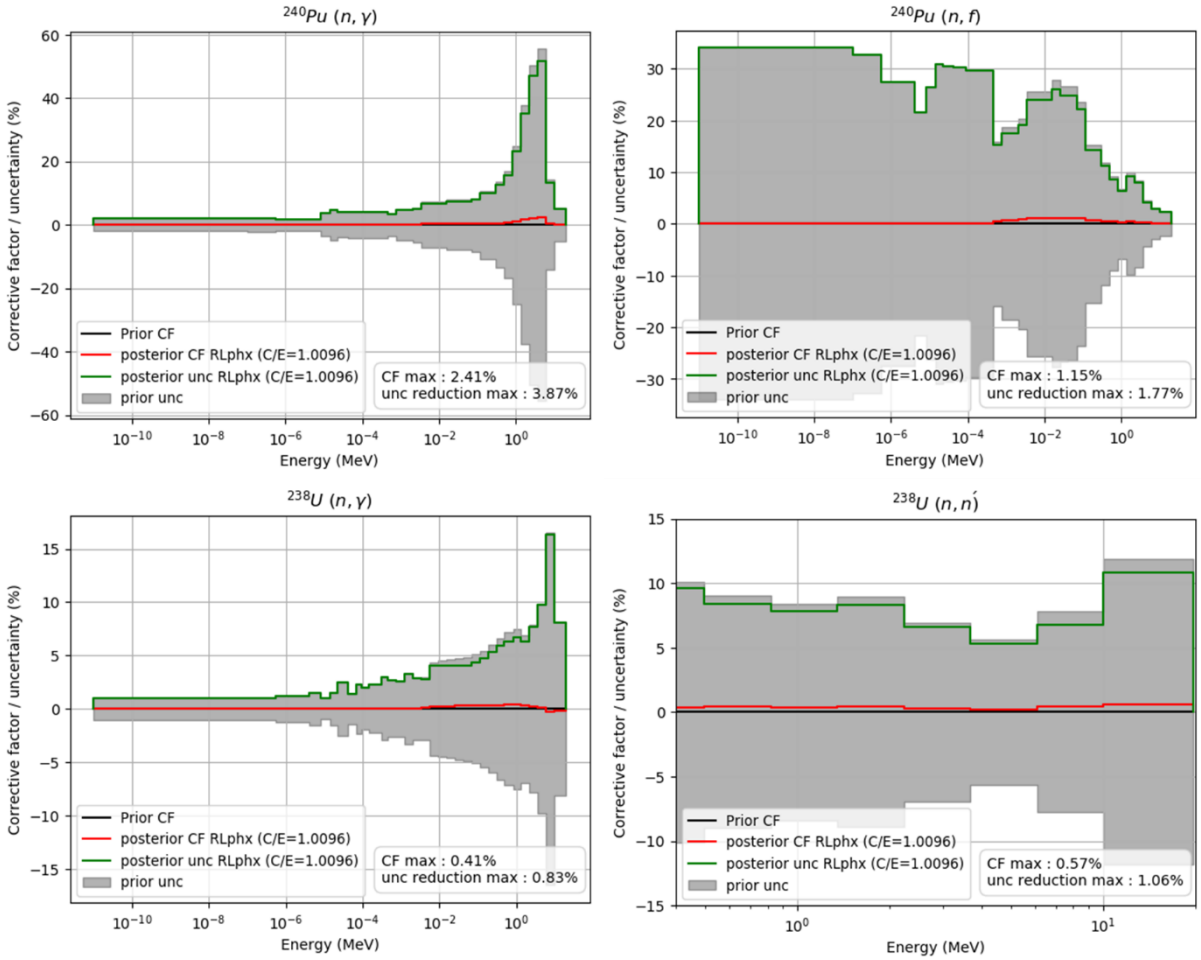

Figure 60. Posterior value and uncertainties of the main isotope-reaction pairs impacted by the IDA with Phenix reactivity loss for C/E=1.0096

Moreover, in the range of assumptions considered for the reactivity loss IDA, posterior covariances are not related with the C/E value. Therefore, the obtained small APOLLO3®/MENDEL bias on the C/E value has no significant impact.

6.4.2. Influence of considering biased sensitivities

It has been shown in the previous chapter that the reactivity loss sensitivities for the Phenix cycle 42-115 suffered from biases of around 20% (but with scarce discrepancies between the different isotope-reaction pairs), due to the lack of consideration of previous irradiations. As data assimilation is driven by sensitivities (in the methodology applied here), the transmitted bias cannot be ignored. To estimate the influence of the consideration of biased sensitivities, data assimilation is performed with a set of perturbed sensitivities. To have perturbed sensitivities that reflect the type of bias that LC sensitivities represent, a naive reconstruction of the irradiation history based on a cell

calculation was carried out (presented in greater detail in Appendix I) to estimate these perturbed sensitivities, hereinafter referred to as CLC.

In Figure 61, corrective factors and posterior uncertainties of the ^{238}U (n,γ), ^{240}Pu (n, γ) and ^{240}Pu (n, f) obtained by data assimilation with CLC sensitivities are compared to those obtained with LC sensitivities. It can be seen that with CLC sensitivities, corrective factors are larger than with LC sensitivities (the same applies to other main heavy nuclei reactions). Since LC sensitivities tend to overestimate the sensitivities of the main heavy nuclei, the cell correction tends to reduce them. Therefore, to minimize the same calculation/experiment difference with lower sensitivities, it necessitates increasing the corrective factors. Nevertheless, the difference between both remains marginal compared to the uncertainty at those energies.

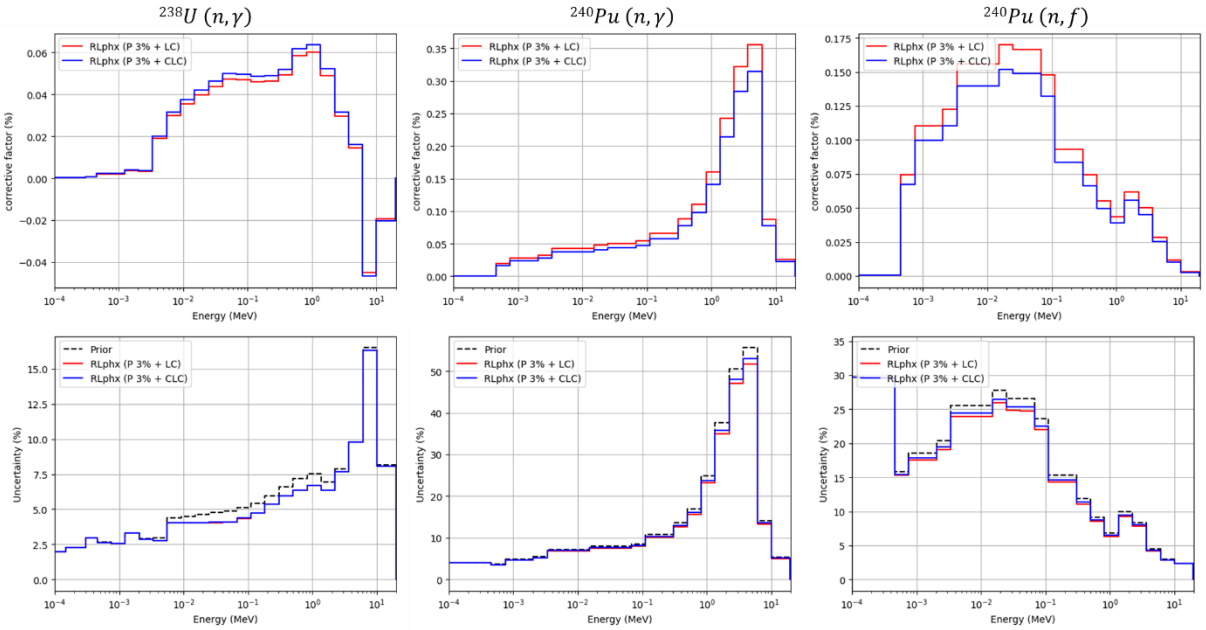

Figure 61. Comparison of posterior corrective factors (top) and uncertainty (bottom) for ^{238}U (n, γ) (left), ^{240}Pu (n, γ) (centre) and ^{240}Pu (n, f) (right) between two different sets of sensitivities. Respectively the nominal case with LC sensitivities (red) and the one with perturbed sensitivities CLC (blue)

For uncertainty and correlations, the impact is much smaller, as shown in Figure 61 and Figure 62. This can be explained by the fact that it is the ratios between the main contributors that influence the posterior covariances (variances + correlations). While the magnitude of LC sensitivities with respect to FB ones is significantly affected, the ratio between the different contributors is less impacted (as can be seen through the similar biases betwwen LC and FB sensitivities observed in Table XIII in the previous chapter).

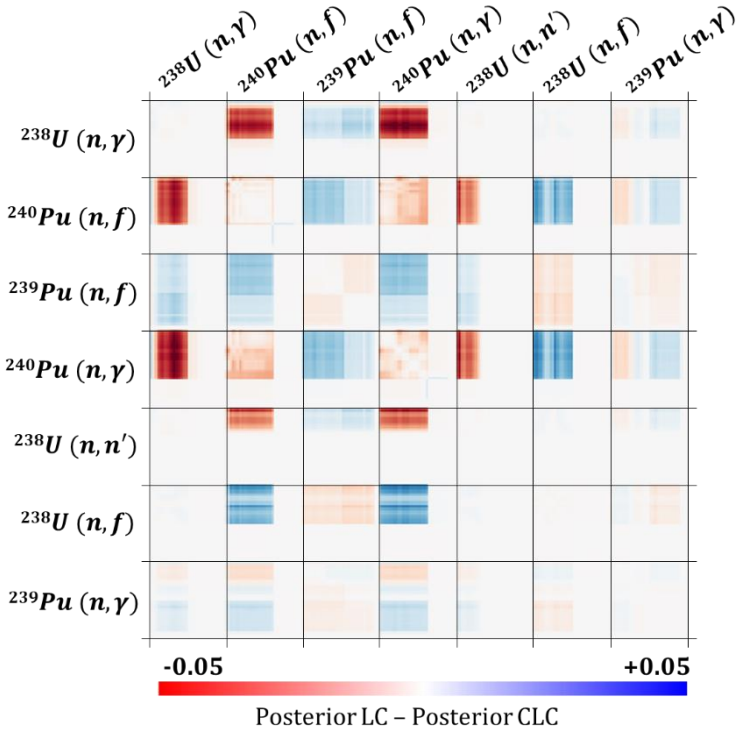

Figure 62. Posterior correlations difference between DA performed with LC sensitivities and CLC sensitivities

Even though the LC formalism induces biased sensitivities, the main trends and order of magnitudes are similar and allow for an understanding of the contribution that such a new integral experiment can have on data assimilation.

6.4.3. Prior covariances impact on IDA

Finally, the sensitivity of IDA to the prior covariance matrix is addressed. Other covariance matrices available related to nuclear data libraries such as ENDF/B-VII.1 [85] or JENDL 4 [86], have in common a global shape with almost diagonal with rare cross-correlations as illustrated in see Figure 63 for ENDF/B-VII.1 correlation matrix.

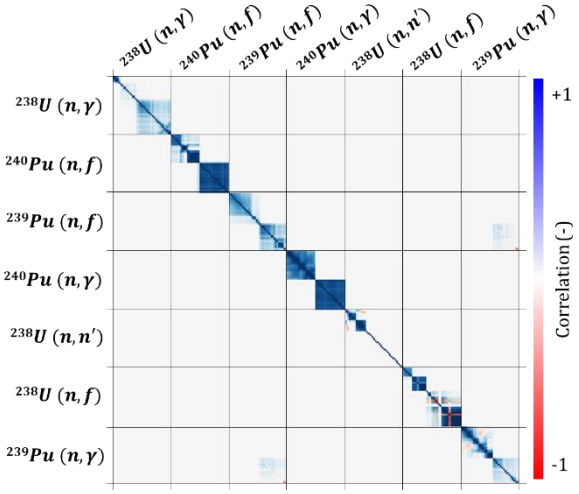

Figure 63. ENDF/B-VII.1 33G-covariance matrix for the seven main isotope-reaction pairs considered

To investigate such an effect compared to COMAC V1, the data assimilation calculation is performed with COMAC1 without the Cross-Correlations (CC) between different isotope-reaction pairs (only cross-correlations between groups of an isotope-reaction pair are kept).

The impact of not considering cross-correlations is that ^{238}U (n,γ) is favored over other contributors. Indeed, without initial cross-correlations, each isotope-reaction pair can be individualized, which means that corrective factors and uncertainty reduction are not propagated to secondary contributors via initial cross-correlations. Hence, both are larger for ^{238}U (n,γ) (see Figure 64) and it is the opposite for other contributors as ^{240}Pu (n,γ) (which is the most impacted but the same conclusions could be drawn for other contributors).

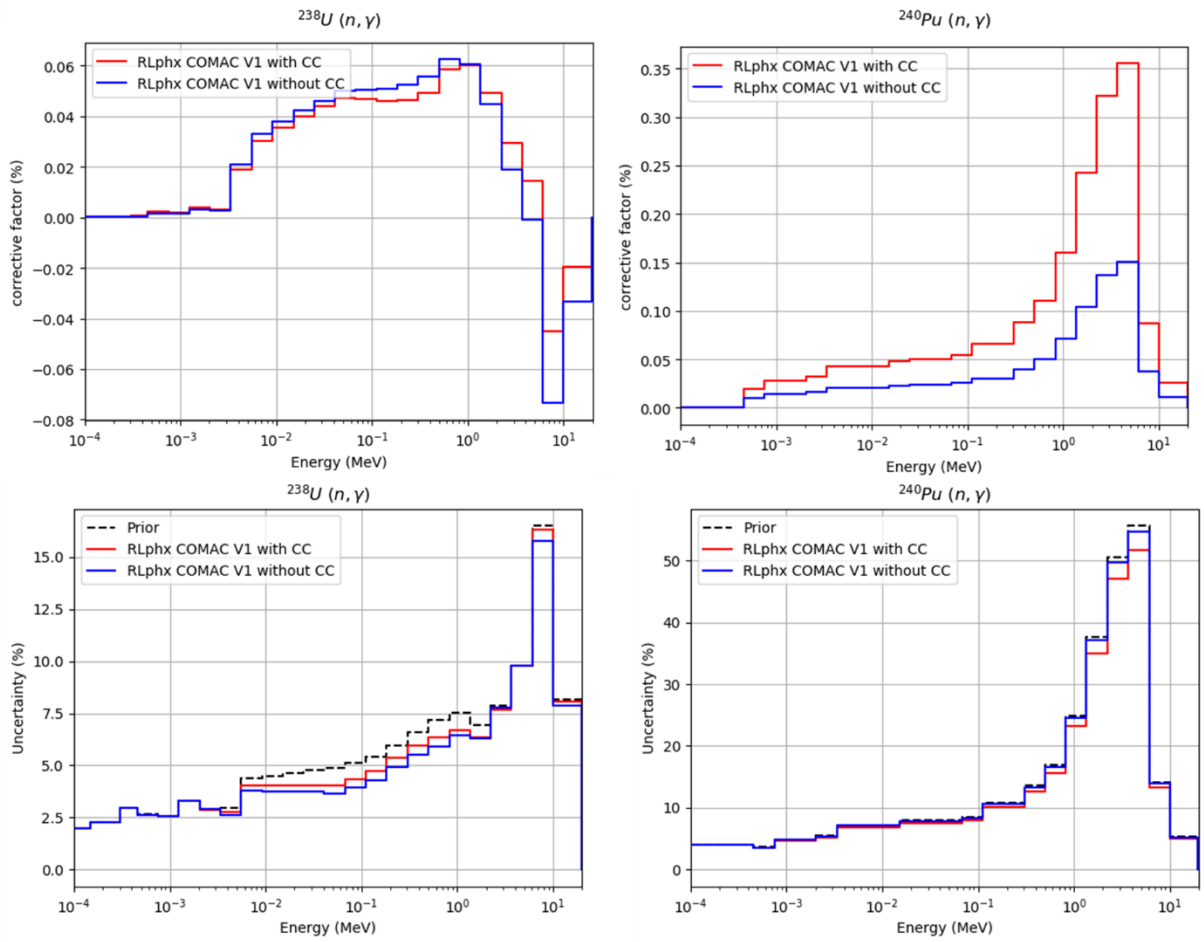

Figure 64. Posterior corrective factors (top) and uncertainties (bottom) when performing DA with the Phenix reactivity loss starting with COMAC V1 (red) and COMAC V1 without cross-correlations (blue) for ^{238}U (n, γ) (left) and ^{240}Pu (n, γ) (right)

For the *a posteriori* correlations in the case where there were no a priori cross-correlations, each contributor correlates with the others to the extent of its contribution to the uncertainty. The ^{238}U capture therefore correlates much more with the others and the second contributors only have minor correlations with each other. The presence of cross-correlations in the *a priori* matrix tends to produce many more cross-correlations, by propagating through the a priori cross-correlations. This can be seen inside the red ellipses in Figure 65. The ^{238}U and ^{240}Pu cross-correlations propagate the influence of ^{238}U capture throughout the space between the cross-correlations, where there is none in the case without cross-correlations.

Hence, confidence for the use of posterior correlations will directly depend on the initial confidence of the related correlations. The establishment of such confidence is outside of the scope of this work, and dedicated studies on this subject should be carried out, using the new methodologies, the current requirements as stated in [87], the most recent nuclear data library to come (as JEFF 4) and a large set of various integral experiments, in order to address this question.

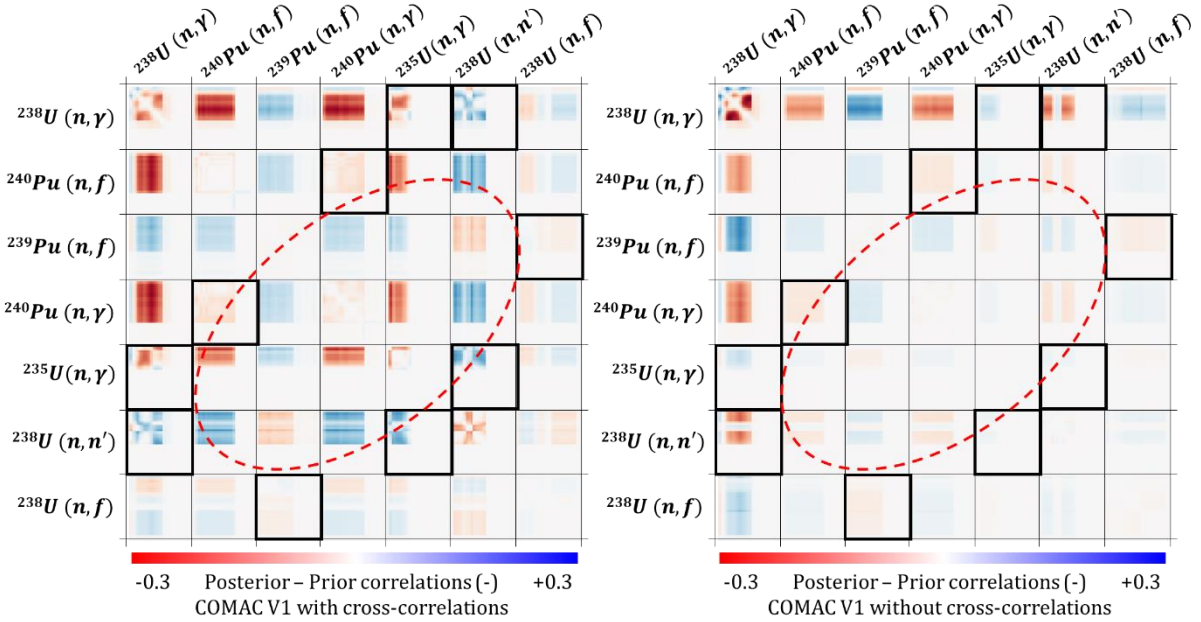

Figure 65. Posterior/Prior correlations difference when performing DA with the Phenix reactivity loss starting with COMAC V1 (left) and COMAC V1 without cross-correlations (right). Black squares represent the locations of the initial cross-correlations

6.5. Application of posterior nuclear data to other experiments

The most straightforward way to use integral data assimilation results is "as they are" for a targeted reactor. This method has been used to produce an adjusted nuclear database (or so-called "Engineering library" in [88]) for the Superphenix reactor as the one associated with CARNAVAL-IV which was able to predict the critical mass with a 300 pcm uncertainty [89] and later with the ERALIB library [77], [90]. However, using such adjusted nuclear data with confidence is restricted to cases similar to the integral experiment database used for the adjustment process. To quantify this similarity and specifically the lack of knowledge shared by two different integral experiments, the representativity factor can be used [5], [91]:

$$r_{ij} = \frac{S_i^T M S_j}{\sqrt{(S_i^T M S_i)(S_j^T M S_j)}} \tag{6-10}$$

With r_{ij}, the representativity factor between experiment i and j, represented respectively by the sensitivity vector S_i and S_j. If it is close to +1, the lack of knowledge is very similar, so that improving one will greatly improve the other. If it is close to 0, both experiments complement each other so that improving one will not improve the other, but using both experiments in data assimilation will bring different information. Finally, if the

representativity factor is negative and tends to -1, the lack of knowledge is also similar, but the corrective factor will have a global opposed behavior on the C/E value.

New innovative designs will not necessarily fit with the current experimental database in terms of representativity. To evaluate the adjustment process, the posterior value obtained could be applied to a non-representative and well-known experiment to estimate whether the posterior nuclear data produce inconsistencies.

Such a well-known experiment may be accessible in the International Criticality Safety Benchmark Evaluation Project (ICSBEP) Handbook [92] and International Handbook of Evaluated Reactor Physics Benchmark Experiments (IRPhE) [93]; with tools able to facilitate the access to benchmark inputs (DICE [94] and IDAT [95]); and tools for sensitivity analyses/uncertainty quantifications, such as NDaST [96], [97]. Dedicated work should be done in the future to use such powerful tools for detailed assessment and properly characterizing this type of new integral experiment as reactivity loss.

In the meantime, with the time-constraint of this work, an exercise to demonstrate the potential application of the IDA and towards the production of an "engineering library" has pointed to the following integral experiment set:

- The 42nd Phenix cycle reactivity loss
- The JOYO MK-1 2nd cycle at 50 MW [98] available in the IRPhE handbook which has been computed [99] along with its related coupled Boltzmann/Bateman sensitivities with the scheme presented in Figure 50 in the previous chapter
- The JOYO MK-1 64-Fuel-Subassembly Core criticality measurement also available in the IRPhE handbook
- A Phenix control rod worth experiment that has been computed in the scope of this work. The experiment considered is one measurement of the rod balancing performed at the beginning of Phenix cycle 49 (rod balancing presented in 3.2.1)
- A Superphenix control rod worth experiment that has been computed in previous work [34]
- The SEFOR Doppler coefficient that was computed within the framework of the work presented in [100]

The C/E values come from a TRIPOLI-4® reference calculation for control rod worths, criticallity and Doppler experiments while sensitivities to nuclear data have been computed with the used of APOLLO3® perturbation engine (SPT, EGPT, Boltzmann/Bateman coupling and son on). Performing assimilation with the C/E ratios from reference calculations ensures that the discrepancy between calculation and experiment originates from nuclear (and technological) data rather than numerical biases. However, to ensure that no numerical bias is transferred to the nuclear data, the sensitivities should also be calculated using a reference method. Such Monte Carlo methods exist [101], [102] but require high computational costs to minimize statistical

bias and prevent its transfer to the nuclear data. In this manuscript, such calculations could not be conducted, and only sensitivities calculated using the deterministic scheme were used. In [103], a comparison is presented, considering sensitivity coefficients from different calculations (including a multi-group Monte Carlo calculation) for multiplication factors, void coefficient, and reaction rates ratios on well-known fast spectrum experiments (including JOYO). This report shows that the sensitivity profiles are in good agreement despite the different codes and nuclear data used. Based on this, it is considered that for the analysis presented, the deterministic sensitivities are sufficient to represent the physics of the different phenomena and can be associated with the C/E value from a reference code.

Table XXIII summarizes the main integral experiment used for the IDA along with the representativity factors between each experiment. The all-set experiment comes from MOX fuel reactors with a difference for JOYO that is composed of MOX fuel with enriched uranium (^{235}U is part of the main contributors). First, it can be seen that the range of representativities is diversified between +1 and -1. Then, the potential information brought by these experiments for data adjustment is also different. To quantify this accessible knowledge, the Ishikawa factor [104], defined as follows is used:

$$IS_i \equiv \frac{S_i^T M S_i}{\left(\frac{\Delta E_i}{E_i}\right)^2 + \left(\frac{\Delta C_i}{C_i}\right)^2} \tag{6-11}$$

With $\frac{\Delta C}{C}$ in this case being the calculation uncertainties not due to nuclear data (for instance, power in the case of reactivity loss calculation, which gives an Ishikawa factor of 2.6). If the Ishikawa factor is greater than one, the experiment can bring information to reduce nuclear data uncertainty, whereas if it is significantly lower than one, variances will remain unchanged by the IDA.

The experiment set is then separated into two groups. The first one for data adjustment with an Ishikawa factor greater than 1 (significantly higher in green and higher and around 1 in orange in Table XXIII). The second one is a target to study the impact of posterior corrective factor and covariances with an Ishikawa factor below 1 (red in Table XXIII). For each experiment, the individual chi-value measured in sigma is below one, so that there are *a priori* no inconsistencies:

$$\chi_{ind,i} = \frac{|E_i - C_i|}{\sqrt{S_i^T M S_i + \left(\frac{\Delta E_i}{E_i}\right)^2 + \left(\frac{\Delta C_i}{C_i}\right)^2}} \tag{6-12}$$

If $\chi_{ind,i} \gg 1$, it means that the computed value and its related uncertainties are not consistent with the experiment value and its uncertainties, so that there is a problem in

the calculation or in the covariance data and/or in the experiment value and its uncertainty.

Table XXIII. Integral experiment available for this work

Integral experiment	$\frac{C}{E}-1$ [%]	$\frac{\Delta E}{E}$ [%]	$\frac{\Delta C_{ND}}{C}$ [%]	representativity factor (prior COMAC V1)					
REACTIVITY LOSS PHENIX cycle 42 (RL PX)	+0.13	3.35	7.33	1.00	0.54	0.28	0.22	0.06	-0.14
REACTIVITY LOSS JOYO MK-I 50MW 2nd cycle (RL JOYO)	+3.34	3.84	2.80	0.54	1.00	-0.61	0.49	0.44	0.30
KEFF JOYO MK-I (KEFF)	+0.09	0.18	1.39	0.28	-0.61	1.00	-0.32	-0.39	-0.36
CRW PHENIX cycle 49 (CRW PX)	-0.95	1.71	1.95	0.22	0.49	-0.32	1.00	0.93	0.76
CRW SUPERPHENIX (CRW SPX)	+0.44	4.78	1.63	0.06	0.44	-0.39	0.93	1.00	0.87
DOPPLER SEFOR (DOP)	-1.35	0.80	3.49	-0.14	0.30	-0.36	0.76	0.87	1.00

Data adjustment is performed with CONRAD for different combinations of experiment of the first subset (RL PX – DOP – KEFF – CRW PX) for the IDA. Posterior data are then applied for each integral experiment not concerned by the data adjustment and the second subset (CRW SPW – RL JOYO), which lead to Table XXIV for the posterior χ_{ind} values and Table XXV for the posterior nuclear data uncertainties[29]. In these tables, the columns indicate the experiments considered for IDA, where the posterior corrective factors and covariances have been applied to a target experiment listed in the first column. For example, by applying the posterior data from the assimilation of the "RL PX + KEFF" set to the DOP experiment, a posterior χ_{ind} of 0.40 (compared to a prior χ_{ind} of 0.38) and an uncertainty reduction of 13% are obtained. Therefore, for target experiments that are also in the experiment set for adjustement, cells are shaded as the χ_{ind} values will be close to zero and the nuclear data uncertainty close to the experimental one, due to data assimilation constraints.

[29] In this study, the power uncertainty for the Phenix reactivity loss is considered during data assimilation but all posterior data related to power are not conserved, as they do not apply to other experiments.

Table XXIV. Posterior χ_{ind} of the experiment database

χ_{ind} [-]	PRIOR	Experiment considered for adjustment					
		RL PX	RL PX DOP	RL PX KEFF	RL PX CRW PX	DOP KEFF CRW PX	RL PX DOP KEFF CRW PX
RL PX	**0.02**					0.10	
DOP	**0.38**	0.39		0.40	0.25		
KEFF	**0.07**	0.06	0.08		0.05		
CRW PX	**0.33**	0.33	0.13	0.33			
CRW SPX	**0.09**	0.09	0.19	0.10	0.16	0.19	0.20
RL JOYO	**0.70**	0.70	0.79	0.84	0.78	0.79	0.84

Table XXV. Posterior uncertainty of the experiment database

$\frac{\Delta C_{ND}^{post}}{\Delta C_{ND}^{prior}} - 1$ [%]	PRIOR	Experiment considered for adjustment					
		RL PX	RL PX DOP	RL PX KEFF	RL PX CRW PX	DOP KEFF CRW PX	RL PX DOP KEFF CRW PX
RL PX	**7.333**					-12.3	
DOP	**3.492**	-6.5		-13.0	-23.7		
KEFF	**1.392**	-3.2	-9.6		-8.4		
CRW PX	**1.945**	-1.0	-34.1	-10.5			
CRW SPX	**1.632**	-1.4	-35.5	-11.6	-14.8	-40.6	-41.4
RL JOYO	**2.796**	-2.5	-6.8	-44.6	-7.0	-32.3	-44.7

Globally the different posterior χ_{ind} stay lower than 1, which implies that assimilation with these tests does not produce non-physical compensations for the experiment set considered. Also, the reactivity loss, when considered alone for the IDA, is associated with an uncertainty reduction that is rather small but consistent with the representativities between the different experiments and the reactivity loss.

Then, in the framework of the tested experimental set, adding reactivity loss to data adjustment improves the uncertainty reduction (7th and 8th column of Table XXV) and in a larger proportion than reactivity loss alone for the JOYO reactivity loss (3rd column of Table XXV). This implies that additional constraints brought by other experiments allow a better use of the reactivity loss knowledge that would be brought directly. This study is preliminary, yet it helps to provide some insight on the potential details of moving towards creation of an engineering library.

6.6. Conclusion

The Best-Estimate modeling of the 42nd Phenix cycle reactivity loss using the reinterpreted experimental value along with the correct sensitivity formalism allowed this experiment to be considered for data assimilation and the range of experiments for such a process to be extended.

To study the potential of such an experiment, a preliminary data assimilation was conducted using the available tools and data. It has been shown that data assimilation mainly reduce nuclear data uncertainty by producing new correlations. These posterior correlations are sensitive to the existence of prior cross-correlations between different reactions, highlighting the open question of confidence in the initial covariance matrix.

The various limitations of the data used, such as biased sensitivities, were examined and were found not to show any particular inconsistencies. This instills confidence in the exercise, suggesting that the subject can be further explored in future work, particularly with fully backtracked Boltzmann/Bateman coupled sensitivities. Moreover, as the uncertainty in power contributes to both the experimental and calculation uncertainties, it has been shown that its impact on the posterior covariances is significant. The question of how to account for this uncertainty then remains and needs to be addressed in further work using more advanced methodologies than those employed in this exercise, such as marginalization.

Consideration of a small set of other integral experiments with various representativity factors has shown that data assimilation with the Phenix reactivity loss (and other experiments) improved the uncertainty of some target coefficients as the reactivity loss of the JOYO reactor or the control rod worth of the Superphenix reactor. In addition, the new C/E values obtained do not show inconsistencies with the experimental and posterior nuclear data uncertainties. Therefore, the use of the Phenix cycle reactivity loss provides a valuable perspective for covariances calibration and uncertainty quantification for design purposes.

In order to generalize these results, a study on a broader integral experimental database and state-of-the-art methodologies for IDA must be conducted. A specific effort could be made to look at the reliability of the initial covariance matrix, to give credit to the nuclear data a posteriori and especially to asses on the reliability of the posterior covariances that would be used for uncertainty quantification purposes. In addition, the sensitivities and C/E of the different phenomena considered will need to be used as references, in order to avoid transmission of numerical bias into nuclear data. For most commonly used coefficients, a Monte Carlo reference method can be used, but in some cases, like the reactivity loss of a power reactor, this reference method is prohibitive. Therefore, additional specific validation work and studies on the impact of deterministic bias on

nuclear data should also be carried out, to enable potential use of such an experiment in engineering libraries.

Chapter 7. General Conclusion

In a context where numerical simulation will play a major role in the development of future reactors, experimental validation for all possible phenomena occurring in the selected technologies is crucial. For Sodium Fast Reactors, the changes in the neutronics quantity of interest during irradiation is of prime importance for safety, in addition to economic criteria. However, there are only a relatively limited number of experiments providing this type of data. The goal of this manuscript, therefore was to study the possible contribution of the determination of the Phenix reactor irradiation cycles in support to the experimental validation of modern SCTs.

Firstly, fuel depletion in a power reactor has been shown to be a complex phenomenon that coupled the neutron flux with the isotopic composition and also the geometry and the temperature via thermal expansion, irradiation swelling and pellet restructuring, among others. To approach such a problem the APOLLO3®/MENDEL fuel depletion deterministic scheme was used, composed of the APOLLO3®-FR scheme for the Boltzmann equation and the MENDEL code for the Bateman equation. Thanks to the inovative features of the APOLLO3® code, it is now possible to increase the accuracy of calculations by lifting some commonly used assumptions, such as the homogenization of control rods and experimental devices. Moreover, it facilitates the implementation of multiphysics studies, making it feasible to consider a coupling with the fuel performance code GERMINAL V2. Nevertheless, addressing this exercise directly at core level for the Phenix reactor might conceal compensations.

To initiate this bias decomposition work, a numerical validation was performed on a simplified model of the Phenix core (Phenix-Like) to assess and quantify bias related to calculation scheme for the transport equation alone. This showed good agreement with the TRIPOLI-4® stochastic reference calculations for the control rod worth and the reaction rates distribution. This indicates that this scheme can be considered as apropriate for fuel depletion calculations in more complex cases. Next, the coupling with GERMINAL V2 was implemented, applied and tested for an infinite lattice subassembly case in irradiation, demonstrating the relevancy of such coupling for reactivity loss purpose and suggested that it should be extended to core calculations.

To perform the calculation for a Phenix cycle, it was necessary to study the various cycles carried out during its operation and select one that would allow for accurate calculation conditions as well as the extraction of experimental data. The cycle 42 was chosen because it operated at a stable power for more than 80 days and included a control rod worth

experiment at the beginning of cycle, which was necessary to determine the experimental reactivity loss.

Considering that the method used during operation show some important limitations, a reinterpretation of the reactivity loss of the cycle 42 was performed. Notably, a number of coefficients, such as the shadow-effect, which was considered constant over time, were updated with reference Monte-Carlo calculations. This greatly improved the reactivity loss coefficient, giving a reinterpreted value of **-4.644 ¢/EFPD** compared to -5.622 ¢/EFPD for former analysis. To establish confidence in this new value, an uncertainty propagation of the input parameters was performed using random sampling. This approach allowed the reactivity loss coefficient uncertainty to be quantified at a **conservative value of 3.35%** and identified the main contributing factors:

- Power (3%)
- Actual position of the control rods (0.7%)
- Statistical uncertainty of the shadow effect (0.2%)

For statistical uncertainty due to TRIPOLI-4®, an additional computational effort could be made to mitigate the experimental uncertainty. For the actual control rod driveline during cycle, a mechanical analysis with advanced computational tool could potentially help to reduce the remaining uncertainty of this aspect. For the experimental power used to normalize the reactivity loss coefficient, the main limitation is the availability of such information. The various sources of information found in the archives can be used to estimate a conservative uncertainty for this value. The reconstruction of experimental data from old power reactors using modern methods is therefore possible and provides a significant improvement over previous interpretations. However, the limited availability of the uncertainty of some components is restrictive regarding the significant reduction of experimental uncertainty achievable with modern tools.

With the newly interpreted experimental value, it has been possible to assess the APOLLO3®/MENDEL scheme experimentally towards the Phenix cycle 42 using the JEFF-3.1.1 cross sections library. To carry out this validation, assumptions commonly used in fuel depletion calculations have been partly removed in order to achieve the most realistic simulation possible with APOLLO3®/MENDEL up to the multiphysics coupling with GERMINAL V2. This has made it possible to quantify the contribution of the various hypothesis to the reactivity loss coefficient and to identify the important modelling choices to consider when calculating this coefficient. Thus, it has been shown that the following modeling parameters are important to consider:

- Boron depletion in control rods
- Temperature map evolution
- Fission gas migration
- Control rod extraction during cycle

Removing all these assumptions has allowed the Best-Estimate value for the APOLLO3®/MENDEL scheme to be quantified as **-4.650 ¢/EFPD** (C/E = 1.0013), in very good agreement with the experiment.

For current experimental validation requirements, the discrepancy with the experiment must be considered in regard to both experimental and computational uncertainties, consisting of the nuclear data uncertainty and the remaining numerical biases. To estimate these calculation uncertainties, it has been shown that sensitivities of the reactivity loss coefficient to nuclear data can be utilized.

Sensitivities for the coefficient in the Boltzmann/Bateman coupled problem follow a specific formalism called Depletion Perturbation Theory. This formalism has recently been implemented in APOLLO3® and has made it possible to compute the sensitivities for the reactivity loss coefficient of Phenix cycle 42, with the current Phenix model and the APOLLO3®/MENDEL scheme.

With these sensitivities, it has been possible to estimate the APOLLO3®/MENDEL bias on the reactivity loss coefficient at around 1%. Nevertheless, the current implementation of this formalism in APOLLO3® implies that the irradiation history prior to cycle 42 cannot be taken into account, due to the impossibility of extrapolating the adjoint composition field between two cycles. In order to quantify the uncertainty due to the nuclear data, the adjoint depletion should be made back to the beginning of irradiation of each subassembly present in cycle 42. Hence, ignoring the irradiation history introduces a bias in the sensitivities.

The bias of such an assumption has been studied on a subassembly case in an infinite lattice. It showed a sensitivity overestimation of “last-cycle” sensitivities, of 20% for the capture and fission of heavy nuclei and a 10% underestimation for the fission yields sensitivities. Given the similarities between the subassembly case and the core case, this trend could have been extrapolated to the Phenix cycle sensitivities. It therefore allowed the JEFF 3.1.1 nuclear data uncertainty for the reactivity loss to be computed.

To quantify such uncertainty the COMAC V1 covariance matrix was used. As the sensitivities related to fission yields, branching ratio, constant decay, and fission energy release were hardly accessible, their covariances were not directly available. Hence, the COMAC V1 matrix was updated with the missing data, which allowed quantification of the total uncertainty due to nuclear data as **6.94%** for the reactivity loss coefficient of Phenix cycle 42. Since the main contribution is made by the capture and fission of heavy nuclei, it could have been considered that this uncertainty computed with the "last-cycle" sensitivities was conservative. Moreover, the comparison with the experiment needed the delayed neutron fraction for normalization purposes, which increased the total uncertainty due to nuclear data to **7.33%**.

Nuclear data	Uncertainty [%] RL only	Uncertainty [%] RL normalized with β_{eff}
COMAC V1	**6.943**	**7.333**
Former COMAC V1	6.856	7.250
PF20	*0.191*	*0.191*
HN20	*0.067*	*0.067*
γ	1.019	1.019
$B - \lambda$	0.016	0.016
κ_f	0.343	0.343

Finally, experimental analysis, coupled with a best-estimate approach for determining the calculated value and the DPT formalism for the sensitivities, made it possible to characterize the reactivity loss of cycle 42 and the APOLLO3®/MENDEL scheme:

- $\frac{C}{E} - 1 = -0.13\ \%$
- $\frac{\Delta E}{E} = 3.35\ \%$
- $\frac{\Delta C_{ND}^{JEFF3.1.1}}{C} = 6.94\ \%$ (7.33% with β_{eff}) $\left| \frac{\Delta C_{bias}}{C} = 1\ \% \right| \frac{\Delta C_{power}}{C} = 2.76\ \%$

It made it possible to determine that the numerical bias is significantly lower than the experimental and nuclear data uncertainty. With these conditions, data assimilation could be studied to incorporate the reactivity loss experimental information into the nuclear data. This made it possible to reduce the uncertainty due to the nuclear data to a value close to the experimental uncertainty. All of this was achieved without producing any particular inconsistencies, despite the various limitations of the input data, such as "last-cycle" sensitivities. By carrying out this exercise with other available experiments, it has been possible to obtain a significant reduction in nuclear data uncertainty for integral experiments on other reactors, such as the Superphenix control rod worth or the reactivity loss of the JOYO reactor. Thus, in the context of a future intention of producing engineering libraries to help in deployment of certain reactors with lower and controlled uncertainties, the Phenix reactivity loss experiment could be important to consider. However, to achieve this goal, some limitations will still need to be addressed:

- The ability to perform the total adjoint depletion for DPT sensitivities by being able to extrapolate the adjoint isotopic field between cycles
- Reduction in the APOLLO3®/MENDEL numerical bias to prevent its transmission to nuclear data by considering more advanced numerical schemes and deepening the numerical validation of the APOLLO3®/MENDEL tool by aiming for a Monte Carlo calculation irradiation for a Phenix cycle.
- Expansion of the VVUQ domain to the multiphysics one by quantifying the uncertainties of input data from other physics and proposing a multiphysics

coupling with the latest tools for fuel performance and a dedicated thermal-hydraulic tool

- Investigation of the influence of multiphysics coupling on coupled Boltzmann/Bateman sensitivities to determine whether the formalism should be generalized to incorporate new components.
- Consideration of state-of-the-art methodologies for data assimilation with a large set of experiments capable of covering as many phenomena as possible to be able to assess and test the contribution of reactivity loss as an integral experiment. Such work could be considered, particularly with the experiments available in shared databases like DICE and IDAT, as well as analysis tools like NDaST

In the meantime, the full potential of the now-available coupled Boltzmann/Bateman sensitivities can be explored. A number of irradiation experiments, such as PROFIL, can be utilized with the appropriate formalism for uncertainties due to nuclear data. Additionally, the study on reactivity loss, primarily conducted for a specific cycle of the Phenix reactor, can be applied to other cycles but also to other reactors and other technologies. Furthermore, with the end of cycle able to be connected to its beginning and fuel depletion reduced to a representative sensitivity vector, this formalism offers prospects for meta-modeling fuel depletion in domains with a large number of parameters to study, where neutron calculation time is a significant constraint (e.g., design, scenarios, etc).

The VVUQ and assimilation exercise presented for the Phenix reactivity loss made it possible to extend reliance on the APOLLO3®/MENDEL scheme. This evidenced that the late generation codes allowed for elimination of the previous hypothesis and assumptions, whilst also considering advanced methods and coupling capabilities. The former experimental challenges can be addressed with enhanced reliance on these late generation tools.

With these new tools, the various physical phenomena are increasingly accessible from a multiphysics perspective. The experimental constraints for VVUQ of codes supporting the development of new nuclear technologies are then evolving, and experimental programs must be adapted. Consequently, an experimental program supporting R&D is necessary, in order to study reactor power phenomena across all multiphysics components simultaneously, matching the levels of detail achieved by current and future modeling. Thus, the latest limitations due to uncertainties in input data (nuclear data or otherwise) can be surpassed through assimilation, enabling their transposition to developing reactors within a unified VVUQ-AT (VVUQ – Assimilation/Transposition) approach. In this context, advanced design and instrumentation work will be required to determine the necessary level of flexibility and target uncertainties to meet these new needs.

Reference

[1] M.-A. Eyl-Mazzega and V. Faudon, “Nuclear revival in the world-Intelligence report,” 2023.

[2] “GIF R&D Outlook for Generation IV Nuclear Energy Systems 2018 Update new cover,” GIF Portal. Accessed: Jun. 14, 2024. [Online]. Available: https://www.gen-4.org/gif/jcms/c_196887/gif-r-d-outlook-for-generation-iv-nuclear-energy-systems-2018-update-new-cover?details=true

[3] J.-F. Parisot and France, Eds., *Sodium-cooled nuclear reactors*. in DEN monographs. Paris: Editions Le Moniteur : CEA, 2016.

[4] A. de sûreté French Nuclear Safety Agency, “Qualification of scientific computing tools used in the nuclear safety case - ASN Guide n° 28.” Accessed: Jun. 15, 2024. [Online]. Available: https://www.french-nuclear-safety.fr/asn-regulates/asn-guides/asn-guide-no.-28

[5] G. Palmiotti and M. Salvatores, “The role of experiments and of sensitivity analysis in simulation validation strategies with emphasis on reactor physics,” *Ann. Nucl. Energy*, vol. 52, pp. 10–21, Feb. 2013, doi: 10.1016/j.anucene.2012.06.002.

[6] A. Calame, “Contribution à la validation du calcul de la puissance résiduelle des réacteurs à neutrons rapides : aspects expérimentaux et méthodologiques,” These de doctorat, Aix-Marseille, 2020. Accessed: Jul. 28, 2022. [Online]. Available: http://www.theses.fr/2020AIXM0424

[7] J. Tommasi and G. Noguère, “Analysis of the PROFIL and PROFIL-2 Sample Irradiation Experiments in Phénix for JEFF-3.1 Nuclear Data Validation,” *Nucl. Sci. Eng.*, vol. 160, no. 2, pp. 232–241, Oct. 2008, doi: 10.13182/NSE160-232.

[8] M. Foissy, “Développement d’une méthode de qualification et quantification des incertitudes des caractéristiques neutroniques du cœur d’ASTRID en fin de cycle,” These de doctorat, Aix-Marseille, 2020. Accessed: Jul. 26, 2022. [Online]. Available: http://www.theses.fr/2020AIXM0264

[9] P. Reuss, *Précis de neutronique*. in Génie atomique. Les Ulis: EDP sciences, 2003.

[10] K. M. Case, F. de Hoffman, and G. Placzek, *Introduction to the Theory of Neutron Diffusion, Volume 1*. Los Alamos, New Mexico, 1953.

[11] D. Dubbers and B. Märkisch, “Precise Measurements of the Decay of Free Neutrons,” *Annu. Rev. Nucl. Part. Sci.*, vol. 71, no. 1, pp. 139–163, 2021, doi: 10.1146/annurev-nucl-102419-043156.

[12] Commissariat à l’énergie atomique et aux énergies alternatives, Ed., *Neutronics*. in E-den. Paris Gif-sur-Yvette: Éditions “Le Moniteur” CEA, 2015.

[13] H. Bateman, “The solution of a system of differential equations occurring in the theory of radio-active transformations,” *Proc. Camb. Philos. Soc.*, vol. XV, p. pp.423-427, 1910.

[14] W. Rubinson, “The Equations of Radioactive Transformation in a Neutron Flux,” *J. Chem. Phys.*, vol. 17, no. 6, pp. 542–547, Jun. 1949, doi: 10.1063/1.1747317.

[15] G. Valocchi, “Modélisation neutronique de coeurs complexes en cinétique multidimensionnelle : application au coeur astrid faible vidange et à la préparation d’expériences de validation,” These de doctorat, Aix-Marseille, 2020. Accessed: Jul. 26, 2022. [Online]. Available: http://www.theses.fr/2020AIXM0101

[16] G. Rimpault *et al.*, “The ERANOS Code and data system for fast reactor neutronic analyses,” p. 15, 2002.
[17] S. Lahaye, P. Bellier, H. Mao, A. Tsilanizara, and Y. Kawamoto, *First verification and validation steps of MENDEL Release 1.0 cycle code system*. 2014.
[18] S. Lahaye, T. D. Huynh, and A. Tsilanizara, “Comparison of deterministic and stochastic approaches for isotopic concentration and decay heat uncertainty quantification on elementary fission pulse,” *EPJ Web Conf.*, vol. 111, p. 09002, 2016, doi: 10.1051/epjconf/201611109002.
[19] N. Metropolis and S. Ulam, “The Monte Carlo Method,” *J. Am. Stat. Assoc.*, vol. 44, no. 247, pp. 335–341, Sep. 1949, doi: 10.1080/01621459.1949.10483310.
[20] E. Brun *et al.*, “Tripoli-4®, CEA, EDF and AREVA reference Monte Carlo code,” in *Annals of Nuclear Energy*, 2015. doi: 10.1016/j.anucene.2014.07.053.
[21] B. Faure, “Development of neutronic calculation schemes for heterogeneous sodium-cooled nuclear cores in the Apollo3 code : application to the ASTRID prototype,” These de doctorat, Aix-Marseille, 2019. Accessed: Jul. 26, 2022. [Online]. Available: http://www.theses.fr/2019AIXM0289
[22] A. Santamarina, D. Bernard, Y. Rugama, and OECD Nuclear Energy Agency, *The JEFF-3.1.1 nuclear data library: JEFF report 22, validation results from JEF-2.2 to JEFF-3.1.1*. Issy-les-Moulineaux, France: Nuclear Energy Agency, Organisation for Economic Cooperation and Development, 2009.
[23] J.-F. Vidal, “Contributions à l’amélioration des méthodes déterministes et des schémas de calcul neutronique des réacteurs nucléaires,” Université Grenoble Alpes, 2018.
[24] M. COSTE-DELCLAUX, *GALILEE: A nuclear data processing system for transport, depletion and shielding codes*. Switzerland: Paul Scherrer Institut - PSI, 2008.
[25] D. Sciannandrone, S. Santandrea, L. Mao, R. Sanchez, and J.-F. Vidal, *COUPLED FINE-GROUP THREE-DIMENSIONAL FLUX CALCULATION AND SUBGROUPS METHOD FOR A FBR HEXAGONAL ASSEMBLY*. 2015.
[26] T. Tone, “A Numerical Study of Heterogeneity Effects in Fast Reactor Critical Assemblies,” *J. Nucl. Sci. Technol.*, vol. 12, no. 8, pp. 467–481, Aug. 1975, doi: 10.1080/18811248.1975.9733139.
[27] L. Mao and I. Zmijarevic, “A new Tone’s method in APOLLO3® and its application to fast and thermal reactor calculations,” *Nucl. Eng. Technol.*, vol. 49, no. 6, pp. 1269–1286, Sep. 2017, doi: 10.1016/j.net.2017.08.002.
[28] P. Archier, J.-M. Palau, J.-F. Vidal, S. Santandrea, and D. Sciannandrone, “Validation of the Newly Implemented 3D TDT-MOC Solver of APOLLO3 Code on a Whole 3D SFR Heterogeneous Assembly,” in *PHYSOR 2016-Unifying Theory and Experiments in the 21st Century*, 2016.
[29] J.-J. Lautard and J.-Y. Moller, “MINARET, A DETERMINISTIC NEUTRON TRANSPORT SOLVER FOR NUCLEAR CORE CALCULATIONS.” Dec. 13, 2010. Accessed: Feb. 07, 2022. [Online]. Available: https://hal-cea.archives-ouvertes.fr/cea-00545919
[30] A. Conti, A. Gerschenfeld, Y. Gorsse, T. Cadiou, and R. Lavastre, “Numerical analysis of core thermal-hydraulic for sodium-cooled fast reactors,” presented at the NURETH 2015 - 16th International Topical Meeting on Nuclear Reactor Thermal Hydraulics, Aug. 2015. Accessed: Mar. 03, 2024. [Online]. Available: https://cea.hal.science/cea-02489500
[31] D. Tenchine *et al.*, “Status of CATHARE code for sodium cooled fast reactors,” *Nucl. Eng. Des.*, vol. 245, pp. 140–152, Apr. 2012, doi: 10.1016/j.nucengdes.2012.01.019.

[32] B. Michel *et al.*, “Two fuel performance codes of the PLEIADES platform: ALCYONE and GERMINAL,” in *Nuclear Power Plant Design and Analysis Codes*, Elsevier, 2021, pp. 207–233. doi: 10.1016/B978-0-12-818190-4.00009-7.
[33] M. Jeannin, “Développement d’une méthodologie de calcul multiphysique des accidents de remontées intempestives de barre de contrôle dans un réacteur à neutrons rapides refroidi au sodium avec prise en compte des incertitudes,” These de doctorat, Aix-Marseille, 2022. Accessed: Jan. 26, 2024. [Online]. Available: https://www.theses.fr/2022AIXM0344
[34] E. Y. Garcia Cervantes, “Modeling and analysis of Superphénix fast reactor tests with the neutronic calculation scheme APOLLO-3®-SFR for application to the ASTRID reactor,” These de doctorat, Aix-Marseille, 2019. Accessed: Jul. 26, 2022. [Online]. Available: http://www.theses.fr/2019AIXM0274
[35] M. Lainet, B. Michel, J.-C. Dumas, M. Pelletier, and I. Ramière, “GERMINAL, a fuel performance code of the PLEIADES platform to simulate the in-pile behaviour of mixed oxide fuel pins for sodium-cooled fast reactors,” *J. Nucl. Mater.*, vol. 516, pp. 30–53, Apr. 2019, doi: 10.1016/j.jnucmat.2018.12.030.
[36] H. Guo *et al.*, “Advanced method for neutronic simulation of control rods in sodium fast reactors: Numerical and experimental validation,” *Ann. Nucl. Energy*, vol. 129, pp. 90–100, Jul. 2019, doi: 10.1016/j.anucene.2019.01.042.
[37] H. Guo, P. Archier, J.-F. Vidal, and L. Buiron, “Advanced method for depletion calculation of control rods in sodium fast reactors,” *Ann. Nucl. Energy*, vol. 129, pp. 160–168, Jul. 2019, doi: 10.1016/j.anucene.2019.01.045.
[38] E. Privas, P. Archier, C. D. S. Jean, G. Noguere, and J. Tommasi, “The Use of Nuclear Data as Nuisance Parameters in the Integral Data Assimilation of the PROFIL Experiments,” *Nucl. Sci. Eng.*, vol. 182, no. 3, pp. 377–393, Mar. 2016, doi: 10.13182/NSE15-21.
[39] A. Calame, J.-F. Lebrat, and L. Buiron, “Analysis of the TRAPU irradiation in PHENIX with TRIPOLI-4® and DARWIN-3 for the validation of fast reactor fuel depletion calculations,” *Ann. Nucl. Energy*, vol. 157, p. 108167, Jul. 2021, doi: 10.1016/j.anucene.2021.108167.
[40] J.-F. Vidal *et al.*, “APOLLO3 homogenization techniques for transport core calculations—application to the ASTRID CFV core,” *Nucl. Eng. Technol.*, vol. 49, no. 7, pp. 1379–1387, Oct. 2017, doi: 10.1016/j.net.2017.08.014.
[41] B. Faure, P. Archier, J.-F. Vidal, and L. Buiron, “A 2D/1D Algorithm for Effective Cross-Section Generation in Fast Reactor Neutronic Transport Calculations,” *Nucl. Sci. Eng.*, vol. 192, no. 1, pp. 40–51, Oct. 2018, doi: 10.1080/00295639.2018.1480190.
[42] J. Guidez, *Phénix: the experience feedback*. Les Ulis: EDP Sciences, 2013.
[43] J. Tommasi, “ERANOS user’s manual–applications of perturbation theory with finite difference diffusion and Sn transport flux solvers’,” *CEA Rep. SPRCLEPh*, pp. 07–003, 2007.
[44] V. Pascal, M. Vaniere, G. Prulhière, and B. Fontaine, “Interpretation of the Control Rod Withdrawal Test in the Sodium-Cooled Fast Reactor Phénix,” *Nucl. Sci. Eng.*, vol. 175, pp. 109–123, Oct. 2013, doi: 10.13182/NSE12-19.
[45] J. Benoit, “Développement d’un code de propagation des incertitudes des données nucléaires sur la puissance résiduelle dans les réacteurs à neutrons rapides,” These de doctorat, Paris 11, 2012. Accessed: Jul. 26, 2022. [Online]. Available: http://www.theses.fr/2012PA112254

[46] D. Gibiat and V. Pascal, “Calcul des Cycles de Fonctionnement PHENIX avec PROJERIX (ERANOS2.2) - Comparaison avec GEPHIX et Expérience,” 2012, doi: SPRC/LEDC/12-410.
[47] V. Viallon, E. Y. Garcia Cervantes, and L. Buiron, “Impact of the multiphysics coupling on the reactivity swing and fuel depletion of an SFR Phenix like subassembly,” San Francisco-USA, Proceedings of the international conference on physics of reactors (PHYSOR2024), 2024.
[48] J. C. Gauthier *et al.*, “Measurement and Predictions of Control Rod Worth,” *Nucl. Sci. Eng.*, vol. 106, no. 1, pp. 18–29, Sep. 1990, doi: 10.13182/NSE90-02.
[49] G. Girardin, G. Rimpault, P. Coddington, and R. Chawla, “Control rod shadowing and anti-shadowing effects in a large gas-cooled fast reactor,” in *Proceedings of ICAPP*, 2007.
[50] H. K. Louis, R. M. Refeat, and M. I. Hassan, “Control rod shadowing effect in PWR core utilizing Urania-Gadolinia fuel,” *Prog. Nucl. Energy*, vol. 142, p. 103993, Dec. 2021, doi: 10.1016/j.pnucene.2021.103993.
[51] J. Cetnar, G. Domańska, P. Gajda, and J. Janczyszyn, “Assessment of the control rods shadow effect in the VENUS-F core,” *Nukleonika*, vol. 59, no. 4, pp. 137–143, Dec. 2014, doi: 10.2478/nuka-2014-0020.
[52] J. Zhang, “Modern Monte Carlo methods for efficient uncertainty quantification and propagation: A survey,” *WIREs Comput. Stat.*, vol. 13, no. 5, p. e1539, Sep. 2021, doi: 10.1002/wics.1539.
[53] C. De Boor, *A practical guide to splines: with 32 figures*, Rev. ed. in Applied mathematical sciences, no. v. 27. New York: Springer, 2001.
[54] “scipy.interpolate.CubicSpline — SciPy v1.11.2 Manual.” Accessed: Sep. 06, 2023. [Online]. Available: https://docs.scipy.org/doc/scipy/reference/generated/scipy.interpolate.CubicSpline.html#id2
[55] S. Kokoska and D. Zwillinger, *CRC standard probability and statistics tables and formulae*, Student ed. Boca Raton, Fla: Chapman & Hall/CRC, 2000.
[56] “scipy.optimize.curve_fit — SciPy v1.11.3 Manual.” [Online]. Available: https://docs.scipy.org/doc/scipy/reference/generated/scipy.optimize.curve_fit.html#scipy.optimize.curve_fit
[57] BIPM, IEC, IFCC, ISO, IUPAC, and OIML, “Evaluation of measurement data — Guide to the expression of uncertainty in measurement,” 2008. [Online]. Available: https://www.bipm.org/documents/20126/2071204/JCGM_100_2008_E.pdf
[58] J. Blázquez, A. García-Berrocal, C. Montalvo, and M. Balbás, “The coverage factor in a Flatten–Gaussian distribution,” *Metrologia*, vol. 45, no. 5, pp. 503–506, Oct. 2008, doi: 10.1088/0026-1394/45/5/002.
[59] P. Archier, C. De Saint Jean, G. Noguere, O. Litaize, P. Leconte, and C. Bouret, “COMAC. Nuclear data covariance matrices library for reactor applications,” Japan, Proceedings of the international conference on physics of reactors (PHYSOR2014) JAEA-CONF--2014-003, 2015. [Online]. Available: http://dx.doi.org/10.11484/jaea-conf-2014-003
[60] G. Truchet, P. Leconte, A. Santamarina, E. Brun, F. Damian, and A. Zoia, “Computing adjoint-weighted kinetics parameters in Tripoli-4® by the Iterated Fission Probability method,” *Ann. Nucl. Energy*, vol. 85, pp. 17–26, Nov. 2015, doi: 10.1016/j.anucene.2015.04.025.

[61] G. Valocchi, P. Archier, and J. Tommasi, “BETA EFFECTIVE SENSITIVITY TO NUCLEAR DATA WITHIN THE APOLLO3® NEUTRONIC PLATFORM,” *EPJ Web Conf.*, vol. 247, p. 15003, 2021, doi: 10.1051/epjconf/202124715003.
[62] I.-A. Kodeli, “Sensitivity and uncertainty in the effective delayed neutron fraction (<math><msub is="true"><mrow is="true"><mi is="true">β</mi></mrow><mrow is="true"><mi is="true">eff</mi></mrow></msub></math>),” *Nucl. Instrum. Methods Phys. Res. Sect. Accel. Spectrometers Detect. Assoc. Equip.*, vol. 715, pp. 70–78, Jul. 2013, doi: 10.1016/j.nima.2013.03.020.
[63] E. D. Pendlebury, “General Perturbation Theory in Neutronics,” *Proc. Phys. Soc. Sect. A*, vol. 68, no. 6, pp. 474–481, Jun. 1955, doi: 10.1088/0370-1298/68/6/302.
[64] A. Gandini, G. Palmiotti, and M. Salvatores, “Equivalent generalized perturbation theory (EGPT),” *Ann. Nucl. Energy*, vol. 13, no. 3, pp. 109–114, Jan. 1986, doi: 10.1016/0306-4549(86)90001-0.
[65] A. Gandini, “Time-dependent generalized perturbation methods for burn-up analysis,” Comitato Nazionale per l’Energia Nucleare, 1975.
[66] M. L. Williams, “Development of Depletion Perturbation Theory for Coupled Neutron/Nuclide Fields,” *Nucl. Sci. Eng.*, vol. 70, no. 1, pp. 20–36, Apr. 1979, doi: 10.13182/NSE79-3.
[67] T. Takeda and T. Umano, “Burnup Sensitivity Analysis in a Fast Breeder Reactor—Part I: Sensitivity Calculation Method with Generalized Perturbation Theory,” *Nucl. Sci. Eng.*, vol. 91, no. 1, pp. 1–10, Sep. 1985, doi: 10.13182/NSE85-5.
[68] N. Linden, “Elaboration d’une méthodologie d’analyse de sensibilité couplées fondée sur la théorie des perturbations généralisée. Application aux grandeurs physiques du cycle du combustible.,” These en préparation, Aix-Marseille, 2020. Accessed: Apr. 18, 2024. [Online]. Available: https://theses.fr/2023AIXM9066
[69] T. Zu, C. Yang, L. Cao, and H. Wu, “Nuclear data uncertainty propagation analysis for depletion calculation in PWR and FR pin-cells,” *Ann. Nucl. Energy*, vol. 94, pp. 399–408, Aug. 2016, doi: 10.1016/j.anucene.2016.04.006.
[70] T. J. Downar and H. Khalil, “Uncertainty in the Burnup Reactivity Swing of Liquid-Metal Fast Reactors,” *Nucl. Sci. Eng.*, Nov. 1991, doi: 10.13182/NSE91-A23853.
[71] L. Fiorito, G. Žerovnik, A. Stankovskiy, G. Van den Eynde, and P. E. Labeau, “Nuclear data uncertainty propagation to integral responses using SANDY,” *Ann. Nucl. Energy*, vol. 101, pp. 359–366, Mar. 2017, doi: 10.1016/j.anucene.2016.11.026.
[72] L. Fiorito, A. Stankovskiy, G. Van den Eynde, C. J. Diez, O. Cabellos, and P. E. Labeau, “Generation of fission yield covariances to correct discrepancies in the nuclear data libraries,” *Ann. Nucl. Energy*, vol. 88, pp. 12–23, Feb. 2016, doi: 10.1016/j.anucene.2015.10.027.
[73] L. Fiorito, C. J. Diez, O. Cabellos, A. Stankovskiy, G. Van den Eynde, and P. E. Labeau, “Fission yield covariance generation and uncertainty propagation through fission pulse decay heat calculation,” *Ann. Nucl. Energy*, vol. 69, pp. 331–343, Jul. 2014, doi: 10.1016/j.anucene.2014.01.038.
[74] V. Huy, “Contribution to nuclear data improvement by assimilation of integral experiments for the ASTRID core neutronic characterization,” These de doctorat, Aix-Marseille, 2018. Accessed: Jun. 09, 2024. [Online]. Available: https://theses.fr/2018AIXM0333
[75] O. Cabellos, N. García-Herranz, and SG46 members, “Target Accuracy Requirements Exercise within WPEC/SG46 and Feedback on Nuclear Data Needs,” *EPJ Web Conf.*, vol. 294, p. 05003, 2024, doi: 10.1051/epjconf/202429405003.

[76] E. Dupont *et al.*, “HPRL – International cooperation to identify and monitor priority nuclear data needs for nuclear applications,” *EPJ Web Conf.*, vol. 239, p. 15005, 2020, doi: 10.1051/epjconf/202023915005.
[77] E. FORT, W. ASSAL, G. Rimpault, J. ROWLANDS, I. SMITH, and R. Soule, “Realisation and Performance of the Adjusted Nuclear Data ERALIB1 for Calculating Fast Reactor Neutronics,” May 2012.
[78] E. Ivanov, C. De Saint-Jean, and V. Sobes, “Nuclear data assimilation, scientific basis and current status,” *EPJ Nucl. Sci. Technol.*, vol. 7, p. 9, 2021, doi: 10.1051/epjn/2021008.
[79] B. Habert, “Estimation des incertitudes dans l’évaluation des sections efficaces de réactions nucléaires,” These de doctorat, Grenoble INPG, 2009. Accessed: May 13, 2024. [Online]. Available: https://theses.fr/2009INPG0128
[80] C. E. Shannon, “A mathematical theory of communication,” *Bell Syst. Tech. J.*, vol. 27, no. 3, pp. 379–423, Jul. 1948, doi: 10.1002/j.1538-7305.1948.tb01338.x.
[81] C. P. Robert and G. Casella, *Monte Carlo statistical methods*, 2. ed. in Springer texts in statistics. New York, NY: Springer, 2004.
[82] C. De Saint Jean, P. Tamagno, P. Archier, and G. Noguere, “CONRAD – a code for nuclear data modeling and evaluation,” *EPJ Nucl. Sci. Technol.*, vol. 7, p. 10, 2021, doi: 10.1051/epjn/2021011.
[83] B. Habert, C. D. S. Jean, G. Noguere, L. Leal, and Y. Rugama, “Retroactive Generation of Covariance Matrix of Nuclear Model Parameters Using Marginalization Techniques,” *Nucl. Sci. Eng.*, vol. 166, no. 3, pp. 276–287, Nov. 2010, doi: 10.13182/NSE09-85.
[84] “Investigation of Covariance Data in General Purpose Nuclear Data Libraries,” Nuclear Energy Agency (NEA). Accessed: May 16, 2024. [Online]. Available: https://www.oecd-nea.org/jcms/pl_78107/investigation-of-covariance-data-in-general-purpose-nuclear-data-libraries?details=true
[85] M. B. Chadwick *et al.*, “ENDF/B-VII.1 Nuclear Data for Science and Technology: Cross Sections, Covariances, Fission Product Yields and Decay Data,” *Nucl. Data Sheets*, vol. 112, no. 12, pp. 2887–2996, Dec. 2011, doi: 10.1016/j.nds.2011.11.002.
[86] K. SHIBATA *et al.*, “JENDL-4.0: A New Library for Nuclear Science and Engineering,” *J. Nucl. Sci. Technol.*, vol. 48, no. 1, pp. 1–30, Jan. 2011, doi: 10.1080/18811248.2011.9711675.
[87] M. Salvatores and G. Palmiotti, “Method and approaches to provide feedback from nuclear and covariance data adjustment for improvement of nuclear data files: Major findings of the NEA WPEC Subgroup 39,” *EPJ Web Conf.*, vol. 239, p. 13001, 2020, doi: 10.1051/epjconf/202023913001.
[88] P. Talou, “Making sense of uncertain nuclear data,” *Ann. Nucl. Energy*, vol. 164, p. 108568, Dec. 2021, doi: 10.1016/j.anucene.2021.108568.
[89] “International Evaluation Co-operation, Volume 33,” Nuclear Energy Agency (NEA). Accessed: May 18, 2024. [Online]. Available: https://www.oecd-nea.org/jcms/pl_14876/international-evaluation-co-operation-volume-33?details=true
[90] E. Fort *et al.*, “Improved performances of the fast reactor calculational system ERANOS-ERALIB1 due to improved a priori nuclear data and consideration of additional specific integral data1,” *Ann. Nucl. Energy*, vol. 30, no. 18, pp. 1879–1898, Dec. 2003, doi: 10.1016/S0306-4549(03)00161-0.
[91] V. Orlov, A. Van’Kov, A. Voropaev, Y. A. Kazanskii, V. Matveev, and V. Murogov, “Problems of fast reactor physics related to breeding,” *Energy RevInternational At. Energy Agency IAEA*, vol. 18, no. 4, 1980.

[92] J. B. Briggs and others, “International handbook of evaluated criticality safety benchmark experiments,” *Nucl. Energy Agency NEANSCDOC 95*, vol. 3, p. l, 2004.
[93] IRPhE, “International Handbook of Evaluated Reactor Physics Benchmark Experiments (IRPhE).” OECD/NEA/NSC/DOC(2006)1, 2006. Accessed: Jul. 26, 2022. [Online]. Available: https://www.oecd-nea.org/jcms/pl_20279/international-handbook-of-evaluated-reactor-physics-benchmark-experiments-irphe
[94] A. Nouri, P. Nagel, J. B. Briggs, and T. Ivanova, “DICE: Database for the International Criticality Safety Benchmark Evaluation Program Handbook,” *Nucl. Sci. Eng.*, vol. 145, no. 1, pp. 11–19, Sep. 2003, doi: 10.13182/NSE03-15.
[95] I. Hill, N. Soppera, and M. Bossant, “IDAT: The International Handbook of Evaluated Reactor Physics Benchmark Experiments Database and Analysis Tool,” *Nucl. Sci. Eng.*, vol. 178, no. 3, pp. 280–294, Nov. 2014, doi: 10.13182/NSE14-37.
[96] J. Dyrda, I. Hill, M. Bossant, J. Gulliford, and N. Soppera, “The New OECD-NEA Nuclear Data and Sensitivity Tool (NDaST),” in *ANS Winter meeting proceedings, Washington DC, USA*, 2015.
[97] J. Dyrda, N. Soppera, I. Hill, M. Bossant, and J. Gulliford, “New features and improved uncertainty analysis in the NEA nuclear data sensitivity tool (NDaST),” *EPJ Web Conf.*, vol. 146, p. 06026, 2017, doi: 10.1051/epjconf/201714606026.
[98] K. Yokoyama and M. Ishikawa, “Evaluation of Burnup Reactivity Coefficients Measured in Experimental Fast Reactor JOYO MK-I Duty Power Operation Cycles,” *Nucl. Sci. Eng.*, vol. 178, no. 3, pp. 350–362, Nov. 2014, doi: 10.13182/NSE14-11.
[99] N. Materne, “Validation et Quantification des Incertitudes des grandeurs neutroniques des RNR-Na,” Université Clermont Auvergne, Master thesis, Sep. 2024.
[100] E. Y. Garcia Cervantes *et al.*, “Status of the WPRS SEFOR Benchmark Phase I: Isothermal Tests,” presented at the BEPU 2024, 2024.
[101] C. M. Perfetti, B. T. Rearden, and W. R. Martin, “SCALE Continuous-Energy Eigenvalue Sensitivity Coefficient Calculations,” *Nucl. Sci. Eng.*, vol. 182, no. 3, pp. 332–353, Mar. 2016, doi: 10.13182/NSE15-12.
[102] N. Terranova, D. Mancusi, and A. Zoia, “New perturbation and sensitivity capabilities in Tripoli-4®,” *Ann. Nucl. Energy*, vol. 121, pp. 335–349, Nov. 2018, doi: 10.1016/j.anucene.2018.07.031.
[103] M. Salvatores *et al.*, “Methods and Issues for the Combined Use of Integral Experiments and Covariance Data: Results of a NEA International Collaborative Study,” *Nucl. Data Sheets*, vol. 118, pp. 38–71, Apr. 2014, doi: 10.1016/j.nds.2014.04.005.
[104] “Intermediate Report on Methods and Approaches to Provide Feedback from Nuclear and Covariance Data Adjustment for Improvement of Nuclear Data Files,” Nuclear Energy Agency (NEA). Accessed: May 16, 2024. [Online]. Available: https://www.oecd-nea.org/jcms/pl_19760/intermediate-report-on-methods-and-approaches-to-provide-feedback-from-nuclear-and-covariance-data-adjustment-for-improvement-of-nuclear-data-files?details=true
[105] D. Foligno, “New evaluation of delayed-neutron data and associated covariances,” These de doctorat, Aix-Marseille, 2019. Accessed: Jul. 28, 2022. [Online]. Available: https://www.theses.fr/2019AIXM0295
[106] E. Fermi, “Problem of time dependence of the reaction rate: effect of delayed neutrons emission,” *CP-291 Chic. Proj. Rep. Oct.*, vol. 7, 1942.
[107] A. F. . Henry, “The Application of Reactor Kinetics to the Analysis of Experiments,” *Nucl. Sci. Eng.*, vol. 3, no. 1, pp. 52–70, Jan. 1958, doi: 10.13182/NSE58-1.

[108] W. S. Yang, “FAST REACTOR PHYSICS AND COMPUTATIONAL METHODS,” *Nucl. Eng. Technol.*, vol. 44, no. 2, pp. 177–198, Mar. 2012, doi: 10.5516/NET.01.2012.504.
[109] F. Jeanpierre and M. Livolant, “Autoprotection des résonances dans les réacteurs nucléaires,” *Rapp. CEA R*, vol. 4533, 1974.
[110] J. R. White, “Development, implementation, and verification of multicycle depletion perturbation theory for reactor burnup analysis,” Oak Ridge National Lab., 1980.

APPENDIXES

A.Point Kinetics

For time scales short enough that variations in isotopic compositions are not considered, only the sources of prompt and delayed neutrons are affected. The kinetics of prompt neutrons are primarily governed by their average lifetime in a reactor, which is on the order of 10^{-6} to 10^{-7} seconds, whereas the kinetics of delayed neutrons are mainly controlled by the decay constants of the precursors, which range from tenths of a second to tens of seconds[dd]. The source of prompt neutrons represents the vast majority of the fission source but does not equalise neutron losses in the neutron balance of a critical reactor. Delayed neutrons provide the additional neutrons necessary to achieve criticality, and this margin of delayed neutrons allows for reactor control with reasonable time constants for the control systems.

To study the evolution of the neutron population with the time component in the Boltzmann equation, calculations would need to be performed with a time resolution on the order of the smallest time constants present in the transport equation, which is on the order of microseconds. However, the usual kinetics phenomena (excluding accidents) range from several tens of seconds to several hundreds of days, which would require a considerable amount of computation time. Therefore, direct coupled calculations of the Boltzmann and Bateman equations are never performed for these issues. Instead, a simplification is made by decoupling the spatial, angular, and energy components of the flux (considering an invariant flux shape over time) from the time component. This means treating the reactor with averaged spatial, energy, and angular values as a point reactor. Additionally, instead of representing all precursors (more than a hundred isotopes with their own characteristics), they are grouped into 6 or 8 families[ee]. These families are constructed by considering pseudo-precursors with specific decay constants λ_i and a fraction of delayed neutrons associated with each family β_i (with the sum of all β_i equal to β). The determination of these coefficients can follow different methods detailed in [105].

[dd] In JEFF 3.1.1, ^{87}Br has a half-life of 55.68 seconds with a 2.60% chance of emitting a neutron, while ^{97}Rb has a much shorter half-life of 169.1 milliseconds with a 25.5% chance of emitting a neutron.

[ee] The difference between the two is that the kinetic parameters for each isotope depend on the characteristics of the fuel used and the reactor spectrum in the case of 6 precursor families (the system used in the ENDF nuclear database). In contrast, the kinetic parameters are independent of the fuel and spectrum in the case of 8 precursor families [15].

By adding the assumptions of point kinetics and modeling the precursors in families, the following point kinetics equations are obtained[ff]:

$$\frac{\mathrm{dn(t)}}{\mathrm{dt}} = \frac{\rho - \beta}{\ell}\mathrm{n(t)} + \sum_{\mathrm{i=1}}^{\mathrm{N_f}} \lambda_{\mathrm{i}} \mathrm{C_i} \tag{7-1}$$

$$\frac{dC_i}{dt} = \frac{\beta_i}{\ell} n(t) - \lambda_k C_k \tag{7-2}$$

Where $n(t)$ is the total neutron population in the core, C_k is the concentration of the representative pseudo-precursor of family k, and ℓ is the effective lifetime of prompt neutrons.

The point kinetics equations are a good approximation of spatial kinetics for most reactor physics study cases, allowing the connection of a sensor's count rate variation to a reactivity change and the study of various reactivity effects, such as the impact of control rods.

[ff] Equations demonstrated through a physical approach in [106] and more formally derived from the Boltzmann equation in [107].

B.Deterministic solving methods for fuel transport equation

To accurately solve the steady-state Boltzmann equation with a deterministic method, it is necessary to create a spatial, energy, and angular mesh about the dimensions of various local heterogeneities. For a SFR, the smallest spatial heterogeneities are about a tenth of a millimeter (see Figure 66), involving the thickness of the cladding, the gap, and the dimensions of the spacer wire between fuel pins. The core consists of approximately 200 fissile and fertile subassemblies, and additional radial and axial reflector rings need to be considered, resulting in a spatial mesh size on the order of 10^7.

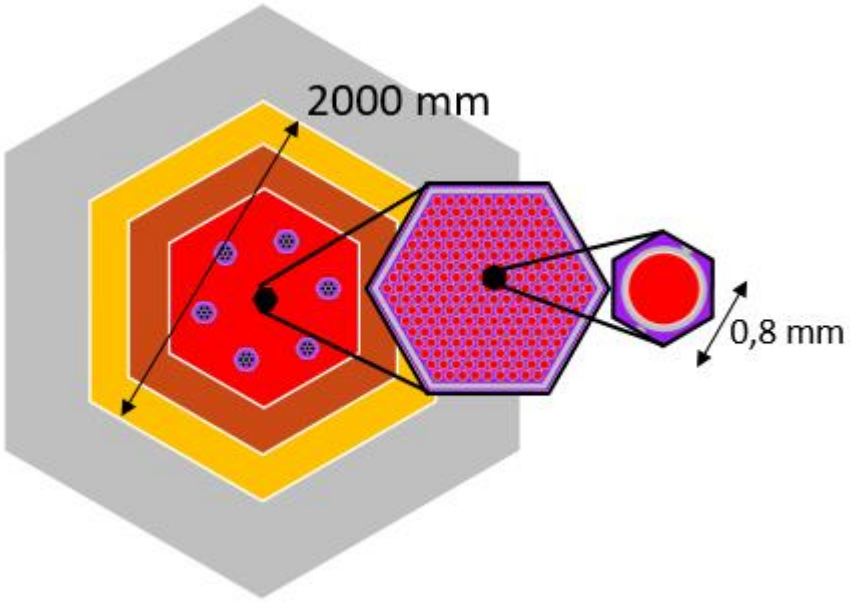

Figure 66. Schematic description of the various spatial dimensions of the Phenix core

Regarding the energy variable, even though the goal in SFRs is to preserve neutrons at high energies as much as possible, the neutron energy spectrum still spans several decades, including the epithermal resonance region. Resonances, with their significant cross-section variations over a very short energy interval (see Figure 67), pose challenges in creating a mesh capable of capturing the smallest heterogeneities. It is commonly accepted that an energy mesh about 10^5 energy groups would be required to adequately represent the influence of resonances from all isotopes on the neutron flux.

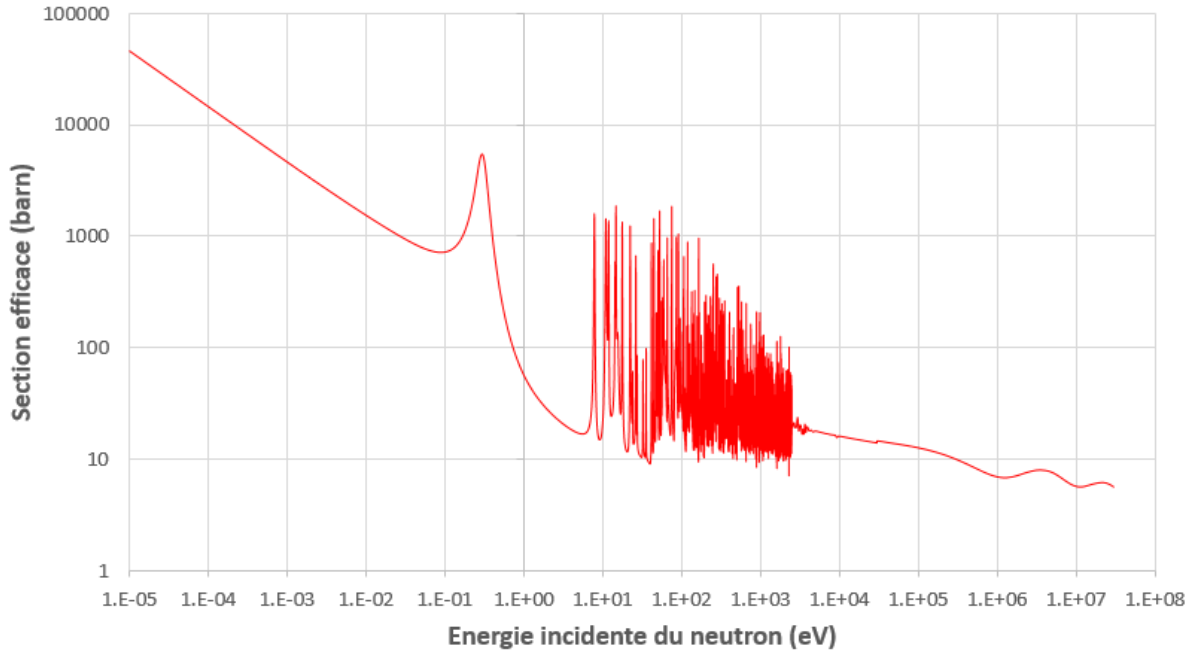

Figure 67. Microscopic total cross-section of the Plutonium 239 [JEFF 3.1.1]

Finally, if an angular description of the order of a hundred directions is added, it would require a phase space mesh on the order of 10^{15} cells, necessitating a RAM and code architecture capable of handling calculations on the order of petabytes. Achieving this type of direct solution to the neutron transport equation for a large reactor core is the ultimate goal of deterministic computing codes but is not yet feasible with standard computational power. Therefore, simplifications are necessary.

Multigroup formalism

To deterministically address the neutron transport equation across the entire phase space at any scale, the initial challenge lies in discretizing the energy variable. The considered energy cells are referred to as energy groups, facilitating the transition from a continuous energy form of the Boltzmann equation to a discrete set of N_g coupled monokinetic transport equations. This form of the Boltzmann equation is known as the multigroup formalism.

In establishing this form, the multigroup angular flux is defined as the sum of contributions from angular fluxes at all energies within the interval $[E_g, E_{g+1}]$:

$$\psi^g(\vec{r},\vec{\Omega}) = \int_{E_g}^{E_{g+1}} \psi^g(\vec{r},E,\vec{\Omega})dE \qquad (7\text{-}3)$$

Next, the input parameters, which are the cross-sections, must be averaged over the same interval. However, the average must preserve all reaction rates within each group. This is achieved by using a flux-weighted average:

$$\Sigma_{\rho}^{i,g}(\vec{r},\vec{\Omega}) = \frac{\int_{E_g}^{E_{g+1}} \Sigma_{\rho}^{i}(\vec{r},E,\vec{\Omega})\psi^{g}(\vec{r},E,\vec{\Omega})dE}{\psi^{g}(\vec{r},\vec{\Omega})} \tag{7-4}$$

$$\Sigma_{s}^{i,g}(\vec{r},\vec{\Omega}'\cdot\vec{\Omega}) = \frac{\int_{E_{g'}}^{E_{g'+1}} dE' \int_{E_g}^{E_{g+1}} \Sigma_{s}^{i}(\vec{r},E'\to E,\vec{\Omega}'\cdot\vec{\Omega})\psi^{g}(\vec{r},E,\vec{\Omega})dE}{\psi^{g}(\vec{r},\vec{\Omega})} \tag{7-5}$$

Which gives for the multigroup Boltzmann equation:

$$\begin{aligned}\left(\vec{\Omega}\cdot\nabla+\Sigma_t^g(\vec{r})\right)\psi^{g}(\vec{r},\vec{\Omega}) &= \sum_i\sum_{g'} d\vec{\Omega}'\Sigma_s^{i,g'\to g}(\vec{r},\vec{\Omega}'\cdot\vec{\Omega})\psi^{g'}(\vec{r},\vec{\Omega'}) \\ &+ \frac{1}{k_{eff}}\frac{1}{4\pi}\Sigma_i\Sigma_{g'}\nu_{g'}^{i}\chi_{g'\to g}^{i}\Sigma_f^{i,g'}(\vec{r})\psi^{g'}(\vec{r},\vec{\Omega'}) \\ &+ S_{ext}^{g}(\vec{r},\vec{\Omega})\end{aligned} \tag{7-6}$$

Or in its operator form:

$$[\mathcal{L}\psi]^{g}(\vec{r},\vec{\Omega}) - \sum_{g'}[\mathcal{H}\psi]^{g'\to g}(\vec{r},\vec{\Omega}) - S_{ext}^{g}(\vec{r},\vec{\Omega}) = \frac{1}{k_{eff}}[\mathcal{F}\psi]^{g}(\vec{r}) \tag{7-7}$$

To solve this set of coupled equations, a process known as power iteration is carried out [23]: The fission source (right-hand side of equation (7-7)) is assumed to be known, enabling the calculation of the terms on the left-hand side of the same equation and obtaining the multigroup fluxes. These fluxes are then used to update the fission source for the next iteration, allowing for the recalculation of the fluxes. This loop is repeated until convergence on the multiplication factor and the multigroup fluxes.

The typical sequential method for determining these fluxes involves solving the multigroup equations in descending order of energy. For a given energy group g, the scattering source comes only from the scattering of groups $g' > g$, which are already known. This method is straightforward for fast and epithermal energies because the collisions are only down-scattering. When thermal energy is approached, an additional phenomenon of up-scattering (neutron acceleration during a collision) occurs, complicating the coupling. In this case, the coupling depends not only on the fluxes of higher groups already calculated but also on the fluxes of lower groups that are still unknown, requiring an additional loop for the relevant groups. However, this phenomenon is negligible in fast spectrum reactors.

The execution of this sweep and the update of the fission source and multiplication factor are referred to as the external iteration. At each step of the sweep, it is necessary to solve the multigroup transport equation for group g with sources considered as known. The

treatment of these monokinetic equations involves handling spatial and angular variables, depending on the application, whether it is lattice or core calculations[gg].

Self-shielding method with TDT/CPM

Self-shielding is the physical phenomenon of flux depletion due to a sharp variation in the cross section. Self-shielding can be spatial in the case of an interface (for example between sodium and ^{10}B contained in a B_4C pellet) and can be energetic in the case of a resonance.

The numerical treatment of self-shielding therefore consists in determining the averaged cross sections in each energy group and spatial mesh (called after this numerical treatment: Self-shielded cross sections) for each isotope considered in each medium considered.

For the spatial aspect, the only special treatment is that the mesh should be smaller than the local neutron mean free path. In fast neutron reactors, the mean free paths between two collisions are about a few centimeters [108], larger than the geometric dimensions of the components of a subassembly (which implies a nearly flat flux). Thus, the refinement necessary to take into account spatial self-shielding is sufficiently affordable not to require a specific physical model associated with this phenomenon.

However, for the energy variable, the mesh necessary for the multigroup formulation to represent, with a low bias, the self-shielding phenomenon is too fine, even for the lattice step. Thus, a specific physical model is necessary to correct the biases introduced by the initial energy condensation. The physical models for the numerical treatment of self-shielding come, like any physical model, with assumptions, which makes them more or less dependent on the types of spectrum and the application case. In deterministic codes (including APOLLO3®), there are mainly two formalisms. The first, called the "fine structure" formalism, based on an equivalence between an infinite homogeneous medium and the heterogeneous medium with assumptions on the slowing down which makes it suitable for the study of thermal spectrum reactors [109]. The second approach, known as the sub-group formalism, relies on the assumption that the slowing down sources are decoupled from the resonance. This formalism is especially suitable for high-energy resonances, making it well suited for fast spectra. It is the sole formalism employed within the framework of this manuscript, predominantly accompanied by an additional approximation: the Tone approximation [26].

[gg] There are many different methods for processing spatial and angular variables in nuclear reactor calculations. These methods can be used at any scale, including the lattice scale and the core scale. However, the accuracy and efficiency of each method depends on the specific type of heterogeneity and the desired precision. In the following, only the methods used in the context of this manuscript are presented.

This decoupling assumption is suitable because the width of high-energy resonances is smaller than the average scattering energy loss on heavy nuclei. A scattering that remains inside the resonance is therefore very unlikely, hence the justification for the decoupling. For low energies, this assumption is no necessarily verfied, but if the energy mesh is fine enough to ensure that the term $\Sigma^{i,g'\to g}$ is negligible, then this method can be exported to all types of spectrum.

The assumption of decoupling between the slowing down sources and the resonance cross-sections therefore implies a high number of groups to ensure that the scattered neutrons leave the group in which they had this reaction. The historical mesh developed to ensure this assumption was the 1968-group mesh. Today, the new reference mesh for lattice calculations on fast spectrum reactors is a 1760-group energy mesh. This new mesh has been optimized for low-energy group and has been developed to unify energy mesh of other spectrum types [23].

Sub-group with Tone approximation are used for the energy parameter but the energy self-shielding is linked with the spatial self-shielding as the flux is not perfectly flat inside the subassembly. For fissile and fertile subassemblies, the outer pins have a different neighboring and have the steel hexagonal tube influence. To take into account the spatial interaction for the self-shielding, the Collision Probability Method (CPM) is used and the Two/three Dimension Transport (TDT) solver in APOLLO-3® ensures it. Hence, for cluster and fundamental mode, the outer ring is considered differently from the rest of the pins in the subassembly (i.e. inner pins have the same self-shielded cross-sections and outer pins have the same self-shielded cross-sections but different from inner pins).

Flux calculation with TDT/MOC

This method is based on the integral form of the transport equation and allows solving it along a 1D trajectory in a given direction $\vec{\Omega}_i$. A trajectory in a given direction is called a characteristic, and the general resolution of the transport equation is achieved by integrating it along each characteristic. This gives then a simple equation to solve on the characteristic scale. Thus, for a trajectory i in the direction $\vec{\Omega}_i$ in the subdomain m and energy group g, the following equation is obtained:

$$\psi^g\left(r^+_{m,i},\vec{\Omega}_i\right)=\psi^g\left(r^-_{m,i},\vec{\Omega}_i\right)e^{-\Sigma^g_m|r^+_{m,i}-r^-_{m,i}|}+\int_0^{|r^+_{m,i}-r^-_{m,i}|}e^{-\Sigma^g_m s'}q^g\left(\vec{r}-s\vec{\Omega}_i,\vec{\Omega}_i\right)ds' \qquad (7\text{-}8)$$

In the previous equation, it can be noticed that the outgoing flux depends on the spatial shape of the source q (and therefore the flux) in the domain m. In order to integrate the second member of equation (7-8), it is assumed that the source (and therefore the flux) has a polynomial form. In the TDT/MOC solver [28] used in APOLLO3®, the source is

considered to be uniform in each domain[hh]. The multiplication of the number of characteristics in a given direction (defined by their spacing Δr, see Figure 68) and the number of directions (defined by N_φ) allows each subdomain to have a discrete set of incoming and outgoing fluxes. With a quadrature formula (which gives a weight ω_i[ii] to each trajectory), it is possible to go from the volume integral in the subdomain to a sum of the incoming/outgoing fluxes on the i characteristics to obtain the angular flux in the subdomain $\psi_m^g(\overrightarrow{\Omega_\iota})$:

$$\psi_m^g(\overrightarrow{\Omega_\iota}) = \frac{q_m^g(\overrightarrow{\Omega_\iota})}{\Sigma_m^g} + \sum_i \omega_i \frac{\psi_m^g(r_{m,i}^+, \overrightarrow{\Omega_\iota}) - \psi_m^g(r_{m,i}^-, \overrightarrow{\Omega_\iota})}{\Sigma_m^g |r_{m,i}^+ - r_{m,i}^-|} \tag{7-9}$$

By propagating from sub-domain to sub-domain along the trajectory, it is possible to consider the outgoing flux from one sub-domain as the incoming flux to its neighbor, enabling the following expression:

$$\psi^g(r_{m,i}^-, \overrightarrow{\Omega_\iota}) = \psi^g(r_{m-1,i}^+, \overrightarrow{\Omega_\iota}) \tag{7-10}$$

With knowledge of the boundary conditions[jj], it is possible to close the equations on the characteristics and obtain all incoming/outgoing fluxes. This enables the solution of the transport equation throughout the entire domain (up to a normalization factor for the flux magnitude).

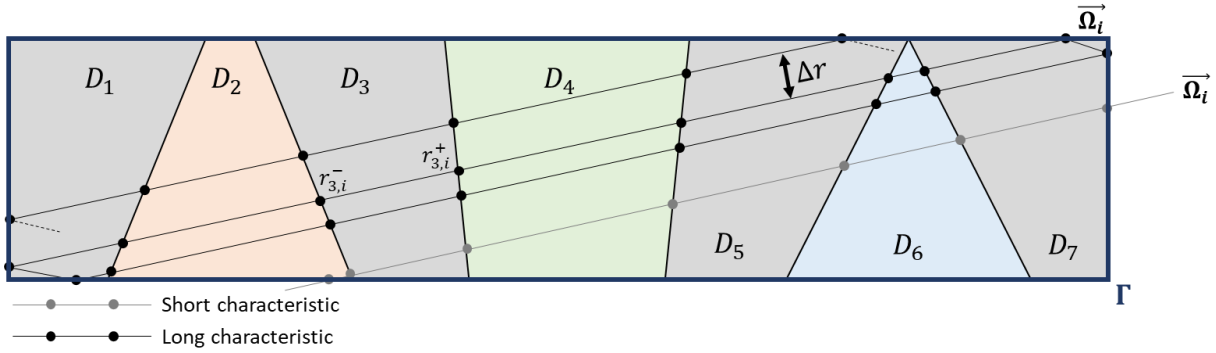

Figure 68. MOC characteristic tracking

[hh] Thus, it is necessary to have a spatial mesh consistent with this assumption of piecewise constant flux in the entire domain.

[ii] The quadrature formula used to calculate the outgoing flux is based on the principle of weighting each trajectory by the surface or volume it sweeps out. The spacing between the trajectories is defined as the distance between two consecutive trajectories. This spacing determines the accuracy of the quadrature formula. The formula for calculating the weight of a trajectory is as follows: $\omega_i = \frac{\Delta r |r_{m,i}^+ - r_{m,i}|}{V_m}$

[jj] For a vacuum boundary condition, the incoming flux is zero, and the trajectories are considered open, extending from one end to the other of the domain. For more complex boundary conditions, such as specular, trajectories must 'stay' within the domain. To achieve this, trajectories are traced until they loop back on themselves, continuing the propagation of incoming/outgoing fluxes. These are referred to as cyclic trajectories.

After obtaining the angular flux, it becomes feasible to update the fission and scattering sources and iterate until the flux converges.

This approach, involving the computation of angular fluxes, enables the consideration of the anisotropy in the diffusion source. The differential cross-section can be expanded using Legendre polynomials to account for shock anisotropy.

$$\Sigma_s^i\left(\vec{r}, E' \to E, \overrightarrow{\Omega'} \cdot \vec{\Omega}, t\right) = \frac{1}{4\pi} \sum_{l=0}^{\infty} (2l+1) \Sigma_{s,l}^i(\vec{r}, E' \to E, t) P_l\left(\overrightarrow{\Omega'} \cdot \vec{\Omega}\right) \tag{7-11}$$

$$\Sigma_{s,l}^i(\vec{r}, E' \to E, t) = \int_{4\pi} d\vec{\Omega} \int_{4\pi} d\overrightarrow{\Omega'}\, \Sigma_s^i\left(\vec{r}, E' \to E, \overrightarrow{\Omega'} \cdot \vec{\Omega}, t\right) P_l\left(\overrightarrow{\Omega'} \cdot \vec{\Omega}\right) \tag{7-12}$$

In the context of numerical resolution, it is not feasible to perform the infinite sum required for exact expansion. Therefore, it is necessary to truncate the expansion. It has been shown in [23] that a third-order expansion is sufficient to accurately represent shock anisotropy in SFR for lattice calculations (referred to as P3).

Cross-section homogenization and condensation

Once the convergence of the flux and the multiplication factor is reached, the lattice calculation can be considered solved. However, the purpose of this step is to provide a set of cross-sections for the large-scale core calculation, with therefore, a coarser energy and spatial mesh. It is refered to the homogenization (spatial) step and the energy collapse step, which allows creating this library of cross-sections for the core calculation.

Similarly to the self-shielding phenomenon, performing a spatial and energy average must conserve the reaction rates and therefore the 1760 energy group cross-sections must be weighted during the homogenization/energy collapse process.

There are therefore several types of weighting depending on whether the weighting parameter is the scalar flux, flux momentum or the current. The approach used in this manuscript is the one by the scalar flux, which gives for the homogenized and energetically collapsed cross-sections and fluxes:

$$\Sigma_{x,D}^{i,G} = \frac{\sum_{m \in D} \sum_{g \in G} \Sigma_{x,m}^{i,g} \phi_m^g}{\phi_M^G} \qquad \forall x \neq s \tag{7-13}$$

$$\Sigma_{sl,D}^{i,G' \to G} = \frac{\sum_{m \in D} \sum_{g' \in G'} \sum_{g \in G} \Sigma_{sl,m}^{i,g' \to g} \phi_m^g}{\phi_M^{G'}} \tag{7-14}$$

$$\phi_D^G = \sum_{g \in G} \sum_{m \in D} \phi_m^g \tag{7-15}$$

Leakage Model at the lattice scale

While homogenization methods and energy collapse enable a more or less accurate recording of information about the flux at the lattice scale, it is still calculated under conditions vastly different from the actual core conditions. Indeed, boundary conditions tend to make the problem highly supercritical in the case of specular or translation boundary conditions, or potentially highly subcritical for absorbers or void boundary conditions. A core in normal operation is critical, and thus, the flux between the hypothetical, highly supercritical (or subcritical) state at the lattice scale and the actual critical core flux differs.

The first step involves considering the flux as the real part of a periodic complex flux (decoupled from the spatial variable) whose periodicity follows a macroscopic form defined by a space and Laplacian-dependent term, $\vec{B}$, $e^{-\vec{B}\cdot\vec{r}}$. This yields the flux in both models:

$$\psi(\vec{r},E,\vec{\Omega}) = \mathcal{R}e\left(\psi_B(E,\vec{\Omega})e^{-\vec{B}\cdot\vec{r}}\right) \tag{7-16}$$

The introduction of the complex flux in the transport equation leads to the following system of equations when the P1 law is used:

$$\Sigma_t^g \phi_{\mathcal{R}e}^g = \sum_{g'=1}^{N_g} \Sigma_{s0}^{g'\to g}\phi_{\mathcal{R}e}^{g'} + Q_f^g - D^g B^2 \phi_{\mathcal{R}e}^g \tag{7-17}$$

$$D^g = \frac{\Lambda\left(\frac{B}{\Sigma_t^g}\right)}{3\Sigma_t^g}\left[1 + 3\sum_{g'=1}^{N_g}\Sigma_{sl}^{g'\to g} D^{g'}\frac{\phi_{\mathcal{R}e}^{g'}}{\phi_{\mathcal{R}e}^{g}}\right] \tag{7-18}$$

$$\Lambda\left(\frac{B}{\Sigma_t^g}\right) = 3\left(\frac{1-\frac{\Sigma_t^g}{B}arctg\left(\frac{B}{\Sigma_t^g}\right)}{\frac{B}{\Sigma_t^g}arctg\left(\frac{B}{\Sigma_t^g}\right)}\right) \tag{7-19}$$

$$D^g B^2 \phi_{\mathcal{R}e}^g = B\, J_{l,m}^g \tag{7-20}$$

Considering that $\phi_{\mathcal{R}e}$ is the scalar flux of the real part of the complex flux ψ_B and $J_{\mathcal{I}m}$ is the integrated imaginary current of the imaginary part of the same flux, these equations depend on the value of the Laplacian B. Since it is not possible to determine the value of B in advance, an additional iteration loop is necessary to determine its value and achieve criticality.

Therefore, the B1-Homogeneous model allows obtaining a system of real equations despite introducing a complex flux. As the obtained fluxes are real, the homogenized and condensed cross-sections are also real, without adding any additional complications.

Flux calculation with MINARET

The S_n method handled by the MINARET involves solving the transport equation for a discrete number of directions and transforming angular integrals into quadrature formulas for the resolved directions. For a given direction $\vec{\Omega}_n$ and energy group g, solving the transport equation within a geometric cell involves dealing with the advection operator $(\vec{\Omega}_n \cdot \vec{\nabla})\psi_n^g$. In neutronics, the spatial treatment of this operator is often carried out using finite difference, finite volume, or finite element methods. In APOLLO3®, the MINARET S_n solver [29] employs the finite element method, specifically discrete Galerkin finite elements, for spatial treatment. Handling the transport equation through this method requires employing the variational form of the equation (i.e., projecting the equation onto an arbitrary vector in the Sobolev space of integrable L^2 functions).

The spatial mesh of the entire domain allows transforming the spatial integral over the domain into a sum of integrals over each spatial cell. The classical formulation of finite elements requires continuity of the flux at the interface of each cell, coupling all cells, which would involve high-dimensional matrix inversions. To simplify the problem, continuity of the flux is not considered, leading to the discrete formulation. This formulation provides, at the scale of a cell K in the domain and for a given direction (the following equation:

$$\int_K \vec{\Omega} \cdot \vec{\nabla}\, \psi w \overrightarrow{dr} + \int_{\Gamma_e} \vec{\Omega} \cdot \overrightarrow{\mathrm{n_e}}\, (\psi_e^+ - \psi_e^-) w \overrightarrow{dr} + \int_K \Sigma\, \psi w \overrightarrow{dr} = \int_K \mathrm{q}\, \psi w \overrightarrow{dr} \;\; \forall w \in V(K) \qquad (7\text{-}21)$$

With w as an arbitrary vector in $V(K)$ (the Sobolev space of L^2 integrable functions over K), ψ_e^+ representing the incoming flux (respectively outgoing for ψ_e^-),), and Γ_e denoting the boundaries of cell K and $\psi = \psi^g(\vec{r}, \overrightarrow{\Omega_n})$.

To solve the energy group transport equation g in direction $\vec{\Omega}$ in a mesh K, a polynomial basis is used to define the set of w (the maximum order of this basis and the number of points calculated in the mesh depends on the type of finite element and the orders chosen by the user). The flux is then calculated at the characteristic points of the type of finite element. The discrete variational formulation and the non-continuity of the flux at the interfaces allow the flux in each mesh to be solved independently of the other meshes. This is because the calculation of the flux in a mesh only depends on the incoming fluxes. Therefore, it is possible to solve the flux, mesh after mesh, by considering a propagation front moving in the direction of the chosen direction. Additionally, the directions being independent, it is possible to parallelize the computation of the flux in each direction.

C. APOLLO3®-FR deterministic characteristics

Parameter considered for the APOLLO3-FR scheme in this study are summarized in Table XXVI for the lattice calculation in the cluster paradigm and in Table XXVII for the core calculation with MINARET.

Table XXVI. APOLLO3®-FR lattice calculation solver and parmaeters

Geometry	Exact geometry with the cluster paradigm
Energy group	1760
Self-Shielding	TDT | exact CPM + subgroup + Tone
Δr [cm]	0.05
Nφ	24
Anisotropy	3
Flux	TDT/MOC
Δr [cm]	0.05
Nφ	48
Anisotropy	3
Leakage model	B1 (fuel and absorber) – B^2=0 (structures)
Homogenization model	Scalar flux weighting
Homogenization angular order	P1

Table XXVII. APOLLO3®-FR core calculation solver and parameters

Geometry	Homogenized SA with explicit modeling of control rod absorber lattice
Energy group	33
Flux	MINARET (S_N)
Radial mesh length [cm]	0.5, 1, 2, 4 (fine around control rod, coarse in the reflector)
Radial mesh order	1
Axial mesh length [cm]	10
Axial mesh order	2
S_N order	6 (72 directions + hexagonal quadrature)
Anisotropy	P1

D. TRIPOLI-4® modeling

The different reference calculations for the Phenix-like and BoC 42nd Phenix configuration are performed with TRIPOLI-4®. Every geometrical part of the reactor is created as close to the design dimensions as possible and with the same dimensions as the APOLLO3® lattice and core calculations. Zones with inherent geometrical complexity are described as homogenized, assuming that this does not lead to relevant discrepancies. This is the case for the Plenum (ZTRS zone in the Figure 17), the lower axial reflector (SPN in the Figure 17) and upper and lower part of the control rod (SSVS, SSVSS, SSVI, SSVII and SSVIII in the Figure 17). The spacing wire, as in the lattice calculation is homogenized within the cladding.

Monte-Carlo simulations are performed with 30 000 batches of 30 000 neutrons to ensure a statistical error of approximately $\pm 3.\,10^{-5}$ on the reactivity and less than 0.1% (in the fissile zone) for local isotopic reaction rates of heavy nuclei. The number of discarded batches was automatically chosen by TRIPOLI-4® with a convergence criterion for the multiplication factor (mainly 80-discarded batch).

E. Data exchange between GERMINAL and APOLLO3®

In order to couple APOLLO3® and GERMINAL for a multiphysics calculation, they need to exchange data. The only input data related to neutronics for GERMINAL input data is the local heat rate, which can be easily, compute by APOLLO3® and provided to GERMINAL. GERMINAL and APOLLO3® do not have common API interface so that it must have been created for this work.

In the other direction, GERMINAL output data cannot be directely provided to APOLLO3®. Data available from GERMINAL for each pin slice are the central and surface temperatures of the pellet (T^0_{fuel},T^R_{fuel}), the inside and outside cladding temperature (T^{in}_{clad}, T^{out}_{clad}), the canal temperature (T_{canal}), and the quantity of fission gases produced and remained in the pellet (N^{prod}_{FG},N^{ret}_{FG}). This fission gas quantity is computed by GERMINAL independently from APOLLO3® and MENDEL. Moreover, APOLLO3® for the given multiparametrization can understand only:

- T_{fuel} : uniform temperature inside the pellet
- T_{Na} : uniform temperature of the coolant in the all subassembly section, including the interassembly sodium
- T_{steel} : uniform temperature of the cladding and the hexagonal tube).
- $N^t_{FG,AP3}$: the local isotopic composition of FG isotopes in APOLLO3®

Hence, the GERMINAL data availbale should be tansform to obtain the four APOLLO3® input data.

T_{fuel} must be determined in order to conserve the global reaction rate of the pellet. By considering a constant flux inside the pellet, a linear behavior of the cross-sections in regards of the temperature (which is the hypothesis used to interpolate the cross-sections in the MPO) and a quadratic temperature distribution inside the pellet, the uniform temperature can be considered as follows:

$$T_{fuel} = a \cdot T^0_{fuel} + (1-a) \cdot T^R_{fuel} \mid a = 0.5$$

For the coolant and the structures, the hexagonal tube and the sodium outside the subassembly are considered at the same temperature than the sodium inside the hexagonal tube, which gives:

$$T_{Na} = T_{canal}$$

$$T_{steel} = \frac{N_{pins} \cdot S_{clad} \cdot \left(0.5 \cdot T^{in}_{clad} + 0.5 \cdot T^{out}_{clad}\right) + S_{HT} \cdot T_{canal}}{N_{pins} \cdot S_{clad} + S_{HT}}$$

For the fission gas quantity (Xenon and Krypton isotopes), a leakage coefficient is created:

$$\chi^t_{FG} = \frac{N^{ret,t}_{FG}}{N^{ret,t-\delta t}_{FG} + N^{prod,t}_{FG} - N^{prod,t-\delta t}_{FG}}$$

This coefficient is then used in APOLLO3® to correct the isotopic composition of the fission gases computed by MENDEL:

$$N^t_{FG,AP3} = \chi^t_{FG} \cdot N^t_{FG_{MENDEL}}$$

F. Uncertainty propagation with sensitivities and the first linear approximation

Sensitivities define the behavior of the quantity of interest around the calculated point. With the first linear approximation, the analytical formula of the quantity of interest can then be expressed as follow:

$$R(\delta p_1, \delta p_2, \dots, \delta p_N) = R^0 \cdot \left(1 + \sum_{i \in [i,N]} S^R_{p_i} \delta p_i\right) \tag{7-22}$$

With R^0 the non-perturbed quantity of interest and δp_i the variation on the input nuclear data p_i (related to the sensitivity $S^R_{p_i}$).

If δp_i are considered as random variables centered on zero where $Var(\delta p_i) = \frac{Var(p_i)}{p_i^2}$ and $corr(p_i, p_j) = corr(\delta p_i, \delta p_j)$. The propagated uncertainty is then the variance square root of the random variable linear combination:

$$\begin{aligned} \Delta R = \sqrt{Var(R)} &= \sqrt{\sum_{i \in [i,N]} \sum_{j \in [1,N]} corr(\delta p_i, \delta p_j) \cdot S^R_{p_i} \cdot \sqrt{Var(\delta p_i)} \cdot S^R_{p_j} \cdot \sqrt{Var(\delta p_j)}} \\ &= \sqrt{\sum_{i \in [i,N]} \sum_{j \in [1,N]} corr(p_i, p_j) \cdot S^R_{p_i} \cdot \Delta p_i \cdot S^R_{p_j} \cdot \Delta p_j} \\ &= \sqrt{S^T \cdot M \cdot S} \end{aligned} \tag{7-23}$$

With:

$$m_{ii} = \frac{Var(p_i)}{{p_i^0}^2} \tag{7-24}$$

$$m_{ij} = corr(p_i, p_j) \cdot \frac{\sqrt{Var(p_i)}}{p_i^0} \cdot \frac{\sqrt{Var(p_j)}}{p_j^0} \tag{7-25}$$

G.Isotopes and reactions initially contain in COMAC V1

Table XXVIII. Isotopes and reactions initially contain in COMAC V1

Isotope	(n,γ)	(n,f)	(n,n)	(n,n')	(n,xn)	ν_p	ν_d	χ_p
^{233}U	x	x	x	x	x	x	x	x
^{234}U	x	x	x	x	x	x	x	x
^{235}U	x	x	x	x	x	x	x	x
^{236}U	x	x	x	x	x	x	x	x
^{237}U	x	x	x		x	x	x	x
^{238}U	x	x	x	x	x	x	x	x
^{237}Np	x	x	x	x	x	x	x	x
^{238}Np	x	x	x	x	x			
^{239}Np	x	x	x	x	x			
^{238}Pu	x	x	x	x	x	x	x	x
^{239}Pu	x	x	x	x	x	x	x	x
^{240}Pu	x	x	x	x	x	x	x	x
^{241}Pu	x	x	x	x	x	x	x	x
^{242}Pu	x	x	x	x	x	x	x	x
^{241}Am	x	x	x	x	x	x	x	x
^{242m}Am	x	x	x	x	x	x	x	x
^{243}Am	x	x	x	x	x	x	x	x
^{242}Cm	x	x	x	x	x	x	x	
^{243}Cm	x	x	x	x	x	x		
^{244}Cm	x	x	x	x		x		
^{245}Cm	x	x	x	x	x	x	x	
^{246}Cm	x	x	x	x	x	x		
^{247}Cm	x	x	x	x	x	x		
^{248}Cm	x	x	x	x	x	x		

Isotope	(n,γ)	(n,n)	(n,n')	(n,xn)	Isotope	(n,γ)	(n,n)
^{1}H	x	x			^{114}Cd	x	
^{10}B	x	x			^{115}In	x	
C	x	x	x		^{123}Sb	x	
^{16}O	x	x	x	x	^{125}Sb	x	
^{23}Na	x	x	x	x	^{127m}Te	x	
^{24}Mg	x	x	x	x	^{129}I	x	
^{25}Mg	x	x	x	x	^{133}Xe	x	
^{26}Mg	x	x	x	x	^{135}Xe	x	
^{27}Al	x	x	x	x	^{133}Cs	x	
^{51}V	x	x	x	x	^{134}Cs	x	
^{50}Cr	x	x			^{135}Cs	x	
^{52}Cr	x	x	x	x	^{137}Cs	x	
^{53}Cr	x	x			^{140}La	x	
^{54}Cr	x	x			^{141}Ce	x	

^{55}Mn	x	x		x	^{141}Pr	x	
^{54}Fe	x	x	x	x	^{143}Pr	x	
^{56}Fe	x	x	x	x	^{147}Nd	x	
^{57}Fe	x	x	x	x	^{148}Nd	x	
^{58}Fe	x	x	x	x	^{150}Nd	x	
^{59}Co	x	x	x	x	^{147}Pm	x	
^{60}Co	x	x	x	x	^{148}Pm	x	
^{58}Ni	x	x	x	x	^{149}Pm	x	
^{60}Ni	x	x	x	x	^{151}Pm	x	
^{61}Ni	x	x	x	x	^{147}Sm	x	
^{62}Ni	x	x	x	x	^{148}Sm	x	
^{64}Ni	x	x	x	x	^{105}Ru	x	
^{89}Y	x				^{150}Sm	x	
^{90}Zr	x	x	x	x	^{151}Sm	x	
^{91}Zr	x	x	x	x	^{152}Sm	x	
^{92}Zr	x	x	x	x	^{153}Sm	x	
^{94}Zr	x	x	x	x	^{154}Sm	x	
^{95}Zr	x	x	x	x	^{153}Eu	x	
^{96}Zr	x	x	x	x	^{154}Eu	x	
^{95}Nb	x				^{155}Eu	x	
^{92}Mo	x	x	x	x	^{156}Eu	x	
^{94}Mo	x	x	x	x	^{157}Eu	x	
^{95}Mo	x	x	x	x	^{155}Gd	x	x
^{96}Mo	x	x	x	x	^{174}Hf	x	x
^{97}Mo	x	x	x	x	^{176}Hf	x	x
^{98}Mo	x	x	x	x	^{177}Hf	x	x
^{99}Mo	x	x	x	x	^{178}Hf	x	x
^{100}Mo	x	x	x	x	^{179}Hf	x	x
^{99}Tc	x				^{180}Hf	x	x
^{103}Ru	x				^{109}Ag	x	
^{149}Sm	x	x	x	x	^{110m}Ag	x	
^{103}Rh	x	x	x	x	^{113}Cd	x	
^{105}Rh	x				^{108}Pd	x	
^{107}Pd	x						

H. Relation between cycles for adjoint depletion

To connect two cycles C and $C-1$ during adjoint fuel depletion, the adjoint isotopic composition field must be extrapolated from the configuration of the cycle C to the configuration of the cycle $C-1$. To achieve this extrapolation, the evolving sub-domains that correspond to the same medium between configurations C and $C-1$ must be identified. Once this identification is complete, the adjoint composition field of the $C-1$ cycle can be initialized. For sub-domains that match those in cycle C, the adjoint composition from the start of cycle C can be directly applied. For sub-domains that do not match any sub-domain in cycle C, the adjoint composition must be set to zero since they do not directly influence the final multiplication coefficient of cycle C [110].

Additionally, the connection between the two cycles must be established at the end of cycle C-1. Between the end of cycle C-1 and the beginning of cycle C, the flux is zero, but radioactive decay still occurs. Therefore, a backward depletion with zero flux must be performed during this period. The transition between the two cycles for adjoint depletion is summarized in Figure 69.

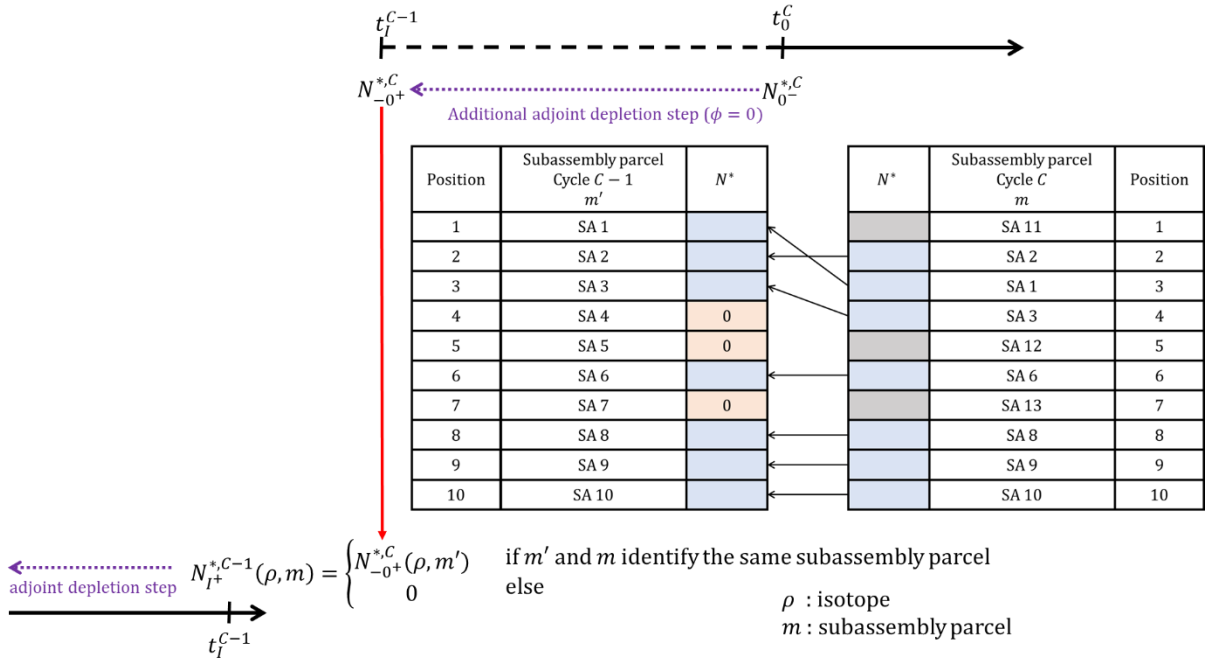

Figure 69. Connection between two cycles if the core configuration changes during an adjoint depletion calculation

I. Overall sensitivity to nuclear data for the reactivity loss coefficient

To compare the calculated reactivity loss coefficient with the experiment, it must be normalized by the delayed neutron fraction β_{eff}. If both quantities, reactivity loss and delayed neutron fraction, are expressed as functions of nuclear data perturbations, assuming a linear behavior around the calculated point, the following formula is obtained:

$$\alpha_{BU}^{¢}(\delta p_1, \delta p_2, \dots, \delta p_N) = \frac{\alpha_{BU}^{pcm,0} \cdot \left(1 + \sum_{i\in[i,N]} S_{p_i}^{\alpha} \delta p_i\right)}{\beta_{eff}^{0} \cdot \left(1 + \sum_{i\in[i,N]} S_{p_i}^{\beta} \delta p_i\right)} \tag{7-26}$$

Given the minor perturbations caused by uncertainties in nuclear data, a first-order Taylor expansion can be performed to linearize the equation, resulting in the following formula:

$$\begin{aligned} \alpha_{BU}^{¢}(\delta p_1, \delta p_2, \dots, \delta p_N) &\approx \frac{\alpha_{BU}^{pcm,0}}{\beta_{eff}^{0}} \left(1 + \sum_{i\in[i,N]} S_{p_i}^{\alpha} \delta p_i\right)\left(1 - \sum_{i\in[i,N]} S_{p_i}^{\beta} \delta p_i\right) \\ &\approx \frac{\alpha_{BU}^{pcm,0}}{\beta_{eff}^{0}} \left(1 + \sum_{i\in[i,N]} \left(S_{p_i}^{\alpha} - S_{p_i}^{\beta}\right) \delta p_i\right) \end{aligned} \tag{7-27}$$

Therefore, the global sensitivity vector can be considered as the difference between the reactivity loss coefficient sensitivity and the delayed neutron fraction ones. The sensitivities of β_{eff} introduce mainly two new contributors: the delayed neutron yields ν_d of ^{239}Pu and ^{238}U, which are among the top six. Additionally, there is a significant impact on the fission reactions of ^{238}U and ^{239}Pu, whose sensitivities have increased. However, the three most important reactions that carry the majority of the uncertainty are only minimally affected, as shown in the following table:

Table XXIX. Global sensitivities when considering delayed neutron fraction for the calculated value

	Sensitivities			COMAC V1 uncertainties		
	$S_{p_i}^{\alpha}$	$S_{p_i}^{\beta}$	$S_{p_i}^{\alpha} - S_{p_i}^{\beta}$	α_{BU}	β_{eff}	α_{BU}/β_{eff}
TOTAL				**6.943**	**2.463**	**7.333**
^{238}U (n,γ)	-1.579	-0.011	-1.568	5.666	0.125	5.632
^{240}Pu (n,γ)	-0.216	-0.002	-0.214	2.261	-0.036	2.166
^{240}Pu (n,f)	-0.157	-0.038	-0.120	2.247	0.268	1.955
^{239}Pu ν_d	**0.000**	**0.413**	**-0.413**	**0.000**	**1.707**	**1.711**
^{239}Pu (n,f)	**0.879**	**-0.192**	**1.071**	**1.295**	**0.327**	**1.620**
^{238}U ν_d	**0.000**	**0.434**	**-0.434**	**0.000**	**1.453**	**1.458**
^{238}U (n,f)	**-0.219**	**0.263**	**-0.482**	**0.652**	**0.878**	**1.435**

^{239}Pu (n,γ)	0.408	-0.007	0.415	0.848	0.047	0.804
^{238}U (n,n')	0.088	0.000	0.088	0.795	0.000	0.781
^{241}Pu (n,γ)	0.038	0.000	0.038	0.558	0.000	0.558
^{239}Pu:^{107}Pd γ	0.027	0.000	0.027	0.507	0.000	0.507
^{239}Pu:^{101}Ru γ	0.039	0.000	0.039	0.499	0.000	0.499
^{99}Tc (n,γ)	0.019	0.000	0.019	0.471	0.000	0.471
^{150}Nd (n,γ)	0.001	0.000	0.001	0.417	0.000	0.417
^{239}Pu:^{153}Sm γ	0.008	0.000	0.008	0.364	0.000	0.364
^{239}Pu χ	-0.493	0.000	-0.493	0.349	0.000	0.349
^{239}Pu κ_f	-0.623	0.000	-0.623	0.341	0.000	0.341
^{240}Pu χ	-0.187	0.000	-0.187	0.284	0.000	0.284
^{240}Pu ν_d	0.000	0.050	-0.050	0.000	0.240	0.242
^{238}U:^{135}I γ	0.002	0.000	0.002	0.226	0.000	0.226
^{148}Sm (n,γ)	0.000	0.000	0.000	0.208	0.000	0.208
^{149}Sm (n,γ)	0.008	0.000	0.008	0.205	0.000	0.205
^{239}Pu:^{109}Ag γ	0.009	0.000	0.009	0.186	0.000	0.186
^{238}U:^{99}Mo γ	0.005	0.000	0.005	0.177	0.000	0.177
^{154}Sm (n,γ)	0.000	0.000	0.000	0.174	0.000	0.174
^{241}Pu χ	-0.169	0.000	-0.169	0.163	0.000	0.163
^{235}U (n,γ)	0.007	0.000	0.008	0.155	0.004	0.159

J. Burnup-based cell correction for “Last-Cycle” sensitivities

This cell correction consists of performing the same type of calculation as the subassembly case but in a 2D fissile subassembly section and to consider that the difference between LC and FB sensitivities are the same for the cell case and the local 2D subdomain case as follow:

$$\frac{S^{\Delta\rho,\mathrm{FB}}_{p,m_{\mathrm{BU}_1\to BU_2}}}{S^{\Delta\rho,\mathrm{LC}}_{p,m_{\mathrm{BU}_1\to BU_2}}} = \frac{S^{\Delta\rho,\mathrm{cell,FB}_{\mathrm{BU}_1\to BU_2}}_{p}}{S^{\Delta\rho,\mathrm{cell,LC}_{\mathrm{BU}_1\to BU_2}}_{p}} \tag{7-28}$$

With $S^{\Delta\rho}_{p,m_{\mathrm{BU}_1\to BU_2}}$, being the reactivity loss sensitivity to the parameter p in the geometrical subdomain m where the local burnup goes from BU_1 to BU_2 for the given reactivity loss. And $S^{\Delta\rho,\mathrm{cell,FB}_{\mathrm{BU}_1\to BU_2}}_{p}$ being the fully backtrack sensitivity to the parameter p for the $BU_1 \to BU_2$ reactivity loss in the cell case.

By appling this naive correction (corrected sensitivities are hereafter called CLC) on the subassembly case, the divergence of the discrepancy with time is stopped (see Figure 70), the median gap and the variation range of the discrepancy is significantly reduced for the Bateman term of fission, heavy nuclei capture and fission yields. For the Power terms, the trend is different. The discrepancy evolution through time is reduced but not stopped, the residual discrepancy is of a similar order of magnitude with an opposite sign and the range of discrepancy is increased.

These corrected sensitivities cannot pretend to replace an actual FB calculation, however it offers a sensitivity pertubation which tends towards FB sensitivities, making it a good way of analysing the impact of changing sensitivities for data assimilation.

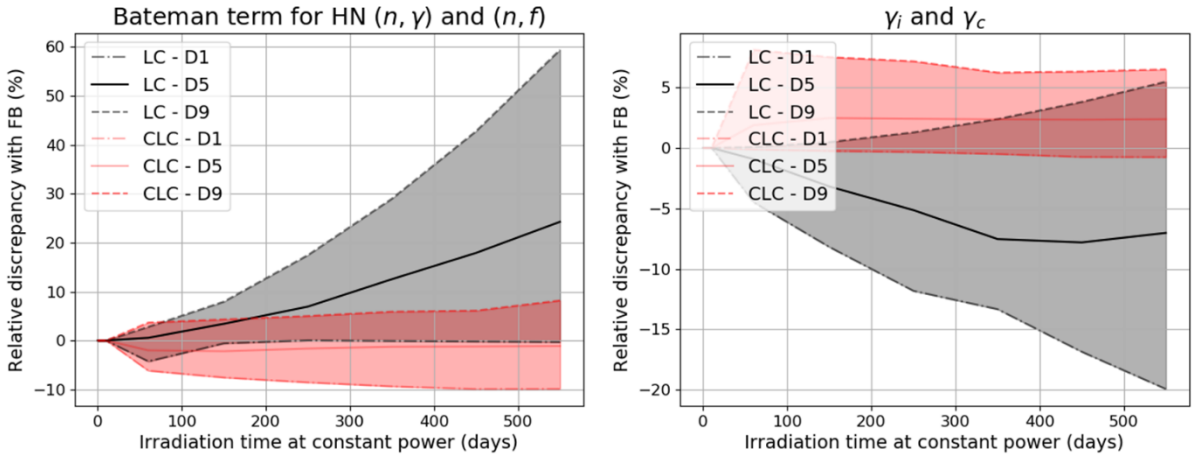

Figure 70. Remaining discrepancy with FB through irradiation time after LC sensitivity cell correction for the 150 main reactivity loss contributors